The Pennsylvania State University
The Graduate School
Department of Energy and Mineral Engineering

DEVELOPMENT OF HYDRAULIC FRACTURE NETWORK PROPAGATION MODEL IN SHALE GAS RESERVOIRS: 2D, SINGLE-PHASE AND 3D, MULTI-PHASE MODEL DEVELOPMENT, PARAMETRIC STUDIES, AND VERIFICATION

A Dissertation in

Energy and Mineral Engineering

by

Chong Hyun Ahn

Submitted in Partial Fulfillment
of the Requirements
for the Degree of

Doctor of Philosophy

August 2016

The dissertation of Chong Hyun Ahn was reviewed and approved* by the following:

John Yilin Wang

Associate professor of Petroleum and Natural Gas Engineering

Dissertation Advisor

Chair of Committee

Russell T. Johns

Professor of Petroleum and Natural Gas Engineering

Derek Elsworth

Professor of Energy and Geo-Environmental Engineering

James Terry Engelder

Professor of Geosciences

Luis F. Ayala H.

Professor of Petroleum and Natural Gas Engineering;

Associate Department Head for Graduate Education

FCMG Chair in Fluid Behavior and Rock Interactions

*Signatures are on file in the Graduate School

ABSTRACT

The most effective method for stimulating shale gas reservoirs is a massive hydraulic fracture treatment. Recent analysis using microseismic technology have shown that complex fracture networks are commonly created in the field as a result of the stimulation of shale wells. The interaction between pre-existing natural fractures and the propagating hydraulic fracture is a critical factor affecting the created complex fracture network; however, many existing numerical models simulate only planar hydraulic fractures without considering the pre-existing fractures in the formation. The shale formations already contain a large number of natural fractures, so an accurate fracture propagation model needs to be developed to optimize the fracturing process.

In this research, we first characterized the mechanics of hydraulic fracturing and fluid flow in the shale gas reservoir. Then, a 2D, single-phase numerical model and a 3D, 2-phase coupled model were developed, which integrate dynamic fracture propagation, interactions between hydraulic fractures and pre-existing natural fractures, fracture fluid leakoff, and fluid flow in a petroleum reservoir. By using the developed model, we conducted parametric studies to quantify the effects of treatment rate, treatment size, fracture fluid viscosity, differential horizontal stress, natural fracture spacing, fracture toughness, matrix permeability, and proppant size on the geometry of the hydraulic fracture network. The findings elucidate important trends in hydraulic fracturing of shale reservoirs that are useful in improving the design of treatments for specific reservoir settings.

TABLE OF CONTENTS

LIST OF FIGURES

LIST OF TABLES

ACKNOWLEDGMENT

I would like to express the deepest appreciation to various people who have been journeyed with me in recent years as I have worked on this dissertation. First, I owe an enormous debt of gratitude to my advisor Dr. John Yilin Wang who has encouraged and challenged me to be a better researcher and a student. Secondly, I would like to extend my sincere gratitude to my committee members, Dr. Derek Elsworth, Dr. Russell Johns and Dr. Terry Engelder, for the numerous ways they have helped me to finish this program. Thirdly, I would like to thank my friends and everyone else who helped contribute to my research. Thanks for keeping me company on long walks.

Lastly, and most of all, I would like to thank my wife, Kay, and my family. Through the struggles and trials of this dissertation they have been a constant source of joy and motivation.

Chapter 1 INTRODUCTION

1.1 Background Information

Natural gas is one of the predominant energy sources used worldwide. The demand for energy from natural gas is increasing because it is considered more environmentally friendly than oil. In the past, most natural gas has been extracted from conventional reservoirs; however, recent innovative technologies have enabled natural gas development from unconventional formations so that tight gas, coal bed methane, and shale gas have recently become available.

Almost 61% of the worldwide natural gas reserves are located in the Middle East and Eurasia, and only 4%, or approximately 283 Tcf, are located in the United States; however, if unconventional natural gas sources are considered, the recoverable natural gas reserves in the United States is approximately 2074 Tcf (Teledyne ISCO 2011); shale gas alone accounts for 750 Tcf of the total technically recoverable natural gas reserves in the United States (EIA 2011).

Shale gas reservoirs are organic-rich formations and include the source rock as well as the reservoir. Gas is stored in the pore space of the fracture and matrix, and it is adsorbed on the organic material and dissolved in brine. Shale formations have a permeability of less than 10^{-3} md. In addition, typical shale gas reservoirs have a net thickness of 50 to 600 ft., a porosity of 0.02 to 0.08, and a total organic carbon (TOC) of 1-14%, and they are found at depths of 1,000-13,000 ft. Shale gas accounts for approximately 40% of total U.S. natural gas production. The U.S Energy Information Administration (EIA) has predicted that shale gas will be the primary source used to meet this demand, with production anticipated to increase from 9.7 Tcf in 2012 to 19.8 Tcf in 2040. This will increase the shale gas share of the total US natural gas production to 53% in 2040 (EIA 2014).

As shale gas production has expanded into more basins and the technology has improved, the amount of shale gas reserves has increased dramatically; however, our understanding of the fracture propagation in low-permeability formations is still limited. New knowledge in this area leads to increased reserves and improved gas recovery for the US as well as globally. In sections 1.2, 1.3, and 1.4, critical literature for developing hydraulic fracture network propagation models is discussed.

1.2 Natural fractures

A significant amount of oil and gas reserves—more than 60% of the world's known conventional oil reserves and 40% of the world's gas reserves (Schlumberger Market Analysis, 2007)—are found in fractured reservoirs. **Figure 1-1** presents a clear example of the existence of subsurface natural fractures in the Marcellus shale in central Pennsylvania. The blue and green lines in the figure indicate the J1 and J2 natural fracture patterns.

In reservoirs with natural fractures, the opening fractures control the fluid flow paths so that the production mechanism in naturally fractured reservoirs is significantly different from that in conventional reservoirs. These natural fractures may close as the reservoir pressure drops, and they also influence the growth and final geometry of the hydraulic fractures used to enhance production (Lorenz, et al., 1988; Teufel and Clark, 1984). It is essential to determine the properties and the geometry of the natural fractures in a reservoir to design optimal recovery processes, such as hydraulic fracturing.

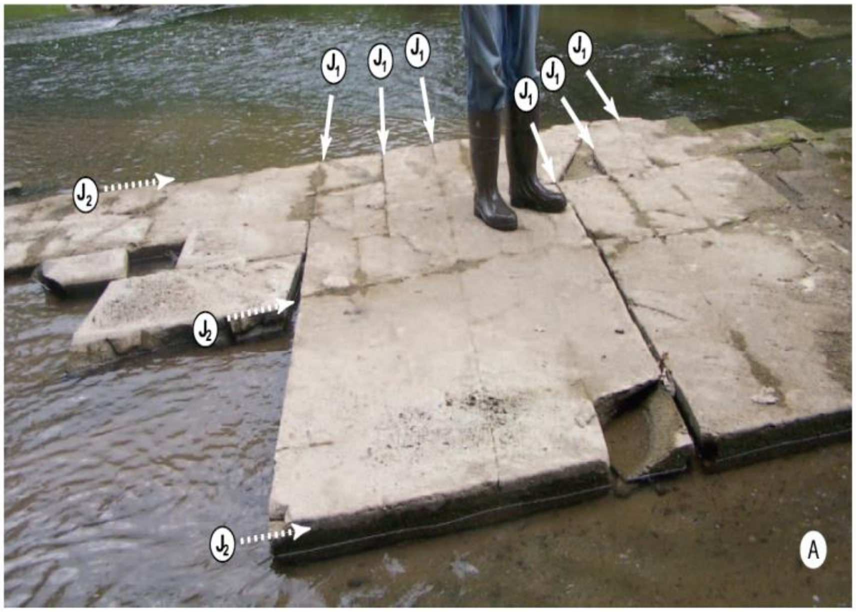

Figure 1-1. Marcellus Shale fracture pattern in central Pennsylvania.

(Engelder et al. 2009)

Numerous authors have investigated fracture propagation behavior in naturally fractured reservoirs both experimentally (Blanton 1986; Renshaw and Pollard 1998; Warpinski and Teufel 1987) and numerically (Taleghani et al. 2011, 2013; Weng et al. 2011; Zhang et al. 2007a, 2007b, 2008; Keshavarzi et al. 2012; Meyer and Bazan 2011; Yoon et al. 2014). The Renshaw and Pollard criterion has been extended to the intersection at the non-orthogonal angles by Gu and Weng (2010). Mathematical models of interactions between hydraulic fractures and natural fractures were reviewed and summarized by Poltluri at el. (2005).

Several events may occur during hydraulic fracture propagation in a naturally fractured reservoir, as shown in **Figure 1-2.**

First, the fracture tip reaches the interface, but the fluid front remains further back due to the fluid lag. At this stage, the net fluid pressure at the intersection point can be considered zero, but the natural fracture is already under the influence of the stress field generated by the induced fracture. This step can be analyzed by the mechanical interaction between the hydraulic fracture and the natural fracture without considering the effect of fluid flow. Possible outcomes from this interaction are shear slippage, arrest, and crossing, which are depicted in **Figure 1-2 (a), (b), and (c)**, respectively. This phenomenon happens rare when low viscosity fracture fluid such as slickwater is used.

When the fluid front reaches the natural fracture and the fluid pressure at the intersection point rises, the fluid may open the natural fracture if the fluid pressure is greater than the normal confining stress on the natural fracture. In other words, the hydraulic fracture propagates along the natural fracture in this case, as shown in **Figure 1-2 (d)**.

After crossing, it is possible that the natural fracture will remain closed if the fluid pressure is less than the normal stress that affects the natural fracture (**Figure 1-2 (e)**). In this case, the hydraulic fracture remains planar, and there may be enhanced leakoff if the natural fracture is filled with permeable material. If the fluid pressure is greater than the normal stress, the natural fracture will be opened, allowing the fluid to flow inside. This behavior is illustrated in **Figure 1-2 (f)**.

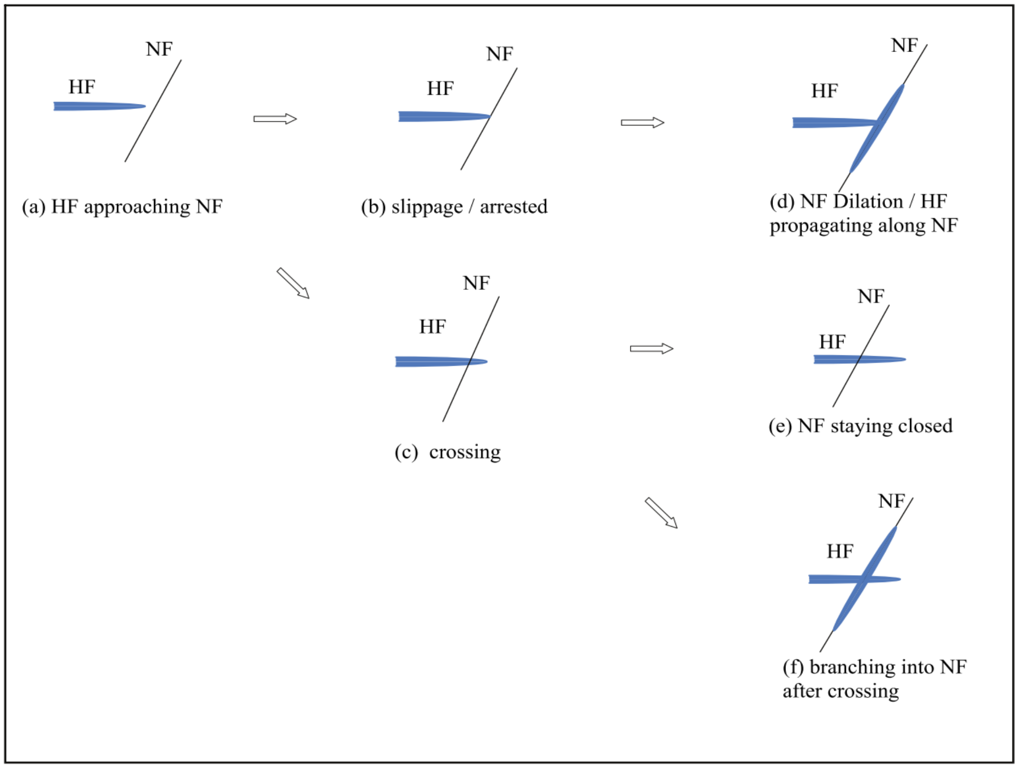

Figure 1-2. Breakdown of the interaction process between a hydraulic fracture and a natural fracture. (Gu and Weng et al, 2011)

1.3 Classic models of hydraulic fractures

Hydraulic fracturing was first used in the oil and gas industries during the 1930s when Dow Chemical Company discovered that by applying a large enough down-hole fluid pressure, it was possible to deform and fracture rock formations to maximize stimulation efficacy (Grebe et al., 1935). Currently, hydraulic fracturing is extensively used to increase oil and gas productivity and recovery. Numerous treatments are performed each year in a wide range of geological formations, including low-permeability gas fields, weakly consolidated offshore sediments, such as the Gulf of

Mexico, soft coal beds exploited for methane extraction, naturally fractured reservoirs, and geometrically complex formations.

A hydraulic fracture is created in two phases (Weijers, 1995). First, a fluid called "pad" is injected into the formation. When the down-hole pressure exceeds the "breakdown pressure," a fracture is initiated and then propagates into the formation. The second phase is called the "slurry phase." A mixture of viscous fluid and proppant is pumped into the formation to extend the fracture and to transport the proppants further into the created fracture (Veatch et al., 1989). The geometry of the created fracture is dependent on the rock's mechanical properties, in-situ stresses, the rheological properties of the fracturing fluid, and local heterogeneities, such as natural fractures and weak bedding planes (Weijers, 1995).

The process of modeling hydraulic fracturing is complex, not just because of the heterogeneity of the formation properties but also because of the physical complexities of the problem. It involves three processes: (i) mechanical deformation of the formation caused by the pressure inside the fracture, (ii) fluid flow within the fracture networks, and (iii) fracture propagation. There are two widely used fracture models: PKN and KGD.

The Perkins, Kern, and Nordgren (PKN) model (1961): The PKN model assumes that each vertical 2D strain-plane acts independently such that pressure changes along the height direction (z) is neglected while the changes in longitudinal is captured. This is reasonable if the length is two times greater than the height. In this model, the focus is on the effect of fluid flow and corresponding pressure gradients.

The Khristianovic, Geertsma, and de Klerk (KGD) model (1969): In the KGD model, all horizontal strain-planes act independently, which involves assuming that the fracture width changes along the length direction rather than through height. KGD may be reasonably accepted if the fracture height is much greater than the length or if a free slip occurs at the boundaries of the pay zone. In the KGD model, the fracture tip plays a more important role.

1.4 Recent existing simulation methods

In this section, three recent models will be discussed as well as the effect of pre-existing natural fractures. The modeling approaches, advantages, and disadvantages for each model will be summarized.

Zhang et al.'s 2D model: Zhang and colleagues (Zhang et al., 2007) have developed a 2D hydraulic fracture model using the Discrete Discontinuity Method (DDM) technique (Crouch and Starfield, 1983), which considers the criteria outlined above (Section 1.2) and includes elastic rock deformation coupled with both fluid flow and frictional slippage. In the model, discretization is only performed along the fractures. To improve the accuracy of these calculations, the model employs a mesh adaptive scheme, which reapplies discretization as the fracture grows (**Figure 1-5**).

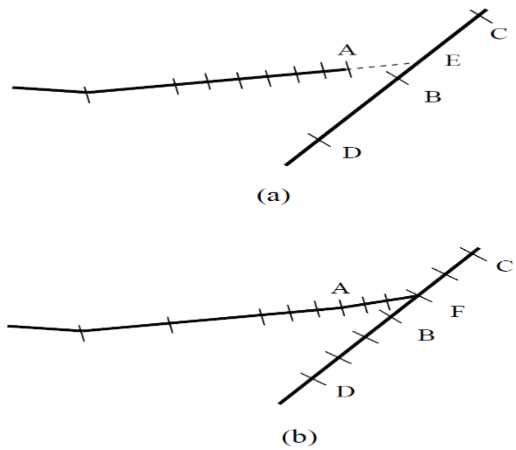

Figure 1-3. Schematic for the process of fracture coalescence (Zhang *et al.*, 2007). (a) Prior to coalescence and (b) post coalescence.

Since only the fracture itself is discretized and updated through the Finite Difference Method (FDM), the reservoir properties only slightly influence the model. In other words, simulations performed in different reservoir conditions, such as a low-permeability environment with a complex pre-existing fracture network, would not be suitable for this model. In addition, it is limited to the 2D plain-strain.

Keshavarzi et al.'s Extended Finite Element Method (XFEM): The most notable advantage provided by the use of the extended finite element method (XFEM) is the fact that fracture propagation can be modeled without any grid refinement. The crack is not modeled as a geometric entity and does not need to conform to element edges (Keshavarzi *et al.*, 2012); thus, it can reduce the computation time when simulating large-scale problems. **Figure 1-6** shows examples of the XFEM simulation results; however, this method has not yet been proven for the complex fracture network using multiple fracture propagations as provided by the UFM.

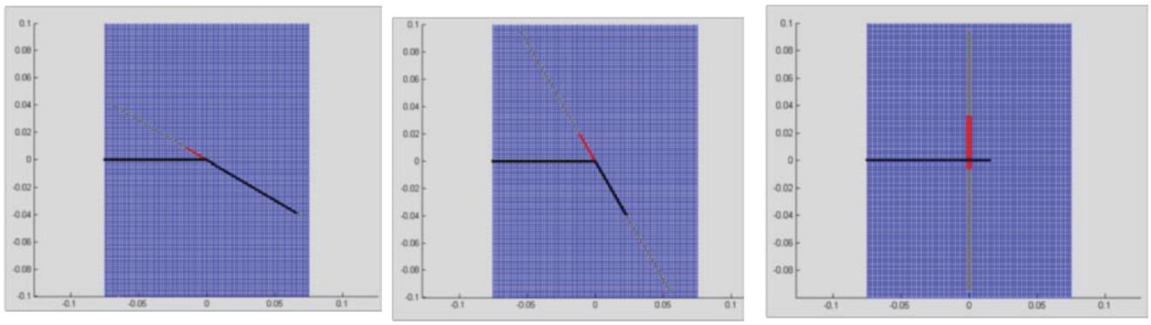

Figure 1-4. Fracture geometry as predicted by XFEM (Keshavarzi *et al.*, 2012).

Weng et al.'s Unconventional Fracture model (UFM): A new hydraulic fracture model was developed by Weng et al. (2011) to simulate the propagation of complex fracture networks in a formation with pre-existing natural fractures. Similar to Zhang's model, this model solves a system of equations governing fracture deformation in a complex fracture network with multiple propagating fracture tips. Fracture height growth is modeled in the same manner as in conventional pseudo-3D models. **Figures 1-7** and **1-8** show an example of the fracture geometry generated by UFM simulation. This model appears to be quite advanced and practical, but it has critical limitations: UFM is not fully coupled with a reservoir simulation, and the fracture leakoff model is based on Carter's model, which has a constant leakoff rate (Carter 1957). Various reservoir property changes, such as pressure and saturation changes, which occur continuously during the hydraulic fracture process, cannot be calculated with UFM.

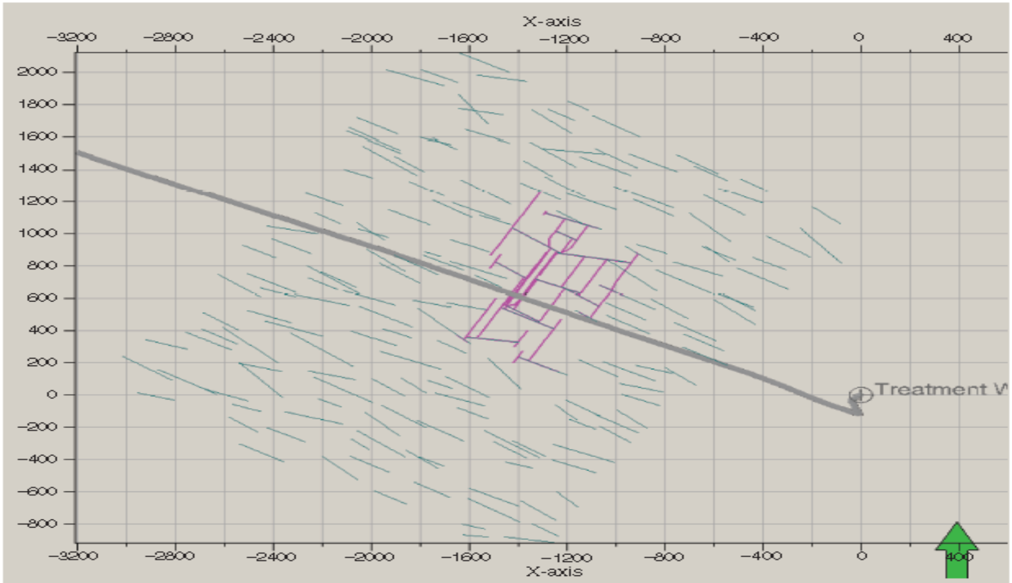

Figure 1-5. Schematic of a natural fracture and a hydraulic fracture using UFM (Weng *et al.*, 2011).

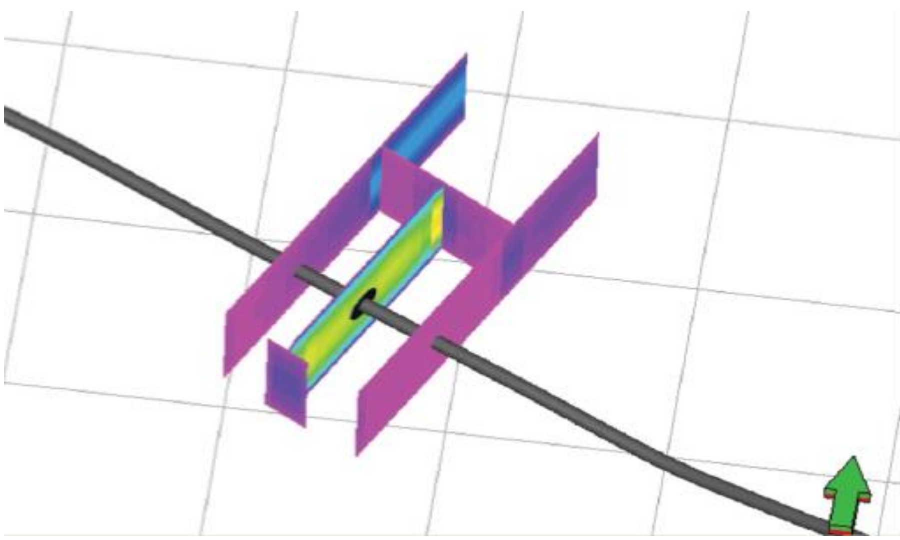

Figure 1-6. Fracture geometry using UFM (Weng *et al.*, 2011).

Meyer's Discrete Fracture Network (DFN): The DFN model is based on satisfying continuity, mass conservation, constitutive relationships, and momentum equations. This model could predict the final fracture geometry of a naturally fractured reservoir. As illustrated in **Figure 1-9**, DFN simulates the created fracture network in a reservoir, but it is not capable of simulating the change of reservoir properties during the fracture treatments.

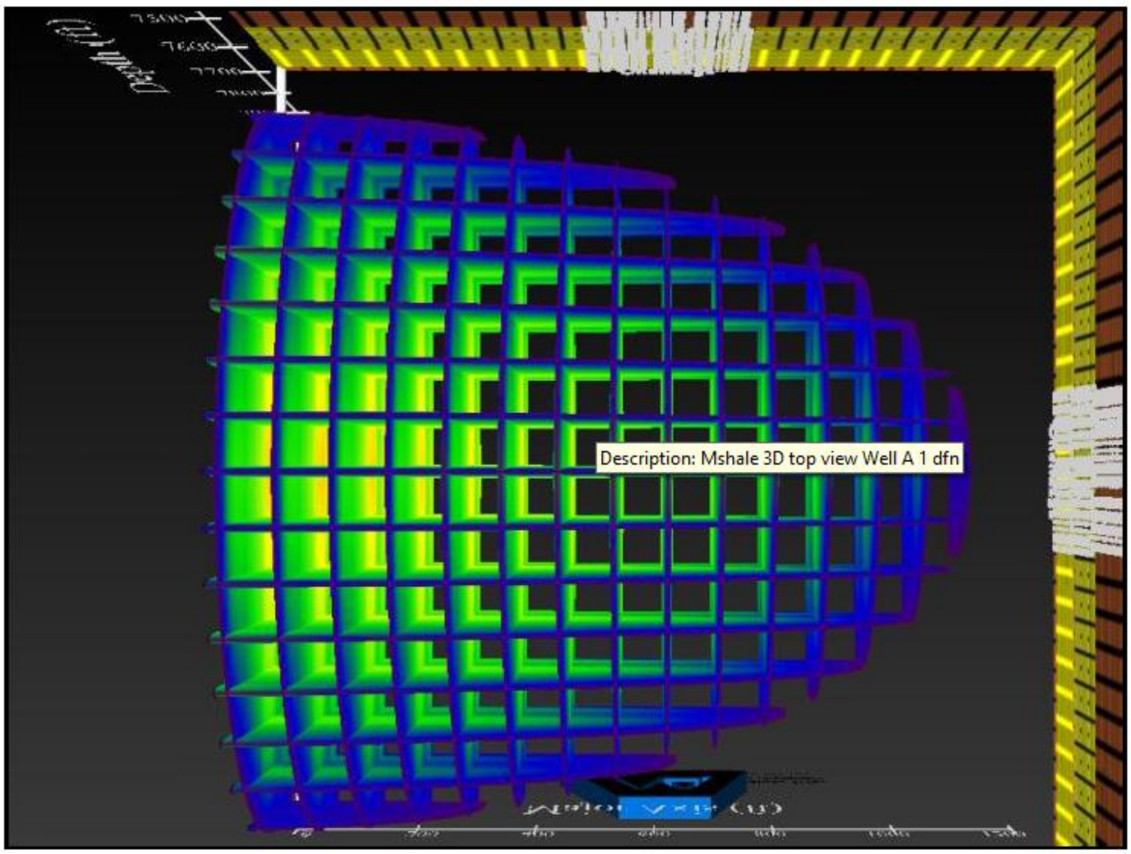

Figure 1-7. Fracture network simulated using the Discrete Fracture Network model (Meyer, 2011).

In summary, most of the available models used either commercially or in academia are not capable of capturing the complexity of hydraulic fracture propagation, fracture fluid leakoff, proppant transport, and the change of reservoir properties during treatment in shale gas reservoirs. For my study, I developed an advanced, coupled hydraulic fracture simulation model that addresses the complexity of fracture propagation in shale reservoirs.

1.5 Chapter reference

1. Blanton T.L. 1982 Experimental Study of Interaction Between Hydraulicalyy Induced and Pre-Existing Fractures. Paper SPE 10847 presented at the SPE Unconventional Gas Recovery Symposium, Pittsburgh, Pennsylvennia, USA, 16-18 May. doi: 10.2118/10847-MS.
2. Carter R.D. 1957. Derivation of the General Equation for Estimation the Extent of the Fracture Area. *In Drill. And Prod. Prac.* API, ed. Howard, G.C. and Fast, C.R., 261-268. NY.
3. Crouch, S.L. and Starfield, A.M. 1983. *Boundary Element Methods in Sold Mechanics: With Application in Rock Meechanics and Geological Engineering.* London: George Allen and unwin.
4. EIA (2011). Review of Emerging Resources: U.S. Shale Gas and Shale Oil Plays, U.S. Energy Information Adminstration.
5. EIA (2014). Annual Energy Outlook 2014, U.S. Energy Information Adminstration.
6. Engelder, T., Lash, G.G. and Uzkategui, R.S. Joints sets that enhances Middle and Upper Devonian gas shales of the Appalechian Basin. AAPG Bulletin **93** (7): 857-889. July, 2009.
7. Geertsma, J. and de Klerk, F. 1969. A Rapid Method of Predicting Width and Extent of Hydraulic Induced Fractures. J Pet Technol 21 (12): 1571-1581. SPE-2458-PA. http://dx.doi.org/10.2118/2458-PA.
8. Grebe, J.J. and Stoesser, M. 1935. Increasing crude production 20,000,000 bbl. from established fields. *World Petroleum J*, (August), 473-82.
9. Gu, H., Weng, X., Lund, J.B., Mack, M.G., Ganguly, U. and Suarez-Rivera, R. 2011. Hydraulic Fracture Crossing Natural Fracture at Non-Orthogonal Angles, A Criterion, Its Validation and Applications. Paper SPE-139984-MS presented at the SPE HFTC, Woodland, Texas, 24-26 Jan. doi: 10.2118/139984-MS.
10. Keshavarzi, R. and Mohammadi, S. 2012. A new Approach for numerical Modeling of Hydraulic Fracture Propagation in Naturally Fractured Reservoirs. SPE 152509-MS.
11. Lorenz, J. C. and Warpinski, N. R. 1996. Natural fracture characteristics and effects. Leading Edge, 15(8), 909-911.
12. Meyer, R. B. and Lucas W. Bazan. 2011. A Discrete Fracture Network Model for Hydraulically Induced Fractures - Theory, Parametric and Case Studies. Paer SPE 140514 presented at SPE Hydraulic Fracturing Technology Conference, 24-26 January 2011, The Woodlands, Texas, USA. doi: 10.2118/140514-MS.
13. Nordgren, R.P. 1972. Propagation of a Vertical Hydraulic Fracture. *SPEJ* **12** (4): 306-314. SPE-3009-PA. doi: 10.2118/3009-PA
14. Perkins, T.K. and Kern, L.R.1961. Widths of Hydraulic Factures. *J Pet Technol* **13** (9):

934-949; *Trans*., AIME, **222**. SPE-89-PA. doi: 10.2118/89-PA

15. Poltluri, N., D. Zhu, and Hill, A.D. 2005.The Effect of Natural Fractures on Hydreaulic Fracture Propagation. Paper SPE 94568 presented at the SPE European Foramtion Damgae Conference, Sheveningen, The Netherlands, 25-27 May. doi: 10.2118/94568-MS.
16. Renshaw, C. E., and D.D. Pollard. 1998. An experimetal Verified Criterion for Propagation Across Unbounded Frictional Interfaces in Brittle Linear Elastic Materials. International Journal of Rock Mechanics and Mining Science & Geomechanics, **32** (3): 237-249. doi: 10.1016/0148-9062(94)00034-4.
17. Taleghani, A.D. and Olson, J.E. 2011. Numerical modeling of Multistranded-hydraulic-Fracture Propagation: Accounting for the interaction Between Induced and Natural Fractures. *SPEJ* **16** (3): 575-581. SPE-124884-PA. doi: 10.2118/124884-PA.
18. Taleghani, A.D. and Olson, J.E. 2013. How Natural Fractres Could Affect Hydraulic-Fracture Geometry. *SPEJ* SPE-167608-PA. doi: 10.2118/167608-PA.
19. Teledyne ISCO (2011). Unconventional Natural Gas: Laboratory Modeling with High-Precision Syringe Pumps.
20. Teufel, L.W. and Clark, J.A. 1984. Hydraulic fracture propagation in layered rock: Experimental studies of fracture containment. *SPEJ* **24** (1): 19-32. SPE-9848-PA. doi: 10.2118/9878-PA.
21. Veatch, R.W., Moschovidis, Z. A., and Fast, C.R. 1989. An overview of hydraulic fracturing. In: Gidley, Holditch, Nierode, Veatch, editors. Recent advances in hydraulic fracturing. Monograph, Vol. 12, Richrdson: SPE, 1-38.
22. Warpinski, N.R. and Teufel, L.W. 1987. Influence of Geologic Discontinuities on Hydrauli Fracture Propagation. *J Pet Technol* **39** (2): 209-220; *Trans*., AIME, **283.** SPE 13224-PA. doi: 10.2118/13224-PA.
23. Weijers, L. 1995. The newar-wellbore geometry of hydraulic fractures initiated from horizontal and deviated wells. Ph.D. Dissertation, Delft Univ. of Tech.
24. Weng, X., Kresse, O., Cohen C., Wu R., and Gu H. 2011. Modeling of Hydraulic Fracutre Network Propagation in a Naturally Fractured Formation. *SPE Production & Operations* **26** (4): 368-380. SPE-140253-PA. doi: 10.2118/9878-PA. doi: 10.2118/140253-PA.
25. Zhang, X., Jeffery, R.G. 2008. Reinitiation or termination of fluid driven fractures at frictional bedding interfaces. *J. Geophys. Res.* 113: B08416. doi: 10.1029/2007JB005327.
26. Zhang, X., Jeffery, R.G., and Thiercelin, M. 2007a. Deflection and propagation of fruid-driven fractures at frictional bedding interfaces: A numerical investigation. *Journal of Structrual Geology* 29 (3): 396-410. Doi: 10.1016/j.jsg.2006.09.013.
27. Zhang, X., Jeffery, R.G., and Thiercelin, M. 2007b. Effects of Frictional Geological Discontinuities on Hydraulic Fracture Propagation. Paper SPE 106111 presented at the SPE Hydraulic Fracture Technology Conference, College Station, Texas, USA, 29-31 Jan. doi: 10.2118/106111-MS.Stoner, M.A.: *"Steady-State Analysis of Gas Production, Transmission and Distribution Systems"* paper SPE 2554 presented at the 1969 Annual Meeting of the SPE of AIME, Denver, Sept. 28-Oct.1

Chapter 2 PROBLEM STATEMENT AND OBJECTIVE

The literature review has demonstrated that there is a scarcity of knowledge in the areas of modeling hydraulic fracture propagation in shale gas reservoirs as well as in its application to improve current stimulations. It is also evident that this knowledge void extends to designing a fracture treatment because the sensitivity and the geometry of the final fracture network geometry is not predicted accurately. The aim of our research was to begin the process of filling this void. Our findings will improve the petroleum industry's understanding of hydraulic fracture propagation and its dynamic influence on shale formations, which is essential in planning and implementing efficient and profitable shale gas development.

Therefore, the goal of this research was to develop a model that is capable of simulating fracture propagation. Furthermore, the focus of this work was to obtain further understanding of the hydraulic fracture network resulting from a stimulation treatment as a function of key stimulation and geologic system parameters. Using the model developed, a series of parametric studies to evaluate the SRV, fracture-reservoir contact area, fracture width, and the intensity factor (indicates the complexity of a fracture network) were conducted to investigate the characteristics of hydraulic fracture geometry. The treatment rate, treatment size, fracture fluid viscosity, geomechanical parameters, differential horizontal stress, natural fracture spacing, and fracture toughness were studied to quantify the sensitivity.

To solve the problem and to achieve the research objectives, the following procedure was designed:

1. Conduct a complete and critical review of the relevant publications on the modeling of hydraulic fracturing in shale gas reservoirs;
2. Understand the fundamental science and physics of hydraulic fracture mechanics;
3. Develop a method for modeling a hydraulic fracturing process with the interaction of pre-existing natural fractures and formation property changes due to fracture fluid leakoff;
4. Conduct systematic numerical studies to identify novel engineering techniques and optimal stimulation parameters;
5. Document research results in papers and in a dissertation.

Chapter 3 DEVELOPMENT 2D, 1-PHASE HYDRAULIC FRACTURE PROPAGATION MODEL: PARAMETRIC STUDY OF RESERVOIR FRACTURE CONTACT AREA.

The most effective method for stimulating unconventional reservoirs is using properly designed and successfully implemented hydraulic fracture treatments. The interaction between pre-existing natural fractures and the engineered propagating hydraulic fracture is a critical factor affecting the complex fracture network. However, many existing numerical simulators use simplified model to either ignore or not fully consider the significant impact of pre-existing fractures on hydraulic fracture propagation. Pursuing development of numerical models that can accurately characterize propagation of hydraulic fractures in naturally fractured formations is important to better understand their behavior and optimize their performance.

In this paper, an innovative and efficient modeling approach was developed and implemented which enabled integrated simulation of hydraulic fracture network propagation, interactions between hydraulic fractures and pre-existing natural fractures, fracture fluid leakoff and fluid flow in reservoir. This improves stability and convergence, and increases accuracy, and computational speed. Computing time of one stage treatment with a personal computer is now reduced to 2.2 minutes from 12.5 minutes than using single porosity model.

Parametric studies were then conducted to quantify the effect of horizontal differential stress, natural fracture spacing (the density of pre-existing fractures), matrix permeability and fracture fluid viscosity on the geometry of the hydraulic fracture network. Using the knowledge

This chapter was presented on SPE Eastern regional meeting on October 2014 (SPE-171016-MS) and published at JUOGR 2014 vol 8. pg 25-45.

learned from the parametric studies, the fracture-reservoir contact area is investigated and the method to increase this factor is suggested. This new knowledge helps us understand and improve the stimulation of naturally fractured unconventional reservoirs.

3.1 Introduction

In recent years, development of shale gas reservoirs (organic-rich gas bearing shale formation) has become a more important means of accessing fossil energy resources. The key to that development is to stimulate these low-permeability reservoirs with successful and effective fracture treatments. In addition to field pilot studies, numerical modeling of the hydraulic fracture process is vital means of in improving understanding and improving effectiveness of fracture treatments in gas shales. Robust modeling of fracture propagation requires an integration of fracture fluid flow mechanics, particle transport, rock mechanics, petrophysics and fluid flow through porous media. Rock properties include 3 dimensional Young's modulus, shear modulus and Poisson ratio, tensile strength, fracture toughness, 3 dimensional insitu stresses, etc. Fracture fluid properties of interest include rheological models, viscosity, density, leakoff behavior, proppant transporting capacity, etc. which may be pressure, temperature, and shear rate dependent.

In reservoirs with natural fractures, the opening fractures control fluid flow paths such that the production mechanism in naturally fractured reservoirs is significantly different from that in conventional reservoirs. These natural fractures may close as the reservoir pressure drops, which also influences the growth and final geometry of hydraulic fractures that serve to enhance production (Lorenz, et al. 1988; Teufel and Clark 1984; Cipolla et al. 2010). Because natural fractures will significantly impact stimulation behavior, knowing the properties and geometry of pre-existing natural fractures in a reservoir can facilitate the design of effective hydraulic fracturing for efficient resource recovery.

Numerous authors have investigated fracture propagation behavior in naturally fractured reservoirs both experimentally (Blanton 1986; Renshaw and Pollard 1998; Warpinski and Teufel 1987) and numerically (Taleghani et al. 2011, 2013; Weng et al. 2011; Zhang et al. 2007a, 2007b, 2008; Keshavarzi et al. 2012; Meyer and Bazan 2011; Yoon et al. 2014). Renshaw and Pollard criterion was extended to implement the intersection behavior for non-orthogonal case by Gu and Weng (Gu and Weng, 2010). Mathematical models of interaction between hydraulic fracture and natural fractures were reviewed and summarized by Poltluri at el. (2005).

Fracture fluid leakoff impacts the reservoir significantly such that fracture-to-matrix flow needs to be captured into the hydraulic fracturing model. Howard and Fast (1970) expressed the fracture fluid filtration rate as a function of leak off coefficients. This is the same leakoff model used in the PKN (Perkins and Kern 1961; Nordgren 1972) and KGD models (Geertsma and de Klerk 1969). The widely used leakoff theory was developed by Carter and Settari (Carter, 1957; Settari, 1985). This approach uses a constant fluid leakoff coefficient to characterize the fluid leakoff rate. In fact, the net fracturing pressure changes with an increase in pumping time, which has an important effect on fluid loss. Therefore, the pressure dependent leakoff model derived (Carslwa and Jaeger 1956; Abousleiman 1991; Fan and Economides 1995; Baree and Mukherjee 1996).

Formation damage or the impact of fracture fluid leakoff may be classified as damage inside the fracture and damage inside the matrix (Han and Wang 2014; Han et al. 2014; Wang and Holditch et al. 2008, 2010) and it relates primarily to permeability reduction (Ning and Marcinew et al. 1995). Absolute permeability damage may result from clay swelling or migration, polymer invasion, and scale or paraffin precipitation; relative permeability damage is usually concomitant with absolute permeability damage, and is the direct result of fluid saturation and rock wettability changes triggered by fracturing fluid invasion.

The economic viability of many unconventional gas developments hinges on effective stimulation of extremely low-permeability rock. In most cases, economic production is possible only if a very complex, highly nonlinear fracture network can be crated that effectively connects a huge reservoir surface area to the well bore (Cipolla and Lolon et al. 2010; Mayerhofer et al. 2010; Palisch et al. 2010). Many conventional fracture treatments tends to promote planar fractures with high viscosity fracture fluid but stimulation in unconventional reservoirs, mostly in shale, use low viscosity fluid (Slickwater) to generate complex fracture network such that fracture-reservoir contact area is one of adequate indicator to measure the complexity and effectiveness of slickwater treatment.

Hydraulic fracturing simulators, especially for naturally fractured reservoirs, usually contain large complexity so that the solution method is not often computationally time efficient. Large heterogeneity of the properties in a solution domain generates stability and convergence problems such that required simulation time increases dramatically. Warren and Root proposed a methodology for capturing flow in such heterogeneous systems in a time efficient way; the proposed method was referred to as Dual-Porosity Modeling (Warren and Root 1963). In 1976, Kazemi et al. published a 2-phase, 3-Dimensional extension of the Warren and Root single-phase, 1-dimensional dual porosity model. Kazemi's model also accounted for gravity segregation, and redefined the fracture network shape factor (Kazemi, Merrill Jr. et al. 1976). Thomas and colleagues extended Kazemi's model by incorporating a third phase and further redefined the shape factor (Thomas, Dixon et al. 1983). These models all assumed pseudo steady-state flow in the matrix domain, and were incapable of capturing phase segregation in the matrix. Zhang stated that failure to model transient flow within the matrix blocks results in an underestimation of early time production (Zhang, Du et al. 2009). Saidi adopted such an approach in a 3-phase, 3-dimensional dual-porosity simulator (Saidi 1983). Similar approaches were taken Gilman (Gilman 1986), Wu (Wu and Pruess 1988), and by Beckner (Beckner, Chan et al. 1991). To develop a time efficient model, rather than solving fracture and matrix in a single domain, the dual porosity approach separates the reservoir into two sub-domains: fracture and matrix, and integrates to simulate fracture-to-matrix flow (fluid leakoff) in the new model.

The goal of this paper is to develop a model that is capable of simulating fracture propagation and reservoir property changes simultaneously in unconventional naturally fractured reservoirs. This model will then be exercised to conduct a series of parametric studies on the final hydraulic fracture geometry to investigate the sensitivity of key fracture network characteristics to those parameters. This methodology is intended to help researchers and engineers develop similar models to optimize the engineering processes and hydraulic fracture treatment in field.

3.2 Model development & validation

A new coupled hydraulic fracture model is presented that simulates propagation of complex fractures in a formation with pre-existing natural fracture. The fully coupled model of fluid flow in the fracture network and the elastic deformation of the fractures are brought together with another fully coupled model of fluid flow in the fracture and matrix through stationary and dynamic (moving) fracture/matrix grid system. In this way, the model takes into consideration the mutual influence between dynamic fracture propagation and the fluid flow across the entire domain (fracture and matrix). A numerical method has been used to solve both sets of governing equations (reservoir fluid flow and fracture propagation equations). Using an iterative procedure, pressure changes inside the matrix and fracture, change of principal stresses and fracture propagation boundaries (fracture length and width) are calculated in each time step during and after the fracture treatment. The interactions between hydraulic and natural fractures are also integrated into the model.

In this section, we detail the methodology to build this coupled, 2-diemnsional numerical model for simulating dynamic hydraulic fracture propagation, its interaction with existing natural fracture, and fracture fluid leakoff in unconventional reservoirs.

3.2.1 Discretization

The modeling starts with the construction of a grid system. In order to include all of the relevant physics, such as natural fracture effect on the fracture propagation, fluid leakoff, and reservoir fluid flow an advanced gridding system is employed. A moving coordinate system is developed to discretize the fracture domain. In the fracture domain, stationary coordinate and moving coordinate are both employed to capture the interaction between natural fracture and hydraulic fracture and dynamic fracture propagation. **Figure 3-1** provides 2-D schematic of the fracture domain discretization approach. Circle is stationary coordinate and triangle represents moving coordinate. In an index notation, even numbered coordinate in any axis is defined as a moving coordinate. In 3-dimensional system, another moving coordinate will be stacked in vertical direction.

When fracture propagates, moving coordinates will move dynamically toward the neighboring stationary coordinate. Reaching that neighboring stationary coordinate triggers examination of interaction criteria and the moving coordinate at that stationary coordinate will be activated to move toward the direction prescribed according to the interaction criteria. **Figure 3-2** depicts this methodology. In both stationary and moving coordinates, fracture width, fluid pressure and stress change will be calculated. Stationary coordinates are employed to incorporate the effect of natural fracture during fracture propagation and moving coordinates are used to capture dynamic fracture propagation. The element is a line that connects two coordinates in the fracture domain. The matrix domain is discretized using conventional system used by most finite difference method (FDM) reservoir simulators.

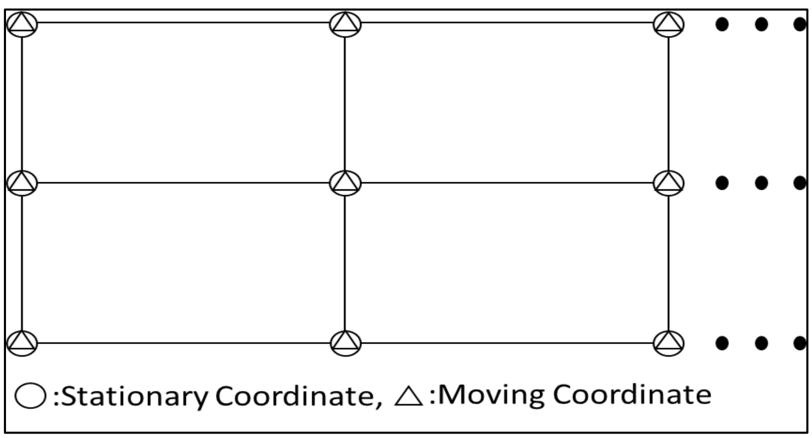

Figure 3-1. Schematic of Fracture Domain Discretization.

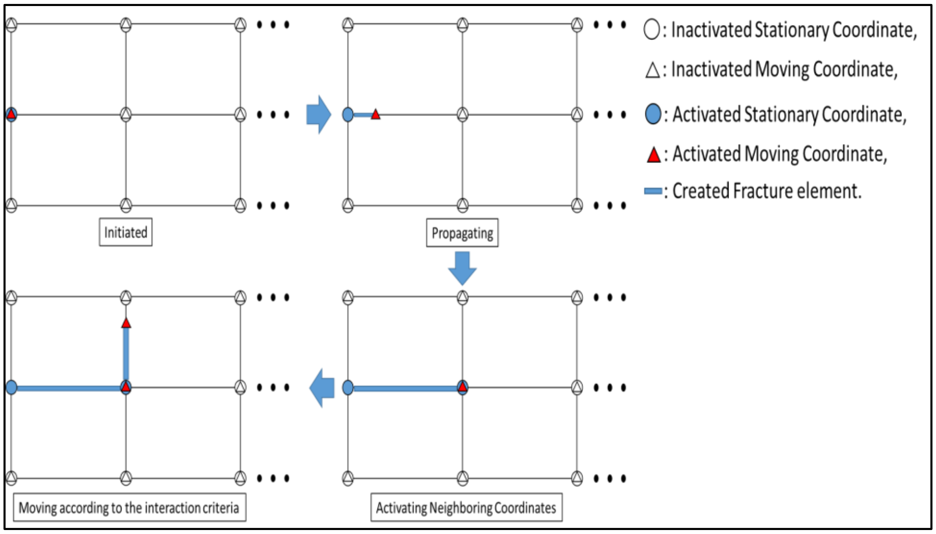

Figure 3-2. Coordinate System during fracture propagation.

Using this dual-porosity and moving coordinate approach, simulation time can be reduced dramatically compare to the single porosity approaches proposed by Ji et al. and Zeini Jahromi et al. (Ji et al. . When the domain is separated into fracture and matrix domains, grid refinement surrounding fracture grid blocks can be avoided to reduce calculation matrix size. In addition, convergence issue in single porosity system due to large heterogeneity between fracture and matrix also can be overcome. Therefore, more efficient simulation time is observed in our approach without losing accuracy. **Table 3-1** depicts the comparison between Zeini Jahromi's single porosity approach and our model. Using identical input values and simulating same domain size of 2500 ft by 3000 ft, simulation time is reduced about 82%.

Table 3-1. Simulation time comparison between single porosity model versus our model.

	Zeini Jahromi's single porosity model	Our model	%Reduced
Simulation time (min)	12.5	2.21	82.32

3.2.2 Fluid flow models

The fluid flow model is describes 2-dimensional flow of a single slightly compressible or compressible fluid. The equation for flow inside the fracture branch can be expressed using Newtonian fluid model (Lamb 1932):

$$\boldsymbol{q} = -\frac{\bar{w}^3 h_f}{12\mu B}\nabla \boldsymbol{p} \tag{3-1}$$

where p is fracture fluid pressure; q is the local flow rate in the fracture; and $\overline{w}$ is the average width. The flow through perforation is not modeled individually. The fracturing fluid is assumed to be injected at the natural fracture along the direction perpendicular to the minimum insitu stress.

Darcy's law for single-phase matrix-to-matrix flow may be substituted into the mass-conservation equation (**Equation 3-2**) to obtain the following fluid (aqueous)-flow equation.

$$\frac{\partial}{\partial x}\left[\beta_c K_x A_x \frac{K_r}{\mu_w B_w}\left(\frac{\partial p_w}{\partial x} - \gamma_w \frac{\partial Z}{\partial x}\right)\right]\Delta x + \frac{\partial}{\partial y}\left[\beta_c K_y A_y \frac{K_{rw}}{\mu_w B_w}\left(\frac{\partial p_w}{\partial y} - \gamma_w \frac{\partial Z}{\partial y}\right)\right]\Delta y = \frac{V_b}{a_c}\frac{\partial}{\partial t}\left(\frac{\varphi S_w}{B_w}\right) - q_{wsc} \tag{3-2}$$

where k is permeability in the x, y and z direction; k_r is relative permeability; μ is viscosity; B is formation volume factor; φ is porosity; γ is gravity of phase; R_s is solution GOR/GWR; S_w is the saturation of the aqueous phase; βc is transmissibility conversion factor; and ac is volumetric conversion factor.

Fracture fluid leakoff is integrated as modifying the boundary of the reservoir block which is associated with the fracture. The source term q_{wsc} (**Equation 3-3**) is modified when one of six boundaries of a cubic block becomes fractured as described in Equation 3. It is assumed that fracture fluid is an aqueous phase.

$$q_{leakoff} = q_{wsc} = -G_{f-m}\left(\frac{k_{rw}}{\mu_{avg}B_{avg}}\right)(p_p - p_f),$$

$$G_{f-m} = \beta_c\left(\frac{2A_{f,d}A_{m,d}}{A_{f,d}+A_{m,d}}\right)\left(\frac{1}{\Delta d}k_a\right). \tag{3-3}$$

Where $q_{leakoff}$ is fracture fluid leakoff rate; $G_{f\text{-}m}$ is modified geometric factor between matrix and fracture; p_p is the pore pressure; p_f is the pressure of fracture fluid; A is cross sectional area; f refers to fracture; m refers to matrix; *a* is associated direction (x, y or z); d is the distance between fracture and matrix coordinate. In a given time step and in each grid block which contains fractured boundary, **Equation 3-3** is incorporated into **Equation 3-2** to implement fracture fluid leakoff. In addition, to mimic the dynamic fracture growth, incremental length of each fracture branch in a given timestep is linearly interpolated and implemented in $G_{f\text{-}m}$.

This leakoff model generally follows the theory of pressure-dependent leakoff using boundary condition approach of the dual-continuum concept (Moinfar et al. 2013, 2014; Kazemi et al. 1976; Ozkan et al. 2010; Azom et al. 2012; Lemonnier et al. 2010). This approach involves obtaining the fracture-to-matrix transfers explicitly by imposing appropriate boundary condition between a fracture and its matrix block at each timestep of the simulation and it also contributes to the time efficient numerical solution method.

3.2.3 Geomechanics models

Fracture-width theories are based on the assumption that the fracture surface deforms in a linear elastic manner. This seems justified because of the usually large insitu stress, on which only small additional stress systems are superimposed (with the exception of the fracture tip area). For 2D plan-strain conditions, England and Green derived an equation for the width of a line crack between $x=-L$ and $x=+L$ (or $z=-h_f/2$ and $z=+h_f/2$) opened by an equal and opposite normal pressure distribution, p, on each side of the crack as exerted by a fluid (England and Geen, 1963). Assuming a symmetrically distributed in-situ normal stress, σ_h, opposing p, the pressure/width equation is:

$$\boldsymbol{w(x)=\frac{4(1-\nu^2)L_f}{E}\int_{x/L}^{1}\frac{f_{L1}df_{L2}}{\sqrt{(f_{L2}^2-l^2)}}\int_{0}^{f_{L2}}\frac{\Delta p(f_{L1})df_{L1}}{\sqrt{(f_{L2}^2-f_{L1}^2)}}}$$ (England and Green, 1963)

(3-4)

where E and υ represent Young's modulus and Poisson's ratio, respectively; p is fluid pressure; x/L, f_{L1} and f_{L2} are all fractions of fracture half-length. It could be simplified by using average pressure of a discrete fracture element between two fracture coordinates as describe in **Equation 5**.

$$\boldsymbol{w(x,t)=\frac{2(1-\nu^2)h_f}{E}\,(p_f-\sigma_n)} \qquad (3\text{-}5)$$

where p_f is the fluid pressure inside fracture and σ_n is normal stress acting perpendicular to fracture element. One can also substitute z or y for x and h_f for $2L_f$ to obtain the width in different principle axis.

Mechanical interaction between the hydraulic fracture (HF) and the natural fracture (NF) is incorporated using Renshaw and Pollard's method (1998). The criterion is given as

$$\frac{-\sigma_3}{T_o - \sigma_1} > \frac{\left(0.35 + \frac{0.35}{K_f}\right)}{1.06} \tag{3-6}$$

where σ_1 and σ_3 are far-field effective stresses (tensile is positive) acting parallel with and perpendicular to a propagating hydraulic fracture, respectively, T_0 is tensile strength of rock and K_f is coefficient of friction.

An explicit method is used to propagate the fracture tips. The algorithm first finds all the fracture tips and initiated tips that satisfy the criterion describes in **Equation 3-6**. For each propagating tip, the flow rate into that tip is calculated on the basis of the flow equation inside the fracture (**Equation 3-1**) to find the corresponding tip velocity as shown in **Equation 3-7** (Weng et al., 2011). It is assumed that tip velocity is equal to fluid velocity near the tip meaning all the hydraulically opened fractures are fully saturated with fracture fluid. The fluid or tip dilatancy is ignored because this models is designed for slickwater which generally has relatively low fluid viscosity around 2 cp.

$$v_{tip} = \frac{q_{tip}}{H_{fl}\bar{w}} \tag{3-7}$$

The tip with the highest velocity is extended by a prescribed distance d_{presc}. The other tips are extended proportionally to their velocities (Weng et al., 2011):

$$\boldsymbol{d_{tip}} = \frac{\boldsymbol{d_{presc} v_{tip}}}{\boldsymbol{v_{tip}^{max}}} \tag{3-8}$$

where d is extended distance. When a tip intersects with a natural fracture, it propagates to the direction satisfying the interaction criteria, as outlined above. Furthermore, a new fracture tip is initiated if the fluid pressure at the body of any fracture exceeds the normal stress acting on the associated natural fracture. Therefore, a complex fracture network is able to be created.

3.2.4 Solution method

At any given timestep, the created hydraulic fracture network is represented by connected fracture elements and coordinates. New elements and coordinates are activated (joins fracture) as described in the discretization section. Multiple element and coordinates can be activated in a single timestep as multiple tips are propagating and initiated. Each step of the simulation starts with extending the tips of the fracture branches. At the fracture tip, the following boundary conditions are satisfied:

$$\boldsymbol{p = \sigma_n, \quad w = 0, \quad q = 0} \tag{3-9}$$

where p, w and q are pressure, width and flowrate at the tip coordinates and using this boundary condition, width/pressure relation (**Equation 3-5**) and flow equation in the fracture (**Equation 3-1**), we can solve for the pressure, width and flowrate in each fracture element iteratively. The incremental volume of the fracture network and corresponding timestep also can be calculated.

Using the fracture pressure and the timestep calculated from the incremental total fracture volume as an initial guess, coupled dual continuum model using boundary condition approach, combination of **Equation 3-1, 3-2** and **3-3** can be solved to demonstrate the leakoff of the fracture fluid. Calculated leakoff volume will update the timestep for next iteration until the system satisfies mass balance equations (**Equation 3-10** to **3-12**). The local mass balance is given by continuity equation as

$$\frac{\partial q}{\partial s} + h_f \frac{\partial \overline{w}}{\partial t} + q_{Leak} = 0 \tag{3-10}$$

where s is the distance along the fracture and q_{leak} is defined in **Equation 3-3**. The global mass balance equation for this solution method is:

$$\int_0^t Q(t)dt = \int_0^{L(t)} \left[\left(\int_0^t q_{Leak}\, dt \right) + h_f \overline{w} \right] ds \tag{3-11}$$

where $Q(t)$ is injection rate, $L(t)$ is the total length of all fracture branches at time t, and H is fracture height. The resulting mass balance equation in the form of pressure, fracture dimension, and flowrate at element i is in **Equation 3-12**.

$$-\sum_{j=1}^{N_f} q_{ij}^t dt = \left(h_{fl,i}^t \overline{w}_i^t l_i^t - h_{fl,i}^{t-dt} \overline{w}_i^{t-dt} l_i^{t-dt} \right) - q_{leakoff}^t \tag{3-12}$$

where j is index of the element connected to i; N_f is the number of elements connected to i; h_f, w and l are height, width and length of the element i; and q_{leak} is the leakoff rate from element i to the connected matrix. The flowchart of numerical model is illustrated in **Figure 3-3**.

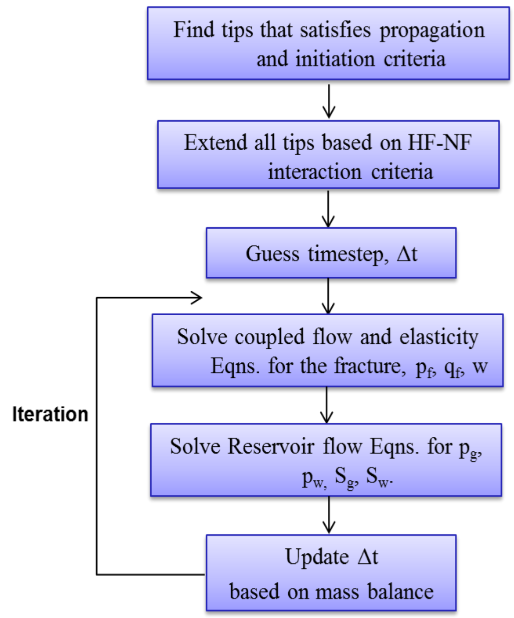

Figure 3-3. Schematic Flowchart of the numerical solution.

3.2.5 Validation

To check the validity of this model, it is compared with the PKN analytical solution. Using the same input values: injection rate = 10 bpm; minimum in-situ stress = 8497 psi; fluid viscosity = 1 cp; fracture height = 100 ft; Young's modulus = 3.74×10^6 psi, both models are exercised and results used for cross-validation. **Figure 3-4** shows the comparison and the predicted length and width versus time are identical.

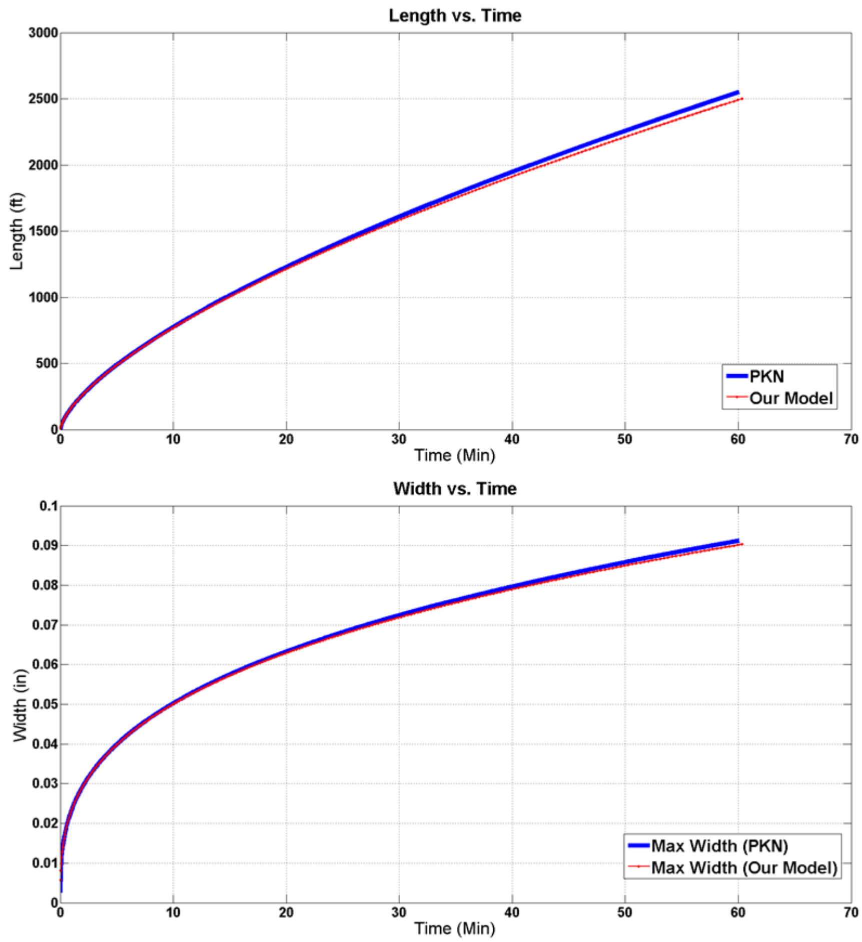

Figure 3-4. Validation results showing favorable comparison between PKN and model developed herein.

3.2.6 Sensitivity Study

Next, sensitivity study of gridding was carried out with grid size of 0.1 ft, 1 ft, 10 ft and 100 ft in the fracture domain. The results showed that sensitivity on the grid size is negligible between 0.1 ft to 1 ft having less than 0.001% differences in final length and width. If the grid size is increased to 10 ft final length is 1.2% larger and width is 0.3%

larger than 0.1 ft case. Using 100 ft showed 7% larger length and 4% larger width. **Figure 3-4** and **3-5** depicts the length and width versus time comparison plots for different grid settings. The simulations are performed on the same setting.

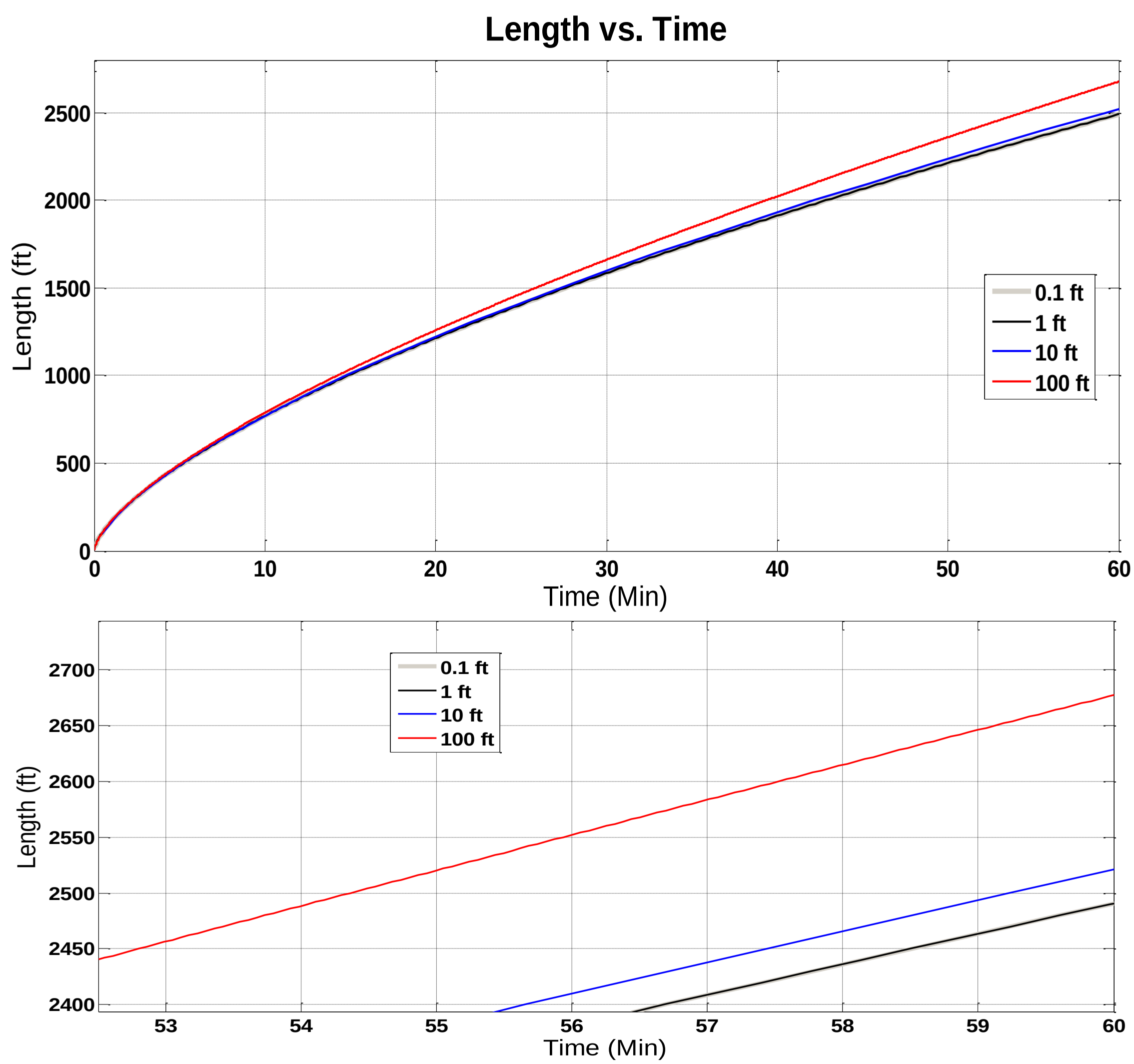

Figure 3-5. Length (ft) versus time (min). Top figure is from 0 min to 60 min and bottom figure shows zoomed over 53 min to 60 min.

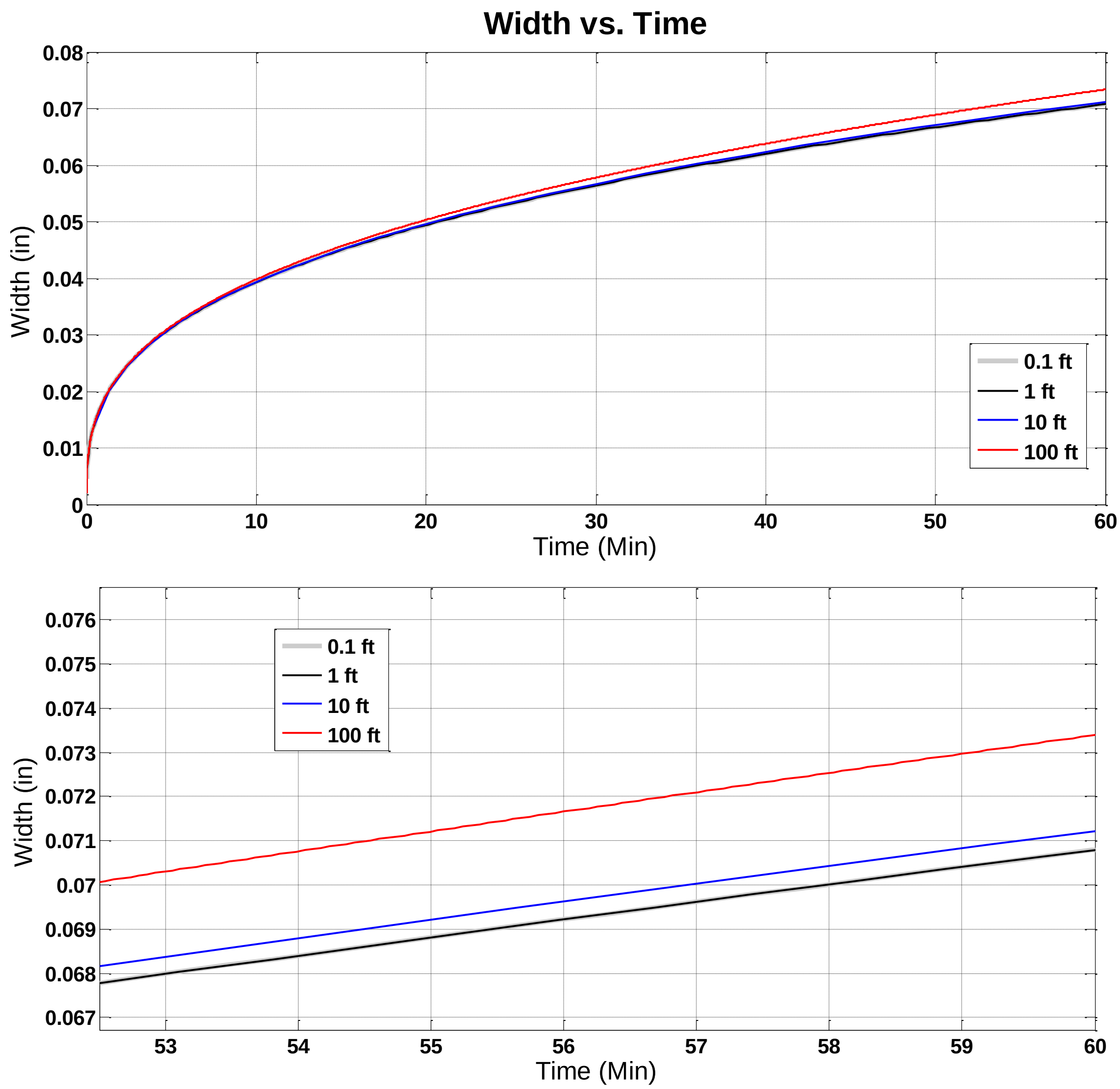

Figure 3-6. Width (in) versus time (min). Top figure is from 0 min to 60 min and bottom figure shows zoomed over 53 min to 60 min.

Lastly, parametric studies of reservoir permeability and fracture fluid viscosity were performed in this section. **Figure 3-6** shows the pressure distributions for k= 1 md, 0.1 md, 0.01md and 0.001 md and for μ= 1 cp, 10 cp and 20 cp. We can see that for k= 1 md, fracture geometries are sensitive to fracture fluid properties. When viscosity is low at μ= 1 cp, fracture could not propagate because leakoff is high; while viscosity is high at μ= 20 cp, fracture length is not longest because frictional pressure loss inside fracture is high; as optimized fluid (such as μ= 10 cp), fracture length is the largest. **Figure 3-7** show fracture fluid efficiency for three different fluids at permeability of 1 md, 0.1 md, 0.01 md, and 0.001 md. All the cases are simulated under same input values used for the validation case.

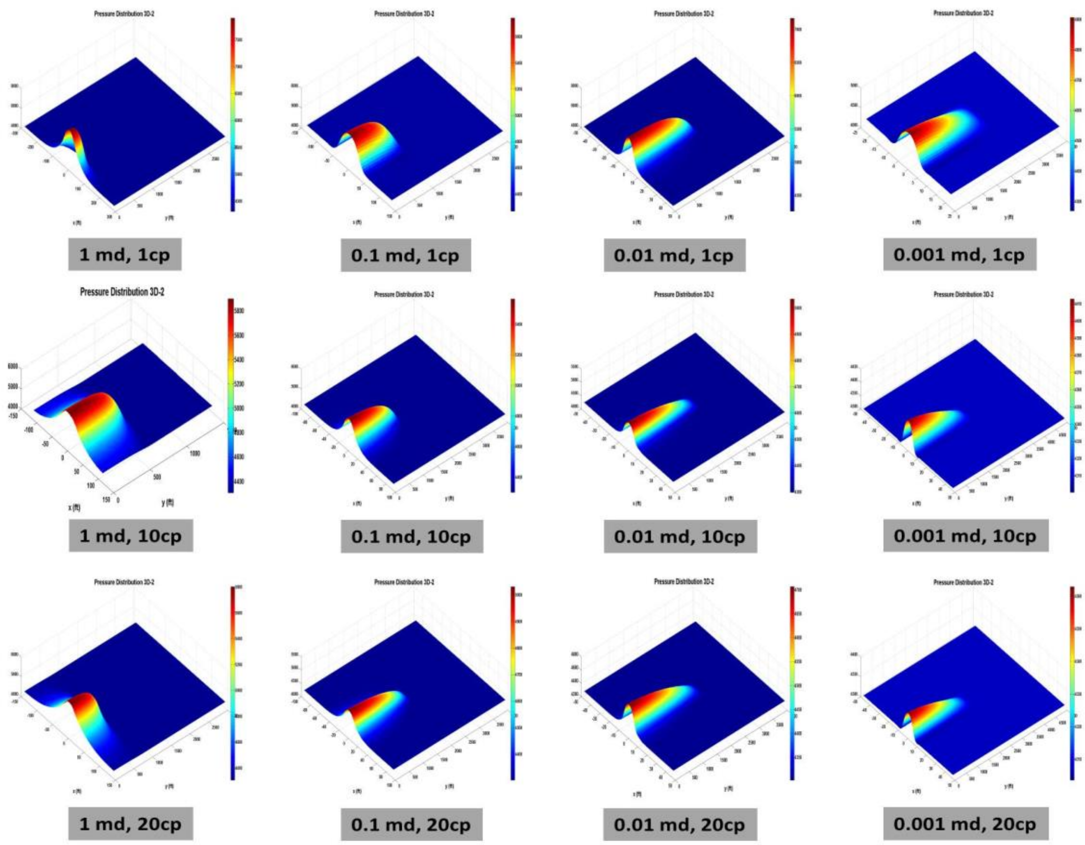

Figure 3-7. Pressure distributions from parametric analysis (permeability is shown in md and viscosity is in cp).

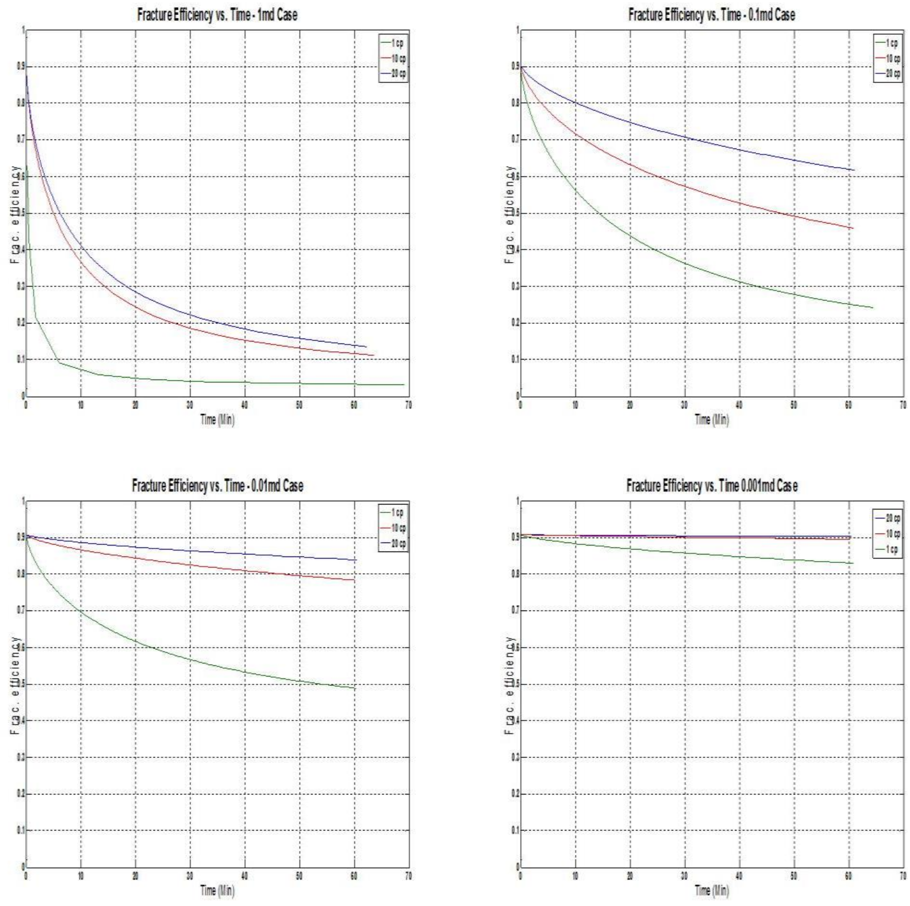

Figure 3-8. Fracture Efficiency from parametric analysis (green: 1cp, red: 10cp, blue: 20cp).

3.3 Parametric studies & analysis

We have developed and validated fully coupled model of complex hydraulic fracture propagation that can generate fracture network in a naturally fractured shale gas reservoir. Therefore, our coupled model will be used to investigate the impact of pertinent factors on ultimate fracture geometry, such as horizontal differential stress, natural fracture spacing, fracture fluid viscosity and matrix permeability. Numerical experiments and analysis are documented as follows.

In section 3.3.1, we performed a numerical experiment to quantify how horizontal differential stress affects fracture geometry. This exercise also allowed us to quantify the impact of differential stress on final fracture geometry.

In section 3.3.2, we conducted a study that quantifies the impact of natural fracture spacing on the fracture network. The density of the natural fracture were changed through spacing the pre-existing natural fractures by 1 ft, 10 ft and 100 ft in x-direction (minimum insitu stress direction) and 2 ft, 20 ft and 200 ft in y-direction (maximum insitu stress direction). This analysis allowed characterization of the impact of natural fracture spacing on fracture growth.

In section 3.3.3, the effect of fracture fluid viscosity is evaluated by performing several simulations using different viscosities that are widely used during slickwater fracturing.

In section 3.3.4, the effect of matrix permeability is evaluated by performing several simulations using different matrix permeability.

In section 3.3.5, the results from above are analyzed in terms of the fracture-reservoir contact area (*i.e.* reservoir surface area). Through this study, the fracture treatment parameters (injection rate and fracture fluid viscosity) that enlarge the area are investigated.

All parametric studies are performed using the input values listed in **Table 3-2, 3-4 and 3-5.** The minimum in-situ stress is acting perpendicular to the y-direction and the maximum horizontal in-situ stress is acting perpendicular to the x-direction in all simulation problems considered in this study, and fluid injection point is at (0,0) coordinate of the domain in all cases.

3.3.1. Effect of Horizontal Differential Stress ($\sigma_{H,max} - \sigma_{h,min}$)

The effect of stress anisotropy is investigated in this study. Input parameters are shown in **Table 3-2**. Natural fractures were spaced 1 ft parallel to y-axis and 2 ft parallel to x-axis and perforation is assumed to be located at (0,0) coordinate for all cases. As shown, we simulated the cases of maximum horizontal stresses.

Figure 3-9 illustrates final fracture geometries of the Case 3.1.1 to 3.1.3. The figures are generated in identical setting. As maximum horizontal stress increases, fracture network propagates longer in the direction perpendicular to the minimum horizontal stress (y-direction) but less propagation occurs in the x-direction. The width profile indicated by the colors shows that the fractures propagating perpendicular to the maximum horizontal stress (x-direction) have much smaller apertures than the one propagates to the y-direction. The net pressures acting on these fractures (propagating x-direction) are smaller, resulting in the illustrated fracture aperture response.

Table 3-2. Input parameters for Cases 3.1.1 to 3.1.3.

Perforation Location (0,0)	Cases		
Parameters	3.1.1	3.1.2	3.1.3
Initial Reservoir Pressure (psi)	4307.26	4307.26	4307.26
Fluid Viscosity (μ, cp)	10	10	10
Injection Rate (Q, bbl/min)	100	100	100
σ_h, min (psi)	8348.56	8348.56	8348.56
σ_H, max (psi)	8400	8500	8600
Permeability (k, md)	0.0001	0.0001	0.0001
Porosity (%)	6	6	6
Young's Modulus (E, psi)	3.74E6	3.74E6	3.74E6
Poisson's ratio (v, fractional)	0.2	0.2	0.2
Treatment Time (min)	60	60	60
Natural Fracture Spacing (X by Y, ft by ft)	1 X 2	1 X 2	1 X 2

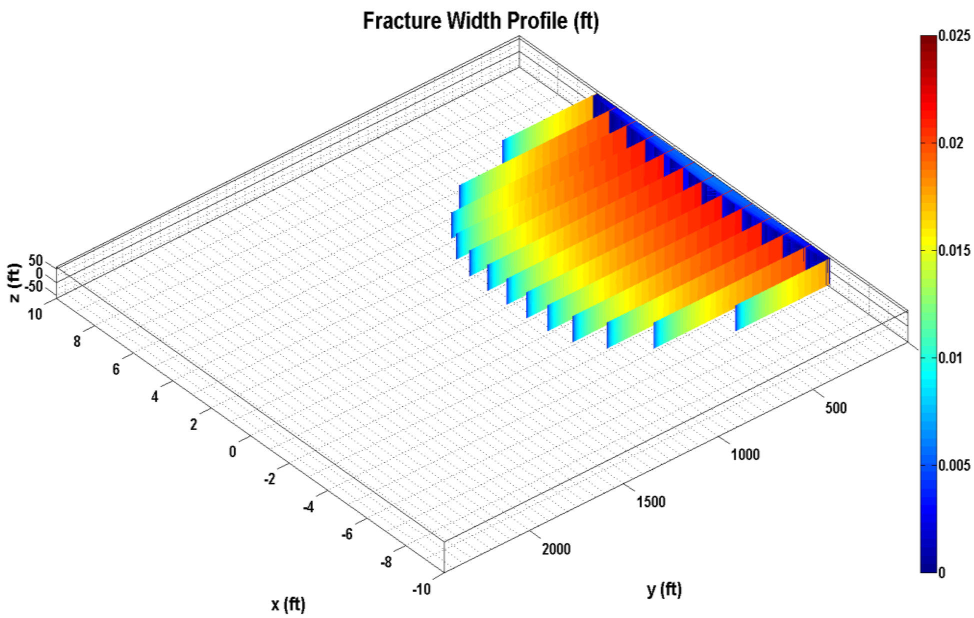

(a) Final Fracture Geometry from Case 3.1.1 ($\sigma_H - \sigma_h$ = 51.44 psi).

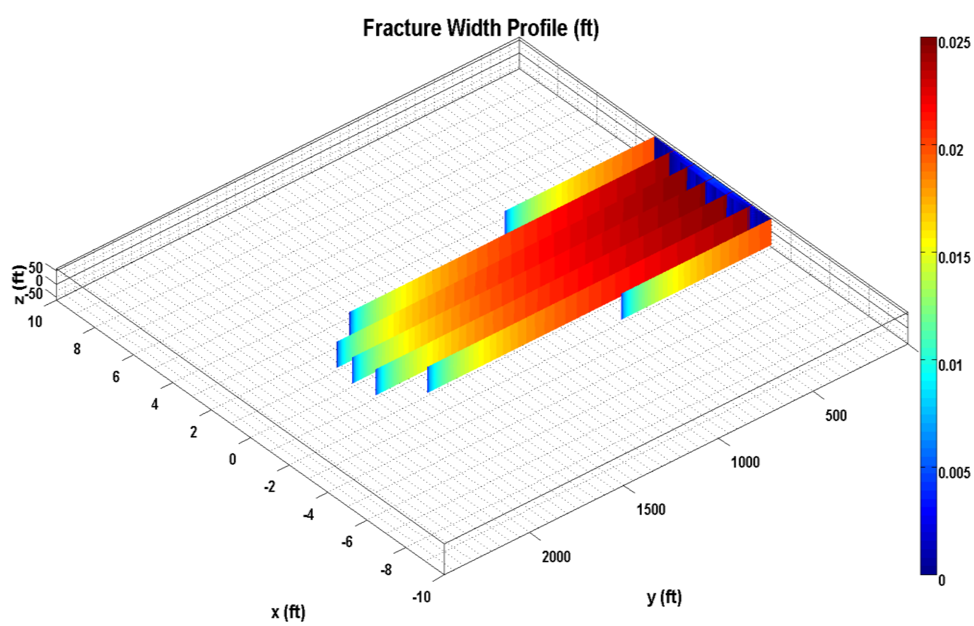

(b) Final Fracture Geometry from Case 3.1.2 ($\sigma_H - \sigma_h$ = 151.44 psi).

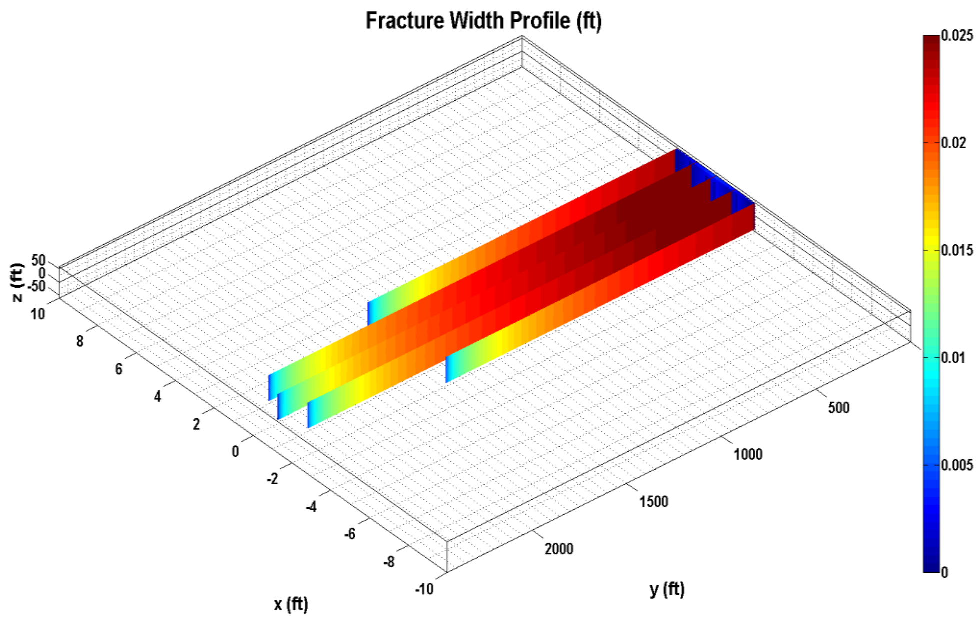

(c) Final Fracture Geometry from Case 3.1.3 ($\sigma_H - \sigma_h$ = 251.44 psi).

Figure 3-9. Final Fracture Geometry for Case 3.1.1 to 3.1.3 showing that, with increasing maximum horizontal stress, fracture network propagates more in the y-direction (perpendicular to minimum horizontal stress), and less in the X-direction, and that those fractures propagating in the X-direction (perpendicular to the maximum horizontal stress) have much smaller apertures.

If we take a closer look of **Figure 3-9** we can see how much further the fractures propagate in x-direction are created to the y-direction **(Figure 3-10**). The fracture branches to x-direction are created up to 60 ft in y-direction for Case 3.1.1, 40 for Case 3.1.2 and 30 for Case 3.1.3 explaining that less differential stress results desenser fracture network.

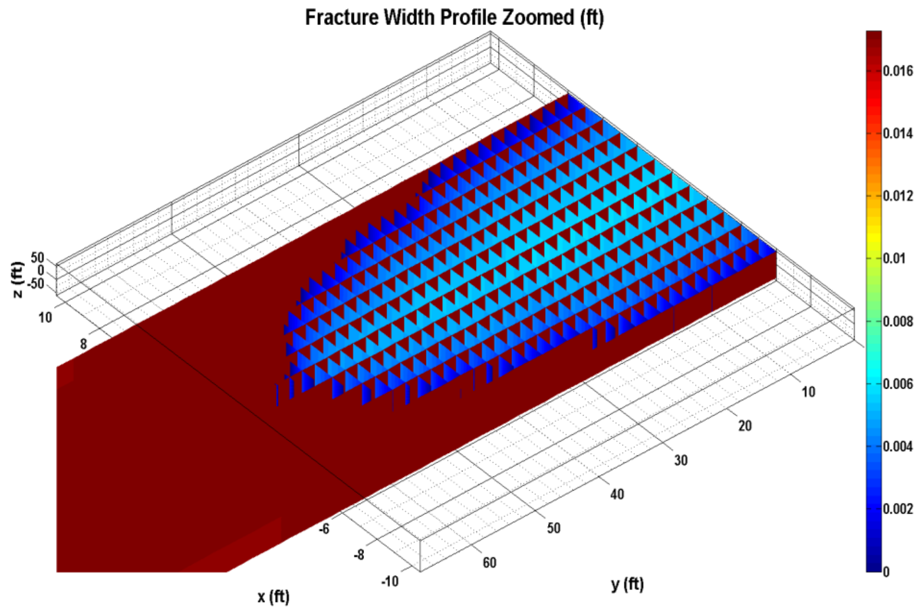

(a) Zoomed view of Final Fracture Geometry from Case 3.1.1 ($\sigma_H - \sigma_h$ = 51.44 psi).

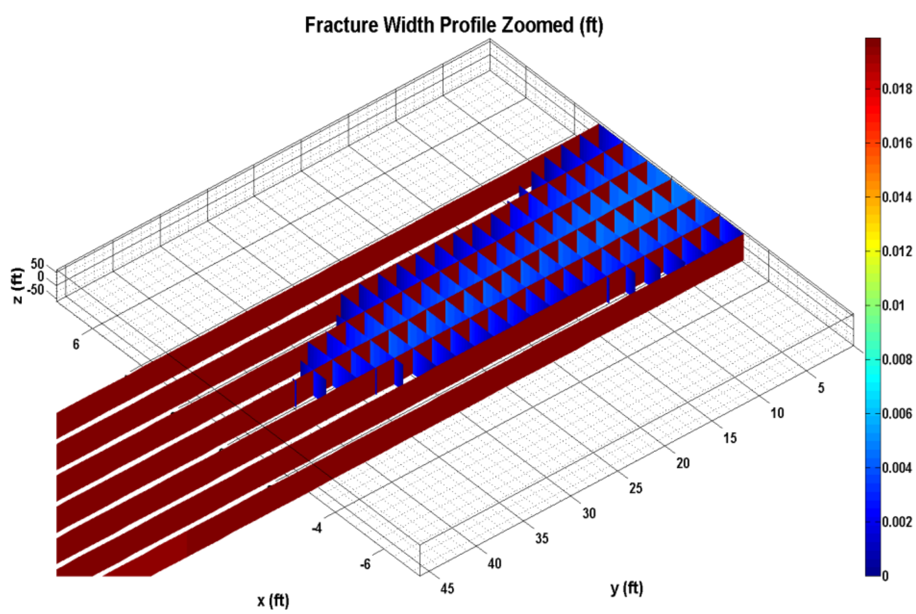

(b) Zoomed view of Final Fracture Geometry from Case 3.1.2 ($\sigma_H - \sigma_h$ = 151.44 psi).

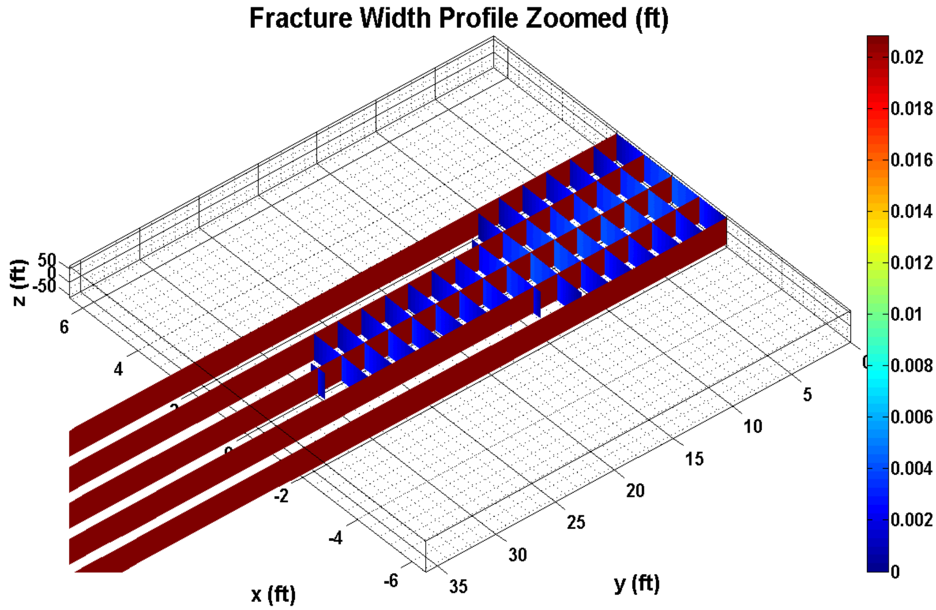

(c) Zoomed view of Final Fracture Geometry from Case 3.1.3 ($\sigma_H - \sigma_h$ = 251.44 psi).

Figure 3-10. Zoomed view of Final Fracture Geometry for Case 1.1 to 1.3 showing that the details of near injection point fracture geometry can be observed.

The pressure profile in the reservoir corresponding to the fracture fluid leakoff is illustrated in **Figure 3-11**. Pressure profiles of each case are directly corresponding to the fracture geometries in **Figure 3-11**. In other word, it implies that the fluid invasions from the created fractures are entering dynamically into the reservoir (matrix).

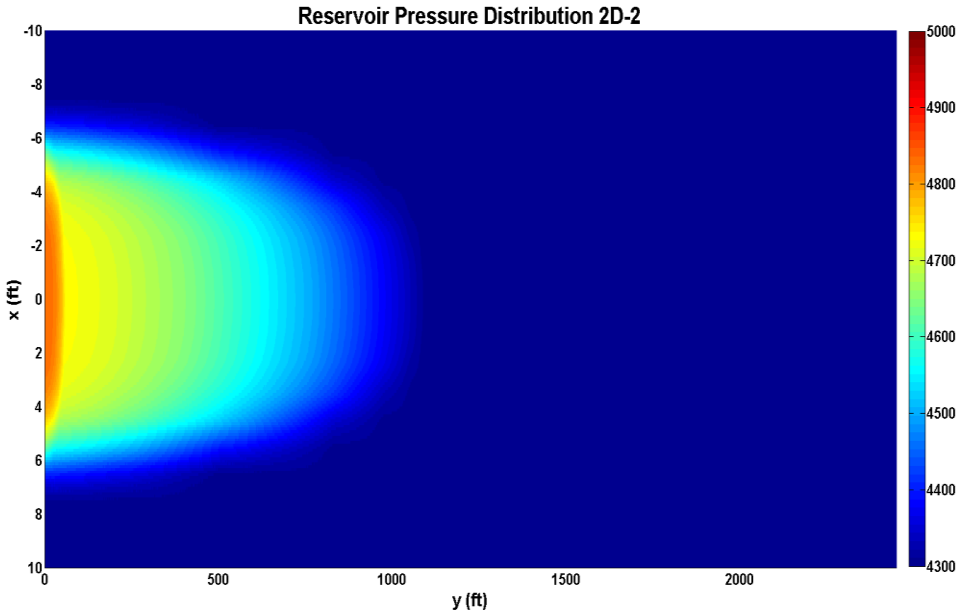

(a) Reservoir Pressure Distribution from Case 3.1.1 ($\sigma_H - \sigma_h$ = 51.44 psi).

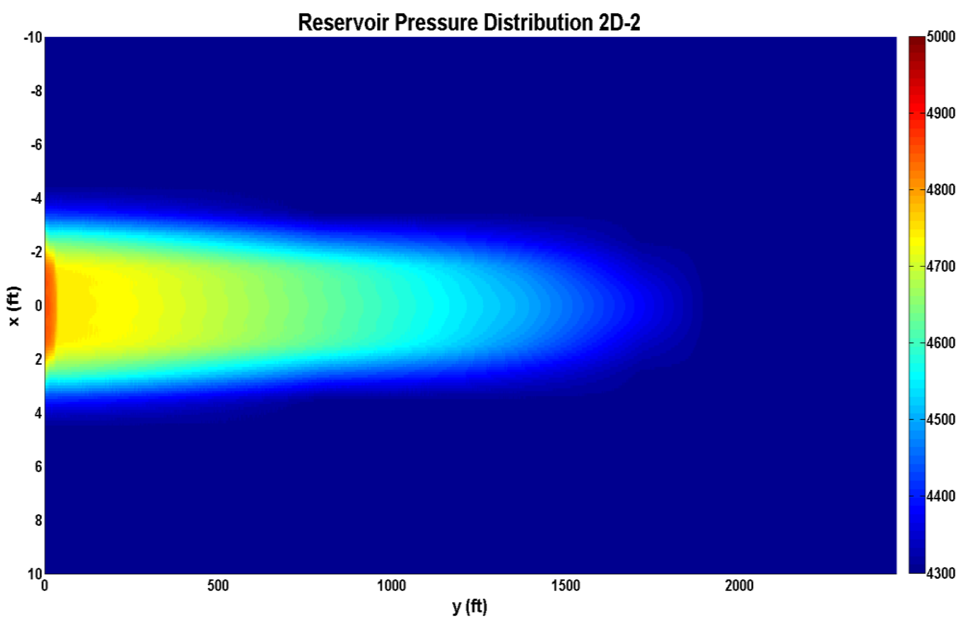

(b) Reservoir Pressure Distribution from Case 3.1.2 ($\sigma_H - \sigma_h$ = 151).

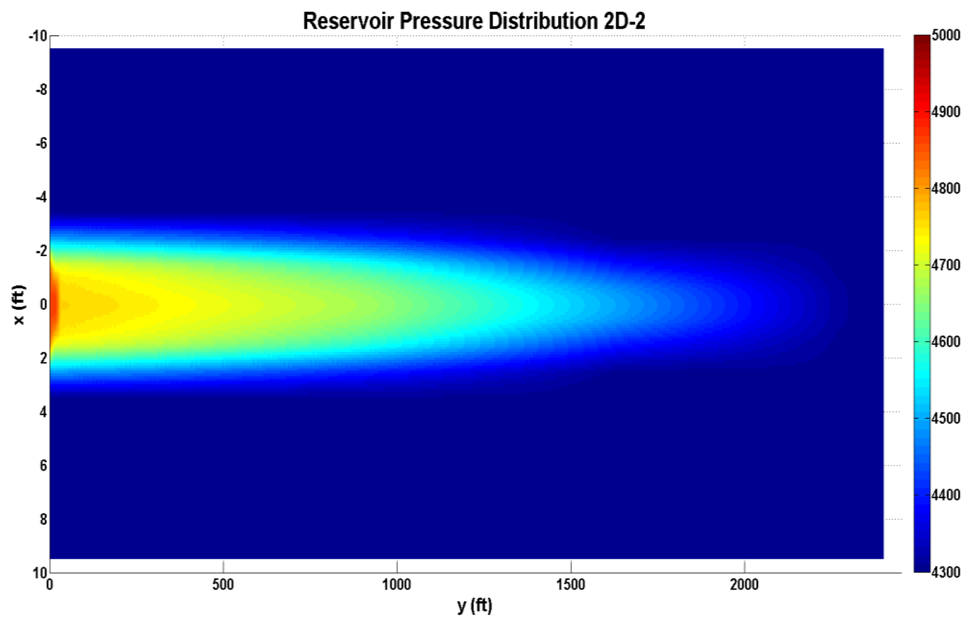

(c) Reservoir Pressure Distribution from Case 3.1.3 ($\sigma_H - \sigma_h$ = 251.44 psi).

Figure 3-11. Reservoir Pressure Distribution for Case 3.1.1 to 3.1.3 illustrating the leakoff-generated pressure changes in the reservoir.

Figure 3-12 is comparing the cumulated leakoff volume for each case. The cases with smaller differential stress resulted higher volume of fluid leakoff. This observation can be justified by comparing the total fracture-reservoir contact area as shown in

Table 3-1Table 3-3, where the fractured area contacted with the matrix corresponds to the difference in cumulative leakoff volumes

.

Table 3-3. Fracture surface area for each case.

	Cases		
Parameters	3.1.1	3.1.2	3.1.3
Fracture-Reservoir contact area (10^6*ft^2)	2.4884	2.1594	2.0331

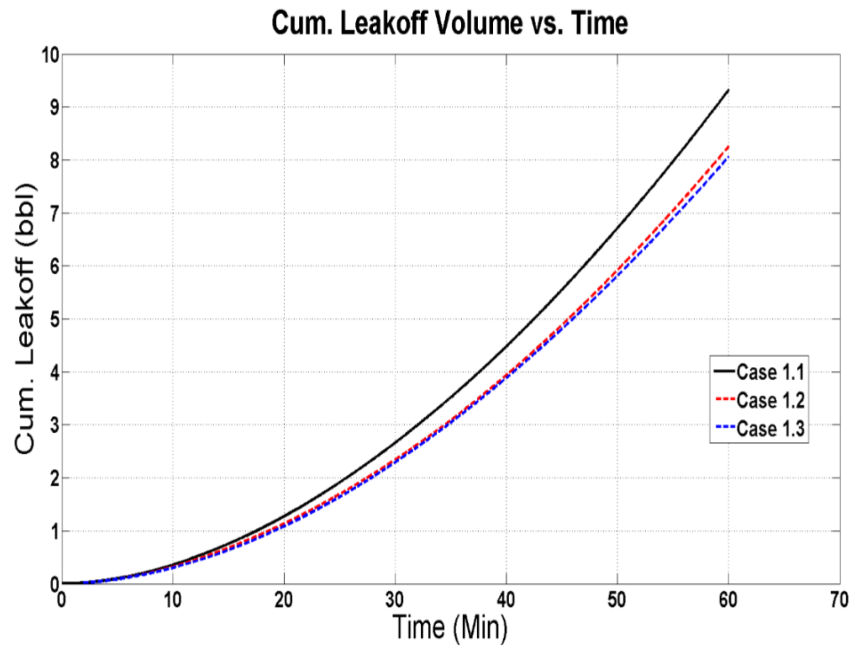

Figure 3-12. Cumulative leakoff volume into the matrix for each case.

3.3.2. Effect of Natural Fracture Spacing

The effect of natural fracture spacing is investigated in this section. Initial input parameters shown in **Table 3-4**. Natural fractures were spaced 1 ft, 10 ft and 100 ft parallel to y-axis and 2 ft, 20 ft, 200 ft parallel to x-axis in the system and all other parameters are constraint to be identical.

Table 3-4. Input parameters for Cases 3.2.1 to 3.2.3.

Perforation Location (0,0)	Cases		
Parameters	3.2.1	3.2.2	3.2.3
Initial Reservoir Pressure (psi)	4307.26	4307.26	4307.26
Fluid Viscosity (μ, cp)	10	10	10
Injection Rate (Q, bbl/min)	100	100	100
σ_h, min (psi)	8348.56	8348.56	8348.56
σ_H, max (psi)	8400	8400	8400
Permeability (k, md)	0.0001	0.0001	0.0001
Young's Modulus (E, psi)	3.74E6	3.74E6	3.74E6
Poisson's ratio (v, fractional)	0.2	0.2	0.2
Treatment Time (min)	60	60	60
Natural Fracture Spacing (X by Y, ft by ft)	1 X 2	10 X 20	100 X 200

Figure 3-13 illustrates final fracture geometries of the Case 3.2.1 to 3.2.3. Different density of the pre-existing natural fractures in the reservoir resulted distinct final fracture geometries for each case. Coarse density of natural fracture created larger fracture network in both x and y directions but the density of created fracture network is much smaller. In Case 3.2.1, the induced network has the size of 14 ft in x-direction and 1100 ft in y-direction and 100 ft by 1300 ft in Case 3.2.2 and 640 ft by 1800 ft in Case 3.2.3. The width profile the cases also show that larger size of the network results the wider width of fracture branches.

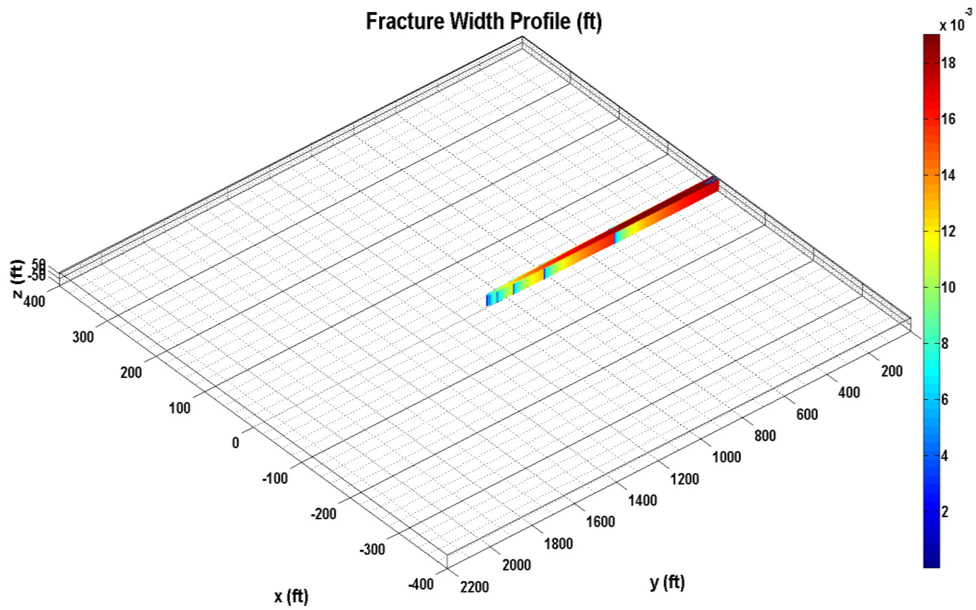

(a) Final Fracture Geometry from Case 3.2.1 (1 ft by 2 ft spacing).

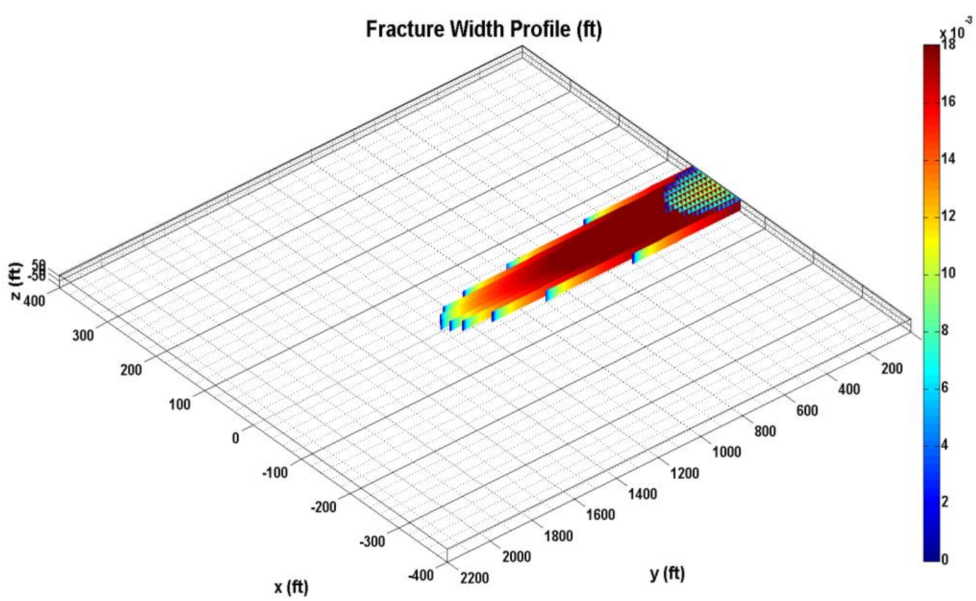

(b) Final Fracture Geometry from Case 3.2.2 (10 ft by 20 ft spacing).

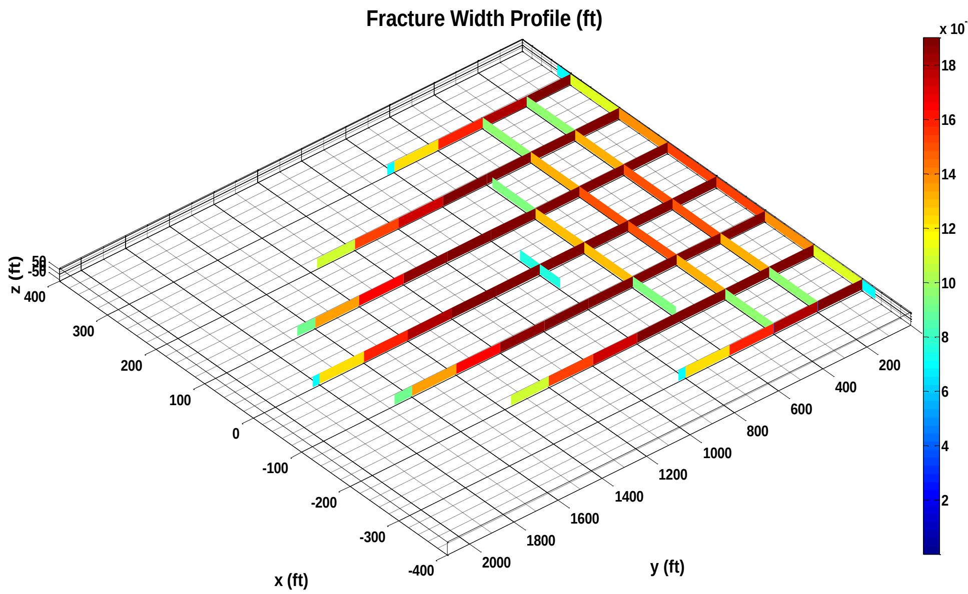

(c) Final Fracture Geometry from Case 3.2.2 (100 ft by 200 ft spacing).

Figure 3-13. Final Fracture Geometry for Case 2.1 to 2.3 showing, with decrease of natural fracture density, final fracture network density decreases but total fractured area increases.

In a dense system, a fracture tip may not extend faster because the energy is released in higher rate to the connected fractures. In other word, in a unit length of a fracture branch, denser system has more branched fractures that take away the energy to extend. This can be observed in **Figure 3-14**. The highlighted regions with yellow in **Figure 3-14 (a) and (b)** emphasizing the difference of how many branches are connected. In Case 3.2.1, there are 32 fractures branched out from the highlighted fracture branch and only 5 in Case 3.2.3.

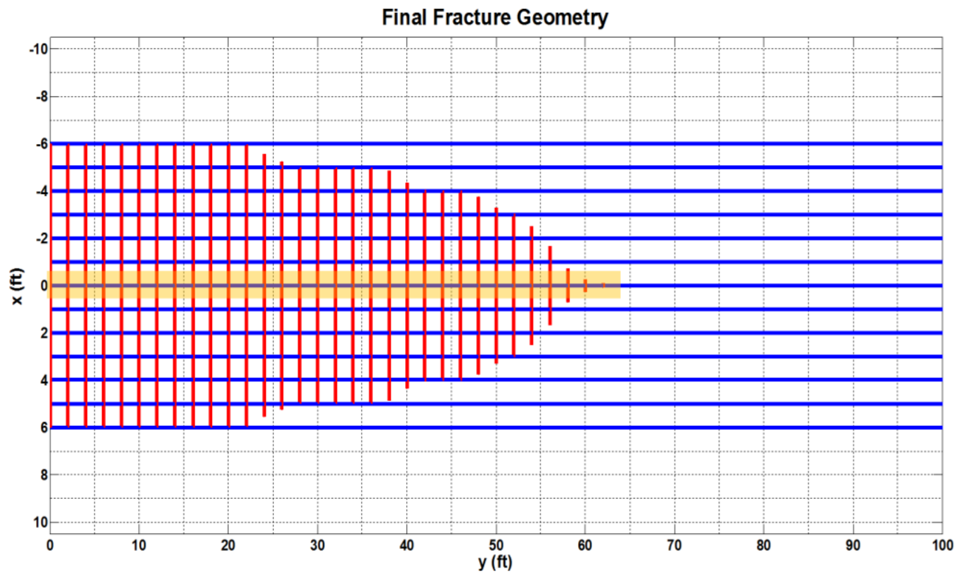

(a) Final Fracture Geometry from Case 3.2.1 (Blue: Fracture along y-axis, Red: Fracture along x-axis).

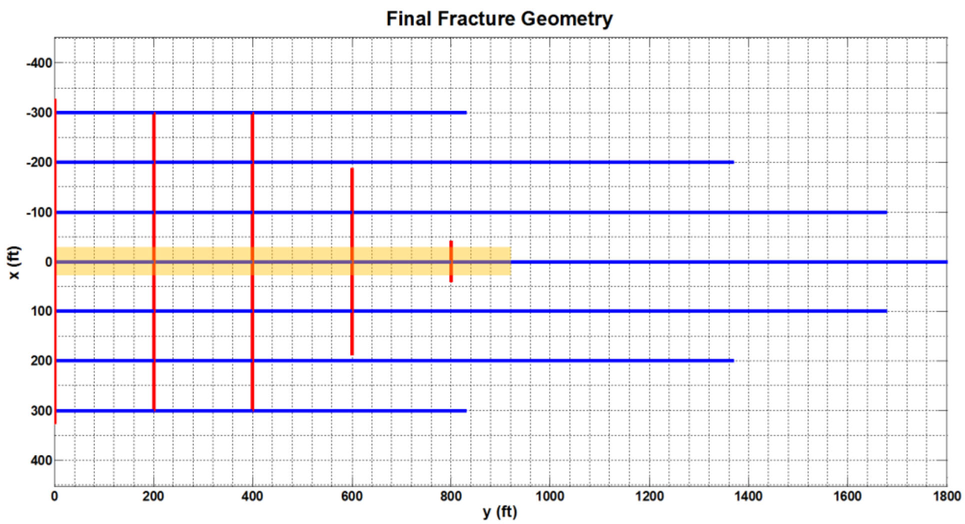

(b) Final Fracture Geometry from Case 3.2.3 (Blue: Fracture along y-axis, Red: Fracture along x-axis).

Figure 3-14. Branching fracture comparison between Case 2.1 and 2.3.

3.3.3. Effect of Fracture Fluid Viscosity

The viscosity of the fluid contributes to the fluid pressure calculation such that different viscosity results distinct final fracture network. **Table 3-5** indicates the input values for the simulation for each cases under 10 ft by 20 ft natural fracture system with three different cases (μ=1 cp, 10 cp, 20 cp).

Table 3-5. Input parameters for Cases 3.3.1 to 3.3.3.

Perforation Location (0,0)	**Cases**		
Parameters	**3.3.1**	**3.3.2**	**3.3.3**
Initial Reservoir Pressure (psi)	**4307.26**	**4307.26**	**4307.26**
Fluid Viscosity (μ, cp)	**1**	**10**	**20**
Injection Rate (Q, bbl/min)	**100**	**100**	**100**
σ_h, min (psi)	**8348.56**	**8348.56**	**8348.56**
σ_H, max (psi)	**8400**	**8400**	**8400**
Permeability (k, md)	**0.0001**	**0.0001**	**0.0001**
Young's Modulus (E, psi)	**3.74E6**	**3.74E6**	**3.74E6**
Poisson's ratio (v, fractional)	**0.2**	**0.2**	**0.2**
Treatment Time (min)	**60**	**60**	**60**
Natural Fracture Spacing (X by Y, ft by ft)	**10 X 20**	**10 X 20**	**10 X 20**

The result of final fracture geometries is depicted in **Figure 3-15**. Due to the differences in viscosity, the result is showing significant difference of the fracture geometries. Case 3.3.1 has the largest contact area of $3.6787*10^6$ ft^2 while Case 3.3.2 and 3.3.3 are having $2.4919*10^6$ ft^2 and $2.1969*10^6$ ft^2, respectively. However, Case 3.3.1 has relatively small width along the network compare to other cases in this section. Due to lower fracture fluid viscosity, the leakoff rate of Case 3.3.1 is higher than other cases such that the fracture in Case 3.3.1 is not able to bear high fluid pressure which yield larger width inside fracture. This observation can be justified by fracture efficiency comparison plot in **Figure 3-16**.

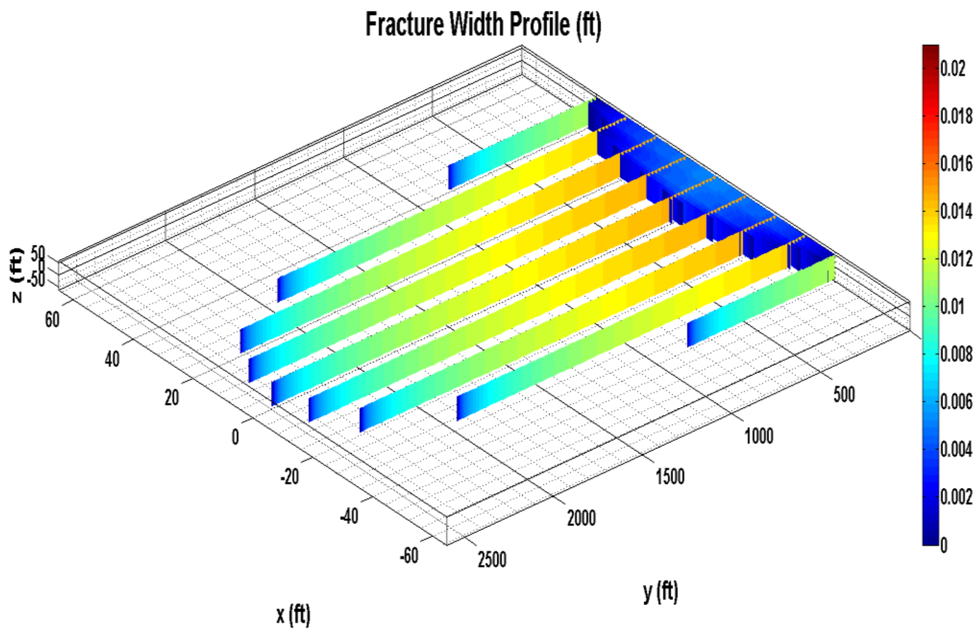

(a) Final Fracture Geometry from Case 3.3.1 (μ = 1 cp).

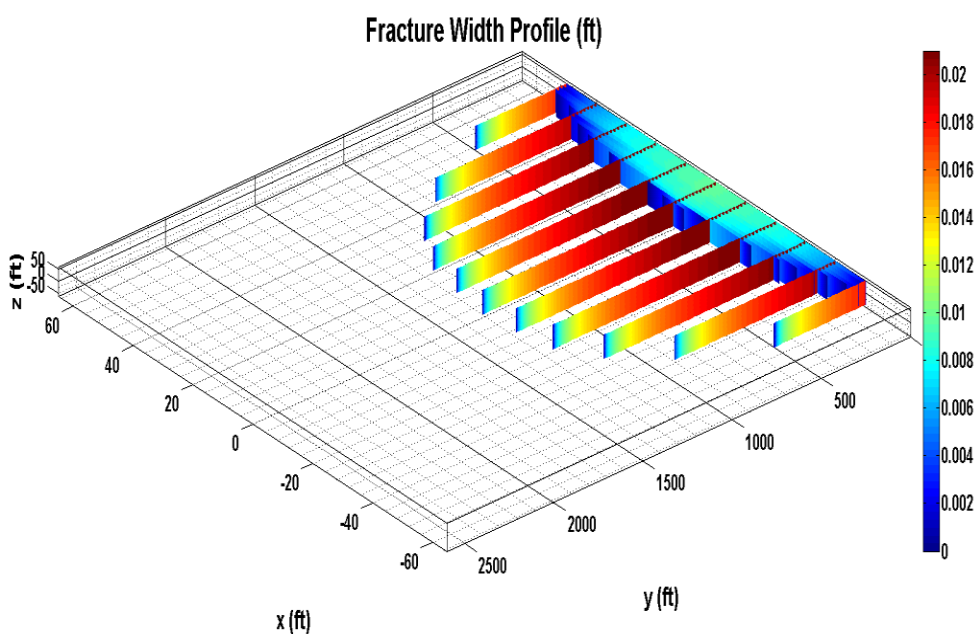

(b) Final Fracture Geometry from Case 3.3.2 (μ = 10 cp).

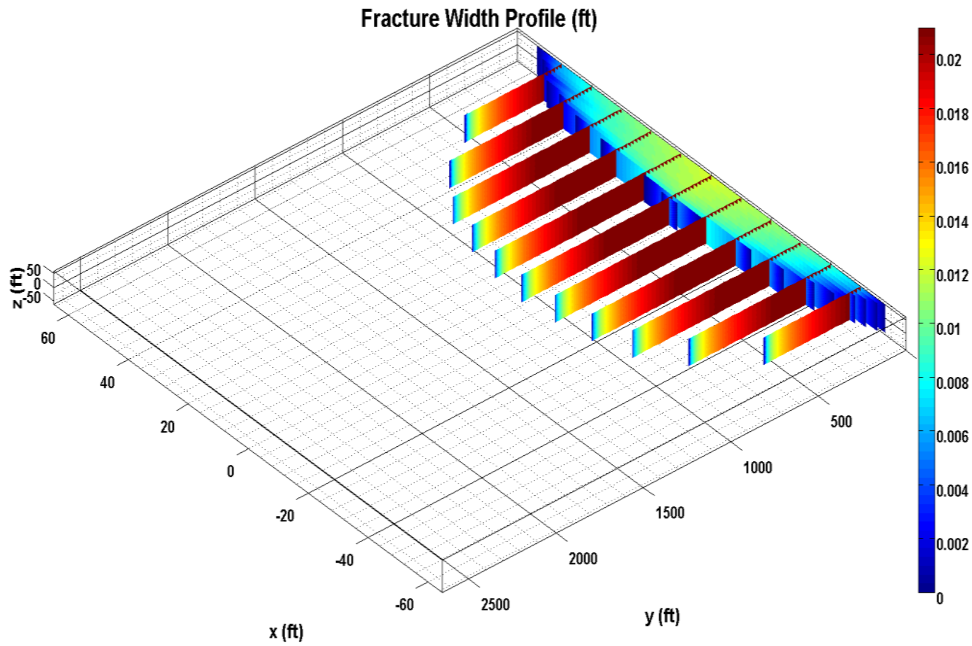

(c) Final Fracture Geometry from Case 3.3.3 (μ = 20 cp).

Figure 3-15. Final Fracture Geometry for Case 3.1 to 3.3 illustrating, with increase of fracture fluid viscosity, fracture network has more penny shape and the aperture of each fracture branch increases.

The fracture efficiency is defined as the ratio of created fracture volume and injected fluid volume and it indicates that Case 3.3.1 has the lowest efficiency at the end of the treatment. All cases started out with same efficiency but Case 3.3.1 is losing fracture fluid to the matrix much faster ended with the lowest fracture efficiency.

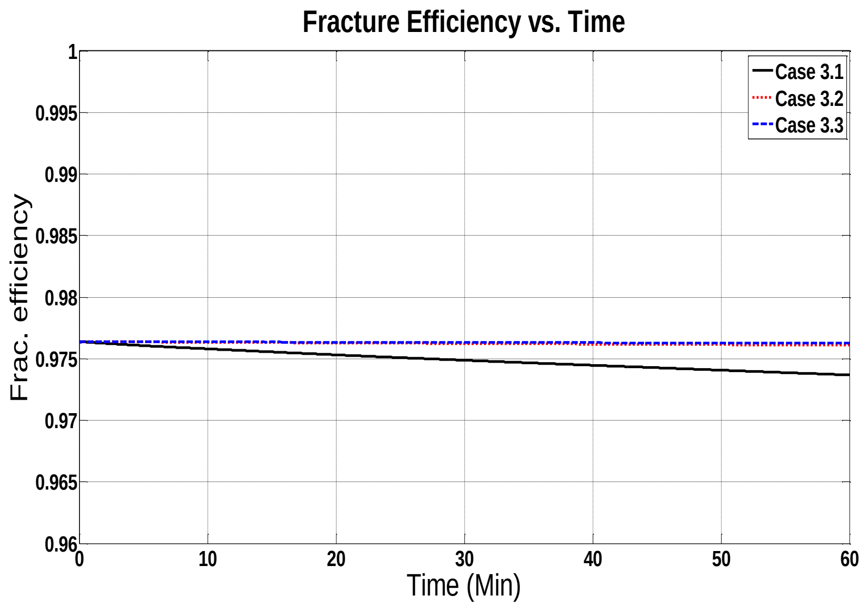

Figure 3-16. Fracture efficiency comparison (Case 3.3.1 to 3.3.3).

3.3.4. Effect of Matrix Permeability

Matrix permeability is a critical factor that contributes to the fracture fluid leakoff further to the fracture geometry as described in previous section. This effect is carried by evaluating four different matrix permeability (10^{-1} md, 10^{-2} md, 10^{-3} md and 10^{-4} md) which may represent unconventional reservoirs. A low-range permeability of 10^{-4} md and 10^{-3} md were selected to represent shale reservoirs and 10^{-1} md and 10^{-2} md to represent tight gas sands. Same natural fracture setting with fluid viscosity of 1 cp is applied through Case 3.4.1 to 3.4.4. **Table 3-6** shows all the input values for the simulation.

Table 3-6. Input parameters for Cases 3.4.1 to 3.4.4.

Perforation Location (0,0)	Cases			
Parameters	3.4.1	3.4.2	3.4.3	3.4.4
Initial Reservoir Pressure (psi)	4307.26	4307.26	4307.26	4307.26
Fluid Viscosity (μ, cp)	1	1	1	1
Injection Rate (Q, bbl/min)	100	100	100	100
σ_h, min (psi)	8348.56	8348.56	8348.56	8348.56
σ_H, max (psi)	8500	8500	8500	8500
Permeability (k, md)	0.1	0.01	0.001	0.0001
Young's Modulus (E, psi)	3.74E6	3.74E6	3.74E6	3.74E6
Poisson's ratio (v, fractional)	0.2	0.2	0.2	0.2
Treatment Time (min)	60	60	60	60
Natural Fracture Spacing (X by Y, ft by ft)	10 X 20	10 X 20	10 X 20	10 X 20

Figure 3-17 illustrates the fracture geometry and width profile of each case. The result indicates that higher permeability drags the fracture growth predominant in y-direction (perpendicular to minimum in-situ stress). As permeability decreases, the difference in fracture geometry becomes small as seen in Case 3.4.3 and 3.4.4. Similar to decrease of fracture fluid viscosity, increase of matrix permeability contributes to the increase of leakoff rate. Hydraulic forces that induce fracture are lessened because those forces are lost through the matrix more quickly and to a larger extent when matrix permeability increases.

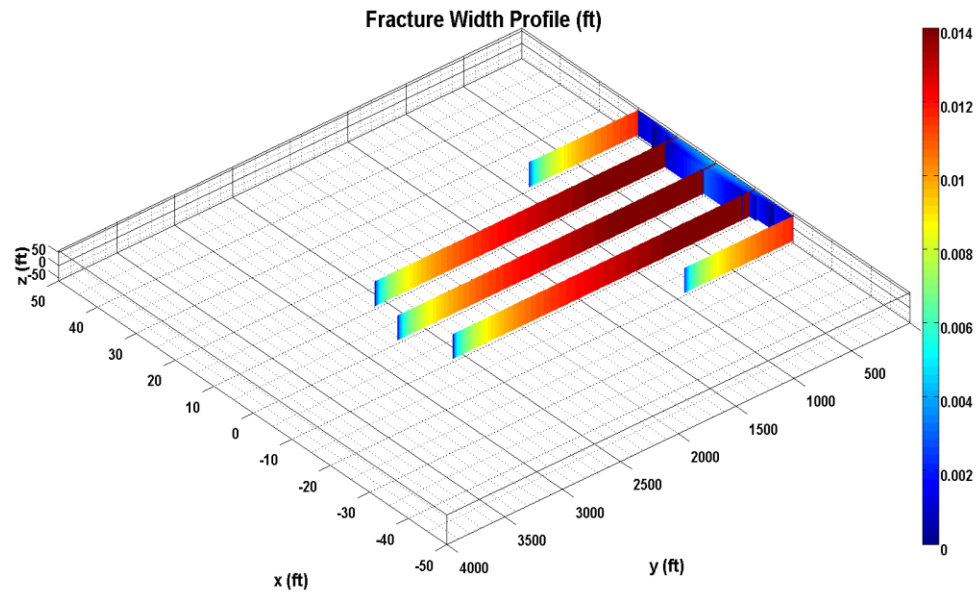

(a) Final Fracture Geometry from Case 3.4.1 (k = 0.1 md).

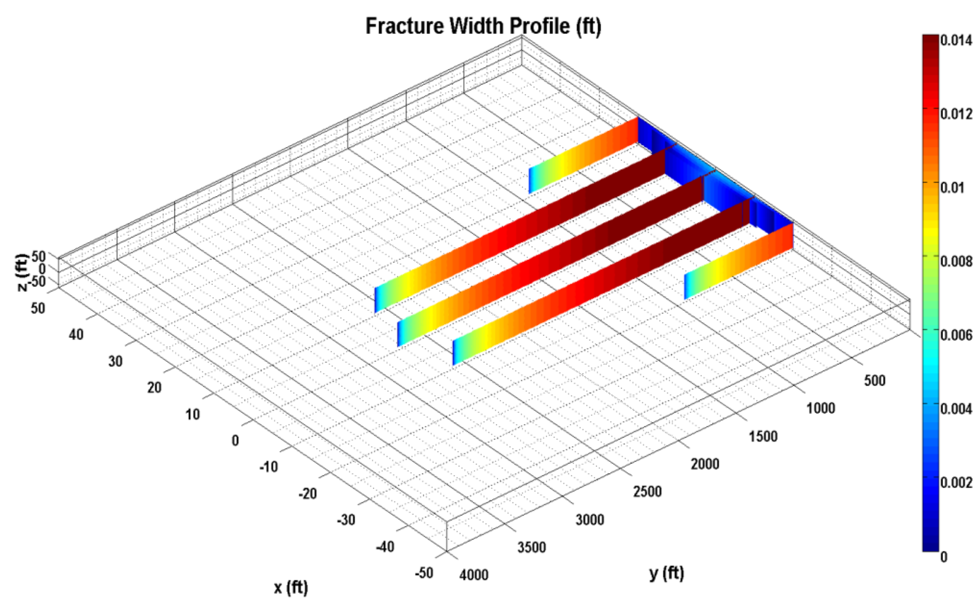

(b) Final Fracture Geometry from Case 3.4.2 (k = 0.01 md).

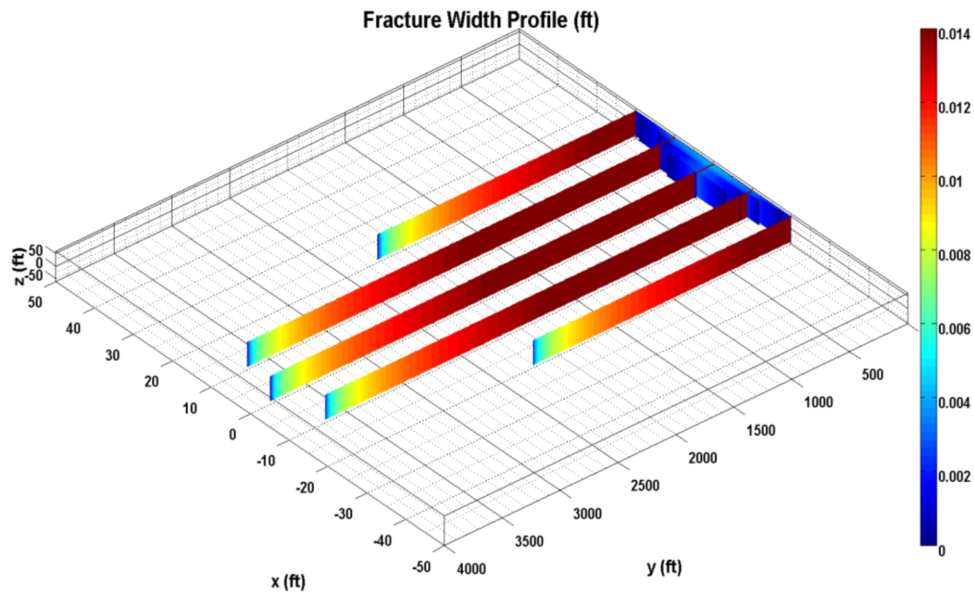

(c) Final Fracture Geometry from Case 3.4.3 (k = 0.001 md).

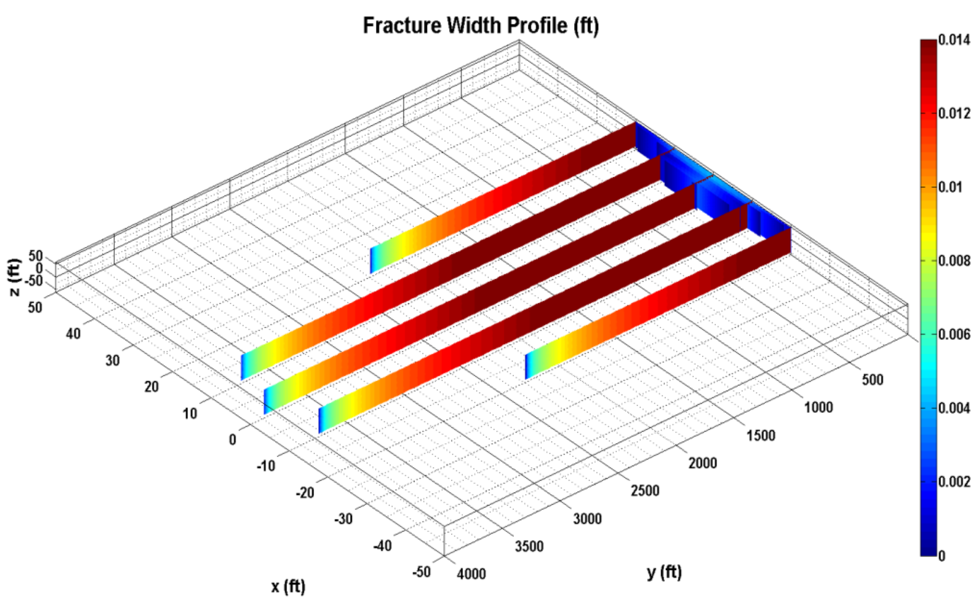

(d) Final Fracture Geometry from Case 3.4.4 (k = 0.0001 md).

Figure 3-17. Final Fracture Geometry for Case 3.4.1 to 3.4.4 showing, with decrease of matrix permeability, fracture length perpendicular to the minimum insitu stress increases and more fracture branches are created.

From **Figure 3-18,** leakoff can be observed in the reservoir in each case. The pressure in this figure indicates the influence of fluid leakoff to the reservoir. As permeability decrease from **Figure 3-18 (a)** to **(d)**, pressure changes in the reservoir dramatically decrease such that Case 3.4.4 shows no comparable pressure changes in the reservoir. This can be explained by comparing fracture efficiencies plotted **Figure 3-19**. At the end of treatment, Case 3.4.1 shows 54% of efficiency explaining that approximately half of the injected volume is leaked off into the matrix. As matrix permeability decreases magnitude of one order, fracture efficiency exponentially increases.

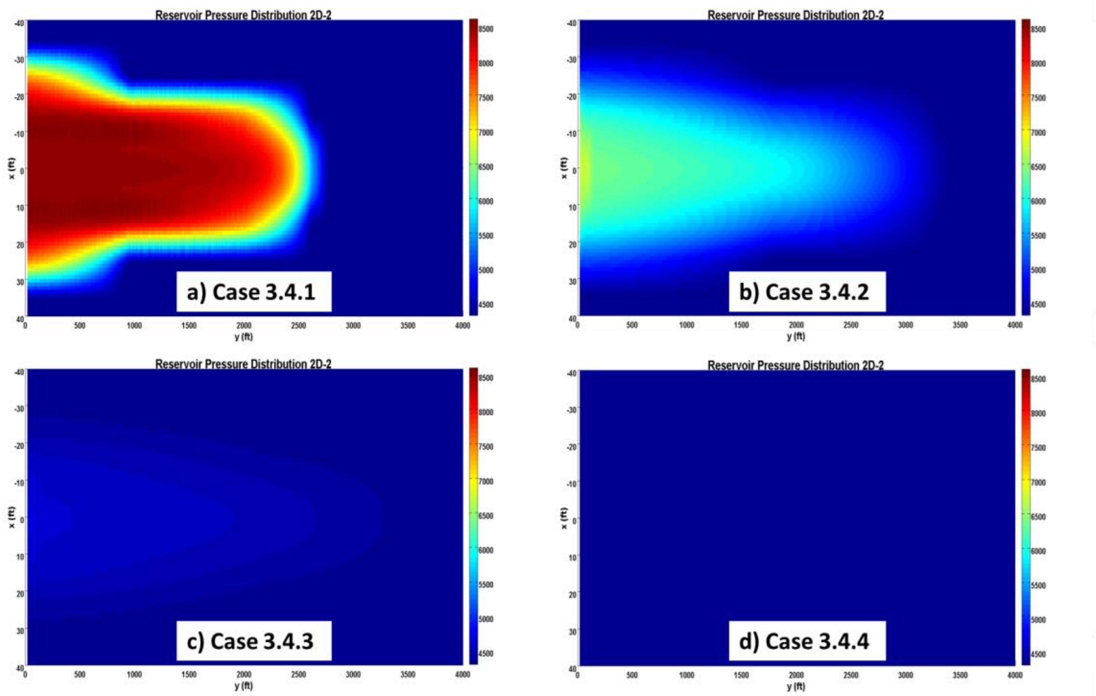

Figure 3-18. Reservoir Pressure showing less reduction in reservoir pressure with decreasing matrix permeability (from Case 3.4.1 to Case 3.4.4).

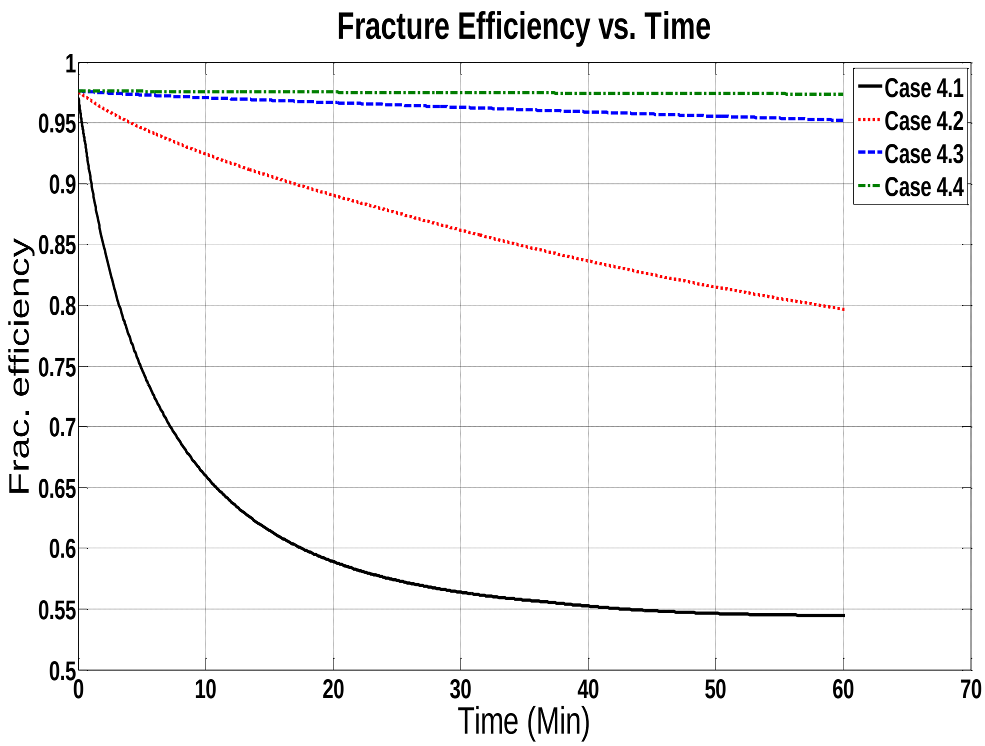

Figure 3-19. Fracture Efficiency Comparison for Case 3.4.1 to 3.4.4.

3.3.5. Fracture-reservoir Contact Area

Fracture-reservoir contact area is one useful indicator of the effectiveness of a fracture treatment. It is the area through which hydrocarbon resource is extracted through, so it is important to have large contact area to recover more resource in common hydraulic fracture treatments.

Figure 3-20 shows the plots of total fracture-reservoir contact versus total fracture volume for all cases considered. In **Figure 3-20 (a)**, smaller differential stress contributes to larger contact area for equivalent fracture volume. This means that fracture length is contributing to generation of fracture volume relatively more in the case with smaller differential stress. As a result, the fracture network in low differential stress has thinner, smaller but denser characteristics.

In **Figure 3-20 (b)**, total fracture volume at the end of the treatment decreases as the density of pre-existing natural fracture increases but the contact area behaves opposite. The area becomes larger as the density increase showing that large fracture volume does not necessarily results larger contact area.

The comparison between **Figure 3-20 (c)** and **(d)** shows that increase of the leakoff due to fluid viscosity and matrix permeability results significantly different fracture-reservoir contact area. **Figure 3-20 (c)** illustrates that viscous fluid results lager fracture volume but less contact area. In other words, smaller viscosity yields thinner fracture branches such that contact area is larger. However, matrix permeability does not influence the contact area change compare to fluid viscosity but it affect the total fracture volume changes. As matrix permeability decreases, the total fracture volume dramatically increases as shown in **Figure 3-20 (d)**.

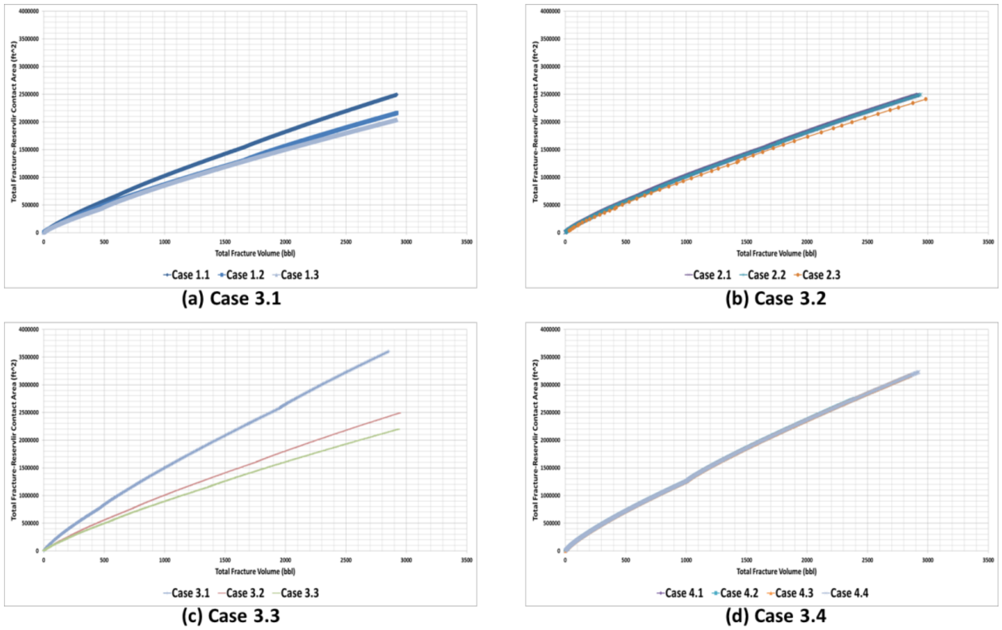

Figure 3-20. Fracture-reservoir Contact Area vs. Fracture Volume for all cases.

If fluid viscosity is increased to 50 cp for Case 3.4.1, the slope of the plot decreases as shown in the **Figure 3-21**. The total volume of the fracture increased by 1188 bbl but the fracture-reservoir contact area has been decreased to 439376.9 ft^2 when the fracture fluid viscosity in increase from 1 cp to 50 cp. The amount of leakoff is significantly decreased when the viscosity rises but the fluid in the fracture contributed to width expansion rather than propagating further. Thus, the fracture-reservoir contact area decreases as viscosity increases. The comparison between fracture geometry of these two cases can justify this change (**Figure 3-22**). The color representing the width of the fracture clearly shows the distinction between the case with 1 cp and 50 cp. Also, we can see that the case with 1cp propagated further to about 3000 ft in y-direction which the other case went 1400 ft.

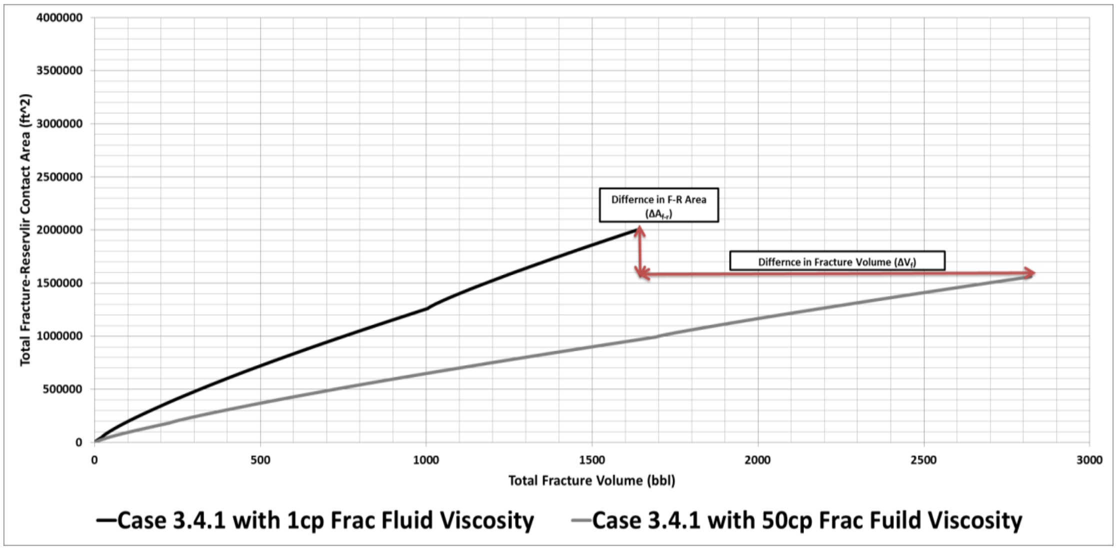

Figure 3-21. Fracture-reservoirContact Area vs. Fracture Volume for Case 3.4.1 with different fracture fluid viscosity.

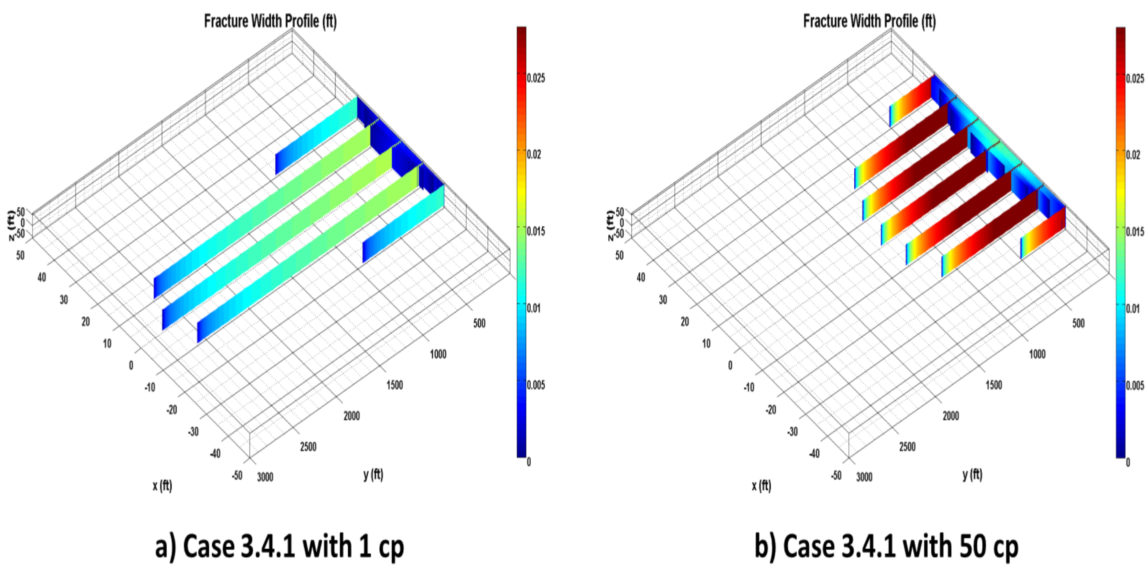

Figure 3-22. The final fracture geometry comparison for Case 3.4.1 with fracture fluid viscosity of 1 cp and 50 cp.

The similar comparison is made for Case 3.4.4 as shown in **Figure 3-23.** The difference between total volumes of the fractures network is negligibly small in this case because the matrix permeability is too small to generate notable difference. However, the area is decreased to 1622394.5 ft^2, approximately reduced to half when the viscosity is 50 cp.

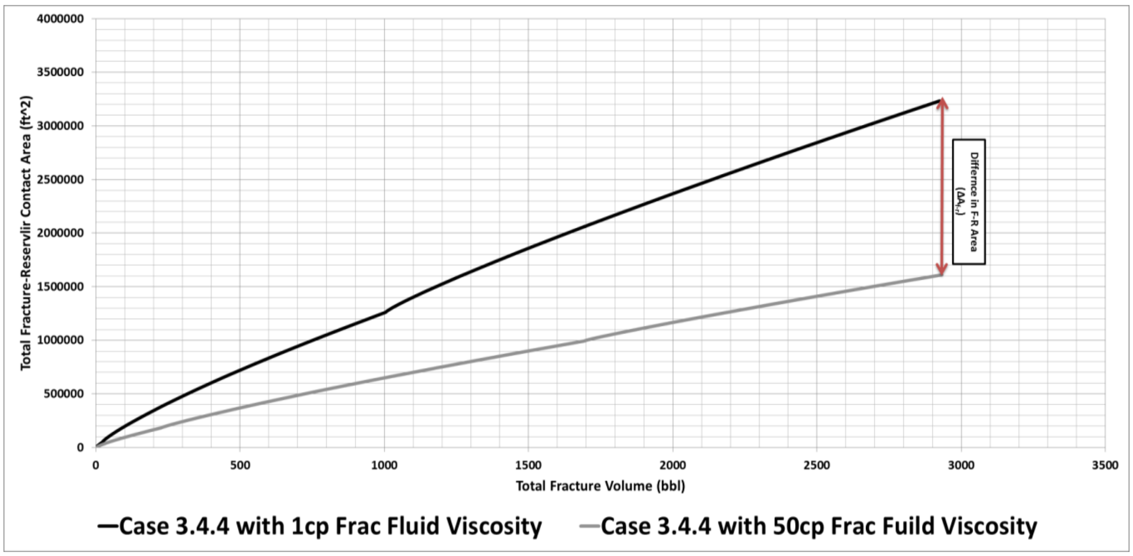

Figure 3-23. Fracture-reservoirContact Area vs. Fracture Volume for Case 3.4.4 with different fracture fluid viscosity.

The injection rate of the fracture fluid also significantly contributes to the change of fracture-reservoir contact area. Case 3.4.4 is evaluated with different injection rate (pumping rate) of 50 bbl/min and 10 bbl/min to see its influence on the fracture-reservoir area. Total volume of fracture fluid injected is fixed to be 30,000 bbl.

Figure 3-24 illustrates the final fracture geometry and reservoir pressure profiles of each case. Longer but thinner final fracture geometry and larger leakoff-generated pressure change is observed when pumping rate is decreased. The fracture-reservoir area is compared in **Figure 3-25** and the result proves that decrease of the pumping rate enlarges the contact area.

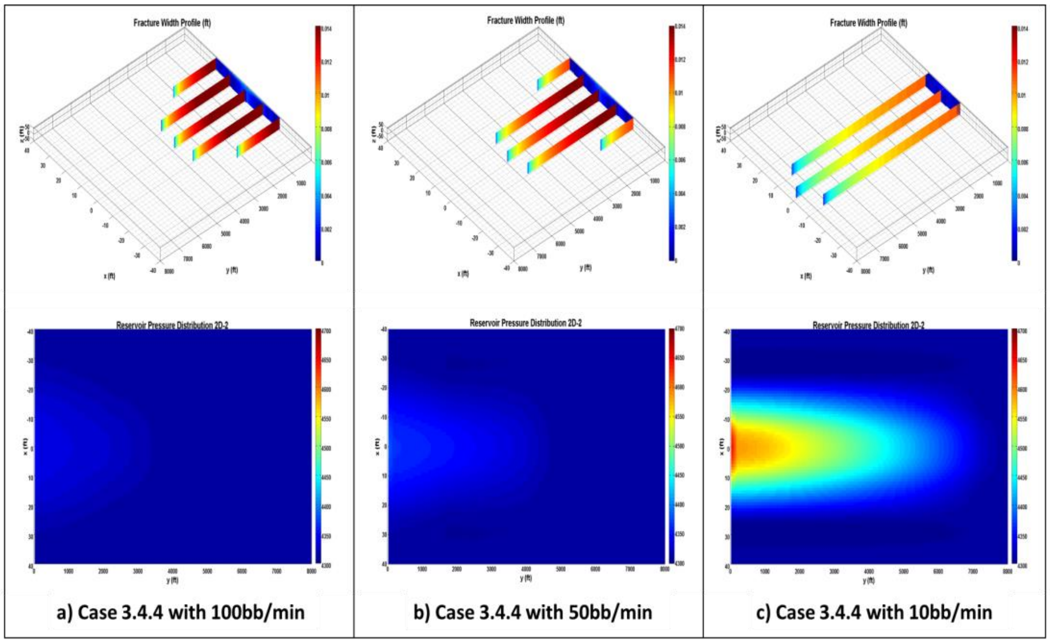

Figure 3-24. The final fracture geometry and Pressure profile comparison for Case 3.4.4 with fracture fluid injection rate of 100 bbl/min, 50 bbl/min and 10 bbl/min.

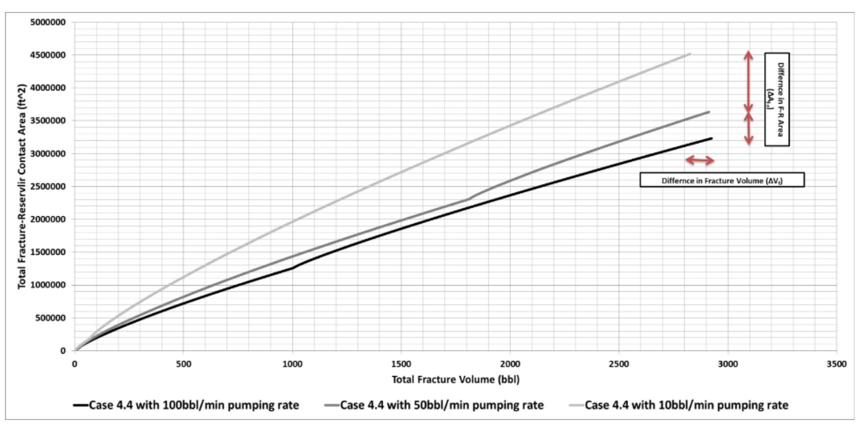

Figure 3-25. Fracture-reservoirContact Area vs. Fracture Volume for Case 3.4.4 with different fracture fluid pumping rate.

From the investigation, we can conclude that, in order to maximize the fracture-reservoir contact area, it is better to use less viscous fracture fluid with smaller pumping rate for the treatment. The final fracture-reservoir area at the end of the treatment is illustrated in **Figure 3-26**. However, we need to do further research by incorporating poroelasticity and stress shadow effects to have more realistic study.

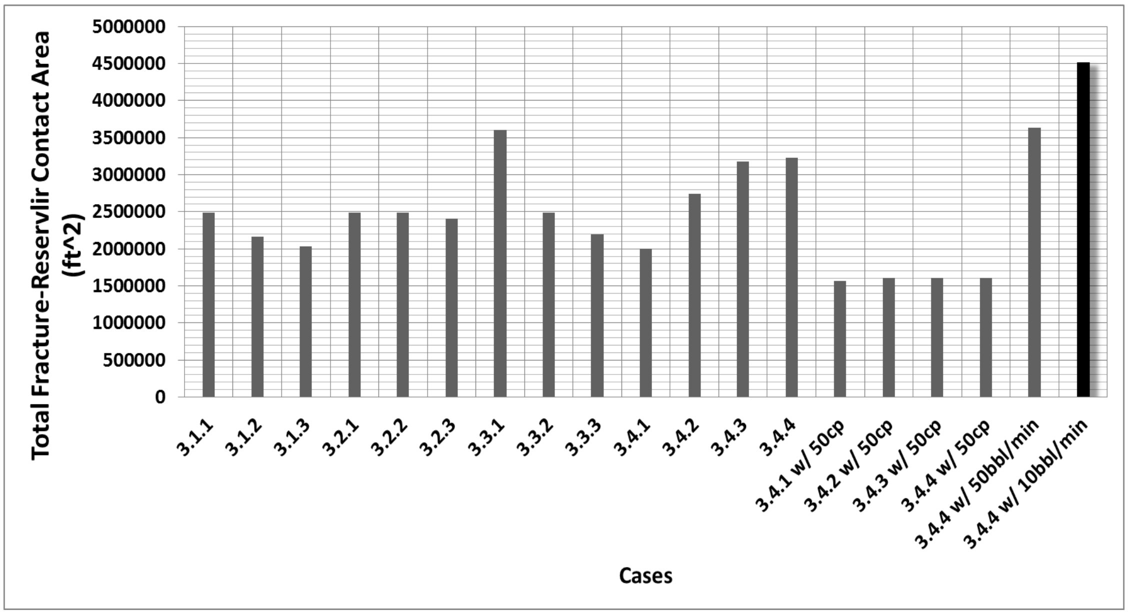

Figure 3-26. Fracture-reservoirContact Area vs. Fracture Volume for all cases.

3.4 Chapter conclusion

Our new hydraulic fracture propagation model is fully coupled geomechanical deformation and fracture flow in a dual porosity system. Using the boundary condition approach, dual porosity model simulates facture-to-matrix flow (leakoff), with fracture flow model linking the two coupled models. This model is capable of simulating propagation of hydraulic fractures into a formation with pre-existing natural fracture. Dynamic change of reservoir pressure due to the fracture flow leakoff is also captured in the model. In addition, separation of domain into fracture and matrix domain and use of moving coordinate approach reduces simulation time compare to single porosity approach such that complex fracture network can be simulated with time efficiency.

The parametric study using the model shows that horizontal differential stress, natural fracture spacing, fracture fluid viscosity and matrix permeability play critical roles in creating fracture network complexity. Key findings are:

1. Decreasing horizontal differential stress can change the induced-fracture network from sharp elliptical shape to radial shape.
2. Increased natural fracture spacing results in larger hydraulic fracture network but the intensity and complexity of the network decreases dramatically such that the quality of fracture network within SRV may be weakened.
3. Higher viscosity yield dense fracture network with relatively shorter and thicker fracture branches.
4. Increase of matrix permeability results in an exponential decrease of fracture efficiency and a small fracture network in both x and y directions.
5. Fracture-reservoir contact area may be enlarged by use of less viscous fracture fluid with small pumping rate such that the size of final fracture network increases.

3.5 Nomenclature

A = cross sectional area (ft^2)

B = Formation volume factor (RB/STB)

C_w = Compressibility of water (psi^{-1})

d = Extended distance (ft)

f_{L1}, f_{L2} = Fractions of fracture half-length (fraction)

G = Shear modulus of rock formation (psi)

h = Fracture gross height (ft)

h_f, H_{fl} = Fracture height (ft)

k = permeability in the x, y and z direction (md)

K_f = coefficient of friction (frictional)

k_r = relative permeability (md)

L_f, l = Fracture length (ft)

p_f = Fluid pressure in the fracture (psi)

q = Fluid injection rate or flowrate of each grid block (bbl/min)

R_s = Solution gas-oil ratio (SCF/STB)

s = Distance along the fracture (ft)

S_w = Water saturation (dimensionless)

T_o = Tensile strength of the rock (psi)

v_{tip} = flow velocity at the tip of fracture (L/T)

w = Fracture width (ft)

$\overline{w}$ = Average fracture width (ft)

α_c = Volumetric conversion factor (dimensionless)

β_c = Transmissibility conversion factor (dimensionless)

μ = Fluid viscosity (cp)

v = Poisson's ratio (dimensionless)

ρ = Fluid density (lbm/ft^3)

$\sigma_{1,}\ \sigma_2$ = far-field effective stresses (psi)

σ_h = Minimum horizontal principal stress (psi)

σ_H = Maximum horizontal principal stress (psi)

σ_n = Normal stress acting on the NF plane (psi)

σ_t = Stress acting parallel to the NF (psi)

φ = Porosity (dimensionless)

γ = Gravity of phase (psi/ft)

3.6 Chapter reference

1. Abousleiman, Y.N. 1991. A Poroelastic PKN Model with Pressure Dependent Leakoff and Formation Permeability Determination, PhD dissertation, Univ. of Delaware.
2. Azom, P.N. and Javadpour, F. 2012. Dual-Continuum Modeling of Shale and Tight Gas Reservoirs. Paper SPE 159584 presented at the SPE Annual technical Conference and Exhibition, San Antonia, TX, 8-10 Oct.
3. Baree, R.D. and Mukherjee, H. 1996. Determination of Pressure Dependent Leakoff and Its Effect on Fracture Geometry. Paper SPE-36424 presented at the Annual Technical Conference and Exhibition, Denver, Co, 6-9 Oct.
4. Beckner, B., H. Chan, et al. 1991. Simulating naturally fractured reservoirs using a subdomain method. SPE Symposium on Reservoir Simulation.
5. Blanton T.L. 1982 Experimental Study of Interaction Between Hydraulicalyy Induced and Pre-Existing Fractures. Paper SPE 10847 presented at the SPE Unconventional Gas Recovery Symposium, Pittsburgh, Pennsylvennia, USA, 16-18 May. doi: 10.2118/10847-MS.
6. Calslaw, H. and Jaeger, J.C. 1956. Conduction of Heat in Solids, end edition. Oxford, UK: Oxfrod Univ. Press.
7. Carter R.D. 1957. Derivation of the General Equation for Estimation the Extent of the Fracture Area. *In Drill. And Prod. Prac.* API, ed. Howard, G.C. and Fast, C.R., 261-268. NY.
8. Cipolla, C.L., Warpinski, N.R., Mayerhofer, M.J., and Lolon, E.P. 2010. The Relationship Between Fracture Complesity, Reservoir Properties, and Fracture-Treatment Desigh. SPE Production & Operations **25** (4): 438-452. SPE-115769-PA. doi: 10.2118/115769-PA
9. Cipolla, C.L., Lolon, E.P., Erdle, J.C., and Rubin, B. 2010. Reservoir Modeling in Shale-Gas Reservoirs. SPE Reservoir Evaluation & Engineering **13** (4): 638-653. SPE-125530-PA. doi: 10.2118/125530-PA
10. England, A.H. and Green, A.E. 1963. Some Two-Dimensional Punch and Crack Problems in Classical Elasticity. Proc., Cambridge Phil Soc., London 59, 489.

11. Geertsma, J. and de Klerk, F. 1969. A Rapid Method of Predicting Width and Extent of Hydraulic Induced Fractures. J Pet Technol 21 (12): 1571-1581. SPE-2458-PA. http://dx.doi.org/10.2118/2458-PA.
12. Gilman, J. R. 1986. An Efficient Finite-Difference Method for Simulating Phase Segregation in the Matrix Blocks in Double-Porosity Reservoirs. SPE Reservoir Engineering **1** (4): 403-413.
13. Gu, H., Weng, X., Lund, J.B., Mack, M.G., Ganguly, U. and Suarez-Rivera, R. 2011. Hydraulic Fracture Crossing Natural Fracture at Non-Orthogonal Angles, A Criterion, Its Validation and Applications. Paper SPE-139984-MS presented at the SPE HFTC, Woodland, Texas, 24-26 Jan. doi: 10.2118/139984-MS.
14. Han, J.,Puri, V., & Wang, J. Y. (2014, February 4). A Fully Coupled Geomechanics and Fluid Flow Model for Proppant Pack Failure and Fracture Conductivity Damage Analysis. Society of Petroleum Engineers. doi:10.2118/168617-MS
15. Han, J., Wang, J. Y. Development and Application of a Type Curve for Gel Damage Identification in Tight Gas Wells. 34 Int. J. Petroleum Engineering, Vol. 1, No. 1, 2014
16. Howard, G.C. and Fast, C.R. Hydraulic Fracturing. 1970. Society of Petroleum.
17. Ji, L., Settari A. 2007. A Novel Hydraulic Fracturing Model Fully Coupled With Geomechanics and Reservoir Simulator. Paper SPE 110845-PA presented at SPE Annual Technical Conference and Exhibition, Anaheim, California, 11-14 November.
18. Kazemi, H., Merrill, L.S., Porterfield, K.L. and Zeman, P.R. 1976. Numerical Simulation of Water-Oil Flow in Naturally Fracture Reservoirs. SPE 5719.
19. Keshavarzi, R. and Mohammadi, S. 2012. A new Approach for numerical Modeling of Hydraulic Fracture Propagation in Naturally Fractured Reservoirs. SPE 152509-MS.
20. Lamb, H., Ed. 1932. Hydrodynamics, 6th edition. New York, Dover Publications.
21. Lemonnier, P. and Bourbiaux, B. 2010. Simulation of naturally fractured reservoirs-State of the Art. Oil & Gas Science and Technology - Rev. IFP **65** (2): 263-286. doi: 10.2516/ogst/2009067
22. Lorenz, J. C. and Warpinski, N. R. 1996. Natural fracture characteristics and effects. Leading Edge, 15(8), 909-911.
23. Maeryhofer, M.J., Lolon, E.P. Warpinski, N.R. Cipolla, C.L., Walser, D. and Rightmire, C.M. What Is Stimulated Reservoir Volume? SPE Production & Operation **25** (1): 89-98. SPE-119890-PA. doi: 10.2118/119890-PA
24. Meyer, R. B. and Lucas W. Bazan. 2011. A Discrete Fracture Network Model for Hydraulically Induced Fractures - Theory, Parametric and Case Studies. Paer SPE 140514 presented at SPE Hydraulic Fracturing Technology Conference, 24-26 January 2011, The Woodlands, Texas, USA. doi: 10.2118/140514-MS.
25. Moinfar, A. Varavei, A. Sepehrnoori, K. and Johns, R.T. 2013. Development of a Coupled Dual Continuum and Discrete Fracture Model for the Simulation of Unconventional Reservoirs. Paper SPE 163647 presented at the SPE Reservoir Simulation Symposium, Woodland, TX, 18-20 Feb.
26. Moinfar, A. Varavei, A. Sepehrnoori, K. and Johns, R.T. 2014. Development of an Efficient Embedded Discrete Fracture Model for 3D Compositional Reservoir Simulation in Fractured Reservoirs. SPEJ **19** (2): 289-303. SPE-154246-PA. doi: 10.2118/154246-PA
27. Ning, X., R. Marcinew, et al. 1995. The Impact of Fracturing-fluid Cleanup And Fracture-face Damage On Gas Production. Annual Technical Meeting.
28. Nordgren, R.P. 1972. Propagation of a Vertical Hydraulic Fracture. *SPEJ* **12** (4): 306-314. SPE-3009-PA. doi: 10.2118/3009-PA

29. Ozkan, E., Raghavan, R. and Apaydin, O.G. 2010. Modeling of Fluid Transfer from Shale Matrix to Fracture Netwrok. SPE 134830
30. Palisch, T.T., Vincent, M., and Handren, P.J. 2010. Slickwater Fracturing: Food for Thought. SPE Production & Operation **25** (3): 327-344. SPE-115766-PA. doi: 10.2118/115766-PA
31. Perkins, T.K. and Kern, L.R.1961. Widths of Hydraulic Factures. *J Pet Technol* **13** (9): 934-949; *Trans*., AIME, **222**. SPE-89-PA. doi: 10.2118/89-PA
32. Poltluri, N., D. Zhu, and Hill, A.D. 2005.The Effect of Natural Fractures on Hydreaulic Fracture Propagation. Paper SPE 94568 presented at the SPE European Foramtion Damgae Conference, Sheveningen, The Netherlands, 25-27 May. doi: 10.2118/94568-MS.
33. Renshaw, C. E., and D.D. Pollard. 1998. An experimetal Verified Criterion for Propagation Across Unbounded Frictional Interfaces in Brittle Linear Elastic Materials. International Journal of Rock Mechanics and Mining Science & Geomechanics, **32** (3): 237-249. doi: 10.1016/0148-9062(94)00034-4.
34. Taleghani, A.D. and Olson, J.E. 2011. Numerical modeling of Multistranded-hydraulic-Fracture Propagation: Accounting for the interaction Between Induced and Natural Fractures. *SPEJ* **16** (3): 575-581. SPE-124884-PA. doi: 10.2118/124884-PA.
35. Taleghani, A.D. and Olson, J.E. 2013. How Natural Fractres Could Affect Hydraulic-Fracture Geometry. *SPEJ* SPE-167608-PA. doi: 10.2118/167608-PA.
36. Teufel, L.W. and Clark, J.A. 1984. Hydraulic fracture propagation in layered rock: Experimental studies of fracture containment. *SPEJ* **24** (1): 19-32. SPE-9848-PA. doi: 10.2118/9878-PA.
37. Thomas, L., T. Dixon, et al. 1983. Fractured reservoir simulation. *SPE Journal* **23** (1): 42-54.
38. Saidi, A. M. 1983. Simulation of Naturally Fractured Reservoirs. SPE Reservoir Simulation Symposium. San Francisco, California, Society of Petroleum Engineers of AIME.
39. Settari A. 1985. A New General Model of Fluid Loss in Hydralic Fracturing. SPEJ 25 (4) 491-501.
40. Wang, J., S. Holditch, et al. 2010. Modeling Fracture-Fluid Cleanup in Tight-Gas Wells. SPE Journal **15** (3): 783-793.
41. Wang, Y., S. A. Holditch, et al. 2008. Simulation of Gel Damage on Fracture Fluid Cleanup and Long-Term Recovery in Tight Gas Reservoirs. SPE Eastern Regional/AAPG Eastern Section Joint Meeting. Pittsburgh, Pennsylvania, USA, Society of Petroleum Engineers.
42. Warren, J. E. and P. J. Root. 1963. The Behavior of Naturally Fractured Reservoirs.
43. Warpinski, N.R. and Teufel, L.W. 1987. Influence of Geologic Discontinuities on Hydrauli Fracture Propagation. *J Pet Technol* **39** (2): 209-220; *Trans*., AIME, **283.** SPE 13224-PA. doi: 10.2118/13224-PA.
44. Weng, X., Kresse, O., Cohen C., Wu R., and Gu H. 2011. Modeling of Hydraulic Fracutre Network Propagation in a Naturally Fractured Formation. *SPE Production & Operations* **26** (4): 368-380. SPE-140253-PA. doi: 10.2118/9878-PA. doi: 10.2118/140253-PA.
45. Wu, Y.-S. and K. Pruess. 1988. A multiple-porosity method for simulation of naturally fractured petroleum reservoirs. *SPE Reservoir Engineering* **3** (1): 327-336.
46. Yoon, Jeoung Seok, Zang, Arno and Stephansson, Ove. 2014. Numerical investigation on optimized stimulation of intact and naturally fractured deep geothermal reservoirs using

hydro-mechanical coupled discrete particles joints model. Geothermics, doi: 10.1016/j.geothermics.2014.01.009

47. Zhang, X., C. Du, et al. 2009. Sensitivity Studies of Horizontal Wells with Hydraulic Fractures in Shale Gas Reservoirs. International Petroleum Technology Conference. Doha, Qatar, 2009, International Petroleum Technology Conference.
48. Zhang, X., Jeffery, R.G. 2008. Reinitiation or termination of fluid driven fractures at frictional bedding interfaces. *J. Geophys. Res.* 113: B08416. doi: 10.1029/2007JB005327.
49. Zhang, X., Jeffery, R.G., and Thiercelin, M. 2007a. Deflection and propagation of fruid-driven fractures at frictional bedding interfaces: A numerical investigation. *Journal of Structrual Geology* 29 (3): 396-410. Doi: 10.1016/j.jsg.2006.09.013.
50. Zhang, X., Jeffery, R.G., and Thiercelin, M. 2007b. Effects of Frictional Geological Discontinuities on Hydraulic Fracture Propagation. Paper SPE 106111 presented at the SPE Hydraulic Fracture Technology Conference, College Station, Texas, USA, 29-31 Jan. doi: 10.2118/106111-MS.Stoner, M.A.: *"Steady-State Analysis of Gas Production, Transmission and Distribution Systems"* paper SPE 2554 presented at the 1969 Annual Meeting of the SPE of AIME, Denver, Sept. 28-Oct.1
51. Zeini Jahromi, M., Wang, J. Y., and Ertekin, T. 2013. Development of a Three-Dimensional Three-Phase Fully Coupled Numerical Simulator for Modeling Hydraulic Fracture Propagation in Tight Gas Reservoirs. Presented SPE HFTC, 4-6 Feb, Woodlands, TX. SPE-163850-MS. doi: 10.2118/163850-MS.

Chapter 4 STUDY OF THE EFFECTIVENESS OF STIMULATION

The most effective method for stimulating shale gas reservoirs is horizontal wells with successful multi-stage hydraulic fracture treatments. Recent fracture diagnostic technologies such as microseismic technology have shown that complex fracture networks are commonly created in the field. However, often times, the stimulated reservoir volume (SRV) obtained from the microseismic interpretation fails to provide propped fracture volume and its conductivity such that, commonly, there is a gap between the SRV that is open for the gas flow and SRV obtained from micro seismic analysis.

In this paper, the coupled hydraulic fracturing model that is capable to simulate dynamic fracture propagation, reservoir flow simulation, the interactions between hydraulic fractures and pre-existing natural fractures, and proppant transportation will be used to conduct numerical experiments. The effects of proppant selection, stress anisotropy, fracture fluid selection, pumping rate and natural fracture spacing on the propped stimulated reservoir volume (PSRV) which is the SRV with propped fractures and hydraulic fracture conductivities is then compared and quantified. At last, using the knowledge gathered during parametric studies will be applied to enhance the effectiveness of stimulation.

Simulation results from the parametric studies show that enlarging SRV does not guarantee better gas production. Increasing the effectiveness with viscous fluid or smaller proppant may result smaller SRV but it has a better chance to increase well performance. Fracture intensity increased in a reservoir with relatively small stress anisotropy or with dense pre-existing natural fracture network may also increase SRV but our result shows that it could decrease PSRV because

This chapter was presented on Unconventional Technology Conference on August 2014 (SPE-1922580-MS).

proppants are distributed inside of network which is already stimulated by adjacent fractures. These results will provide a better understanding to enhance SRV and fracture conductivity through proper proppant, fluid and pumping rate selection depending on the stress anisotropy and the complexity of pre-existing natural fracture network.

4.1 Introduction

The development of unconventional resources has been perhaps the biggest new trend in the petroleum industry in recent decades. The economic production of unconventional resources is enabled through the key technologies of long horizontal wells and massive hydraulic fracturing. It hinges mostly on effective stimulation of ultra-low permeability formation by creating complex fracture networks that functions as the conductive path to recover reservoir fluids.

Stimulated reservoir volume (SRV) is an important concept to describe and evaluate the treatment effectiveness. SRV is strongly related to rate of production and ultimate recovery in ultra-tight reservoirs. Production can be maximized by creating large SRV coverage with high fracture density (Cipolla et al. 2010). Microseismic mapping is most often used to determine the SRV. However, it does not provide any details of the effectively producing fracture structure or spacing (Maeryhofer et al. 2010). The mapped events could be induced from other mechanisms that do not directly indicate the initiation or re-opening of fractures such as shear-slip (Albright et al. 1982; Rutledge et al. 2003; Warpinski et al. 2004). When the created volume is not effectively propped among the entire network, the unpropped part will close during the flowback barely contributing to production. Therefore, instead of using the total created SRV, effective stimulated reservoir volume (PSRV) –stimulated volume which the propped fracture network is capable of delivering hydrocarbon from– is proposed in this paper to be indicating the effectiveness of the stimulation.

Numerous authors have investigated fracture propagation behavior in naturally fractured reservoirs both experimentally (Blanton 1986; Renshaw and Pollard 1998; Warpinski and Teufel 1987) and numerically (Taleghani et al. 2011, 2013; Weng et al. 2011; Zhang et al. 2007a, 2007b, 2008; Keshavarzi et al. 2012; Meyer and Bazan 2011). Renshaw and Pollard criterion was extended to implement the intersection behavior for non-orthogonal case by Gu and Weng (Gu and Weng, 2010). Mathematical models of interaction between hydraulic fracture and natural fractures were reviewed and summarized by Poltluri at el. (2005).

Proppant transport is another important factor of hydraulic fracturing treatment. With successful proppant displacement within fracture network, higher potential of hydrocarbon recovery might be expected. Several works have been done to understand proppant transport through laboratory experiments. Biot et al. conducted a series of experiments of proppant transport behavior in low-viscosity bearing fluid through two parallel glass plates (Biot and Medlin et al. 1985). In most of the cases in low-viscosity slurry injection, settling of proppant is significant that proppant bridging may occur to cause undesired termination of the treatment. Numerical simulation of proppant transport has also been done by several researchers. Tsai et al. combined computational fluid dynamics (CFD) software and a discrete-element typed proppant transport mechanism together to simulate slurry injection process (Tsai et al. 2013). The result indicates that the horizontal fluid flow velocity and proppant density are main factors that control proppant settlement. Several agreements are found among experiments and numerical simulations. In the other hand, fracture geometry and fluid flow velocity will change during the treatment in shale gas reservoir. Therefore, assumptions in the experiments and numerical studies may affect the results to vary from real condition. Hence, an integrated proppant transport model is developed and applied to capture the dynamic process during the treatment.

The objective of this paper is to obtain a valuable knowledge which will lead the engineers to enhance the effectiveness of hydraulic fracture treatment. A numerical simulation model that integrates fracture propagation and proppant transportation in association with the pre-existing natural fracture network and fracture fluid leakoff for shale gas reservoirs will be briefly introduced. Then it will be exercised to conduct a series of parametric studies on the effective SRV (PSRV) and fracture conductivity to investigate the sensitivity of its characteristics to those parameters. This methodology is intended to provide better understanding to enhance the effectiveness of hydraulic fracturing processes in field.

4.2 Proppant transportation model

Proppant transport model is explicitly integrated into the fracture propagation model developed in chapter 3. This model captures fracture fluid flow velocity within fracture network, fracture geometry, pressure distribution, proppant properties and other important input parameters. An assumption is made here that there is no slippage in horizontal direction. The vertical settling velocity is calculated in **Equation 4-4**. The top of the suspending slurry starts to descend during horizontal transport and the settled proppant accumulate at the bottom of the pay creating a proppant bank. Therefore, the total amount of proppant in a fracture block is contributed from two parts, suspending proppant in the slurry and settled proppant in the bank. Concentration contributed from the suspending slurry is calculated from equation 10, and the contribution form the Proppant transport model is explicitly integrated into the fracture propagation model. This model captures fracture fluid flow velocity within fracture network, fracture geometry, pressure distribution, proppant properties and other important input parameters. An assumption is made here that there is no slippage in horizontal direction. The vertical settling velocity is calculated in Equation 13. The top of the suspending slurry starts to descend during horizontal transport and the settled proppant accumulate at the bottom of the pay creating a proppant bank. Therefore, the total amount of proppant in a fracture block is contributed from two parts, suspending proppant in the slurry and settled proppant in the bank. Concentration contributed from the suspending slurry is calculated from equation 10, and the contribution form the settled bank is calculated from **Equation 4-2**.

$$Cp_{suspend}{}^{n+1} = (Cp_{inj} * \frac{H_{suspend}}{H_{pay}} * w)^{n+1} \tag{4-1}$$

$$Cp_{settled}{}^{n+1} = Cp_{settled}{}^{n} + \frac{Vs\Delta t_{avg}}{H_{pay}} * w \tag{4-2}$$

$$Cp_t{}^{n+1} = Cp_{suspend} + Cp_{settled}{}^{n+1} \tag{4-3}$$

$$Vs = \frac{138 d_p^2 (\rho_p - \rho_f)}{\mu} \tag{4-4}$$

For each time step, the module calculates the suspending slurry height, settled proppant mass of each fracture element, and the front of slurry within the fracture network. An illustrative cartoon is shown in **Figure 4-1**.

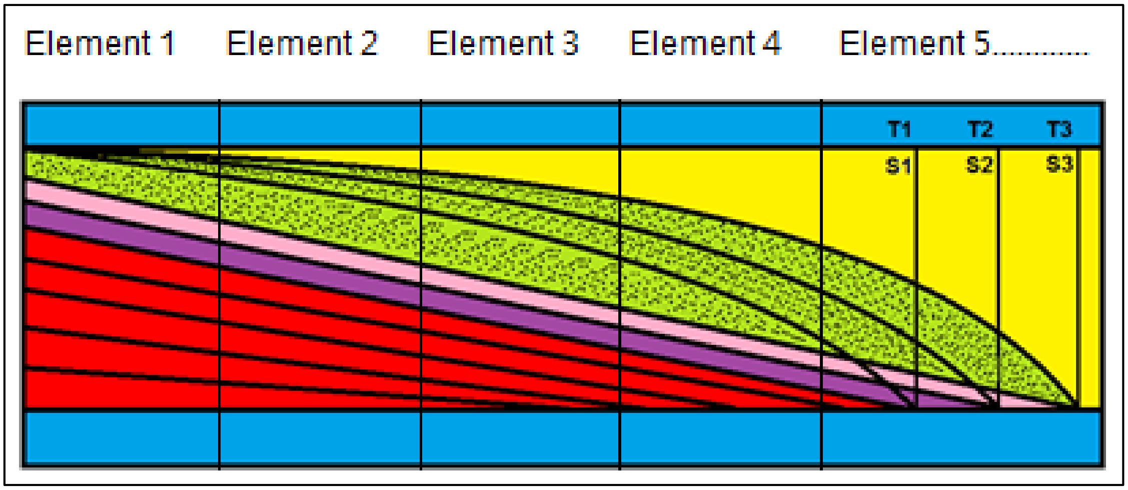

Figure 4-1. Illustration of proppant distributive logic. The Yellow part is the pay. The light green part is the suspending slurry. The red part is the settled proppant.

Proppant mass concentration per unit area (lb/ft^2) is converted into fracture conductivity depending on the proppant type and properties. The corresponding heal permeability of the proppant pack is depending on proppant concentration and is obtained from conductivity test as in **Figure 4-2**. **Figure 4-2 (a)** is permeability curve of different sizes of proppant measured under a base case of average proppant concentration of 2 lb/ ft^2 subjected to different closure stress. Therefore, proppant pack permeability with different concentration is proportional to the base case. **Figure 4-2 (b**) provides the healed width of proppant pack and corresponding proppant concentration. The absolute fracture conductivity is defined as Equation 14 and average conductivity for the propped fracture network, the average conductivity is calculated as Equation 15. To be consistent with **Figure 4-2 (a)**, unit healed width used in the equation is at proppant concentration of 2 lb/ ft^2.

$$C_f = k_f\, w_{hf} = \frac{k_p C p_t w_{uhf}}{C_{unit}} \tag{4-5}$$

$$Average\ Conductivity = \frac{\sum_i \sum_j (C_{f\,i,j} L_{f\,i,j})}{\sum_i \sum_j L_{f\,i,j}} \tag{4-6}$$

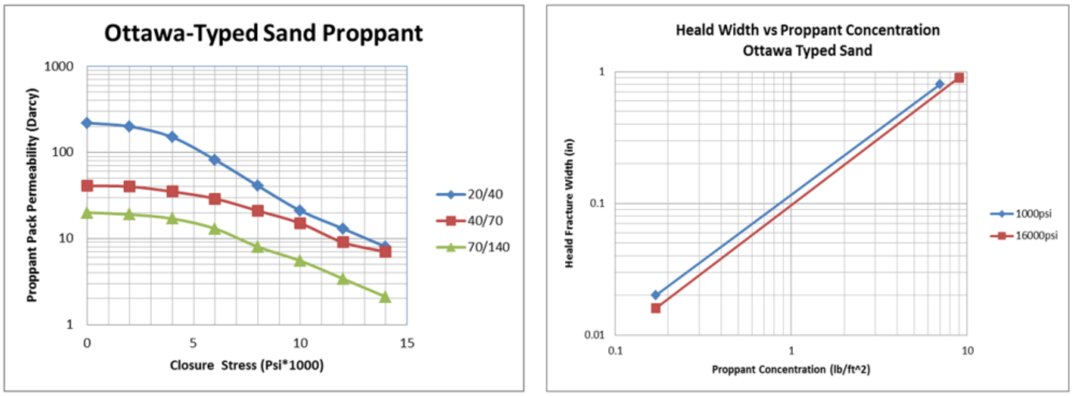

(a) The relationship between proppant pack permeability and closure stress

(b) Healed fracture width and proppant concentration relationship

Figure 4-2. The relationships for absolute conductivity calculation (Hannah and Anderson 1985).

4.3 Parametric studies of effectiveness of stimulation

Parametric studies are carried out to investigate the effectiveness of hydraulic fracture treatment, which is measured in terms of propped SRV (PSRV) and fracture conductivity. The PSRV in this study is defined as the total volume of the matrix blocks with at least one of the boundaries which is propped open assuming all the unpropped fractures will be closed after flowback and become a seal preventing matrix-to-matrix flow. The intensity can be quantified as **Equation 4-7**. Intensity factor reflects how much area is contacted with propped fractures per PSRV. The intensity factor and average conductivity indicate the quality of PSRV.

$$Intensity\ factor\ of\ propped\ fracture\ network = \frac{(\ Reservoir - fracture\ contact\ area\ of\ propped\ fracture, ft^2)}{PSRV, ft^3} \tag{4-7}$$

For all cases, two sets of pre-existing natural fractures are located in the reservoir with one set along the x-direction and the other parallel to y-direction so that only orthogonal interaction between the fractures is considered in this study. All the other assumptions and settings are identical to those in chapter 3 Error! Reference source not found..

The input values for parametric studies are described in **Table 4-1** and the parameters that will be investigated are highlighted. The injection rate of 17 bbl/min for our study represents 102 bbl/min of a fracture treatment stage considering symmetry. The flow through perforation is not modeled individually. The fracturing fluid is assumed to be injected at the natural fracture along the direction perpendicular to the minimum insitu stress. Case 1 is the reference case and Case 2 to 4 are designed to investigate parametric sensitivities for the operation parameters: proppant size, fracture fluid viscosity, and fracture fluid injection rate. Case 5 and 6 will focus on the effect of differential stress and pre-existing natural fracture spacing on PSRV and fracture conductivity. Lastly, the effort to enhance the effectiveness of stimulation will be presented.

Table 4-1. Input values for each cases. The parameter which is studied in each case is highlighted with red.

Perforation Location (0,0)	Cases									
Parameters	4.1	4.2		4.3		4.4	4.5		4.6	
	Reference	4.2.1	4.2.2	4.3.1	4.3.2		4.5.1	4.5.2	4.6.1	4.6.2
Proppane size (mesh)	40/70	20/40	70/140	40/70	40/70	40/70	40/70	40/70	40/70	40/70
Fracture Fluid Viscosity (μ, cp)	2	2	2	5	10	2	2	2	2	2
Injection Rate (Q, bbl/min)	17	17	17	17	17	50	17	17	17	17
Stress anisotropy (psi)	100	100	100	100	100	100	30	300	100	100
Natural Fracture Spacing (Dx X Dy, ft)	10 X 20	10 X 20	10 X 20	10 X 20	10 X 20	10 X 20	10 X 20	10 X 20	1 X 2	100 X 200
Initial Reservoir Pressure (psi)	4000	4000	4000	4000	4000	4000	4000	4000	4000	4000
Permeability (k, md)	0.0001	0.0001	0.0001	0.0001	0.0001	0.0001	0.0001	0.0001	0.0001	0.0001
Porosity (%)	6	6	6	6	6	6	6	6	6	6
σ_h, min (psi)	8000	8000	8000	8000	8000	8000	8000	8000	8000	8000
Young's Modulus (E, psi)	3.0E6	3.0E6	3.0E6	3.0E6	3.0E6	3.0E6	3.0E6	3.0E6	3.0E6	3.0E6
Poisson's ratio (ν, fractional)	0.2	0.2	0.2	0.2	0.2	0.2	0.2	0.2	0.2	0.2
Fracture Height (ft)	100	100	100	100	100	100	100	100	100	100
Proppant concentration (lb/gal)	0.5	0.5	0.5	0.5	0.5	0.5	0.5	0.5	0.5	0.5

4.3.1 Case 4.1- *Reference Case*

This case will be the reference to enable meaningful comparison of the effectiveness of stimulation throughout our parametric study. The matrix permeability of 0.0001 md, Young's modulus of 3.0×10^6 psi are chosen from the acceptable range to represent the shale gas reservoir in North America such as Marcellus, Barnet and etc.

Figure 4-3 illustrates the final hydraulic fracture geometry from Case 4.1 simulation. The maximum length among the primary fractures (propagating perpendicular $\sigma_{h,min}$ or propagating to y-direction) is 1386 ft and the maximum length of secondary (propagating perpendicular $\sigma_{H,max}$ or propagating to x-direction) is 80 ft. The color contour indicates the width for hydraulic fractures showing the maximum width at the wellbore of 0.015 ft (0.18 in). Because of the low fracture fluid viscosity of 2 cp and zero fracture toughness, relatively small width is generated. Also, secondary fractures have smaller width than primary fractures since the confining stress for secondary fractures is larger ($\sigma_{H,max}$). Larger horizontal differential stress ($\sigma_{H,max} - \sigma_{h,min}$) will increase this width difference further.

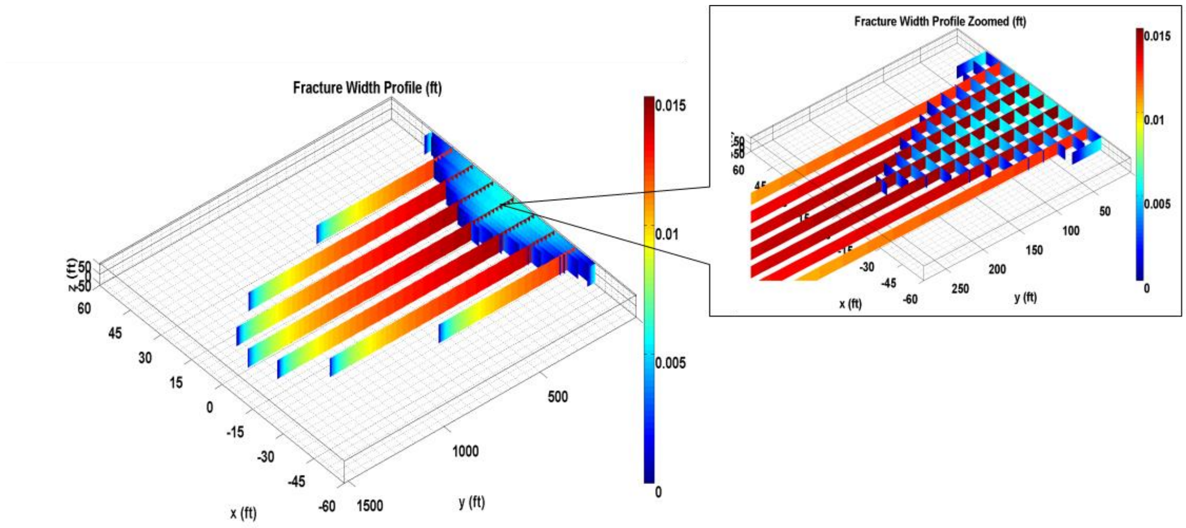

Figure 4-3. Final hydraulic fracture geometry for Case 4.1 including zoomed view near wellbore– Color contour indicates fracture width.

Figure 4-4 (a) presents the average pressure in the matrix which reflects leakoff of fracture fluid into the formation. Corresponding cumulative leakoff volume versus time is plotted in **Figure 4-4 (b)**. Approximately, total volume of 4 bbl of fracture fluid, 2.4% of total injected volume is invaded into the formation as indicated by pressure profile. Ultra-low permeability nature of shale resulted in very low pressure increase and relatively small leakoff volume.

Proppant concentration and fracture conductivity are shown in **Figure 4-5**. Proppant concentration is ranging from 0 to 0.14 lb/ft^2 and conductivity is reached up to 13.56 md-ft. It is also observed that 17 percent of SRV is propped open and has an average absolute conductivity of 7.1791 md-ft. The PSRV for this case is 16,000 ft^2 per ft in height.

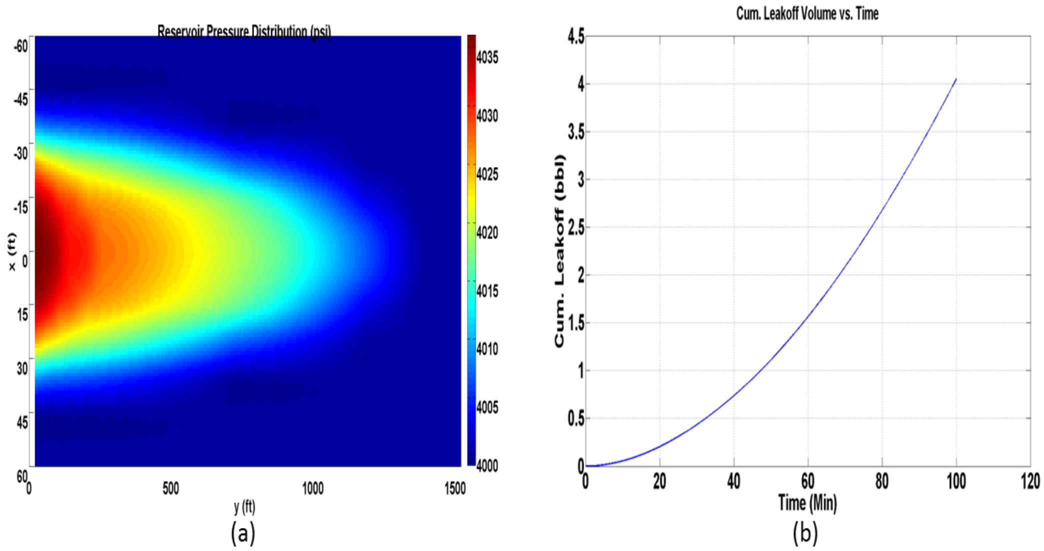

Figure 4-4. (a) Reservoir(Matrix) pressure map in psi for Case 1. (b) Cumulative leakoff volume versus time for Case 4.1.

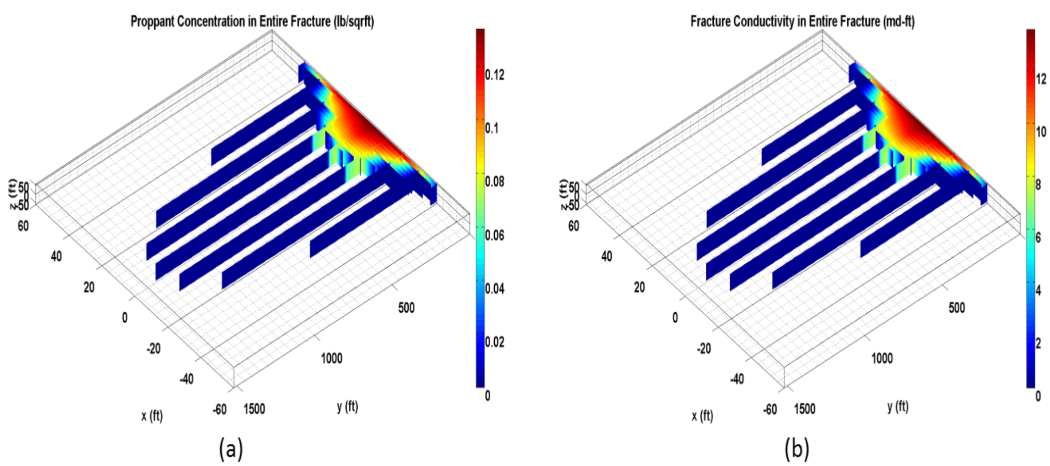

Figure 4-5. (a) Proppant concentration profile (lb/ft^2) for Case 4.1. (b) Fracture conductivity profile (md-ft) for Case 4.1.

4.3.2 Case 4.2- *Proppant size: Case 2.1 with 20/40 mesh sand and Case 2.2 with 70/140 mesh sand*

All the input values except proppant size remains same and the effect of proppant size on PSRV and fracture conductivity are studied in this section. **Figure 4-6** shows the identical final hydraulic fracture geometry as Case 4.1.

In Case 4.2.1, 20/40 mesh sand is used for the simulation and the proppant transportation through the fracture is limited due to high settling velocity of large particle diameter (=600 micron). As illustrated in **Figure 4-6 (a)**, the farthest point the slurry can reach before settling to the bottom of the fracture is around 60 ft along primary fracture and 34 ft to secondary fracture so that only 3.06 percent of the total fracture volume is propped open. PSRV is 2,340 ft^2 which is about 15% of the PSRV in Case 4.1. However, average absolute conductivity for this case is remarkably increased to be 80.1 md-ft, about 1166% of Case 4.1. The result implies that, in Case 4.2.1, the limited amount of reservoir fluid (due to low PSRV) will be recovered at high flowrate (due to high fracture conductivity).

In Case 4.2.2, using 70/140 mesh sand, we can observe a significantly larger conductive region than Case 1 and Case 4.2.1 (**Figure 4-6 (b)**). The settling velocity of the 70/140 sand is relatively lower than that of 20/40 and 40/70 sands so that proppants travel further into the fracture network having 44.26 percent of fracture network to be propped open and PSRV of 40,000 ft^2 which is 250% of Case 4.1. Because the fracture network is propped with fine sand average absolute conductivity is dramatically decreased to be 1.8857 md-ft (27.45% of Case 4.1).

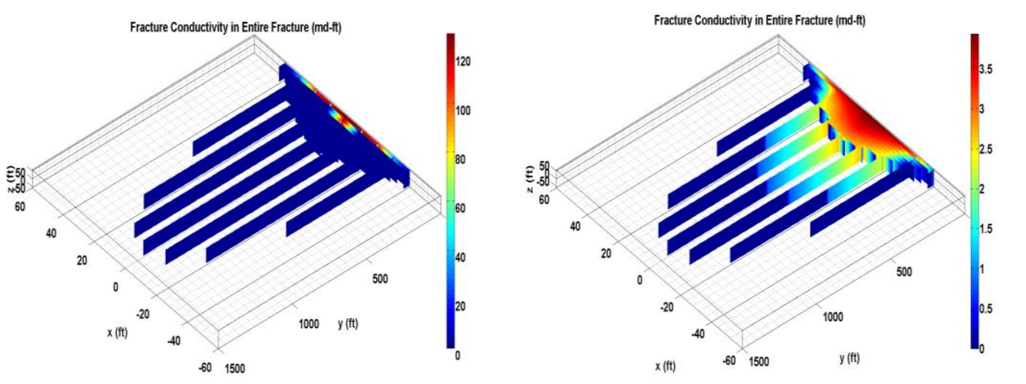

(a) Case 4.2.1 with 20/40 mesh

(b) Case 4.2.2 with 70/140 mesh

Figure 4-6. Final fracture geometry and color contour of absolute fracture conductivity (md-ft). (a) Case 4.2.1 with 20/40 mesh proppant size. (b) Case 4.2.2 with 70/140 mesh proppant size.

Based on **Equation 4-5**, the proppant concentration is determined by the amount of proppant suspending in the slurry and of the settled bank. Thus, the settling-accumulation effect is more dominant in the case using larger proppant where a significant part of the total fracture conductivity is counted from. On the other hand, if the settling is less dominant as in Case 4.2.2, fracture conductivity is obtained by proppant concentration in the suspending slurry rather than from the settled bank. The results also show almost no changes in SRV but PSRV is increased with smaller proppants.

4.3.3 Case 4.3- *Fracture fluid viscosity: Case 4.3.1 with 5 cp and Case 4.3.2 with 10 cp*

Slick water and hybrid fluid are commonly used fluid systems in Marcellus shale. It is known that viscous fluid increases the net pressure in a fracture such that it tends to create wider fracture width having relatively short fracture length. Also, secondary fractures are opened more frequently due to the large net pressure. The comparison between **Figure 4-6** and **Figure 4-7** justifies the effect of fracture fluid viscosity on the final fracture geometry. As fracture fluid viscosity increases to 2 cp, 5cp and 10 cp, SRV length decreases from 1500 ft to 1200 ft and 1000 ft but its width stays about the same between 40 ft and 50 ft.

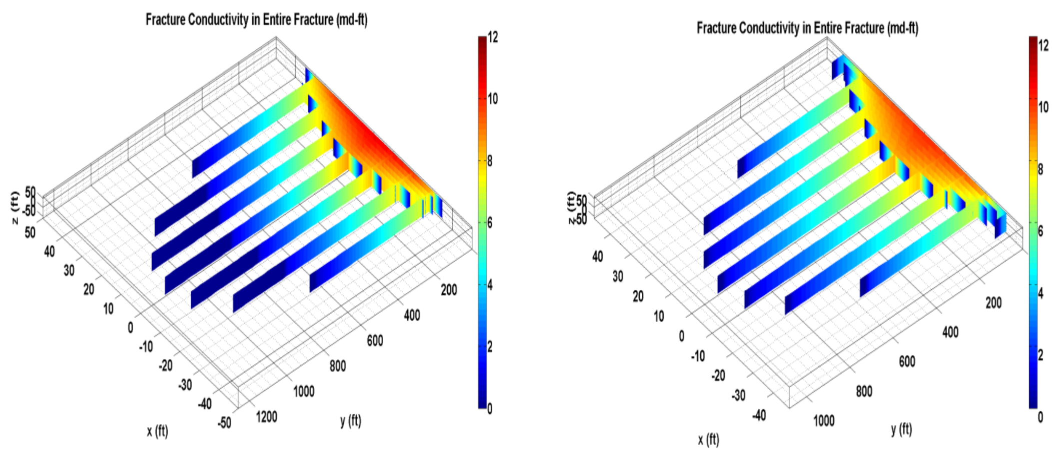

(a) Case 4.3.1 with 5 cp (b) Case 4.3.2 with 10 cp

Figure 4-7. Final fracture geometry and color contour of absolute fracture conductivity (md-ft). (a) Case 4.3.1 with 5 cp fracture fluid viscosity. (b) Case 4.3.2 with 10 cp fracture fluid viscosity.

Although primary fracture length diminishes as fluid viscosity increases, propped length of primary fracture increases to 720 ft for Case 4.3.1 and 880 ft for Case 4.3.2 so that 75.6% of fracture volume is propped in Case 4.3.1 and 94% is propped in Case 4.3.2. In other word, SRV tends to be smaller with high viscous fluid but PSRV is enlarged reflecting effectiveness of stimulation is increased. PSRV of 62,249 ft^2 from Case 4.3.1 and 65599 ft^2 in Case 4.3.2 are obtained through this section. The results are showing unrealistic high efficiency because proppant transportation model simulated the ideal condition without considering fluid friction, wall-effect, fracture damages, and etc. However, the model provides a general sense how PSRV is enhanced by increasing fracture fluid viscosity. The average absolute fracture conductivity in Case 4.3.1 is 4.754 md-ft and 4.66 md-ft in Case 4.3.2. Comparing with Case 4.1, PSRV is 389.05% and average conductivity is 69.2% in Case 4.3.1, and 410% and 67.83% in Case 4.3.2.

4.3.4 Case 4.4- *Fracture fluid injection rate with 50 bbl/min.*

Increasing pumping rate will also increase the net pressure in the fracture network such that the effect of fluid injection rate shows similar result as increasing fracture fluid viscosity as shown in **Figure 4-8**. PSRV and average conductivity are 65,105 ft^2 and 4.3 md-ft which also are similar to the Case 4.3.2. The width of SRV increases but the length decreases. In addition, the velocity of fluid also increases such that proppants travels further into fracture network and consequent PSRV becomes larger.

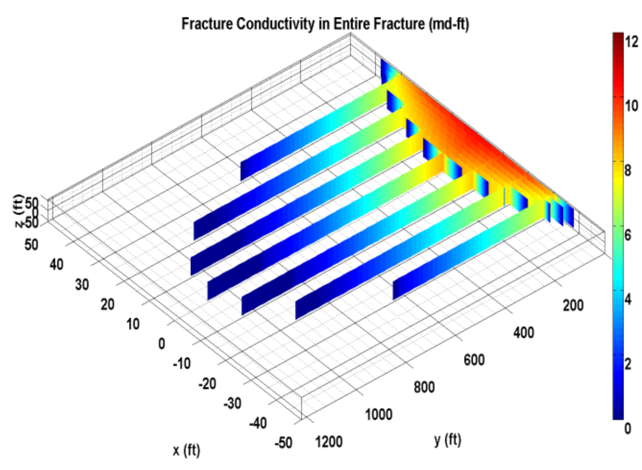

Figure 4-8. Final fracture geometry and color contour of absolute fracture conductivity (md-ft) for Case 4.4 with injection rate of 50 bb/min.

4.3.5 Case 4.5- ***Horizontal differential stress ($\sigma_{H,max} - \sigma_{h,min}$): Case 4.5.1 with 30 psi and Case 4.5.2 with 300 psi.***

Horizontal differential stress influences fracture geometry during propagation. If the differential stress is larger, the fracture network has a tendency of propagating perpendicular to the minimum principle in-situ stress direction so that final fracture network will be narrow and elongated. However, if differential stress is close to zero fracture propagates to x and y direction with almost same velocity creating radial fracture network. **Figure 4-9** illustrates the effect of differential stress.

In Case 4.5.1, the horizontal differential stress is assigned to be 30 psi and consequently, complex and dense fracture network is created with SRV of 96,000 ft^2, PSRV of 15,600 $ft^2$and average conductivity of 6.5685 md-ft. This case shows that enlarging SRV does not necessarily mean it is stimulated effectively in a reservoir with small differential stress. In Case 4.5.2, the fracture geometry is elongated. Three primary fracture branches are created from one secondary fracture branch. The primary fractures are extended nearly 2500 ft with SRV of 93,200 ft^2 which is less than Case 4.5.1. However, PSRV of 34,800 $ft^2$and average absolute conductivity of 10.2 md-ft are obtained from Case 4.5.2 is larger than Case 4.5.1.

Smaller differential stress adds the complexity to the fracture geometry and it decreases the effectiveness of stimulation in both PSRV and fracture conductivity. In contrast, the density and intensity of propped fracture network is higher in Case 4.5.1 than Case 4.5.2. In Case 4.5.1, it is 0.23 ft^2/ft^3 and 0.15 ft^2/ft^3 in Case 4.5.2 which reflect that Case 4.5.1 has 1.53 times more intensive fracture network within PSRV than Case 4.5.2.

The secondary fracture branches contained inside of the fracture network do not contribute to the increase of PSRV; on the other hand, propped open outer-boundary primary fracture branches contribute to dramatic increase of PSRV. The outer-boundary primary fractures in Case 4.5.1 are very short and not effectively propped so that PSRV decreased. The nature of secondary fracture having relatively smaller width than primary fracture also results in slight decrease of average conductivity. Therefore, from this section, we have learned that it is important to prop-open the outer-boundary primary fractures before losing most of the proppants into secondary fractures.

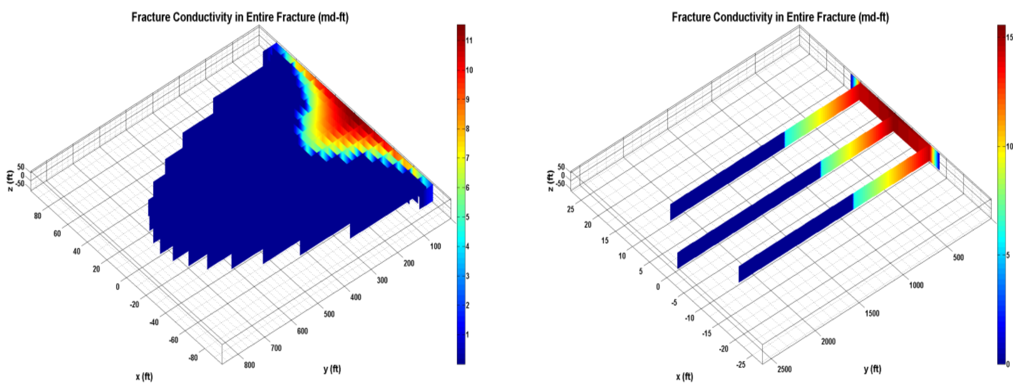

(a) Case 4.5.1 with 30 psi (b) Case 4.5.2 with 300 psi

Figure 4-9. Final fracture geometry and color contour of absolute fracture conductivity (md-ft). (a) Case 4.5.1 with 30 psi differential stress. (b) Case 4.5.2 with 300 psi differential stress.

4.3.6 Case 4.6- *Natural fracture spacing: Case 4.6.1 with 1 ft by 2 ft (Dx by Dy) and Case 4.6.2 with 100 ft by 200 ft.*

In this set of parametric study, the effect of natural fracture spacing of 1 ft x 2 ft (Case 4.6.1) and 100 ft x 200 ft (Case 4.6.2) are investigated on PSRV and fracture conductivity. In case

4.6.1, high density of the pre-existing natural fractures contributed to the complexity of hydraulic fracture network similar to Case 4.5.1 and the efficiency of the propped fracture volume to total fracture volume is only 13% (**Figure 4-10 (a)**). Furthermore, the size of a matrix block volume itself is diminished from 20,000 ft^3 to 200 ft^3. Therefore, PSRV and average conductivity are decreased to 1,424 ft^2 and 5.475 md-ft. In contrast, a matrix block size is 2,000,000 ft^3 in Case 4.6.2 such that PSRV is enlarged to be 160,000 ft^2. However, the increase of the average conductivity is not dramatic as PSRV because relatively large amount of proppant is captured in the secondary fractures (**Figure 4-10 (b)**).

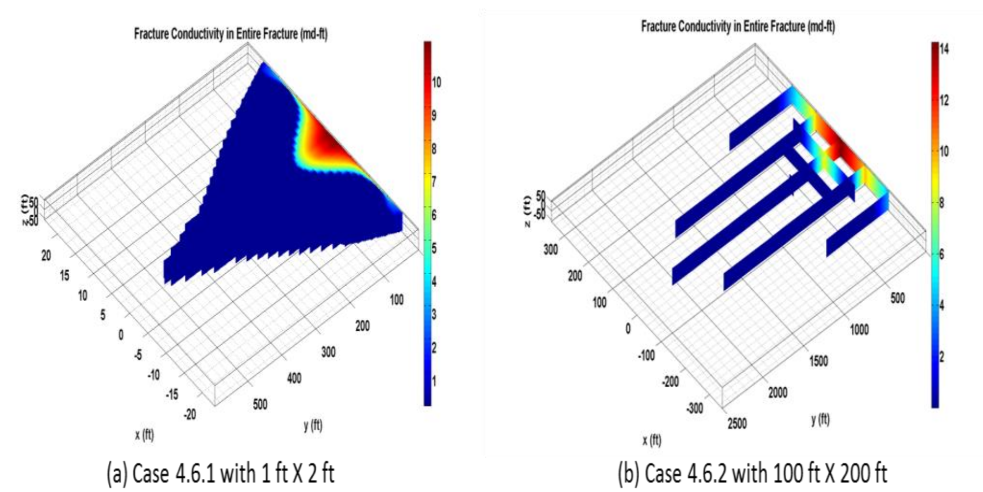

Figure 4-10. Final fracture geometry and color contour of absolute fracture conductivity (md-ft). (a) Case 4.6.1 with 1 ft by 2 ft (Dx by Dy) natural fracture spacing. (b) Case 4.6.2 with 100 ft by 200 ft (Dx by Dy) natural fracture spacing.

In Case 4.6.1, the intensity factor of the propped fracture network is 2.4 ft^2/ft^3 and it is 0.02 ft^2/ft^3 in Case 4.6.2. Natural fracture spacing influence the intensity dramatically showing that denser NF setting results in relatively higher intensity. Although Case 4.6.1 has about 112 times larger PSRV, it has 123 times smaller intensity factor. Therefore, the resource with PSRV in Case 4.6.1 will be recovered with higher rate.

4.3.7 Application to enhance PSRV and Fracture conductivity

The PSRV and fracture conductivity results obtained from Case 4.1 to Case 4.6 are summarized in **Table 4-2**. Taking advantage from the knowledge that we have learned from the parametric study, the effectiveness of the stimulation is Case 4.6.1 will be enhanced in this section.

Table 4-2. The results of PSRV and average absolute conductivity for all cases.

Cases	SRV (ft^2)	PSRV (ft^2)	Average Conducitivity (md-ft)	PSRV % relative to Case 1	Average Conducitivity % relative to Case 1	Propped Fracture Vol./ Total Frac Vol.	Intensity Factor (ft^2/ft^3)
4.1	9.36E+04	1.60E+04	6.9	100.0	100.00	0.21	0.218
4.2.1	9.40E+04	2.40E+03	80.1	15.0	1166.61	0.03	0.217
4.2.2	9.40E+04	4.00E+04	1.9	250.0	27.45	0.44	0.188
4.3.1	7.80E+04	6.22E+04	4.8	389.1	69.20	0.76	0.170
4.3.2	6.80E+04	6.56E+04	4.7	410.0	67.83	0.97	0.182
4.4	7.52E+04	6.51E+04	4.3	406.9	62.70	0.88	0.184
4.5.1	9.60E+04	1.56E+04	6.6	97.5	95.62	0.18	0.233
4.5.2	9.32E+04	3.48E+04	10.2	217.5	148.49	0.39	0.153
4.6.1	1.01E+04	1.42E+03	5.5	8.9	79.70	0.13	2.396
4.6.2	9.60E+05	1.60E+05	7.4	1000.0	107.40	0.20	0.020

The reservoir having such a dense pre-existing natural fracture (Case 4.6.1) tends to generated also very complex hydraulic fracture network with relatively small PSRV. To enhance PSRV for Case 4.6.1, small size of proppant can be used to improve propped fracture volume without harming total fracture volume. This method can enlarge PSRV but fracture conductivity will be decreased. Another reasonable scenario is increasing the net pressure by using more viscous fluid or by higher pumping rate. The scenarios are simulated as shown in **Table 4-3** and best combination of proppant size, fluid viscosity, and pumping rate are highlighted with red. Although total fracture volume decreases with increasing viscosity and pumping rate, incremental amount of PSRV and conductivity are larger so that PSRV, intensity and conductivity both can be improved.

Table 4-3. The results from the simulation runs to enhance PSRV and fracture conductivity for Case 4.6.2

Description	PSRV (ft^2)	Average Conducitivity (ft-md)	Propped Fracture Volume / Total Fracture Volume	Intensity Factor (ft^2/ft^3)
Case 4.6.1	1424	5.48	0.13	2.40
2 cp fluid with 70-140 mesh	2509	1.81	0.29	2.21
10 cp fluid with 70-140 mesh	3820	1.29	0.58	2.66
10 cp fluid with 40-70 mesh	2652	3.63	0.40	2.70
10 cp fluid 50 bpm with 40-70 mesh	3860	4.50	0.69	2.58

4.4 Chapter conclusion

Parametric studies using our fully coupled 2-dimensional, numerical hydraulic fracture-reservoir simulator show that the net pressure and the size of selected proppant are critical in optimizing propped fracture network and conductivity. Conclusions are summarized below.

1. Decreasing the size of proppant can enlarge propped SRV but would decrease the conductivity of propped fractures. Changing proppant size from 20/40 to 40/70 to 70/140, propped SRV (PSRV) has increased from 42,769 ft^2 to 285,128 ft^2 and to 712,820 ft^2 respectively. 70/140 mesh gives low average conductivity of 1.9 md-ft.

2. Increasing the net pressure with relatively high viscosity and pumping rate will increase the ratio of propped fracture volume (total propped fracture volume divided by total fractured volume). From 2 cp to 5 cp and to 10 cp, SRV decreased from 94,000 ft^2 to 78,000

ft^2 and to 68,000 ft^2 but PSRV has been increased from 16,000 ft^2 to 62,249 ft^2 and 65,599 ft^2. Average conductivity for the propped fracture network is changed from 6.9 md-ft to 4.8 md-ft and 4.7 md-ft which shows that conductivity did not change as PSRV changed. Therefore, using viscous fluid may be adequate even though it results in relatively smaller SRV.

3. If the complexity is added to the final hydraulic fracture geometry by decreasing differential stress, PSRV and fracture conductivity both diminish. On the other hand, the intensity of propped fracture network increases. Differential stress of 30 psi resulted PSRV of 15,600 ft^2 while SRV has increased to 96,000 ft^2 from using 100 psi differential stress. Average conductivity also decreases to 6.6 md-ft from 10.2 md-ft. In contrast, the intensity factor for 30 psi case is 1.3 times larger than the case with 300 psi.

4. The density of pre-existing natural fracture also impacts the effectiveness of stimulation. The reservoir having the natural fracture spacing of 1 ft by 2 ft showed dramatic decrease of both SRV and PSRV to be 10,096 ft^2 and 1,424 ft^2 which are approximately 1% of 100 ft by 200 ft case. The intensity of propped fracture network also varied significantly. It increased by 120 times in 1 ft by 2 ft system compare to 100 ft by 200 ft.

5. From the parametric studies, small proppant with relatively higher viscosity fluid (around 5 cp) may be expected to increase PSRV without losing conductivity and intensity too much.

In conclusion, the key findings above will contribute to enhance the effectiveness of hydraulic fracturing in naturally fractured unconventional reservoirs. Using PSRV, intensity factor and average conductivity as indicators, an optimized combination of pump rate, fluid viscosity and proppant size may be found. Future work will link the results to long-term gas recovery to suggest an optimal fracture treatment in unconventional naturally fractured reservoirs.

4.5 Nomenclature

A = cross sectional area (ft^2)

B = Formation volume factor (RB/STB)

Cp_{inj}= proppant concentration of the injected slurry (lb/ft^3)

C_{mono}= proppant concentration of a mono-layer of proppant (lb/ft^2)

$Cp_{settled}$ = proppant concentration of the settled bank (lb/ft^2)

$Cp_{suspend}$= proppant concentration of the suspending slurry (lb/ft^2)

Cp_t= Total proppant concentration (lb/ft^2)

C_w = Compressibility of water (psi^{-1})

d = Extended distance (ft)

f_{L1}, f_{L2} = Fractions of fracture half-length (fraction)

G = Shear modulus of rock formation (psi)

h = Fracture gross height (ft)

h_f, H_{fl} = Fracture height (ft)

$H_{suspend}$ = Height of the suspending slurry (ft)

H_{pay} = Height of the pay (ft)

k = permeability in the x, y and z direction (md)

k_p= permeability of the proppant pack (md)

K_f = coefficient of friction (frictional)

k_r = relative permeability (md)

L_f, l = Fracture length (ft)

p_f = Fluid pressure in the fracture (psi)

q = Fluid injection rate or flowrate of each grid block (bbl/min)

R_s = Solution gas-oil ratio (SCF/STB)

s = Distance along the fracture (ft)

S_w = Water saturation (dimensionless)

T_o = Tensile strength of the rock (psi)

v_{tip} = flow velocity at the tip of fracture (L/T)

Vs = Settling velocity of proppant (ft/s)

w = Fracture width (ft)

w_{hf} = Healed fracture width (ft)

w_{uhf} = Healed fracture width of mono-layer concentration (ft)

$\overline{w}$ = Average fracture width (ft)

α_c = Volumetric conversion factor (dimensionless)

βc = Transmissibility conversion factor (dimensionless)

μ = Fluid viscosity (cp)

ν = Poisson's ratio (dimensionless)

ρ = Fluid density (lbm/ft^3)

σ_{1}, σ_2 = far-field effective stresses (psi)

σ_h = Minimum horizontal principal stress (psi)

σ_H = Maximum horizontal principal stress (psi)

σ_n = Normal stress acting on the NF plane (psi)

σ_t = Stress acting parallel to the NF (psi)

φ = Porosity (dimensionless)

γ = Gravity of phase (psi/ft)

Δt_{avg}= Average time for slurry to travel across a fracture unit length (s)

4.6 Chapter reference

1. Albright, J.N. and Pearson, C.F. 1987. Acoustic Emissions as a Tool for Hydraulic Fracture location: Experience at the Fenton Hill Hot Dry Rock Site. . **22** (4): 529-530. SPE-9509-PA. doi: 10.2118/9509-PA.
2. Blanton T.L. 1982 Experimental Study of Interaction Between Hydraulically Induced and Pre-Existing Fractures. Paper SPE 10847 presented at the SPE Unconventional Gas Recovery Symposium, Pittsburgh, Pennsylvania, USA, 16-18 May. doi: 10.2118/10847-MS.
3. Blot, M. A., & Medlin, W. L. 1985. Theory of Sand Transport in Thin Fluids. Paper SPE 14468 presented at the SPE Annual Technical Conference and Exhibition, Las Vegas, Nevada, 22-26 September.
4. Carter R.D. 1957. Derivation of the General Equation for Estimation the Extent of the Fracture Area. In Drill. And Prod. Prac. API, ed. Howard, G.C. and Fast, C.R., 261-268. NY.
5. Cipolla, C.L., Warpinski, N.R., Mayerhofer, M.J., and Lolon, E.P. 2010. The Relationship Between Fracture Complexity, Reservoir Properties, and Fracture-Treatment Design. SPE Production & Operations 25 (4): 438-452. SPE-115769-PA. doi: 10.2118/115769-PA
6. Cipolla, C.L., Lolon, E.P., Erdle, J.C., and Rubin, B. 2010. Reservoir Modeling in Shale-Gas Reservoirs. SPE Reservoir Evaluation & Engineering 13 (4): 638-653. SPE-125530-PA. doi: 10.2118/125530-PA
7. Gu, H., Weng, X., Lund, J.B., Mack, M.G., Ganguly, U. and Suarez-Rivera, R. 2011. Hydraulic Fracture Crossing Natural Fracture at Non-Orthogonal Angles, A Criterion, Its Validation and Applications. Paper SPE-139984-MS presented at the SPE HFTC, Woodland, Texas, 24-26 Jan. doi: 10.2118/139984-MS.
8. Howard, G.C. and Fast, C.R. Hydraulic Fracturing. 1970. Society of Petroleum.
9. Keshavarzi, R. and Mohammadi, S. 2012. A new Approach for numerical Modeling of Hydraulic Fracture Propagation in Naturally Fractured Reservoirs. SPE 152509-MS.
10. Lamb, H., Ed. 1932. Hydrodynamics, 6th edition. New York, Dover Publications.
11. Lorenz, J. C. and Warpinski, N. R. 1996. Natural fracture characteristics and effects. Leading Edge, 15(8), 909-911.
12. Maeryhofer, M.J., Lolon, E.P. Warpinski, N.R. Cipolla, C.L., Walser, D. and Rightmire, C.M. What Is Stimulated Reservoir Volume? SPE Production & Operation 25 (1): 89-98. SPE-119890-PA. doi: 10.2118/119890-PA
13. Meyer, R. B. and Lucas W. Bazan. 2011. A Discrete Fracture Network Model for Hydraulically Induced Fractures - Theory, Parametric and Case Studies. Paper SPE 140514 presented at SPE Hydraulic Fracturing Technology Conference, 24-26 January 2011, The Woodlands, Texas, USA. doi: 10.2118/140514-MS.
14. Poltluri, N., D. Zhu, and Hill, A.D. 2005.The Effect of Natural Fractures on Hydraulic Fracture Propagation. Paper SPE 94568 presented at the SPE European Formation Damage Conference, Sheveningen, The Netherlands, 25-27 May. doi: 10.2118/94568-MS.

15. Renshaw, C. E., and D.D. Pollard. 1998. An experimental Verified Criterion for Propagation Across Unbounded Frictional Interfaces in Brittle Linear Elastic Materials. International Journal of Rock Mechanics and Mining Science & Geomechanics, 32 (3): 237-249. doi: 10.1016/0148-9062(94)00034-4.
16. Rutledge, J.T. and Phillips, W.S. 2003. Hydraulic stimulation of natural fractures as revealed by induced microearthquakes, Cathage Cotton Valley gas field, East Texas. Geophysics. **68** (2): 441. doi: 10.1190/1.1567212.
17. Taleghani, A.D. and Olson, J.E. 2011. Numerical modeling of Multistranded-hydraulic-Fracture Propagation: Accounting for the interaction Between Induced and Natural Fractures. SPEJ 16 (3): 575-581. SPE-124884-PA. doi: 10.2118/124884-PA.
18. Taleghani, A.D. and Olson, J.E. 2013. How Natural Fractures Could Affect Hydraulic-Fracture Geometry. SPEJ SPE-167608-PA. doi: 10.2118/167608-PA.
19. Teufel, L.W. and Clark, J.A. 1984. Hydraulic fracture propagation in layered rock: Experimental studies of fracture containment. SPEJ 24 (1): 19-32. SPE-9848-PA. doi: 10.2118/9878-PA.
20. Tsai, K., Degaleesan, S. S., Fonseca, E. R., lake, E. 2012. Advanced Computational Modeling of Proppant Settling in Water Fractures for Shale Gas Production. Paper SPE 151607 presented at the SPE Hydraulic fracturing Technology Conference, Woodland, TX, 6-8 Feb.
21. Warpinski, N.R. and Teufel, L.W. 1987. Influence of Geologic Discontinuities on Hydraulic Fracture Propagation. J Pet Technol 39 (2): 209-220; Trans., AIME, 283. SPE 13224-PA. doi: 10.2118/13224-PA.
22. Warpinski, N.R., Wolhart, S.L., and Wright, C.A. 2004. Analysis and Prediction of Microseismicity induced by Hydraulic Fracturing. SPEJ. **9** (1): 24-33. SPE-87673-PA. doi: 10.2118/87673-PA.
23. Weng, X., Kresse, O., Cohen C., Wu R., and Gu H. 2011. Modeling of Hydraulic Fracture Network Propagation in a Naturally Fractured Formation. SPE Production & Operations 26 (4): 368-380. SPE-140253-PA. doi: 10.2118/9878-PA. doi: 10.2118/140253-PA.
24. Zhang, X., C. Du, et al. 2009. Sensitivity Studies of Horizontal Wells with Hydraulic Fractures in Shale Gas Reservoirs. International Petroleum Technology Conference. Doha, Qatar, 2009, International Petroleum Technology Conference.
25. Zhang, X., Jeffery, R.G. 2008. Reinitiation or termination of fluid driven fractures at frictional bedding interfaces. J. Geophysics. Res. 113: B08416. doi: 10.1029/2007JB005327.
26. Zhang, X., Jeffery, R.G., and Thiercelin, M. 2007a. Deflection and propagation of fluid-driven fractures at frictional bedding interfaces: A numerical investigation. Journal of Structural Geology 29 (3): 396-410. Doi: 10.1016/j.jsg.2006.09.013.
27. Zhang, X., Jeffery, R.G., and Thiercelin, M. 2007b. Effects of Frictional Geological Discontinuities on Hydraulic Fracture Propagation. Paper SPE 106111 presented at the SPE Hydraulic Fracture Technology Conference, College Station, Texas, USA, 29-31 Jan. doi: 10.2118/106111-MS.Stoner, M.A.: "Steady-State Analysis of Gas Production, Transmission and Distribution Systems" paper SPE 2554 presented at the 1969 Annual Meeting of the SPE of AIME, Denver, Sept. 28-Oct.1
28. Teufel, L.W. and Clark, J.A. 1984. Hydraulic fracture propagation in layered rock: Experimental studies of fracture containment. SPEJ 24 (1): 19-32. SPE-9848-PA. doi: 10.2118/9878-PA.
29. Tsai, K., Degaleesan, S. S., Fonseca, E. R., lake, E. 2012. Advanced Computational Modeling of Proppant Settling in Water Fractures for Shale Gas Production. Paper SPE 151607 presented at the SPE Hydraulic fracturing Technology Conference, Woodland, TX, 6-8 Feb.

30. Warpinski, N.R. and Teufel, L.W. 1987. Influence of Geologic Discontinuities on Hydraulic Fracture Propagation. J Pet Technol 39 (2): 209-220; Trans., AIME, 283. SPE 13224-PA. doi: 10.2118/13224-PA.
31. Weng, X., Kresse, O., Cohen C., Wu R., and Gu H. 2011. Modeling of Hydraulic Fracture Network Propagation in a Naturally Fractured Formation. SPE Production & Operations 26 (4): 368-380. SPE-140253-PA. doi: 10.2118/9878-PA. doi: 10.2118/140253-PA.
32. Zhang, X., C. Du, et al. 2009. Sensitivity Studies of Horizontal Wells with Hydraulic Fractures in Shale Gas Reservoirs. International Petroleum Technology Conference. Doha, Qatar, 2009, International Petroleum Technology Conference.
33. Zhang, X., Jeffery, R.G. 2008. Reinitiation or termination of fluid driven fractures at frictional bedding interfaces. J. Geophysics. Res. 113: B08416. doi: 10.1029/2007JB005327.
34. Zhang, X., Jeffery, R.G., and Thiercelin, M. 2007a. Deflection and propagation of fluid-driven fractures at frictional bedding interfaces: A numerical investigation. Journal of Structural Geology 29 (3): 396-410. Doi: 10.1016/j.jsg.2006.09.013.
35. Zhang, X., Jeffery, R.G., and Thiercelin, M. 2007b. Effects of Frictional Geological Discontinuities on Hydraulic Fracture Propagation. Paper SPE 106111 presented at the SPE Hydraulic Fracture Technology Conference, College Station, Texas, USA, 29-31 Jan. doi: 10.2118/106111-MS.Stoner, M.A.: “Steady-State Analysis of Gas Production, Transmission and Distribution Systems” paper SPE 2554 presented at the 1969 Annual Meeting of the SPE of AIME, Denver, Sept. 28-Oct.1

Chapter 5 MODELING OF HYDRAULIC FRACTURE PROPAGATION IN SHALE GAS RESERVOIRS: A 3-DIMENSIONAL, 2-PHASE MODEL

ABSTRACT

A 3-dimensional, 2-phase, dual-continuum hydraulic fracture propagation simulator is developed and implemented. This chapter presents a detailed method for efficient and effective modeling of the fluid flow within fracture and matrix as well as fluid leakoff, fracture height growth, and the fracture network propagation. Method for solving the system of coupled equations, and the verification of developed model are presented.

5.1 Introduction

Numerical modeling of hydraulic fracturing enables scientific investigation of the complex process. In reservoirs with natural fractures, opened fractures provide fluid flow paths such that the production mechanism in naturally fractured reservoirs is significantly different from that of production from porous and permeable systems. These natural fractures may close as the reservoir pressure drops in response to flowback of fracture fluid, which also influences the growth and final geometry of hydraulic fractures that serve to enhance production (Lorenz, et al. 1988; Teufel and Clark 1984; Cipolla et al. 2010, Rahman, 2011; Osholake et al. 2012; Ahn et al. 2014; Li and Lior, 2015). Because natural fractures will significantly impact stimulation behavior, knowing the properties and geometry of pre-existing natural fractures in a reservoir will facilitate the design of effective hydraulic fracturing for efficient resource recovery.

Numerous authors have investigated fracture propagation behavior in naturally fractured reservoirs both experimentally (Blanton 1986; Renshaw and Pollard 1998; Warpinski and Teufel 1987) and numerically (Taleghani et al. 2011, 2013; Weng et al. 2011; Zhang et al. 2007a, 2007b, 2008; Keshavarzi et al. 2012; Meyer and Bazan 2011; Zeini Jharomi et al. 2013; Ahn et al. 2014; Salehi et al. 2014; 2014; Hoffmann et al. 2014; Zhou et al. 2015). Renshaw and Pollard criterion was extended to implement the intersection behavior for non-orthogonal case by Gu and Weng (Gu and Weng, 2010). Mathematical models of interaction between hydraulic fracture and natural fractures were reviewed and summarized by Poltluri at el. (2005).

Fracture fluid leakoff needs to be captured into the hydraulic fracturing model. Howard and Fast (1970) expressed the fracture fluid filtration rate as a function of leak off coefficients. This is the same leakoff model used in the PKN (Perkins and Kern 1961; Nordgren 1972) and KGD models (Geertsma and de Klerk 1969). The widely used leakoff theory was developed by Carter and Settari (Carter, 1957; Settari, 1985). This approach uses a constant fluid leakoff coefficient to characterize the fluid leakoff rate. However, the net fracturing pressure changes with an increase in pumping time, which has an important effect on fluid loss. Therefore, the pressure dependent leakoff model is derived (Calslaw and Jaeger 1956; Abousleiman 1991; Fan and Economides 1995; Baree and Mukherjee 1996).

The fracture fluid flow in naturally fractured reservoirs, usually contain large complexity such that the solution method is not computationally time efficient. Large heterogeneity of the properties in a solution domain generates stability and convergence problems such that required simulation time increases dramatically. Warren and Root proposed a methodology for capturing flow in such heterogeneous systems. The proposed method was referred to as Dual-Porosity

Modeling (Warren and Root 1963). In 1976, Kazemi et al. published a 2-phase, 3-Dimensional extension of the Warren and Root single-phase, 1-dimensional dual porosity model. Kazemi's model also accounted for gravity segregation, and redefined the fracture network shape factor (Kazemi, Merrill Jr. et al. 1976). Thomas and colleagues extended Kazemi's model by incorporating a third phase and further redefined the shape factor (Thomas, Dixon et al. 1983). These models all assumed pseudo steady-state flow in the matrix domain, and were incapable of capturing phase segregation in the matrix. Zhang stated that failure to model transient flow within the matrix blocks results in an underestimation of early time production (Zhang, Du et al. 2009). Saidi adopted such an approach in a 3-phase, 3-dimensional dual-porosity simulator (Saidi 1983). Similar approaches were taken by Gilman (Gilman 1986), Wu (Wu and Pruess 1988), and by Beckner (Beckner, Chan et al. 1991). To develop a time efficient model, rather than solving fracture and matrix in a single domain, the dual porosity approach separates the reservoir into two sub-domains: fracture and matrix, and integrates to simulate fracture-to-matrix flow (fluid leakoff) in the new model.

To maximize the effectiveness of stimulation, oil and gas bearing formations need to be fractured with controlled height growth into surrounding layers, and without excessive leakoff. To achieve practical and precise numerical prediction in shale gas reservoir, the simulator needs to implement multi-phase leakoff and height growth models. These factors are important because they impact resource recovery performance and greatly. In addition, to represent heterogeneity of different layers the model also must be extended into three dimensions.

In this chapter, we demonstrate a methodology to build a coupled, 3-diemnsional, 2-phase numerical model for solving coupled fracture fluid flow and elasticity equations, and matrix flow equations through the period of hydraulic fracturing stimulation. Iterative coupling method between fracture and matrix domain through explicit dual-continuum approach is also described in this chapter. Lastly, the model developed herein is verified with various existing models and a published chapter to verify the accuracy of the model developed herein.

5.2 Model development methodology

The model described in this section solves fluid flow and geomechanical deformation in a hydraulic fracture network as well as the fluid flow of fracture-to-matrix and matrix-to matrix. The model has the ability to simulated propagation of multiple fractures, fracture fluid leakoff, multiphase fluid flow in the matrix and fracture height growth at a given simulation timestep.

Following subsections present the modeling methodology in detail, including the governing equations, discretization method, and solution procedures.

5.2.1 Governing equations

Fracture fluid flow: The fracture fluid flow model is describes the flow of a single slightly compressible or compressible fluid. The equation for flow inside the fracture elements can be expressed assuming Newtonian fluid model (Lamb 1932):

$$\boldsymbol{q} = -\frac{\bar{\boldsymbol{w}}^3 \boldsymbol{h_f}}{\boldsymbol{12\mu B}} \boldsymbol{\nabla p} \tag{5-1}$$

where p is fracture fluid pressure; q is the local flow rate in the fracture; and $\overline{w}$ is the average width. Assuming isothermal condition, formation volume facture (B) and viscosity (μ) are functions of pressure and these are calculated using linear interpolation. In vertical direction, fluid flow is neglected in this model but the fluid pressure is calculated using hydrostatic gradient. The flow through perforation is not modeled individually. The fracturing fluid is assumed to be injected at one of the natural fracture along the direction perpendicular to the minimum insitu stress.

Matrix fluid flow: The flow associate with matrix has two parts: matrix-to-matrix flow and fracture-to-matrix. Thus, the entire flow system has 3-dimensioanl, 2-phase dual porosity and dual permeability (i.e., dual continuum) based on the principle of mass conservation and Darcy's law for fluid flow through porous media.

Matrix-to-matrix flow follows the concept of 2-phase (water and gas) flow using a finite volume method (FVM). The model assumes that fluids are at constant temperature (isothermal condition), compressible, and water is wetting phase and gas is the non-wetting phase in this system. Also, the gas and water fluid components are assumed to be immiscible, therefore, there is no mass transfer between the two phases. The flow equation for water and gas are expressed by **Equations 5-2 and 5-3**.

$$\frac{\partial}{\partial x}\left[\beta_c k_x A_x \frac{k_{rw}}{\mu_w B_w}\left(\frac{\partial P_w}{\partial x} - \gamma_w \frac{\partial Z}{\partial x}\right)\right]\Delta x + \frac{\partial}{\partial y}\left[\beta_c k_y A_y \frac{k_w}{\mu_w B_w}\left(\frac{\partial P_w}{\partial y} - \gamma_w \frac{\partial Z}{\partial y}\right)\right]\Delta y + \frac{\partial}{\partial z}\left[\beta_c k_z A_z \frac{k_{rw}}{\mu_w B_w}\left(\frac{\partial P_w}{\partial z} - \gamma_w \frac{\partial Z}{\partial z}\right)\right]\Delta z = \frac{V_b}{a_c}\frac{\partial}{\partial t}\left(\frac{\emptyset S_w}{B_w}\right) + q_{Leakoff} \tag{5-2}$$

$$\frac{\partial}{\partial x}\left[\boldsymbol{\beta_c k_x A_x \frac{k_{rg}}{\mu_g B_g}\left(\frac{\partial P_g}{\partial x} - \gamma_g \frac{\partial Z}{\partial x}\right) + \beta_c k_x A_x \frac{k_{rw} R_s}{\mu_w B_w}\left(\frac{\partial P_w}{\partial x} - \gamma_w \frac{\partial Z}{\partial x}\right)}\right]\Delta \boldsymbol{x} + \frac{\partial}{\partial y}\left[\boldsymbol{\beta_c k_y A_y \frac{k_g}{\mu_g B_g}\left(\frac{\partial P_g}{\partial y} - \gamma_g \frac{\partial Z}{\partial y}\right) + \beta_c k_y A_y \frac{k_w R_s}{\mu_w B_w}\left(\frac{\partial P_w}{\partial y} - \gamma_w \frac{\partial Z}{\partial y}\right)}\right]\Delta \boldsymbol{y} + \frac{\partial}{\partial z}\left[\boldsymbol{\beta_c k_z A_z \frac{k_{rg}}{\mu_g B_g}\left(\frac{\partial P_g}{\partial z} - \gamma_g \frac{\partial Z}{\partial z}\right) + \beta_c k_z A_z \frac{k_{rw} R_s}{\mu_w B_w}\left(\frac{\partial P_w}{\partial z} - \gamma_w \frac{\partial Z}{\partial z}\right)}\right]\Delta \boldsymbol{z} = \boldsymbol{\frac{V_b}{a_c}\frac{\partial}{\partial t}\left(\frac{\emptyset S_g}{B_g} + \frac{\emptyset R_s S_w}{B_w}\right)} \tag{5-3}$$

where k = permeability in the x, y and z direction; k_r = relative permeability; μ = viscosity; B = FVF; Φ= porosity; γ = gravity of phase; R_s = solution GOR/GWR; S = saturation of a fluid; β_c = transmissibility conversion factor; a_c = volumetric conversion factor.

Fracture fluid leakoff (i.e., fracture-to-matrix flow) is incorporated into the model as a modifier to the boundary of the matrix block which is associated with the fractures which contain fluid. This method links fracture fluid flow (fracture-to-fracture flow) to matrix. The source term $q_{Leakoff}$ (**Equation 5-2**) is modified when one of six boundaries of a cubic block is fractured. It is assumed that fracture fluid is an aqueous phase having different rheological property from the insitu water inside matrix pore space. The fracture-to-matrix flow equation is given by:

$$\boldsymbol{q_{leakoff} = q_{wsc} = -2G_{f-m}\left(\frac{k_{rw}}{\mu_{avg} B_{avg}}\right)(p_m - p_f)},$$

$$\boldsymbol{G_{f-m} = \beta_c\left(\frac{2A_{f,d}A_{m,d}}{A_{f,d}+A_{m,d}}\right)\left(\frac{1}{\Delta d}k_a\right)}. \tag{5-4}$$

where $q_{leakoff}$ is fracture fluid leakoff rate; $G_{f\text{-}m}$ is modified geometric factor between matrix and fracture; p_m is the matrix pressure; p_f is the pressure of fracture fluid; A is cross sectional area; f

refers to fracture; *m* refers to matrix; *a* is associated direction (*x,y or z*); *d* is the distance between fracture and matrix coordinate.

Elasticity Equation (Pressure-width relation): The elasticity equation is defined based on the assumption that the fracture surface deforms in a linear elastic plane-strain conditions. This is justified based on the observation that the modeled system typically has large insitu stress, on which only small additional stress systems are superimposed (with the exception of the fracture tip area). For plane-strain conditions, England and Green derived an equation for the width of a linear crack opened by an equal and opposite normal pressure distribution on each side of the fracture as exerted by a fluid (England and Geen, 1963). Assuming a symmetrically distributed in-situ normal stress, σ_h, opposing p_f, the pressure-width equation is:

$$\boldsymbol{w(x,t) = \frac{2(1-v^2)h_f}{E}\,(p_f - \sigma_n)} \tag{5-5}$$

where p_f is the fluid pressure inside fracture and σ_n is normal stress acting perpendicular to fracture element.

Height Growth Equations: The fracture height and width profile of a fracture cross section depends on fluid pressure, in-situ stress, fracture toughness, layer thickness and elastic modulus of each layer. Implementation of height growth allows three dimensional fracture propagation with improved prediction of final fracture geometry. When treatment rate and fracture fluid viscosity is increased, the 2D model suggest in Chapter 3 results in relatively larger SRV because it does not reflect the losses from height growth.

The stress intensity factors at the fracture top and bottom tips are calculated from the fluid pressure inside the fracture, the fracture height and the layer stresses. A stable fracture height is determined by matching the stress intensity factor at the tip to the fracture toughness in the layers that contain the fracture tip. The relations for the stress intensity factor and the width are given in Warpinski and Smith (2000) and it is extended to multi-layer height growth model to incorporate vertically heterogeneous rock properties. The multi-layer equilibrium height growth equations are:

$$\frac{\sqrt{\pi}(K_{IC,m}+K_{IC,n})}{2\sqrt{12a}}=\sum_{i=2,2}^{m}S_i\,arcsin\left(\frac{b_i}{a}\right)+\sum_{j=3,2}^{n}S_j\,arcsin\left(\frac{b_j}{a}\right)-\left(\sigma_m+\sigma_n-2p_f\right)\frac{\pi}{2},$$

$$\frac{\sqrt{\pi a}(K_{IC,n}-K_{IC,m})}{2\sqrt{12}}=\sum_{i=2,2}^{m}S_i\sqrt{a^2-b_i^2}+\sum_{j=3,2}^{n}S_j\sqrt{a^2-b_j^2}$$

(5-6).

where m is number of top layers with fracture tip; n is number of bottom layers with fracture tip; $b_{i\ or\ j}$ is the length from center of fracture to the bottom of *i*th or *j*th layer; $S_i=\sigma_i-\sigma_{i-2}$ for i>2, $S_2=\sigma_2-\sigma_1$ for i=2, i is even number indicating the layers above the perforated layer; $S_j=\sigma_j-\sigma_{j-2}$ for j>3, $S_3=\sigma_3-\sigma_1$ for j=3, j is odd number which indicates the layers below the perforation. The parameters used in **Equation 5-6** are visually represented in **Figure 5-1**.

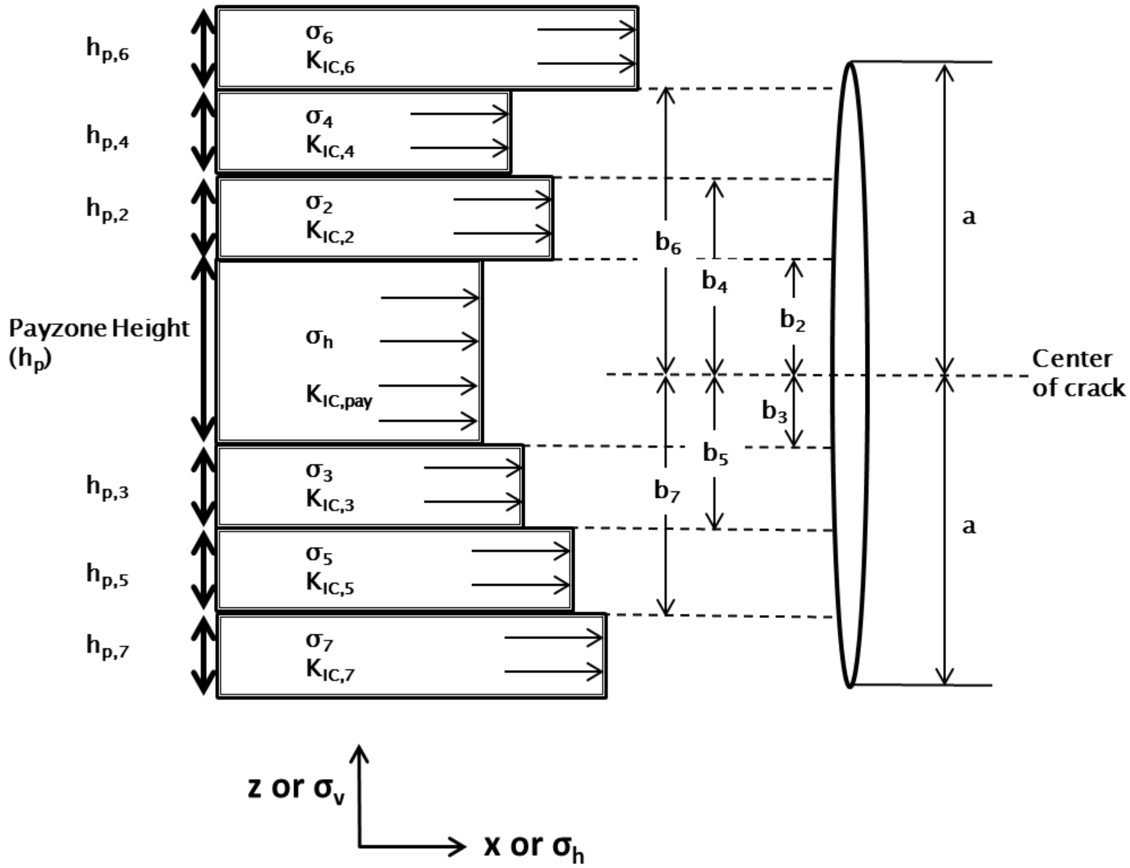

Figure 5-1. Visual representation of Height growth model.

Stress Shadow Equation: The extension of fracture network is influenced by the mechanical interaction among the adjacent fractures known as stress shadow effect. The fracture induced stress field $\Delta\sigma_{xx}$ along the x-axis at the mid-height or center of the fracture can be written as (Pollard and Segall, 1987; Olson, 2004; Warpinski and Teufel, 1987):

$$\boldsymbol{\Delta\sigma_{xx}} = (\boldsymbol{p_f} - \boldsymbol{\sigma_n})\left[\mathbf{1} - \left(\mathbf{1} + \left(\frac{\boldsymbol{h}}{\mathbf{2}\boldsymbol{d_{ij}}}\right)^2\right)^{-\frac{3}{2}}\right]$$

(5-7)

where h is the total fracture height and d_{ij} is the distance between the centers of parallel fracture i and j. In this model 2D effect is considered as in **Equation 5-7** but it can be extended to 3D using the correction factor Φ_{ij} caused by finite fracture height that leads to decaying of interaction between any two fracture elements when the distance increases (**Equation 5-8**).

$$\boldsymbol{\Phi_{ij} = \frac{\Delta\sigma_{xx}}{(p_f - \sigma_n)} = 1 - \left(1 + \left(\frac{h}{2d_{ij}}\right)^2\right)^{-\frac{3}{2}}} \tag{5-8}$$

The 3D correction factor represents the influence of fracture height on the induced stress at the center of fracture a distance of d_{ij}. The stress shadow effect is computed at each timestep and added to the initial in-situ stress field on each fracture and node. The effect of Mode I driving stress field is only considered at present.

Fracture Propagation: The interaction between the hydraulic fracture (HF) and the natural fracture (NF) is incorporated using Renshaw and Pollard's method (1998). The criterion is given as

$$\boldsymbol{\frac{-\sigma_3}{T_o - \sigma_1} > \frac{\left(0.35 + \frac{0.35}{K_f}\right)}{1.06}} \tag{5-9}$$

where σ_1 and σ_3 are far-field effective stresses (tensile is positive) acting parallel with and perpendicular to a propagating hydraulic fracture, respectively, T_0 is tensile strength of rock and K_f is coefficient of friction. This criterion decides whether a HF will cross at the intersection with a

NF or not. This criterion has been validated by laboratory experiments for dry cracks (Renshaw et al. 1998).

Fracture branching is governed by the fracture opening criterion as

$$\boldsymbol{p_f} > \boldsymbol{\sigma_n} \tag{5-10}$$

When fluid pressures at the intersection exceed normal stress (σ_n), NF starts to be opened perpendicular to the direction of that normal stress. A new fracture tip is initiated if the fluid pressure exceeds the normal stress acting on the associated natural fracture. In this way, a complex fracture network is able to be created.

Fracture propagation is estimated based on the assumption that the local extension of the fracture length d_{tip} at the fracture tip is proportional to the velocity of the fluid. The local extension is scaled by a maximum propagation length d_{presc} (Hossain and Rahman, 2008; Weng et al., 2011). It is assumed that tip velocity is equal to fluid velocity near the tip meaning all the hydraulically opened fractures are fully saturated with fracture fluid. The fluid or tip dilatancy is ignored because this models is designed for slickwater which generally has relatively low fluid viscosity around 2 cp.

$$\boldsymbol{v_{tip}} = \frac{\boldsymbol{q_{tip}}}{\boldsymbol{H_{fl}\bar{w}}} \tag{5-11}$$

The tip with the highest velocity is extended by a prescribed distance d_{presc}. The other tips are extended proportionally to their velocities (Weng et al., 2011):

$$\boldsymbol{d_{tip}} = \frac{\boldsymbol{d_{presc}v_{tip}}}{\boldsymbol{v_{tip}^{max}}} \tag{5-12}$$

where d_{tip} is extended distance. When a tip intersects with a natural fracture, it propagates to the direction satisfying the interaction criteria, as outlined above.

5.2.2 Discretization methodology

The 3-dimensional discretization of fracture and matrix domains is the key for time efficient numerical simulation. Schematic discretization of the system is illustrated in **Figure 5-2**. The lines in this figure depict natural fractures in the domain. When a fracture is initiated, both moving and stationary coordinates are activated. The extension of a fracture tip is integrated using a moving coordinate and the information about NF-HF interactions is stored at the stationary coordinates. Therefore, when a moving coordinate reaches a stationary coordinate, the propagation direction is decided according to the analytical interaction criteria. The sensitivity of final fracture geometry over different size of grids are studied in Chapter 3, section 3.2.6.

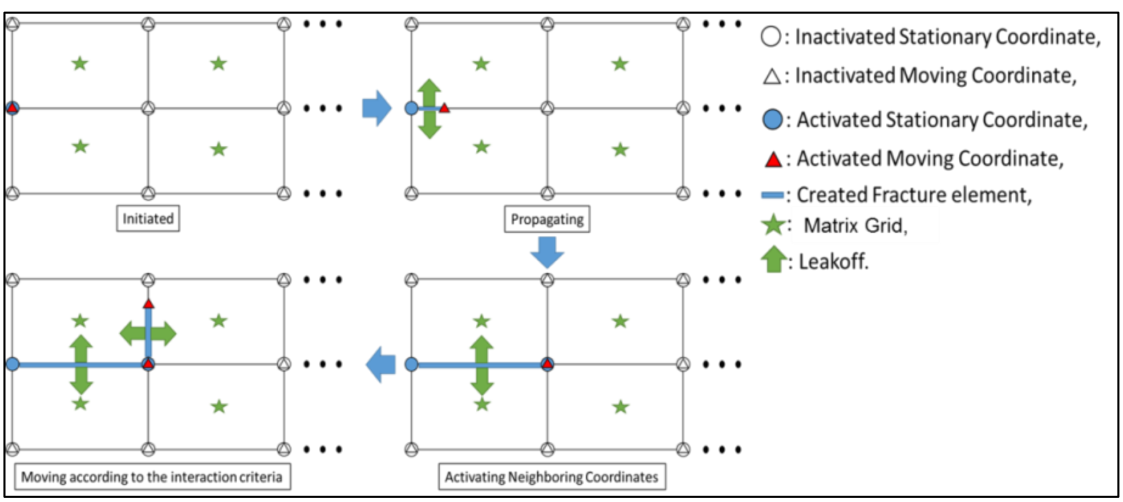

Figure 5-2. Schematic of gridding system in both fracture and matrix domain.

The example of fracture node and element representation is shown in **Figure 5-3**. The element is an elemental volume between two nodes. The figure includes fracture nodes *(i,j)* to *(i+1,j)* and *(i,j+2)*, and fracture element with tip *(i,j+1)*, without tip *(i,j)*. The location *(i, j+2)* represents tip itself having no length and width. p_f is fluid pressure, L_f is fracture length, and w_f is fracture width at the given node.

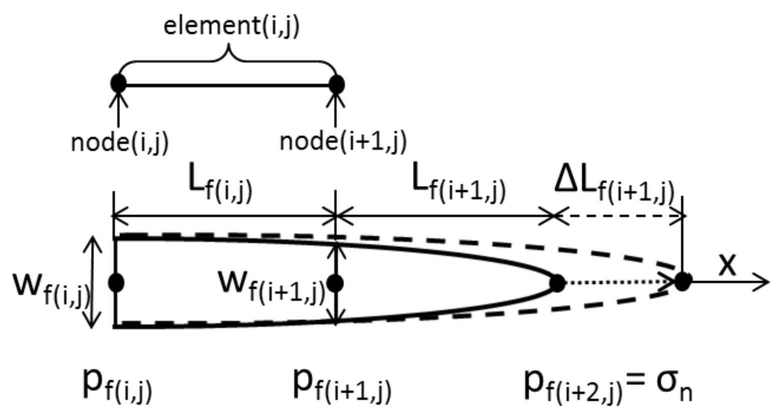

Figure 5-3. Fracture domian discretization along x-direction.

The discretized form of transmissibility for the fracture-to-fracture flow for *(i, j)* element is driven from **Equation 5-1** as

$$\boldsymbol{T_{f-f,(i,j)}} = \left(\frac{\bar{w}^3_{f,(i,j)}\bar{h}_{f,(i,j)}}{L_{f,(ii,j)}/24}\right)\left(\frac{1}{\mu_l B_l}\right)_{upstream} \tag{5-13}$$

where $\bar{w}_f, \bar{h}_f$ is average width and height. Each element has elliptical shape in *x, y, z* direction such that the average width in element *(i, j)* can be calculated by elliptical averaging (**Equation 5-14**).

$$\bar{w}_{f,(i,j)} = w_{f,(i+1,j)} + \frac{1}{L_{f,(i,j)}}\int_0^{L_{f,(i,j)}}\left[\left(w_{f,(i,j)}-w_{f,(i+1,j)}\right)\left(1 - x/L_{f,(i,j)}\right)^{1/4}\right]dx \tag{5-14}$$

where $\bar{w}_f$ is average width. Using this relationship, the width at each node can be solved and corresponding pressure at any location of fracture can be approximated through elasticity equation (**Equation 5-5**). This approach can be applied to the width in vertical (z) direction with consideration of hydrostatic pressure gradient.

Matrix domain is discretized using body centered grid system. Fracture element *(i, j)* correspond to the matrix block *(ii, jj)*. Fracture-to-matrix flow or leakoff is governed by the geometry of fracture associated with the boundary as described in **Equation 5-4** and discretized form of transmissibility for the fracture-to-matrix flow for *(i, j)* block is

$$T_{f-m,(i,j)} = \left(\frac{L_{f,(i,j)}h_{f,(i,j)}}{dyy_{(ii,jj)}/2}\right)\left(\frac{k_m}{\mu_l B_l}\right)(k_{rl})_{upstream} \tag{5-14}$$

The internal flow in a matrix follows finite volume approach. The mass transport in or out of each matrix block is calculated to solve saturation and pressure changes for gas and water phases. The transmissibility equation from *(ii, jj)* to *(ii+1, jj)* for *l = water or gas* is

$$T_{l,m-m} = \beta_c V_b \sigma_{shape}\left(\frac{k_m}{\mu_l B_l}\right)(k_{rl})_{upstream} \tag{5-16}$$

where T is transmissibility; k_m is matrix permeability; μ_l is viscosity of phase l; B_l is formation volume factor of phase l; β_c is unit conversion factor; V_b is bulk volume of a grid block; σ_{shape}

is shape factor; subscript *f-m* refers to fracture-to-matrix flow and *m-m* refers to matrix-to-matrix flow

This flow model consists of **Equations 2** to **5** has four unknowns, p_g, $p_{w,}$ $S_{g,}$ and S_w. The finite-volume approach was used to obtain the numerical solution for the flow system developed herein. With this approach, the flow equations are discretized by the use of algebraic approximations of the second-order derivatives with respect to space and the first-order derivatives with respect to time. Depending on the approximation of the derivatives with respect to time, implicit finite-difference equations may be chosen for the numerical simulation.

The volume of fracture fluid invasion is treated as a source term, q_{wsd}, for associated grid block such that fracture fluid leakoff (the fluid flow from fracture to matrix) can be coupled in the reservoir domain as well. The detail of fracture-to-matrix fluid flow is described in **Equation 5-4**.

5.2.3 Solution methodology

In this section, the numerical methods for solving series of governing equations are described in detail. The model follows the principle of mass conservation (**Equation 5-17**) and Darcy's law for the flow in both matrix and fracture.

$$(\boldsymbol{Mass\ in}) - (\boldsymbol{Mass\ out}) = (\boldsymbol{Mass\ Accumulated}) \tag{5-17}$$

Thus, the simulator solves the unsteady-state mass balance equation, satisfying elasticity equation with stress change due to deformation, height growth equation and pressure dependent leakoff equation for fracture domain, and explicitly solves 3-dimensinal, 2-phase mass balance equation with fracture fluid leakoff rate as source term. Both flow equations are solved using the finite volume method.

Solving coupled fracture fluid flow and elasticity equation: Fracture domain is discretized into elements and nodes as described above. The mass balance equation for the fracture domain can be written as:

$$(\boldsymbol{Mass\ in}) - (\boldsymbol{Mass\ out}) - (\boldsymbol{Mass\ leakoff}) - (\boldsymbol{Incremental\ Fracture\ volum\ change}) = (\boldsymbol{Mass\ Accumulated}) \tag{5-18}$$

Using finite volume method, the mass balance residual equation for a given element (i, j) can be written as

$$\boldsymbol{R_{i,j}} = \sum_{\boldsymbol{nf}=1}^{\boldsymbol{N_f}} \left[\boldsymbol{T_{nf,f-f}}(\boldsymbol{p_{f,nf}} - \boldsymbol{p_{f,(i,j)}})\right]^{\boldsymbol{n+1}} + \boldsymbol{q_{injection}^{n+1}} - \boldsymbol{q_{leakoff}^{n+1}} - \frac{\left[\left(\boldsymbol{L_{f,(i,j)}h_{f,(i,j)}w_{f,(i,j)}}\right)^{\boldsymbol{n+1}} - \left(\boldsymbol{L_{f,(i,j)}h_{f,(i,j)}w_{f,(i,j)}}\right)^{\boldsymbol{n}}\right]}{\Delta\boldsymbol{t}} \tag{5-19}$$

where nf is index of the element connected to (i, j); N_f is the number of elements connected to (i, j); h_f, w_f and L_f are height, width and length of the element (i, j); and q_{leak} is the leakoff rate from element (i, j) to the connected matrix; superscript n and $n+1$ denote previous and current timsteps.

At the fracture tip, the following boundary conditions are satisfied:

$$\boldsymbol{p_f = \sigma_n}, \quad \boldsymbol{w = 0}, \quad \boldsymbol{q = 0} \tag{5-20}$$

where p, w and q are pressure, width and flowrate at the tip nodes.

This approach leads to a nonlinear system of equations that must be solved interactively at each timestep. Within this system of coupled equations there are four unknowns/dependent variables:

- •Fracture fluid pressure (p_f)
- •Fracture length, width height and normal stress $(L_f, w_f, h_f, \sigma_n)$
- •Fracture fluid leakoff rate $(q_{leakoff})$
- •Fracture-to-fracture transmissibility (T_{f-t})

Incremental fracture length (L_f) and the stress shadow effect (σ_n) are determined by **Equation 5-12** and **5-8**, respectively, using the fluid pressure from previous timestep. Fluid leakoff rate ($q_{leakoff}$) is first calculated with the matrix pressure (P_m) and iteratively calculated in association with iterative coupling described in the section below (refer to *Iterative coupling*). Fracture width(w_f), height (h_f) are function of fluid pressure as described in **Equation 5-5** and **5-6** so that the principle unknown for the mass balance equation (**Equation 5-19**) can be reduced to one variable P_f.

A combination of the above equations leads to a nonlinear system of equations and it is solved in terms of fracture fluid pressure implicitly by using a Newton-Raphson iteration method (**Equation 5-21**).

$$\boldsymbol{J_{ij}^{k}} = \left(\frac{\boldsymbol{dR_i}}{\boldsymbol{dx_j}}\right)^{\boldsymbol{k}},$$

$$\boldsymbol{x^{k+1}} = \boldsymbol{x^{k}} + \boldsymbol{dx} \tag{5-21}$$

where J_{ij} is an entry in the iteration Jacobian matrix; R_i is an entry in the residual vector; x_j is the vector of unknowns. To solve nonlinear equations, a series of guesses for x has to be made until dx satisfies convergence criteria. If convergence is not reached within a specified number of iteration, initial guesses for x or dt is modified.

Solving coupled matrix flow equations: After solving fracture domain, we can obtain the $q_{leakoff}$ term such that the equation described at **Equation 5-2** and **5-3** can be solved using finite volume method. Residual form of discretized equation of matrix flow for water phase (l=w) is

$$\boldsymbol{R_{l,(i,j,k)}} = \sum_{\boldsymbol{nf=1}}^{\boldsymbol{N_f}} \boldsymbol{q_{nf,leakoff}^{n+1}} + \left[\boldsymbol{T_{w,m-m}}\Delta(\boldsymbol{p_{m,l}} - \gamma_l Z)\right]_{\boldsymbol{in}}^{\boldsymbol{n+1}} + \left[\boldsymbol{T_{l,m-m}}\Delta\big(\boldsymbol{p_{m,l}} - \gamma_l Z\big)\right]_{\boldsymbol{above}}^{\boldsymbol{n+1}}$$

$$+ \left[\boldsymbol{T_{m-m}}\Delta(\boldsymbol{p_{m,l}} - \gamma_l Z)\right]_{\boldsymbol{below}}^{\boldsymbol{n+1}} - \left[\frac{\boldsymbol{V_b}}{\boldsymbol{\alpha_c}}\frac{\boldsymbol{1}}{\boldsymbol{\Delta t}}\left(\frac{\boldsymbol{\phi S_l}}{\boldsymbol{B_l}}^{\boldsymbol{n+1}} - \frac{\boldsymbol{\phi S_l}}{\boldsymbol{B_l}}^{\boldsymbol{n}}\right)\right]_{\boldsymbol{i,j,k}} \tag{5-22}$$

where subscript *in* refers to the flow into the adjacent matrix block, and *above* and *below* refer to flow to direction to top and bottom grid block. Gas residual equation can be written similarly using **Equation 5-3.**

Unknowns for solving matrix flow equation are four (P_w, P_g, S_w, S_g) which are pressures and saturations of each phase, water and gas. The additional relationships completing the matrix flow equations are

$$S_g + S_w = 1 \tag{5-23}$$

and

$$p_{cgw} = p_g - p = f(S_w) \tag{5-24}$$

Using water and gas residual equations and **Equation 5-23** and **5-24**, matrix flow can be solved using gas pressure (p_g) and water saturation (S_w) as principle unknowns. The capillary and relatively permeability curve for this study is illustrated in **Figure 5-4** (Gdanski, Weaver et al. 2005). The finite volume scheme generates system of nonlinear equations and it is solved by the linearization technique Newton-Raphson iteration method described above.

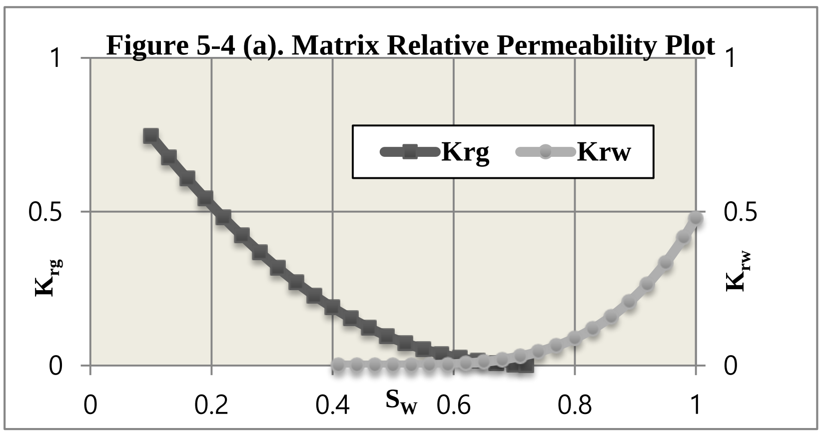

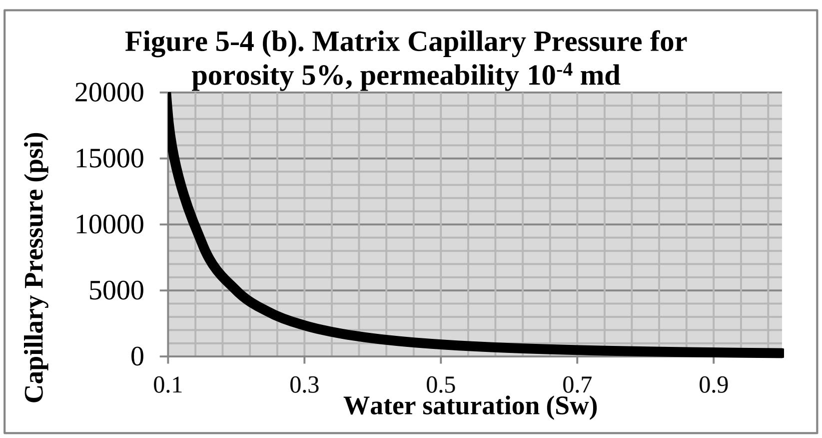

Figure 5-4. (a)Relative permeability relationship and (b) capillary pressre as a function of S_w (Gdanski, Weaver et al. 2005).

Iterative coupling of fracture and matrix domain: As described previously, matrix pressure for fluid leakoff equation is initially assigned as p_m^n - pressure from previous timestep - and then an iterative coupling method is incorporated to find p_m^{n+1} and corresponding $q_{leakoff}^{n+1}$ for the systems of equations for fracture and matrix. The matrix pressure change during the solution to matrix flow equations, and so after solving the equations, matrix pressure residuals are rechecked. Iteration stops when the residuals are less than a specified tolerance value. For the results generated in the paper, the number of iteration was less than seven until convergence.

Iterative coupling offers advantages of computational time efficiency and computer memory load reduction. Matrix and fracture domains are solved independently so that one can take advantage of parallel computing to reduce simulation run time. Also, calculation matrix size is reduced such that we can obtain additional memory size. Flowchart for solution method including iterative coupling is illustrated in **Figure 5-5**.

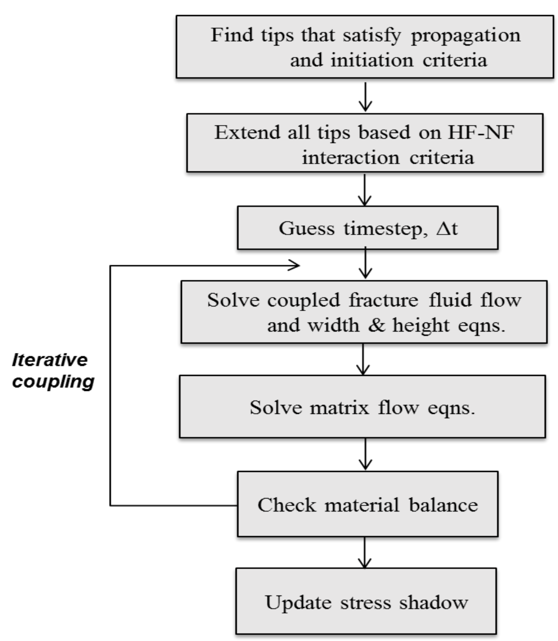

Figure 5-5. Schematic Flowchart of the 3D, 2-phase numerical solution.

5.3 Model verification

The accuracy of the model developed herein is verified in three ways as described below:

1. Fracture tip extension is compared to PKN analytical model.
2. Height growth model verified with the references. Three-layer height growth is compared with the result from Valko and Economides and multi-layer height growth is verified with Gidley et al's results (Valko and Economides 1996; Gidley et al. 1989).
3. Complex multi-branch fracture growth in a naturally fractured formation is compared with the field case study results from Jacot et al. (Jacot et al. 2010).

5.3.1 Comparison with PKN

The model is verified with the PKN analytical model to check validity of fracture geometry of each fracture branch. Using the same input values, the model developed herein is compared with the PKN analytical solution: injection rate = 10 bpm; minimum in-situ stress = 8497 psi; fluid viscosity = 1 cp; fracture height = 100 ft; Young's modulus = 3.74×10^6 psi. Both models are exercised for this scenario, and results used for cross-verification. **Figure 5-6** shows the comparison and the predicted length and width versus time are nearly identical.

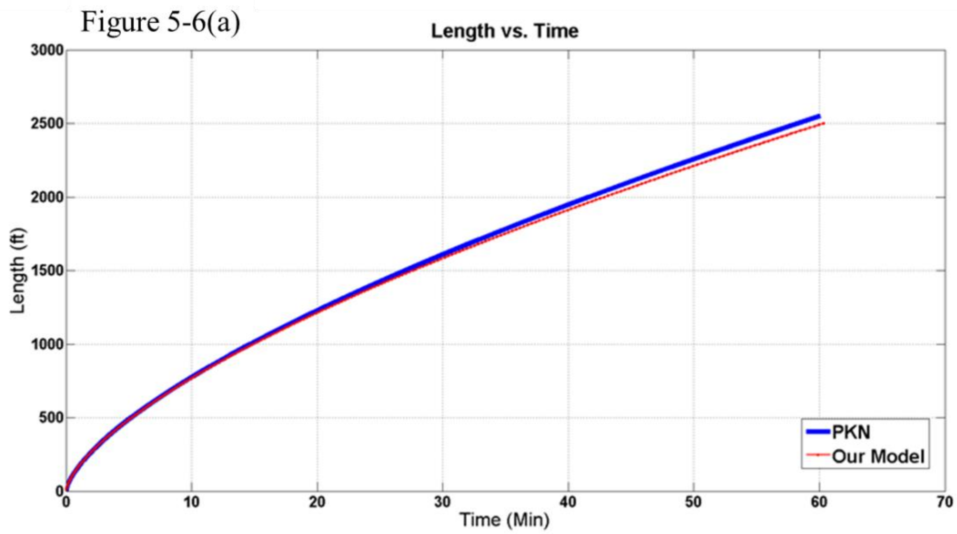

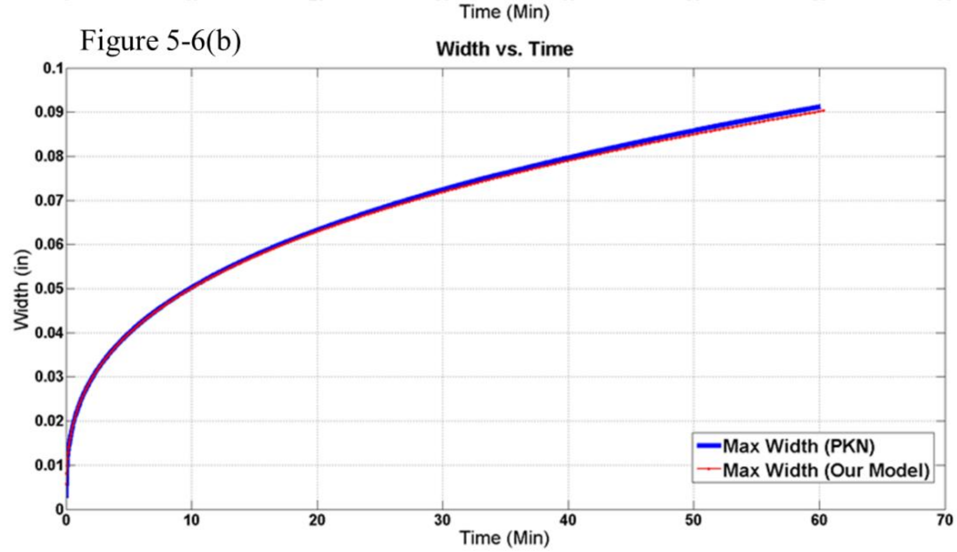

Figure 5-6. Comparison results showing favorable comparison between PKN and model developed herein for fracture height evolution through time (a), and fracture width versus time (b).

5.3.2 Height growth model verification

Fracture height growth module was verified with both a three layer reference case and a multi-layer case. The three layer height growth model is verified using the data collected from the reference (Valko and Economides, 1996). Input parameters for this verification are listed in

Table 5-1 and visual representation of that scenario is shown in **Figure 5-7.** In a given fracture fluid pressure (p_f), fracture height is calculated by the model developed herein and compared. Four distinct case with different vertical stress and fracture toughness are verified.

Table 5-1. Input data for three-layer verification cases

Case No.	σ_2	σ_3	KIC2	KIC3	p_f
1	3500	3500	0	0	3350
2	3500	3500	1000	1000	3360
3	3500	4000	1000	1000	3360
4	3500	4000	4000	1000	3360
σ1=3000 psi, hp=50 ft					

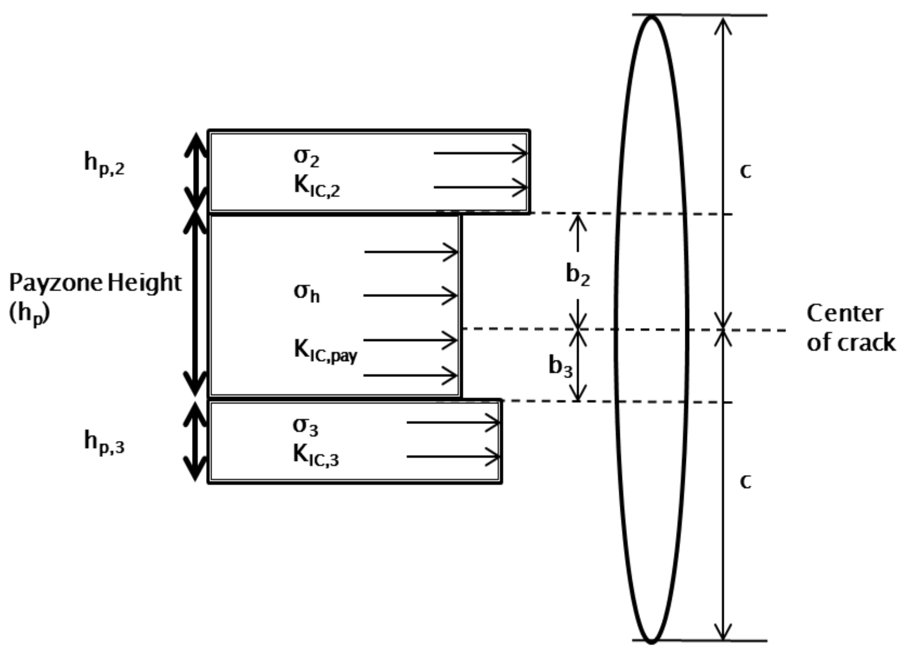

Figure 5-7. Visual representation of three-layer height growth model input values.

The equilibrium fracture height for each case is calculated from **Equation 5-6** using Newton-Rapson method and the result is shown in **Table 5-2**. The difference between results from the reference model and the model developed herein is less than 0.1% for all cases evaluated and are, therefore, considered to be negligible.

Table 5-2. Verification results for 3-layer case.

Case No.	Reference		Model developed herein	
	c (ft)	b_2 (ft)	c (ft)	b_2 (ft)
1	55.0700	25.0000	55.0672	25.0000
2	51.0800	25.0000	51.0819	25.0000
3	38.4955	15.7455	38.4955	15.7450
4	31.6450	22.4060	31.6450	22.4058

A multi-layer case was also considered to verify performance of the new model using the data from Gidley et al. 1989. Input values are for that case are shown in **Table 5-3;** illustration of corresponding layer numbers and parameters is shown in **Figure 5-1**.

Table 5-3. Input values for verification of 7-layer case.

		Cases		
Layer Number		σ_h (psi)	h_p (ft)	K_{IC} (psi-in$^{0.5}$)
Payzone	1	1000	50	1000
Above Pay	2	1500	25	1000
	4	1200	25	1000
	6	2500	Inf	1000
Below Pay	3	1250	25	1000
	5	1700	25	1000
	7	2000	Inf	1000

Using above input data, the result is generated through changed pressures. **Figure 5-8** illustrates the results from the model developed herein, and those from the reference model, with solid lines indicate the result from the model developed herein and square symbols representing results from the reference model. Top, bottom, and center of the fracture all match nearly identically with Gidley et al.'s result.

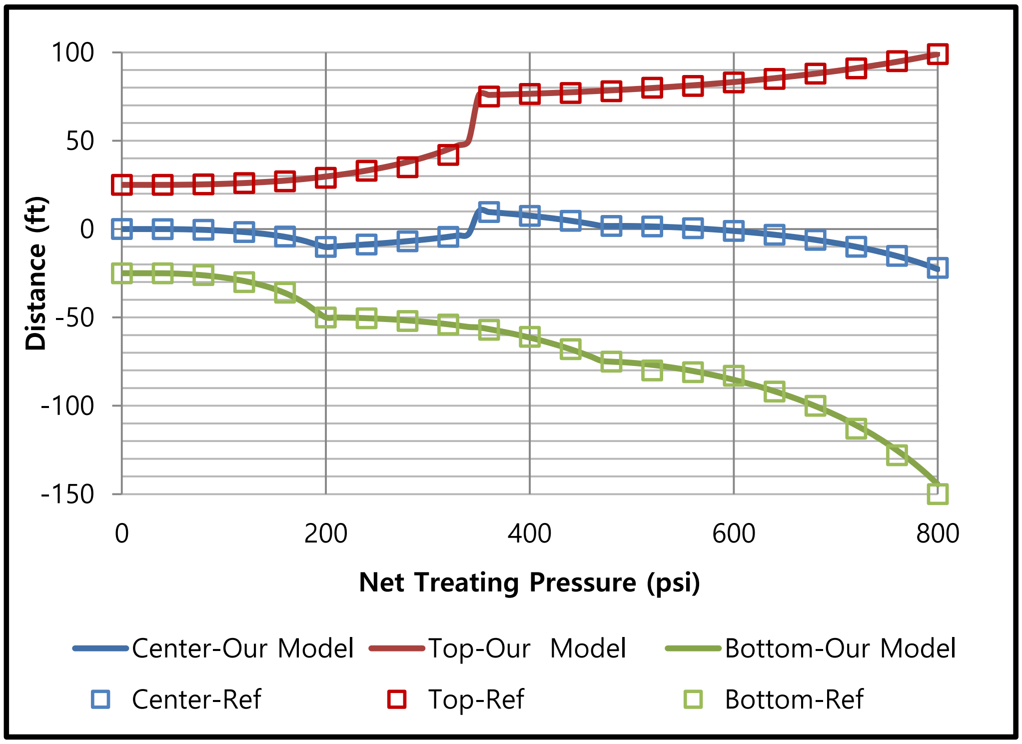

Figure 5-8. Height growth comparison result for 7-layer case. Solid lines indicate the result from the model developed herein and square symbols representing results from the reference model.

5.3.3 Comparison with DFN field case study result (Jacot et al. 2010)

In the next step, the model developed herein is compared with DFN model result found from Jacot et al. (2010). Predictions from the DFN model provided in that reference were verified against microseismic mapping results obtain from a Marcellus field operation. Thus, it may be assumed that comparing results from the model developed herein with those of this DFN model for this same case will provide a certain degree of confidence that the model developed herein provides valid predictions.

Using the same input values, the accuracy of the 3D, 2-phase model is verified with the referenced result. **Table 5-4** contains vertical layer classification and formation matrix properties including permeability, porosity and water saturation for each layer; **Table 5-5** shows treatment parameters for hydraulic fracturing. Pumping rate for a stage is given as 85 bpm and total volume pumped is 125,931 gallons. The spacing between NFs is set to be 75 ft apart from each other in both sets of orthogonal fractures. (Jacot et al 2010).

Table 5-4. Formation property for each layer.

	S_{wi}	Porosity (%)	Thickness (ft)	Permeability (md)
Tully Limestone	0.1	10	30	0.01
Hamilton Shale	1	5	170	0.0001
Upper Marcellus	0.1	5	62	0.000377
Cherry Valley	0.1	5	30	0.000377
Lower Marcellus	0.1	5	70	0.000377
Onondaga	0.1	10	20	0.01
Oriskany	1	15	180	10

Table 5-5. Treatment parameters.

Parameter	Value
Initial Reservoir Pressure (psi)	**4,000**
Fluid Viscosity (μ, cp)	**2**
Injection Rate (Q, bbl/min)	**85**
σ_h, min-σ_H, max (psi)	**100**
Injected Volume (gal)	**125,931**
Payzone Height (ft)	**162**
Natural Fracture Spacing (X by Y, ft by ft)	**75 X 75**

Figure 5-9 is visualization of stress profile for each layer used for height growth calculation. The stresses and layer thicknesses are derived from the stress gradient found at Jacot et al.'s paper (Jacot et al. 2010). Perforation in the Lower Marcellus interval is indicated as LM in the figure.

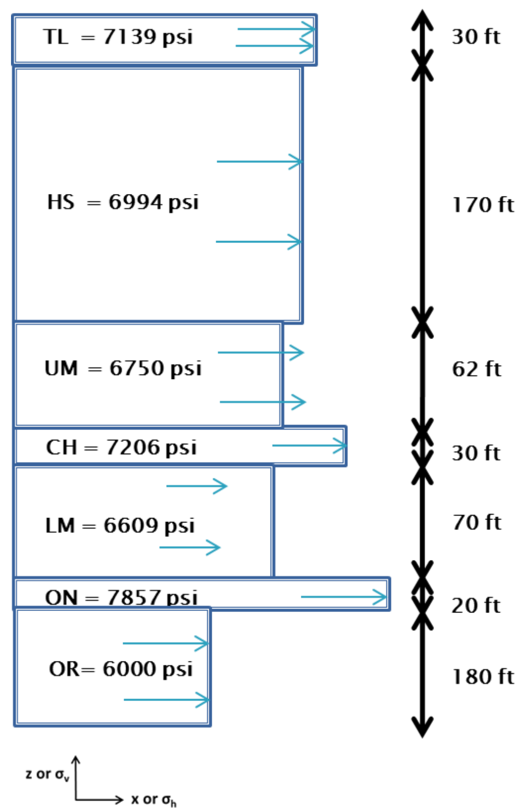

Figure 5-9. Vertical stress profile for each layer.

Figure 5-10 shows the height comparison between the model developed herein and Jacot's results. Jacot 240 ft of final height calculation and the model developed herein has 247.8 ft. Left figure depicts height versus length of the final fracture network from our model and right figure illustrates width versus height from DFN model. **Figure 5-11** shows the top views of final fracture network for each model. Our result has network width of 333.2 ft and length of 938.7 ft, Jacot has a SRV width of 400 ft and length of 870 ft.

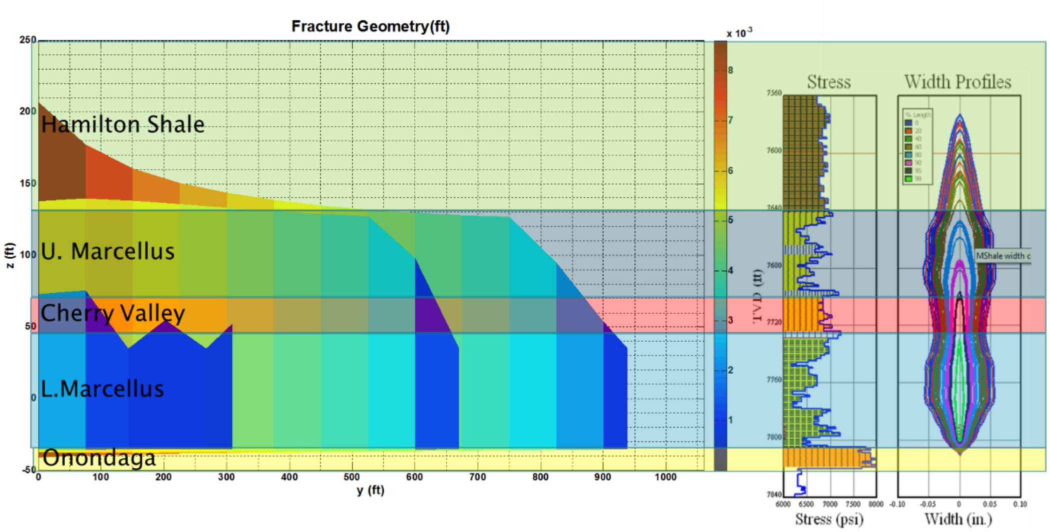

Figure 5-10. Height comparison between the model developed herein and DFN. (Left: Height vs. Network Length from the model developed herein, Right: Height vs. Width from DFN).

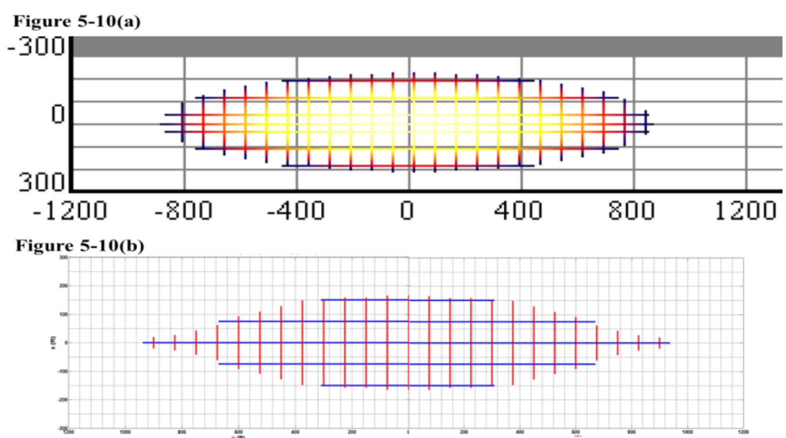

Figure 5-11. Final fracture network comparison (Top view). (a) Jacot's result. (b) The results from the model developed herein. The color from (b) indicates primary (blue) and econdary (red) fractures. The horizontal well is located along the zero in x-axis and perforation is placed at (0, 0).

Table 5-6 summarizes the results from both DFN and the model developed herein. Predicted fracture network width shows the most significant difference of 20%, while fracture network length (7.3%), height (3.1%) and width at the perforation (9.1%) showed less than 10% difference between two models. This difference of width and length results from the fact that the fracture height growth model described herein uses averaged stresses for each vertical layer such that the fracture tends to grow along $S_{H,\,max}$. The choice to use averaged stresses was made to reduce computational burden; this model has the capability to capture details of vertical layer stresses if the computational capacity is available.

Table 5-6. The simulation results from the model developed herein and DFN.

	Jacot et al.	**Model Developed Herein**	**% Difference**
Width (in)	0.12	0.13	9.1
Height (ft)	240	247.8	3.1
Network Length (ft)	870	938.7	7.3
Network Width (ft)	400	333.2	20.0
Network Volume (ft^3) (Length × Width × Height)	83,520,000	77,505,605	7.2

The volume of the predicted fracture network - calculated as the product of fracture network length, width, and height - shows 7.2% difference between the two models. **Figure 5-12** illustrates the full-size of the final fracture network. The figure shows half for the network and the point (0, 0, 0) is perforation.

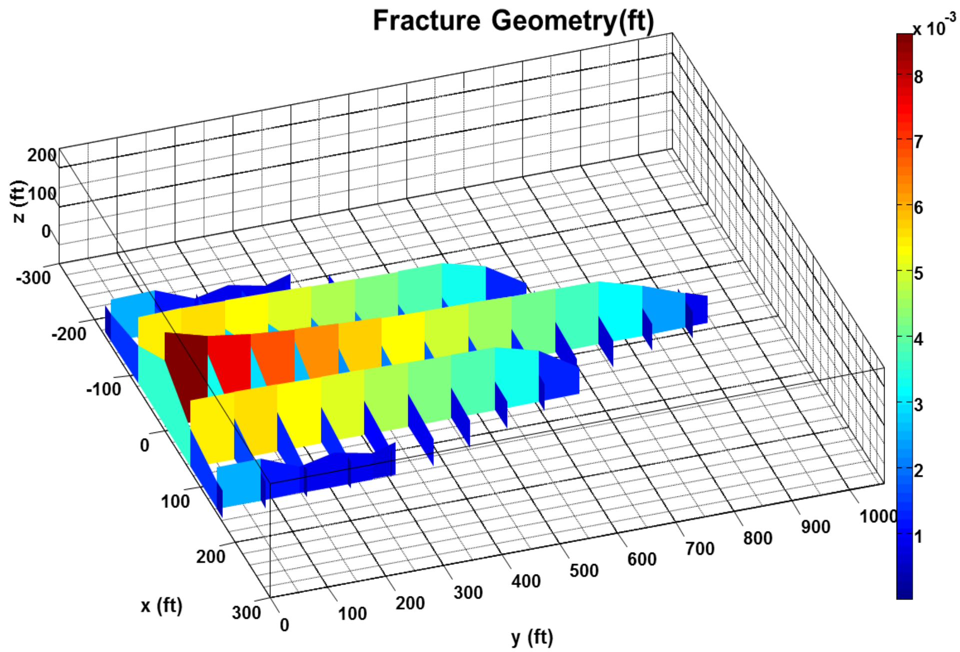

Figure 5-12. Final fracture network characteristics (height, length, width, and aperture) from the model developed herein. This representation is for only half of a fracture network.

5.8 Chapter conclusion

A 3-diemnesional, 2-phase hydraulic fracturing simulator is developed, and its performance is verified against other accepted hydraulic fracture propagation models. Main findings include:

1. 3-diemensianl hydraulic fracture geomechanical changes can be captured using finite volume method with equilibrium multi-layer height growth and accounting for the effect of stress shadow in settings with pre-existing natural fractures.

2. Fracture fluid leakoff, or the flow from fracture-to-matrix, can be modeled with dual-porosity and dual-permeability method, with pressure dependent multi-phase flow applied to simulate the effect of capillary imbibition and relative permeability.

3. Iterative coupling between fracture and matrix domain enables tracing of dynamic reservoir property changes, including three dimensional saturation and effective permeability effects.

This verified model can be exercised to develop credible insights into the dynamics of fracturing in shale, and be used to advance understanding of how a naturally fractured formation can be stimulated to maximize resource recovery.

5.9 Nomenclature

A = cross sectional area (ft^2)

b = Length between the center of fracture to top of bottom of layer (ft)

B = Formation volume factor (RB/STB)

C_w = Compressibility of water (psi^{-1})

d = Extended distance (ft)

f_{L1}, f_{L2} = Fractions of fracture half-length (fraction)

G = Shear modulus of rock formation (psi)

h = Fracture gross height (ft)

h_f, H_{fl} = Fracture height (ft)

k = permeability in the x, y and z direction (md)

K_f = coefficient of friction (frictional)

k_r = relative permeability (md)

L_f, l = Fracture length (ft)

p_f = Fluid pressure in the fracture (psi)

q = Fluid injection rate or flowrate of each grid block (bbl/min)

R_s = Solution gas-oil ratio (SCF/STB)

s = Distance along the fracture (ft)

S_w = Water saturation (dimensionless)

T_o = Tensile strength of the rock (psi)

v_{tip} = flow velocity at the tip of fracture (L/T)

w = Fracture width (ft)

$\overline{w}$ = Average fracture width (ft)

α_c = Volumetric conversion factor (dimensionless)

β_c = Transmissibility conversion factor (dimensionless)

μ = Fluid viscosity (cp)

v = Poisson's ratio (dimensionless)

ρ = Fluid density (lbm/ft^3)

σ_1, σ_2 = far-field effective stresses (psi)

σ_h = Minimum horizontal principal stress (psi)

σ_H = Maximum horizontal principal stress (psi)

σ_n = Normal stress acting on the NF plane (psi)

σ_t = Stress acting parallel to the NF (psi)

φ = Porosity (dimensionless)

γ = Gravity of phase (psi/ft)

5.10 Chapter reference

1. Abousleiman, Y.N. 1991. A Poroelastic PKN Model with Pressure Dependent Leakoff and Formation Permeability Determination, PhD dissertation, Univ. of Delaware.
2. Ahn, C. H., Chang, O. C., Dilmore, R., & Wang, J. Y. (2014, August 28). A Hydraulic Fracture Network Propagation Model in Shale Gas Reservoirs: Parametric Studies to Enhance the Effectiveness of Stimulation. Society of Petroleum Engineers. doi:10.15530/urtec-2014-1922580
3. Ahn, C. H., Dilmore, Robert and Wang, J.Y. 2014. Development of innovative and efficient hydraulic fracturing numerical simulation model and parametric studies in unconventional naturally fractured reservoirs. Journal of Unconventional Oil and Gas Resources Vol. 8: pg25-45. doi:10.1016/j.juogr.2014.06.003
4. Baree, R.D. and Mukherjee, H. 1996. Determination of Pressure Dependent Leakoff and Its Effect on Fracture
5. Beckner, B., H. Chan, et al. 1991. Simulating naturally fractured reservoirs using a subdomain method. SPE Symposium on Reservoir Simulation.
6. Blanton T.L. 1982 Experimental Study of Interaction Between Hydraulicalyy Induced and Pre-Existing Fractures. Paper SPE 10847 presented at the SPE Unconventional Gas Recovery Symposium, Pittsburgh, Pennsylvennia, USA, 16-18 May. doi: 10.2118/10847-MS.
7. Calslaw, H. and Jaeger, J.C. 1956. Conduction of Heat in Solids, end edition. Oxford, UK: Oxfrod Univ. Press.
8. Carter R.D. 1957. Derivation of the General Equation for Estimation the Extent of the Fracture Area. In Drill. And Prod. Prac. API, ed. Howard, G.C. and Fast, C.R., 261-268. NY.
9. Cipolla, C.L., Warpinski, N.R., Mayerhofer, M.J., and Lolon, E.P. 2010. The Relationship Between Fracture Complesity, Reservoir Properties, and Fracture-Treatment Desigh. SPE Production & Operations 25 (4): 438-452. SPE-115769-PA. doi: 10.2118/115769-PA
10. Cipolla, C.L., Lolon, E.P., Erdle, J.C., and Rubin, B. 2010. Reservoir Modeling in Shale-Gas Reservoirs. SPE Reservoir Evaluation & Engineering 13 (4): 638-653. SPE-125530-PA. doi: 10.2118/125530-PA
11. Gdanski, R. D., J. D. Weaver, et al. (2005). Fracture Face Damage—It Matters. SPE European Formation Damage Conference. Sheveningen, The Netherlands, Society of Petroleum Engineers.
12. Gidley, J.L., Holditch, S.A., Nierode, D.E and Ralph W. Veatch Jr. 1989. Recent advances in hydraulic fracturing. SPE Monograph series, Vol. 12.
13. Gu, H., Weng, X., Lund, J.B., Mack, M.G., Ganguly, U. and Suarez-Rivera, R. 2011.

Hydraulic Fracture Crossing Natural Fracture at Non-Orthogonal Angles, A Criterion, Its Validation and Applications. Paper SPE-139984-MS presented at the SPE HFTC, Woodland, Texas, 24-26 Jan. doi: 10.2118/139984-MS.

14. Hofmann H, Babadagli T, Zimmermann G. Numerical Simulation of Complex Fracture Network Development by Hydraulic Fracturing in Naturally Fractured Ultratight Formations. ASME. J. Energy Resour. Technol. 2014;136(4):042905-042905-9. doi:10.1115/1.4028690.
15. Howard, G.C. and Fast, C.R. Hydraulic Fracturing. 1970. Society of Petroleum.
16. Hossain, M.M., Rahman, M.K., 2008. Numerical simulation of complex fracturegrowth during tight reservoir stimulation by hydraulic fracturing. J. Pet. Sci.Eng. 60, 86–104.
17. Jacot, R. H., Bazan, L.W., and Meyer, B.R. 2010. Technology Integration – A Methodology to Enhance Production and Maximize Economics in Horizontal Marcellus Shale Wells. Paper SPE 135262-MS presented at SPE Annual Technical Conference and Exhibition, Florence, Italy, 19-22 September.
18. Kazemi, H., Merrill, L.S., Porterfield, K.L. and Zeman, P.R. 1976. Numerical Simulation of Water-Oil Flow in Naturally Fracture Reservoirs. SPE 5719.
19. Keshavarzi, R. and Mohammadi, S. 2012. A new Approach for numerical Modeling of Hydraulic Fracture Propagation in Naturally Fractured Reservoirs. SPE 152509-MS.
20. Lamb, H., Ed. 1932. Hydrodynamics, 6th edition. New York, Dover Publications.
21. Li M, Lior N. Analysis of Hydraulic Fracturing and Reservoir Performance in Enhanced Geothermal Systems. ASME. J. Energy Resour. Technol. 2015;137(4):041203-041203-14. doi:10.1115/1.4030111.
22. Lorenz, J. C. and Warpinski, N. R. 1996. Natural fracture characteristics and effects. Leading Edge, 15(8), 909-911.
23. Meyer, R. B. and Lucas W. Bazan. 2011. A Discrete Fracture Network Model for Hydraulically Induced Fractures - Theory, Parametric and Case Studies. Paer SPE 140514 presented at SPE Hydraulic Fracturing Technology Conference, 24-26 January 2011, The Woodlands, Texas, USA. doi: 10.2118/140514-MS.
24. Nordgren, R.P. 1972. Propagation of a Vertical Hydraulic Fracture. SPEJ 12 (4): 306-314. SPE-3009-PA. doi: 10.2118/3009-PA
25. Osholake T, Yilin Wang J, Ertekin T. Factors Affecting Hydraulically Fractured Well Performance in the Marcellus Shale Gas Reservoirs. ASME. J. Energy Resour. Technol. 2012;135(1):013402-013402-10. doi:10.1115/1.4007766.
26. Perkins, T.K. and Kern, L.R.1961. Widths of Hydraulic Factures. J Pet Technol 13 (9): 934-949; Trans., AIME, 222. SPE-89-PA. doi: 10.2118/89-PA
27. Poltluri, N., D. Zhu, and Hill, A.D. 2005.The Effect of Natural Fractures on Hydreaulic Fracture Propagation. Paper SPE 94568 presented at the SPE European Foramtion Damgae Conference, Sheveningen, The Netherlands, 25-27 May. doi: 10.2118/94568-MS.
28. Rahman M, Rahman M. Optimizing Hydraulic Fracture to Manage Sand Production by Predicting Critical Drawdown Pressure in Gas Well. ASME. J. Energy Resour. Technol. 2011;134(1):013101-013101-9. doi:10.1115/1.4005239.
29. Renshaw, C. E., and D.D. Pollard. 1998. An experimetal Verified Criterion for Propagation Across Unbounded Frictional Interfaces in Brittle Linear Elastic Materials. International Journal of Rock Mechanics and Mining Science & Geomechanics, 32 (3): 237-249. doi: 10.1016/0148-9062(94)00034-4.
30. Saidi, A. M. 1983. Simulation of Naturally Fractured Reservoirs. SPE Reservoir Simulation Symposium. San Francisco, California, Society of Petroleum Engineers of AIME.

31. Salehi S, Nygaard R. Full Fluid–Solid Cohesive Finite-Element Model to Simulate Near Wellbore Fractures. ASME. J. Energy Resour. Technol. 2014;137(1):012903-012903-9. doi:10.1115/1.4028251.
32. Settari A. 1985. A New General Model of Fluid Loss in Hydralic Fracturing. SPEJ 25 (4) 491-501.
33. Taleghani, A.D. and Olson, J.E. 2011. Numerical modeling of Multistranded-hydraulic-Fracture Propagation: Accounting for the interaction Between Induced and Natural Fractures. SPEJ 16 (3): 575-581. SPE-124884-PA. doi: 10.2118/124884-PA.
34. Taleghani, A.D. and Olson, J.E. 2013. How Natural Fractres Could Affect Hydraulic-Fracture Geometry. SPEJ SPE-167608-PA. doi: 10.2118/167608-PA.
35. Teufel, L.W. and Clark, J.A. 1984. Hydraulic fracture propagation in layered rock: Experimental studies of fracture containment. SPEJ 24 (1): 19-32. SPE-9848-PA. doi: 10.2118/9878-PA.
36. Warpinski, N.R. and Teufel, L.W. 1987. Influence of Geologic Discontinuities on Hydrauli Fracture Propagation. J Pet Technol 39 (2): 209-220; Trans., AIME, 283. SPE 13224-PA. doi: 10.2118/13224-PA.
37. Warpinski, N.R. and Smith, M.B. Rock Mechanics and Fracture Geometry, in Recent advances in Hydraulic Fractureing, (J. Gidley et al. (eds.)), Monograph Series, SPE, Richardson, TX, 1989
38. Warren, J. E. and P. J. Root. 1963. The Behavior of Naturally Fractured Reservoirs.
39. Weng, X., Kresse, O., Cohen C., Wu R., and Gu H. 2011. Modeling of Hydraulic Fracutre Network Propagation in a Naturally Fractured Formation. SPE Production & Operations 26 (4): 368-380. SPE-140253-PA. doi: 10.2118/9878-PA. doi: 10.2118/140253-PA.
40. Wu, Y.-S. and K. Pruess. 1988. A multiple-porosity method for simulation of naturally fractured petroleum reservoirs. SPE Reservoir Engineering 3 (1): 327-336.
41. Zeini Jahromi, M., Wang, J. Y., and Ertekin, T. 2013. Development of a Three-Dimensional Three-Phase Fully Coupled Numerical Simulator for Modeling Hydraulic Fracture Propagation in Tight Gas Reservoirs. Presented SPE HFTC, 4-6 Feb, Woodlands, TX. SPE-163850-MS. doi: 10.2118/163850-MS.
42. Zhang, X., C. Du, et al. 2009. Sensitivity Studies of Horizontal Wells with Hydraulic Fractures in Shale Gas Reservoirs. International Petroleum Technology Conference. Doha, Qatar, 2009, International Petroleum Technology Conference.
43. Zhang, X., Jeffery, R.G. 2008. Reinitiation or termination of fluid driven fractures at frictional bedding interfaces. J. Geophys. Res. 113: B08416. doi: 10.1029/2007JB005327.
44. Zhang, X., Jeffery, R.G., and Thiercelin, M. 2007a. Deflection and propagation of fruid-driven fractures at frictional bedding interfaces: A numerical investigation. Journal of Structrual Geology 29 (3): 396-410. Doi: 10.1016/j.jsg.2006.09.013.
45. Zhang, X., Jeffery, R.G., and Thiercelin, M. 2007b. Effects of Frictional Geological Discontinuities on Hydraulic Fracture Propagation. Paper SPE 106111 presented at the SPE Hydraulic Fracture Technology Conference, College Station, Texas, USA, 29-31 Jan. doi: 10.2118/106111-MS.Stoner, M.A.: "Steady-State Analysis of Gas Production, Transmission and Distribution Systems" paper SPE 2554 presented at the 1969 Annual Meeting of the SPE of AIME, Denver, Sept. 28-Oct.1
46. Zhou D, Zheng P, Peng J, He P. Induced Stress and Interaction of Fractures During Hydraulic Fracturing in Shale Formation. ASME. J. Energy Resour. Technol. 2015;137(6):062902-062902-6. doi:10.1115/1.4030832.

Chapter 6 PARAMETRIC STUDIES OF HYDRAULIC FRACTURE PROPAGATION IN SHALE RESERVOIRS: Evaluation of SRV, Fracture-Reservoir Contact Area, Fracture Width and Fracture Intensity

The most effective commercially available method for stimulating unconventional reservoirs is using properly designed and successfully implemented hydraulic fracture treatments. Recent field experience and simulation findings indicate that the key for a successful stimulation treatment relies on enlarging the effective stimulated reservoir volume and the complexity of fracture network. In this paper, a 3-dimensional, 2-phase, dual-continuum hydraulic fracture propagation model is exercise to investigate the hydraulic fracture geometry resulting from different reservoir and stimulation scenarios. Fracture geometry is quantitatively characterized through four parameters; stimulated reservoir volume (SRV), fracture-reservoir contact area (FR-area), fracture width, and an intensity factor – defined as the FR-area per unit SRV, which indicates the complexity of a fracture network. Parametric studies were conducted to quantify the effect of treatment rate and size, fracture fluid viscosity, differential horizontal stress, natural fracture spacing and fracture toughness. Insights from this exercise have implications for how effectiveness of stimulation of naturally fractured unconventional reservoirs may be improved.

6.1 Introduction

In recent years, the large-scale adoption, by industry, of hydraulic fracturing of multiple stages along laterally extensive horizontal wells has unlocked natural gas and oil resources from shale reservoirs with low-, to extremely low-permeability rock matrix, Such extraction techniques are, however, costly and resource intensive to apply; efficient and environmentally prudent engineering practice calls for maximizing resource recovery from each well and stimulated fracture network.

The concept of stimulated reservoir volume (SRV) introduced by Fisher and colleagues (2002) describes the effectiveness of a treatment to generate fracture network in a resource-bearing geologic interval to enable its timely and economical recovery. SRV is strongly related to the potential amount of resources that can be recovered and it is often measured or estimated through microseismic interpretation based on the spatial distribution of events, proximity to neighboring events, and event density (Daniels et al, 2007; Mayerhofer et al., 2008; Cipolla et al., 2014). Reservoir production can be maximized by creating large SRV coverage with high induced fracture density (Cipolla et al. 2010). However, the SRV calculated by microsiesmic data analysis fails to represent the actual hydraulic fracture geometry including the fracture density, area, and location of proppant which are critical in optimizing a fracture treatment in naturally fracture unconventional reservoirs (Ahn et al., 2014a; Cipolla et al., 2011b and 2012).

To complement information gained from microseismic analysis and better understand final hydraulic fracture geometry, many attempts have been made. Fracture complexity driven from the interaction between natural fractures and hydraulic fractures has been described in the literature (Gu et al., 2011; Wu et al., 2012 and 2015) and numerical simulators have been developed and applied to predict fracture network geometry in unconventional reservoirs (Taleghani et al. 2011, 2013; Weng et al. 2011; Keshavarzi et al. 2012; Meyer and Bazan 2011; Ahn et al., 2014b). While these approaches may be useful for forecasting fracture geometry, they have not been widely studied for their utility to evaluate stimulation performance.

The focus of this work is to obtain further understanding of the hydraulic fracture network resulting from a stimulation treatment as a function of key stimulation and geologic system parameters. Using the model developed previously by the author (Ahn et al., 2016), a series of parametric studies to evaluate the SRV, fracture-reservoir contact area, fracture width, and the intensity factor (indicates the complexity of a fracture network) were conducted to investigate the characteristics of hydraulic fracture geometry. The treatment rate, treatment size and fracture fluid viscosity, and geomechanical parameters, differential horizontal stress, natural fracture spacing and fracture toughness are studied to quantify the sensitivity.

6.2 Simulation settings (Reservoir, Fluids, Geomechanical Properties)

A 3D, two-phase dual continuum model capable of simulating hydraulic fracture propagation was used to conduct parametric studies. In that model, fracture domain and matrix domain are iteratively and explicitly coupled such that fracture propagation and fluid leakoff are captured simultaneously. One perforation cluster was simulated assuming there are five clusters per stage and the stress shadow effect between fracture branches is incorporated in the simulation. The flow through perforation is not modeled individually. The fracturing fluid is assumed to be injected at the natural fracture along the direction perpendicular to the minimum insitu stress.

The discretization of the fracture domain is developed using moving coordinate system. The location of the fracture tips vary in each timestep to capture the dynamic behavior of fracture propagation and height growth. In vertical z-direction, a number of grid blocks are used and the number of grid blocks vary in x and y direction according to the pre-existing natural fracture density and the treatment size. In general, the number of girds varies from 150 × 200 × 7 to 30 × 30 × 7 (x, y, z or $\sigma_{h,min}$, $\sigma_{H,mzx}$, σ_z). More details of the simulation model are reported in Ahn et al. (2014 and

2016). The input data set for the cases considered in this study is shown in detail in **Tables 6-1** and **6-2**. Visual representation of the rock properties of vertical layers is illustrated in **Figure 6-1**. Layers number 3 and 4 are natural gas-bearing payzone (162 ft).

Table 6-1. Reservoir and fracture parameters for the parametric simulation study

Parameters	Values
Initial Reservoir Pressure (psi)	4000
Treatment Rate (q_i, bbl/min)	30, 90, 150
Treatment size per state, K gal	100, 200, 300
Fracture fluid viscosity, cp	2, 10
Water compressibility, psi^{-1}	3×10^{-6}
$\sigma_{H,max}$ - $\sigma_{h,min}$, psi	100, 300
Young's Modulus (E), psi	3.4×10^{6}
Poisson ratio (v), fractional	0.22
Matrix K_{IC}, psi-in$^{1/2}$	0, 1500
Natural fracture (NF) spacing, ft	1 × 2, 10 × 20, 100 × 200

Table 6-2. Input data for each layer.

Layer No.	S_{wi}	Porosity (%)	Thickness (ft)	Perm (md)	Matrix K_{IC} (psi-in$^{1/2}$)	σ_{min} (psi)
1	0.99	20	100	0.01	0, 1500	7800
2	0.99	5	170	0.0001	0, 1500	7150
3 (Payzone)	0.1	5	92	0.0001	0, 1500	6900
4 (Payzone)	0.1	5	70	0.0001	0, 1500	6600
5	0.1	10	20	0.01	0, 1500	7850
6	0.99	30	180	10	0, 1500	6000
7	0.99	30	100	0.0001	0, 1500	8500

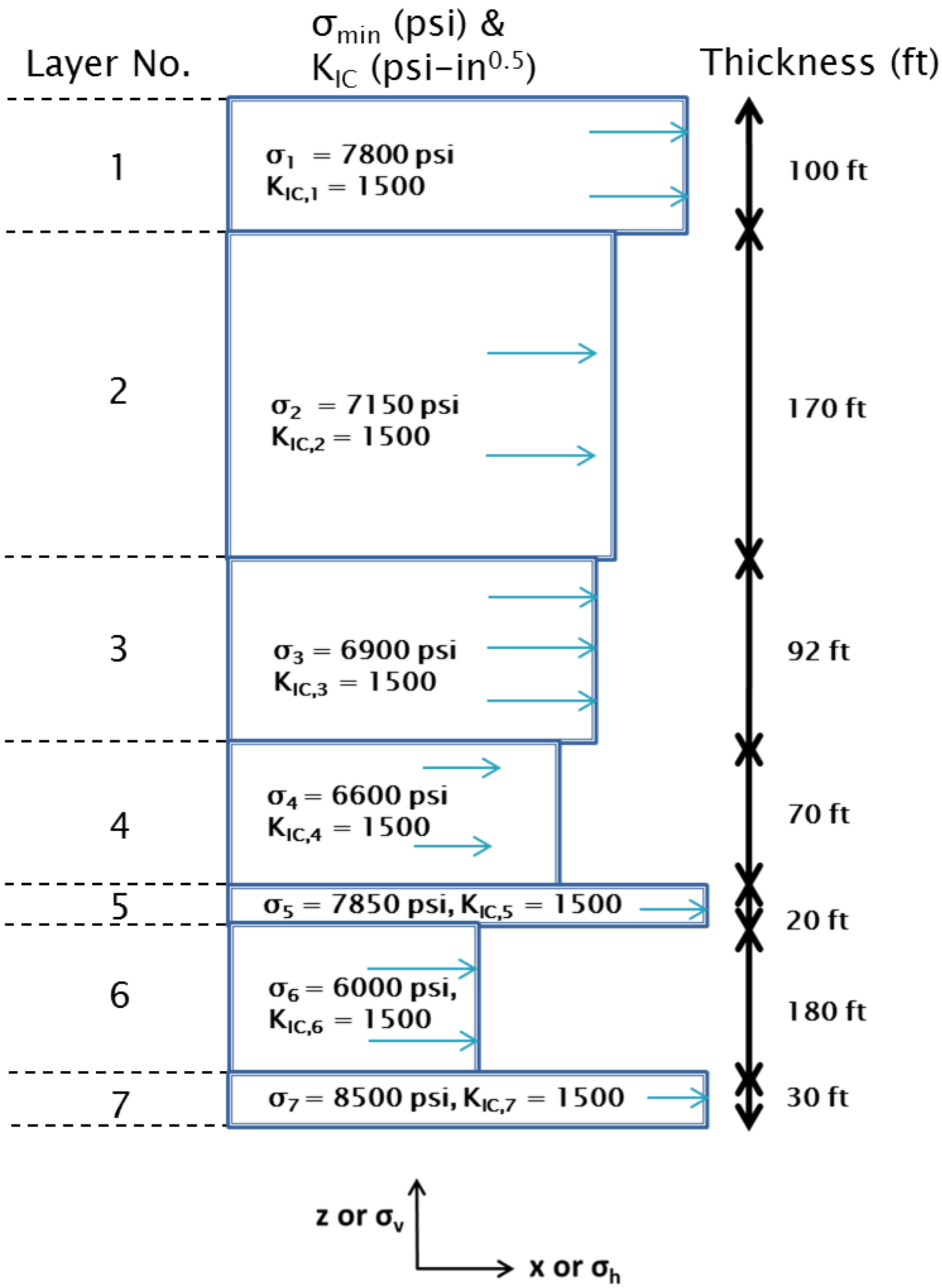

Figure 6-1. Geomechanical properties of each layer.

Using the parameters listed in **Tables 6-1** and **6-2**, a parametric study of 216 simulations was conducted (treatment rates of 30, 90, and 150 bpm, treatment size of 100, 200, and 300 K gal, fracture fluid viscosity of 2 and 10 cp, differential horizontal stress (DHS) of 100 and 300 psi, natural fracture spacing of 1 ft × 2 ft, 10 ft × 20 ft, and 100 ft × 200 ft, and fracture toughness of 0 and 1500 psi-in$^{0.5}$; as shown in **Table 6-3).** Each simulation takes about 30 minutes to 24 hours to run on a PC.

Table 6-3. Parameters for the numerical study

Parametric study sequence		Values		
			Base Case	
1.	Treatment rate, bpm	30	90	150
2.	Treatment size per state, K gal	100	200	300
3.	Fracture fluid viscosity, cp		2	10
4.	Differential horizontal stress (DHS) ($\sigma_{H,max}$ - $\sigma_{h,min}$), psi		100	300
5.	NF spacing, ft × ft	1 × 2	10 × 20	100 × 200
6.	Fracture toughness, psi-in$^{1/2}$	0	1500	

To evaluate how the fracture network propagates, we will investigate SRV in ft^3, fracture-reservoir contact area (F-R area) or fracture surface area in ft^2, fracture intensity factor in ft^2/ft^3, and individual fracture width in inch, the ratio of width and length of created network (W_{HF}/L_{HF}), height of created network in ft, fracture fluid efficiency.

Stimulated Reservoir Volume (SRV): SRV provides an indirect indication of the amount of gas that can be recovered. SRV is calculated using the theory of distance of investigation (DOI) described in **Equation 6-1** (Chatas, 1953: Daungkaew et al, 2000). It provides the drainage radius as a function of production time, porosity, viscosity, permeability, and compressibility. **Figure 6-2** shows calculated DOI, in units of ft, versus time, in days, for 30 years - obtained using the input values from **Table 6-1** and 6-**2**. DOI for 10 year production life DOI of 21.7 ft was calculated; for a 30 year production life, a DOI of 37.7 ft was calculated. This value may also vary significantly depending on the pressure and saturation values at the end of the fracture treatment. In this study, a 10 year production life (value *t*) was used to calculate SRV and only considered SRV that is effective (or that stimulated volume which is contained in the payzone).

$$x_{inv} = c_r \sqrt{0.0002637 \frac{kt}{\phi \mu c_t}} \tag{6-1}$$

where c_r is 1.41 for linear flow given by Chatas, k is permeability in md, ϕ is porosity, μ is viscosity in cp, and c_t is total compressibility in psi^{-1}.

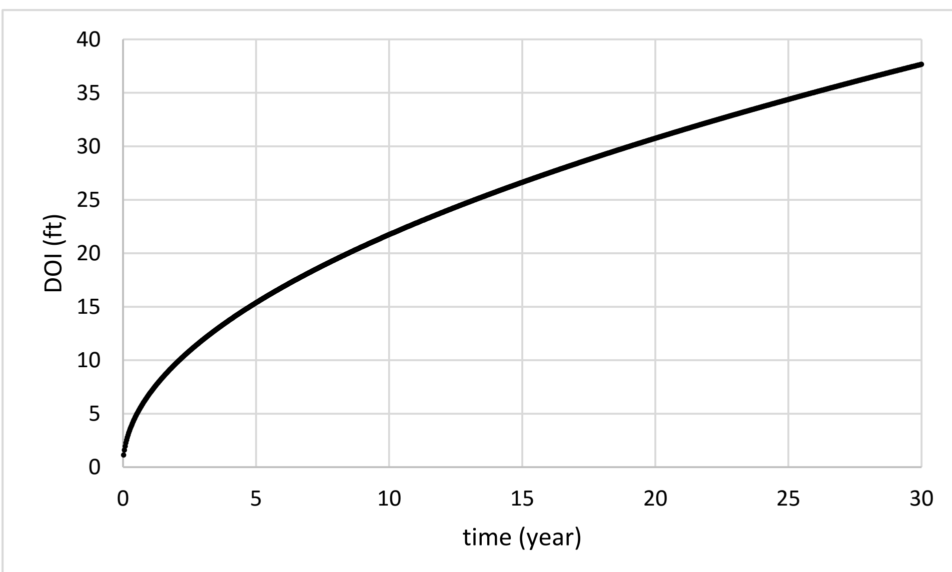

Figure 6-2. Distance of Investigation (ft) versus time (year)

Fracture-reservoir contact area (FR-area): Similar to SRV, we quantified FR-area only within the payzone. R-area is the contact or surface areas of a fracture network, which includes both faces of any individual fracture. A higher FR-area would yield a higher production rate.

Intensity factor: Intensity factor is the F-R area created in a unit SRV (**Equation 6-3**). Higher calculated intensity factors would correspond with larger recovery factor.

$$Intensity\ factor\ = \frac{(\ F - R\ area, ft^2)}{SRV, ft^3} \tag{6-3}$$

6.3 Result and analysis

In this section, simulation results of the base case are considered in detail. Effects of six factors: treatment rate, treatment size, fracture fluid viscosity, DHS, NF spacing, and fracture toughness, upon the hydraulic fracture propagation are then considered through parametric study.

6.3.1 Base case scenario

Numerical study of hydraulic fracture treatment first considered performance of the base case scenario, which then serves as a reference against which all the other cases are compared. The treatment rate of 90 bpm, treatment size of 200 K gal, DHS of 100 psi, NF spacing of 10 ft × 20 ft, fracture fluid viscosity of 2 cp, and fracture toughness of 1500 psi-in$^{0.5}$ is used for the base case simulation. All other input values are listed in **Table 6-1** and **2**. **Figure 6-3** shows the fracture network geometry for the base case on one side of the well. The color indicates the average width of fracture in ft, y-axis is the direction of $\sigma_{H,max}$, and x-axis is $\sigma_{h,min}$ in this figure; the perforation is placed at point (0, 0).

The maximum length of the created primary fracture (y or $\sigma_{H,max}$ direction) is 455.1 ft (910.3 ft assuming symmetry) and the secondary fracture (x or $\sigma_{h,min}$ direction) has maximum length of 198.2 ft. Thus, the ratio between maximum primary and secondary length is 0.218 (max. secondary fracture length / max. primary fracture length). The height of the fractures within that fracture network range from 70 ft to 127 ft, depending on their location with respect to the perforation. The maximum fracture width (aperture) at the perforation versus treatment time is in **Figure 6-4**. At the end of the treatment, the width reaches 0.22 inches. The height growth is illustrated in details in **Figure 6-5**. The generated fracture network extended to a maximum depth of 1.8 ft below the payzone (Layer-4), and grew 55.4 ft into overlying payzone, about 36.6 ft short to fully open both payzones.

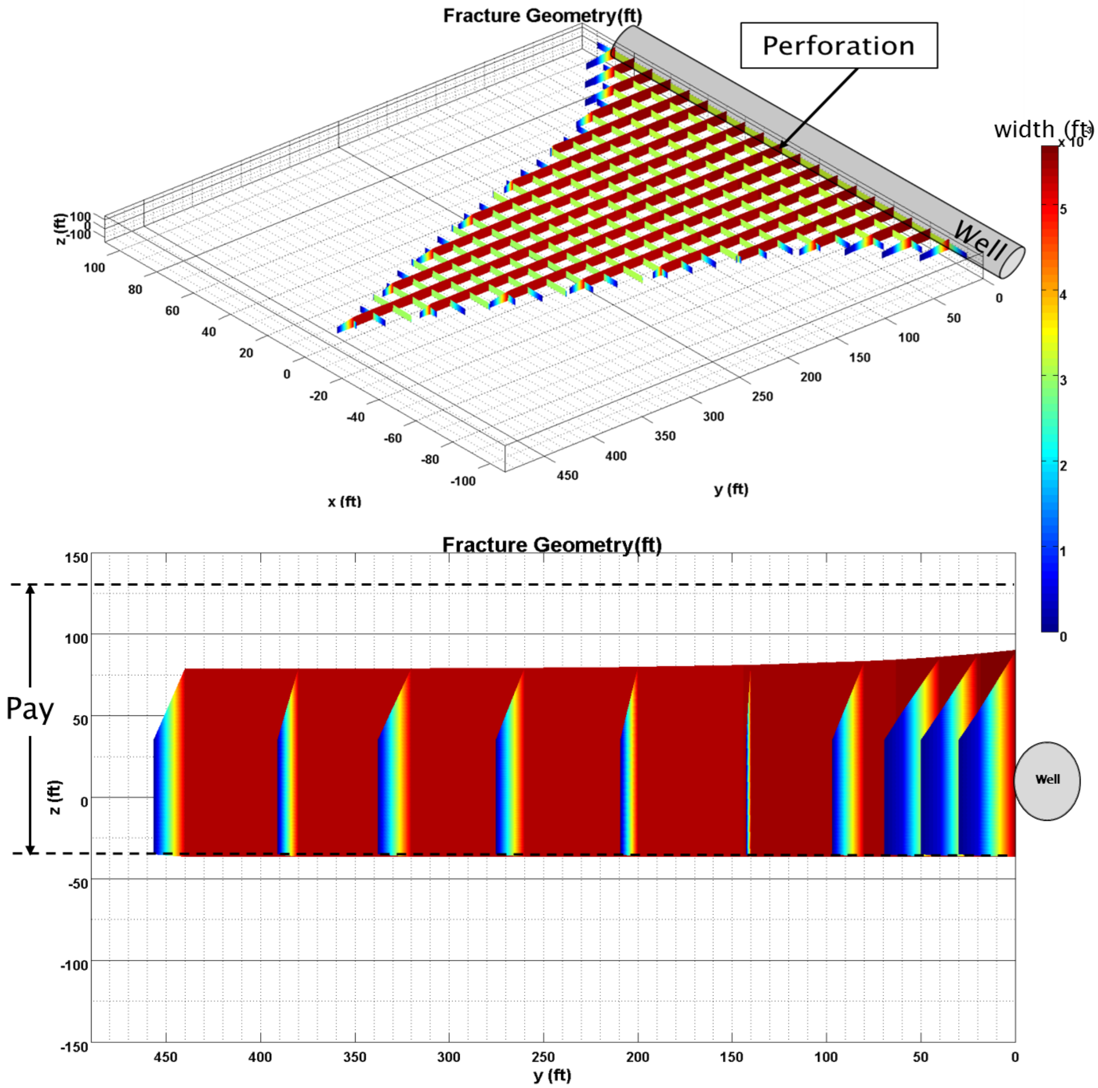

Figure 6-3. Final fracture geometry after the treatment.

(color: fracture width in ft, above: 3D view, below: 2D y-z plane view)

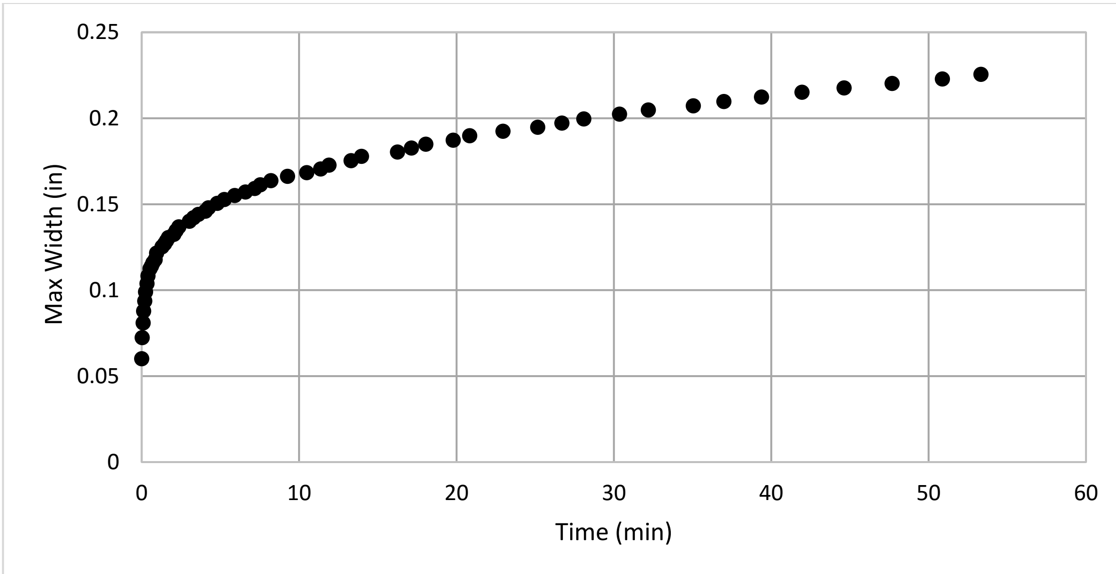

Figure 6-4. Maximum fracture width at wellbore (in) versus time (min).

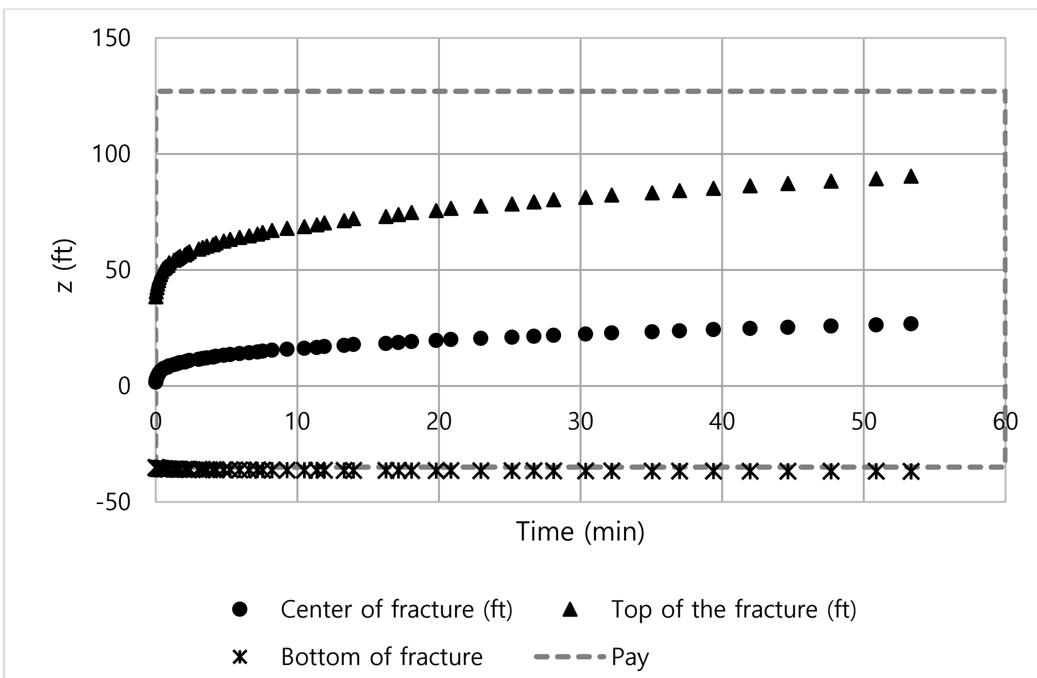

Figure 6-5. Height growth at wellbore versus time.

The total created SRV is 9.38 MMcf and SRV of payzone (SRV-pay) is 9.26 MMcf such that the efficiency of created SRV is 98.6%. For FR-area, total is 2.24 MMsf, FR-area in the pay (FR-pay) is 2.21 MMsf, and the efficiency is 98.85%. In other words, 1.4% of the stimulated volume and 1.15% of the FR-area fall outside of the payzone because of the fracture growth into underlying layer (Layer 5) which is not a payzone. The intensity factor in the pay is 0.239 meaning 0.239 ft^2 of FR-area is created in unit volume (ft^3) of SRV. The results at the end of treatment for the base case are summarized in **Table 6-4**.

Table 6-4. Summary of the result from base case scenario

Total SRV (MMcf)	SRV pay (MMcf)	Effective SRV (%)
9.38	9.26	98.6

Total FR-area (MMsf)	FR-pay (MMsf)	Effective FR-area (%)
2.24	2.21	98.85

Intensity factor	wf at perf (in)	hf at perf (ft)
0.239	0.22	127.00

W_{HF}/L_{HF}
0.218

6.3.2 Effect of treatment rate

The rates used for this study are 30 bpm, 90 bpm, and 150 bpm. 150 bpm is unrealistically high, but it is used as a bounding endpoint to understand the maximum possible impact of this parameter on model performance. As we develop the scenarios associated with hydraulic fracture treatment, we can compare each case to the base case (treatment size of 200 K gal, fluid viscosity of 2 cp, DHS of 100 psi, NF spacing of 10 ft × 20 ft, and fracture toughness of 150 psi-in$^{0.5}$) to analyze its effect on SRV-pay, FR-pay, fracture width, and intensity factor. Results generated from perturbation of those parameters are discussed in Sections **6.3.3** through **6.3.7**.

The effect on SRV-pay: The SRV-pay decreases as the treatment rate increases because higher injection rate develops higher net pressure in a fracture so that the hydraulic pressure creates larger fracture width or height growth out of the payzone (**Figure 6-6(a)**). The figure also illustrates the SRV-pay in different cases. The x-axis indicates the base case, and the results of cases in which single parameters are varied from the base case. In all cases a trend of decreasing SRV-pay is predicted as injection rate increases, with, the sensitivity or the rate change of SRV-pay varying depending on the cases having different engineering parameters.

The percentage differences of SRV-pay from 90 bpm cases are illustrated in (**Figure 6-6(b)**). These results show that the rate of change in SRV-pay is not linear with respect to injection rate. The largest sensitivity is observed at the case using fluid viscosity of 10 cp. From 30 bpm to 150 bpm, SRV-pay drops -29.1%. When the treatment size is increased from 100 to 200 K gal/stage (base case) and 300 Kgal per stage, SRV-pay become less sensitive to the injection rate. The percentage change from 30 to 150 bpm yield -21.1% for 100 K gal, -18.7% for 200 Kgal/stage, and -15.8% after 300 K gal/stage. DHS of 300 psi shows results in larger SRV-pay value than base case with 100 psi but it decreases with the sharper rate when treatment rate is increased. Decrease of NF spacing reduces the impact of treatment rate. From 30 to 150 bpm, 100 ft × 200 ft changes -24.9%, 10 ft × 20 ft differs -18.7%, and 1 ft × 2 ft shows -3.2% change. The reduction of fracture toughness to 0 psi-in$^{0.5}$ slightly increases SRV-pay but its sensitivity diminishes about 2%.

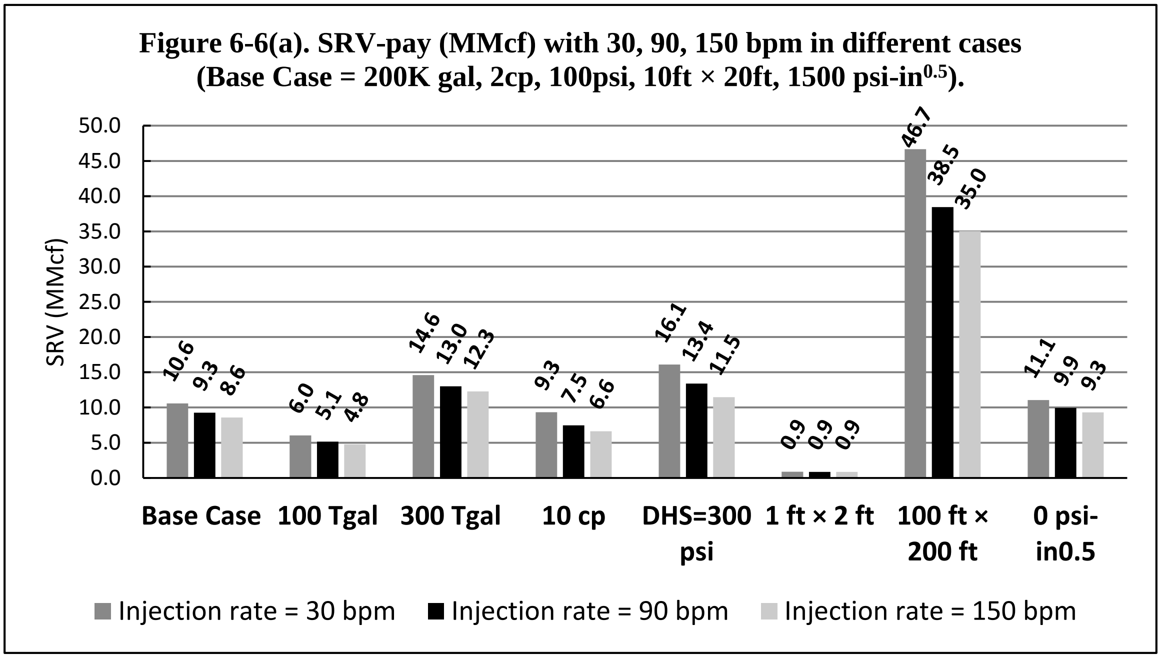

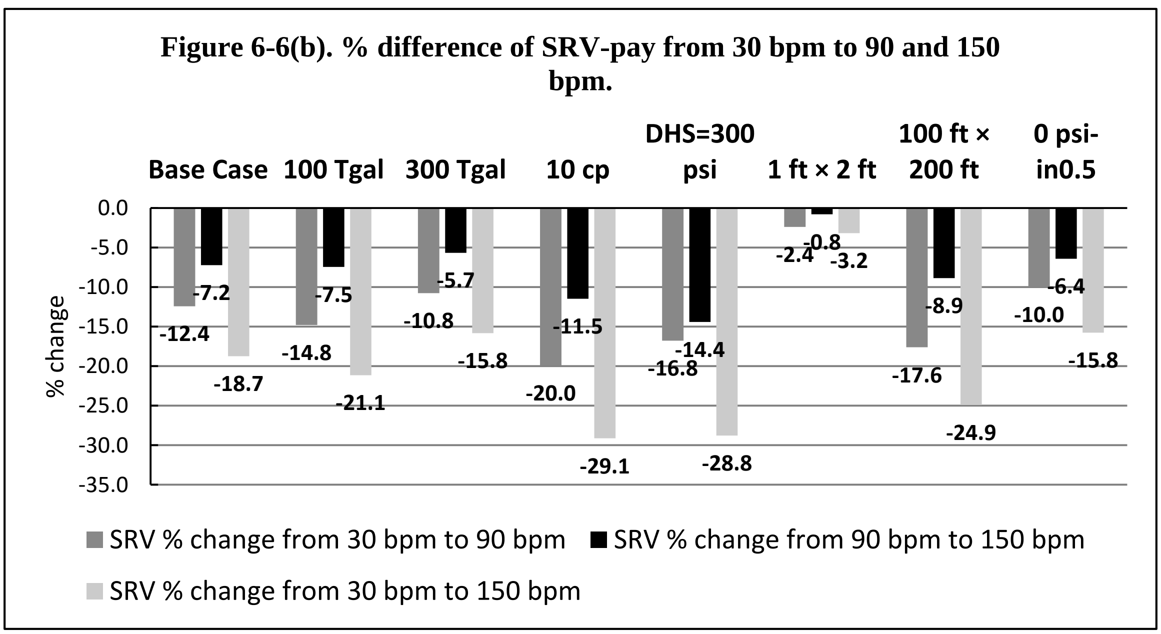

Figure 6-6. (a)SRV-pay and (b) the percentage change of SRV-pay from 30 to 90 bpm, 90 to 150 bpm, and 30 to 150 bpm for different cases. The x-axis indicates treatment size (K gal), fluid viscosity (cp), DHS (psi), NF spacing (ft×ft), and fracture toughness (psi-in$^{0.5}$) accordingly.

The effect on FR-pay: Similar to SRV-pay, FR-pay decreases as treatment rate increases from 30, 90, and 150 bpm for all cases (**Figure 6-7 (a)**). It decreases from 2.65 MMsf to 2.21 MMsf and to 1.99 MMsf in base case. In the case with NF spacing of 1 ft × 2 ft, it increase slightly about 0.4% from 2.55 MMsf at 30 bpm to 2.56 MMsf at 90 bpm. The sensitivity of FR-pay to injection rate is lower than SRV-pay, ranging from -25.9% to 0.4% (**Figure 6-7(b)**). The percentage change of FR-pay from 30 to 90 bpm, increases from -18% to -16.8% and -15.5% with increasing (100, 200, and 300 K gal, respectively). In this case, increasing from 90 to 150 bpm show the results -9.6%, -10.1%, and -9.5% within the range of 1% difference. Compared to the base case, the fluid viscosity of 10 cp yields the sensitivity decrease in both intervals 30 to 90 bpm (-15.2%) and 90 to 150 bpm (-7.4%). The FR-pay sensitivity on the injection rate increasing from 30 to 90 bpm is largest at the case with NF spacing of 100 ft × 200 ft (-18.2%) and minimized at 1 ft × 2 ft (0.4%) case. From 90 to 150 bpm, base case holds the largest of -10.1% and 1 ft × 2 ft case also has the least sensitivity of -4.6%.

Figure 6-7(a). FR-pay in pay (MMsf) with 30, 90, 150 bpm in different cases (Base Case = 200K gal, 2cp, 100psi, 10ft × 20ft, 1500 psi-in$^{0.5}$) .

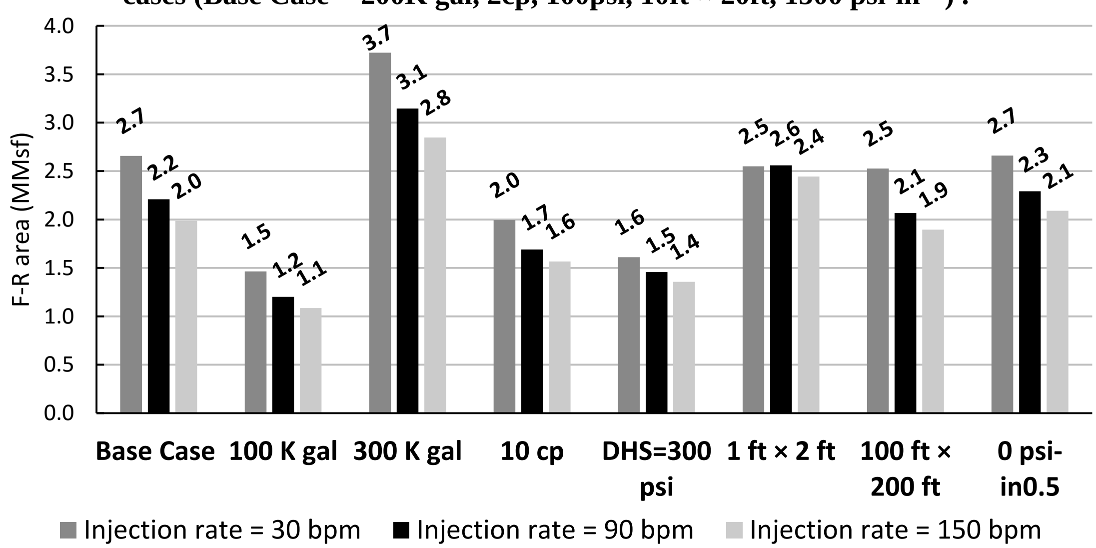

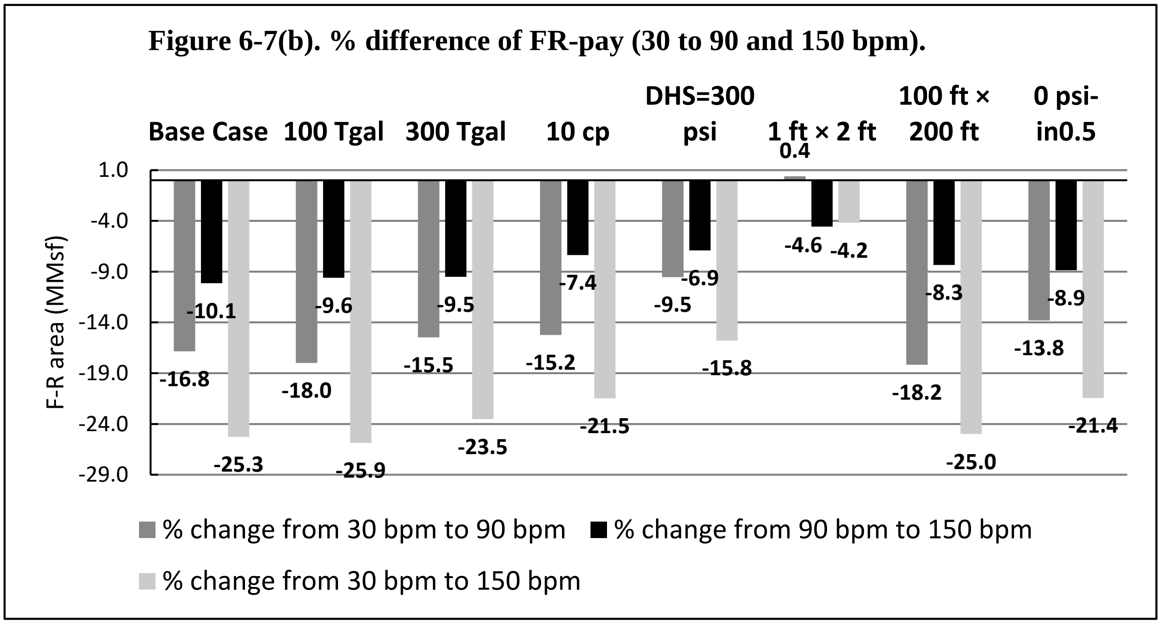

Figure 6-7. (a)FR-pay and (b) the percentage change of FR-pay with 30, 90, 150 bpm injection rates for different cases. The x-axis indicates treatment size (K gal), fluid viscosity (cp), DHS (psi), NF spacing (ft×ft), and fracture toughness (psi-in$^{0.5}$) accordingly.

The effect on the fracture width: Since higher injection rate increases the net pressure, in contrast to SRV-pay and FR-pay, the width shows a positive relationship with injection rate for all cases. In the base case, the width at perforation (wf_{perf}) increases from 0.15 in. to 0.22 in. and 0.29 as the injection rate increases 30 to 90 and 150 bpm (**Figure 6-8 (a)**). The increase rate of wf_{perf} is higher at the interval between 30 and 90 bpm. 18.1% to 53.2% increase are observed from 30 to 90 bpm but, from 90 to 150 bpm, 7.1% to 27.4% is increased (**Figure 6-8(b)**). The case with 300 K gal treatment size shows the most increase from 30 to 150 bpm about 89%. NF spacing of 1 ft × 2 ft case shows 56.4% increase in width which is relatively larger percentage change compare to those of SRV-pay and FR-pay (3% to 4%).

Figure 6-8(a). wf at perforation with 30, 90, 150 bpm in different cases (Base Case = 200K gal, 2cp, 100psi, 10ft × 20ft, 1500 psi-in$^{0.5}$) .

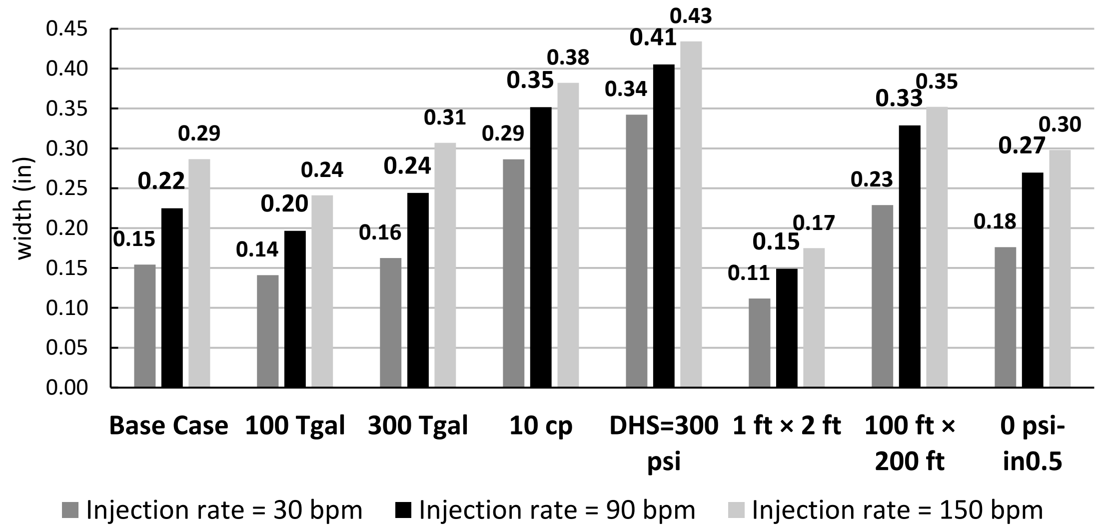

Figure 6-8(b). % difference of wf at perforation from 30 to 90 and 150 bpm.

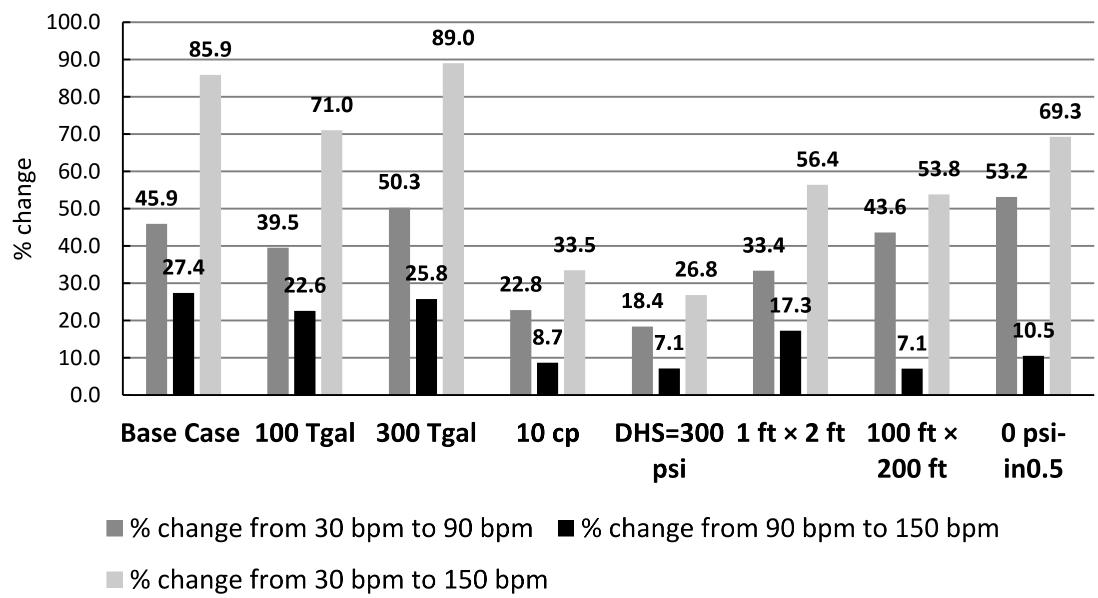

Figure 6-8. (a) wf_{perf} and (b) the percentage change of wf_{perf} with 30, 90, 150 bpm for different cases. The x-axis indicates treatment size (K gal), fluid viscosity (cp), DHS (psi), NF spacing (ft×ft), and fracture toughness (psi-in$^{0.5}$) accordingly.

The effect on intensity factor (ft²/ ft³): As mentioned above, the intensity indicates the quality of SRV-pay and **Figure 9(a)** shows the intensity from the cases we study in this section. The decrease of intensity is observed with increased treatment rate for all cases except the cases with 10 cp and DHS of 300psi. For the base case, it deceases from 0.251 to 0.239 and 0.231 ft^2/ft^3. If the decrease rate of SRV-pay exceeds the decrease rate of FR-pay, according to **Equation 6-3**, positive relationships between the percentage change of intensity factor and treatment rate are observed as in 10 cp and DHS of 300 psi case. Beside these two, the percentage decrease of SRV-pay is smaller than FR-pay such that the intensity decreases as treatment size increases. The percentage change of intensity show –1.3% to 18.3% (**Figure 6-9(b)**). The NF spacing of 100 ft × 200 ft case results in the least change (-1.3%) and the case with DHS of 300 psi has the largest rate change of 18.3% from 30 to 150 bpm.

Figure 6-9(a). Intensity factor with 30, 90, 150 bpm in different cases (Base Case = 200K gal, 2cp, 100psi, 10ft × 20ft, 1500 psi-in$^{0.5}$) .

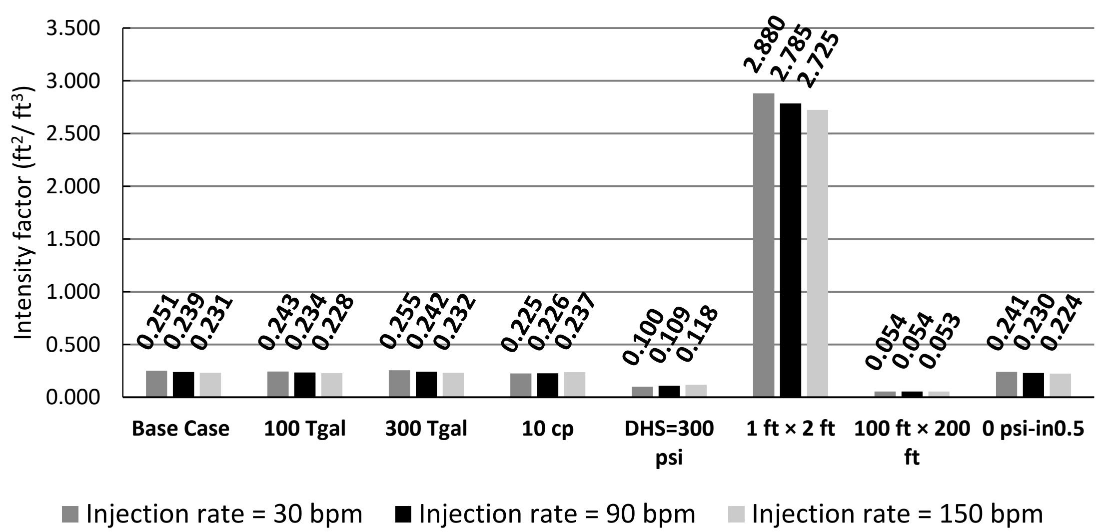

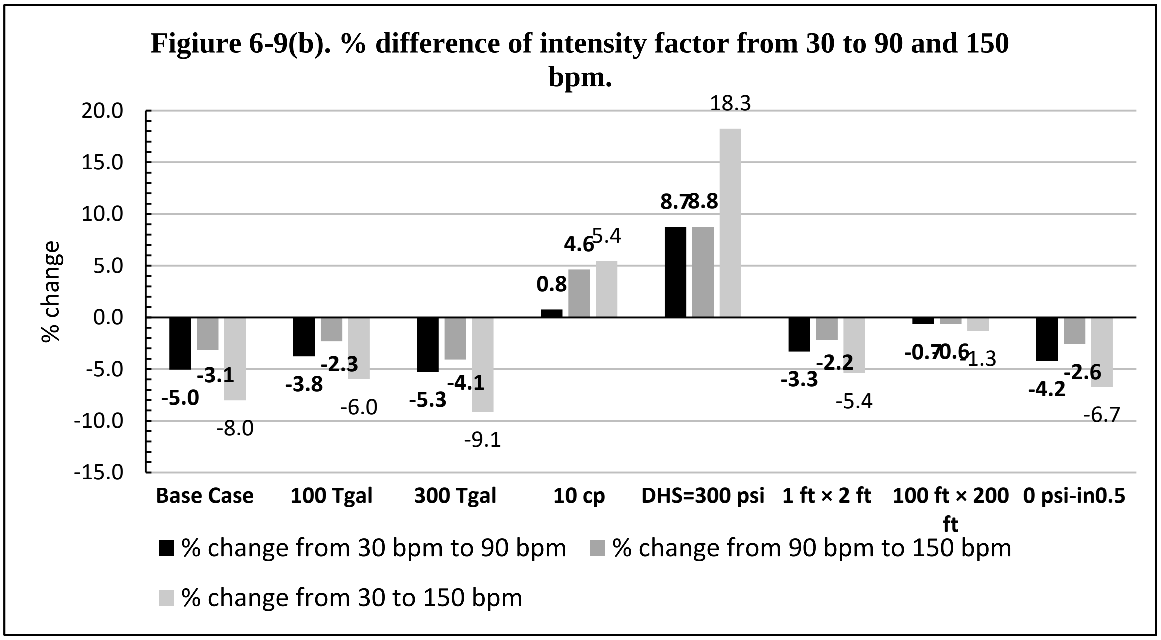

Figure 6-9. (a) Intensity factor and (b) the percentage change of intensity factor with 30, 90, 150 bpm for different cases. The x-axis indicates treatment size (K gal), fluid viscosity (cp), DHS (psi), NF spacing (ft×ft), and fracture toughness (psi-in$^{0.5}$) accordingly.

6.3.3 Effect of treatment size

The size of 100, 200, and 300 K gallons per stage are studied over SRV-pay, FR-pay, fracture width, and intensity factor. Similar to previous section, we simulate the cases with different treatment rate, fluid viscosity, DHS, NF spacing, and fracture toughness as listed in **Table 3**. The base case for this section has treatment rate of 90 bpm, fluid viscosity of 2 cp, DHS of 100 psi, NF spacing of 10 ft × 20 ft, and fracture toughness of 1500 psi-in$^{0.5}$.

The effect on SRV-pay: **Figure 6-10(a)** shows 8 sets of the SRV-pay results in different treatment sizes. In each set, the parameters listed below the bar is changed from the base case. Unlike previous section, SRV-pay and treatment size has positive relationship at all cases ranging from 0.5 MMcf to 57.1 MMcf. SRV-pay increases from 5.1 MMcf to 9.3 and to 13.0 MMcf as treatment size increase from 100, 200, and 300 K gal accordingly. **Figure 6-10(b)** shows the percentage increase of FR-pay from 100 to 200 K gal, 200 to 300 K gal, and from 100 to 300 K gal. 100 ft × 200 ft case shows the most increase of SRV-pay from 100 to 300 K gal about 161.0% (from 21.9 to 57.1 MMcf) and DHS with 300 psi results in the least change of 121.1% (7.8 to 17.3 MMcf). To evaluate the efficiency, SRV-pay per a gallon of fracture fluid (ft^3/gal) is illustrated in **Figure 6-10(c)**. The fracture fluid efficiency on SRV-pay decreases as the treatment size increases. Even though, the bigger treatment size creates larger SRV-pay, its efficiency shows opposite behavior for all the cases. The width expansion, height growth out of pay, or fluid leakoff may cause the loss of efficiency. The base case shows 51.4, 46.3, and 43.4 ft^3/gal as the treatment size increases. The case with DHS of 300 psi has the largest drop from 78.1 to 67.0 and 57.6 ft^3/gal about -26.3%. 100 ft × 200 ft system shows the least change of -23.8%. Therefore, in terms of SRV-pay, increasing treatment size for the reservoir having relatively larger DHS is comparably not effective, whereas it may be encouraged for the reservoir with larger NF spacing.

Figure 6-10(a). SRV-pay (MMcf) with 100, 200, 300 K gallons in different cases (Base Case = 90 bpm, 2cp, 100psi, 10ft × 20ft, 1500 psi-in$^{0.5}$).

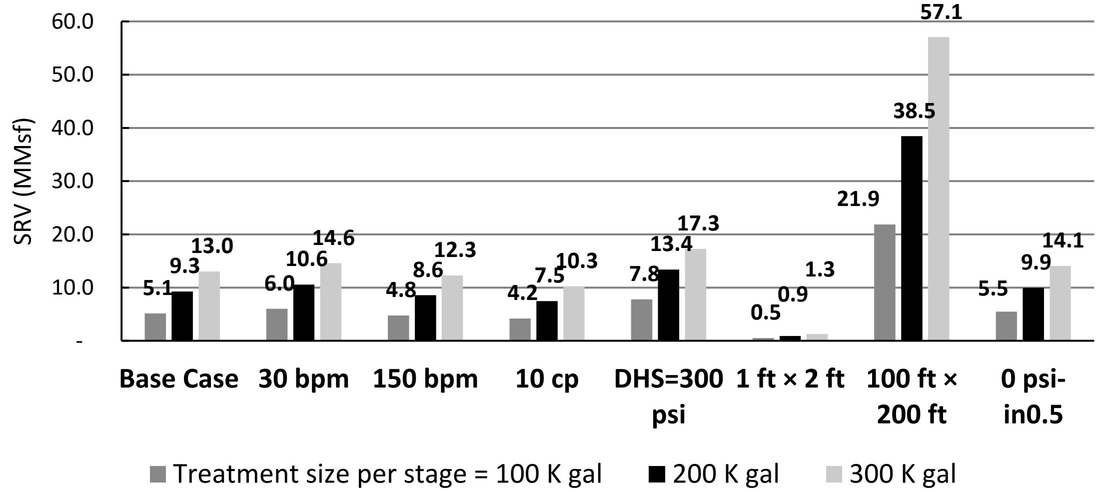

Fgure 6-10 (b). % difference of SRV-pay.

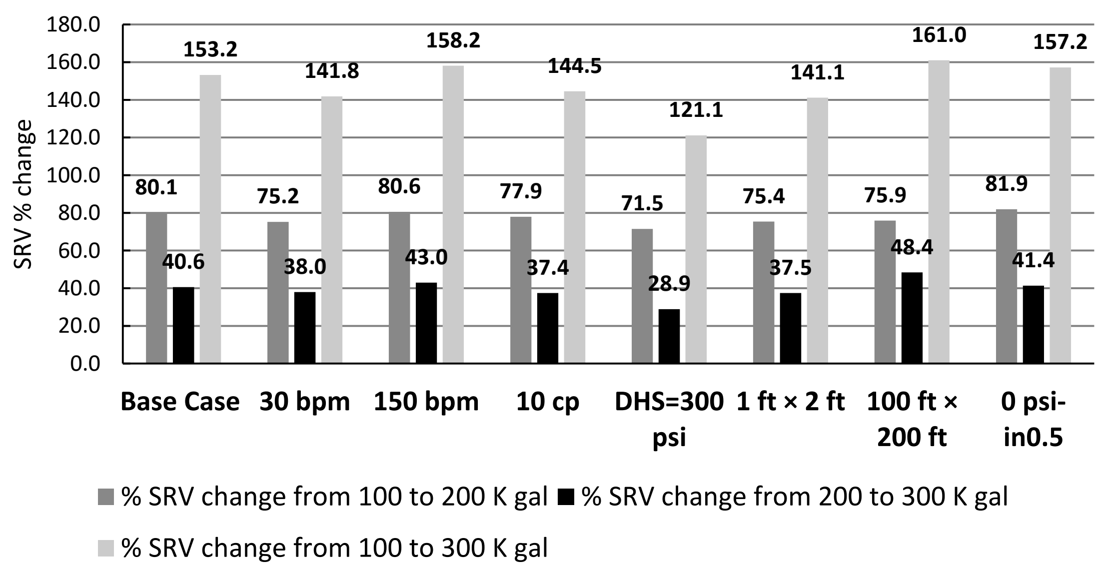

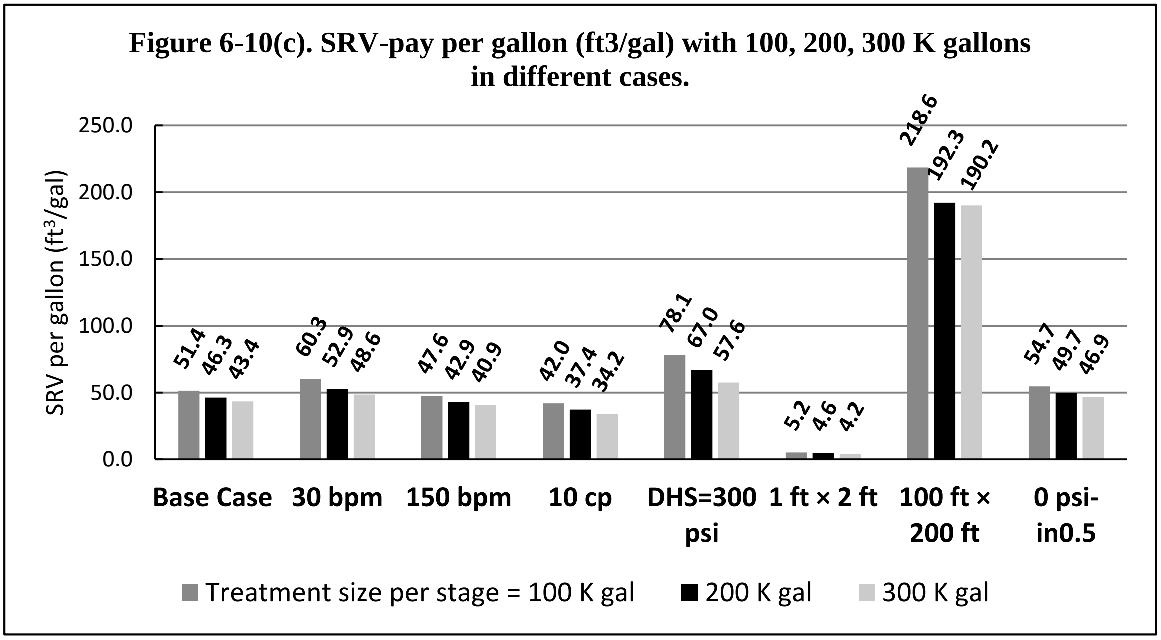

Figure 6-10. (a)SRV-pay , (b) the percentage change of SRV-pay, and (c) SRV-pay per a gallon of fracture fluid for 100, 200, and 300 K gal. The x-axis indicates different cases, treatment rate (bpm), fluid viscosity (cp), DHS (psi), NF spacing (ft×ft), and fracture toughness (psi-in$^{0.5}$) accordingly.

The effect on FR-pay: **Figure 6-11(a)** shows that FR-pay increase as treatment size become larger in all cases. Compare to SRV-pay, FR-pay is slightly more sensitive to treatment size. The percentage increase of FR-pay is 2.9% to 44.3% larger in all cases except the one with NF spacing of 100 ft × 200 ft (**Figure 6-11(b)**). In this case, SRV-pay increases 161% while FR-pay rises 154.7%. Similar to SRV-pay, the efficiency of FR-pay on treatment size decreases (**Figure 6-11(c)**). Since zero toughness has the largest percentage increase of FR-pay, it has the least percentage decrease of the efficiency (-18.7%) from 100 to 300 K gal.

Figure 6-11(a). FR-pay (MMsf) with 100, 200, 300 K gallons in different cases (Base Case = 90 bpm, 2cp, 100psi, 10ft × 20ft, 1500 psi-in$^{0.5}$) .

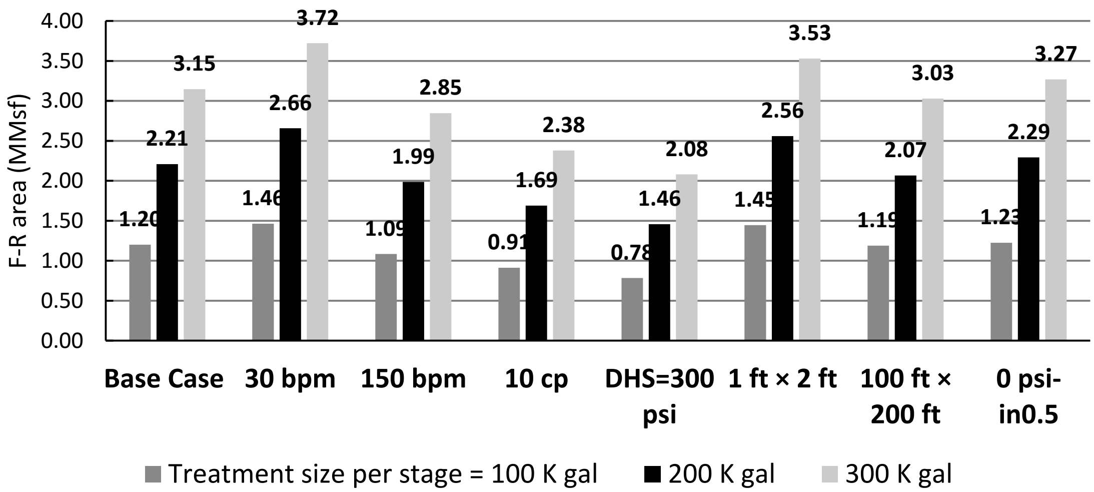

Figure 6-11(b). The percentage difference of FR-pay

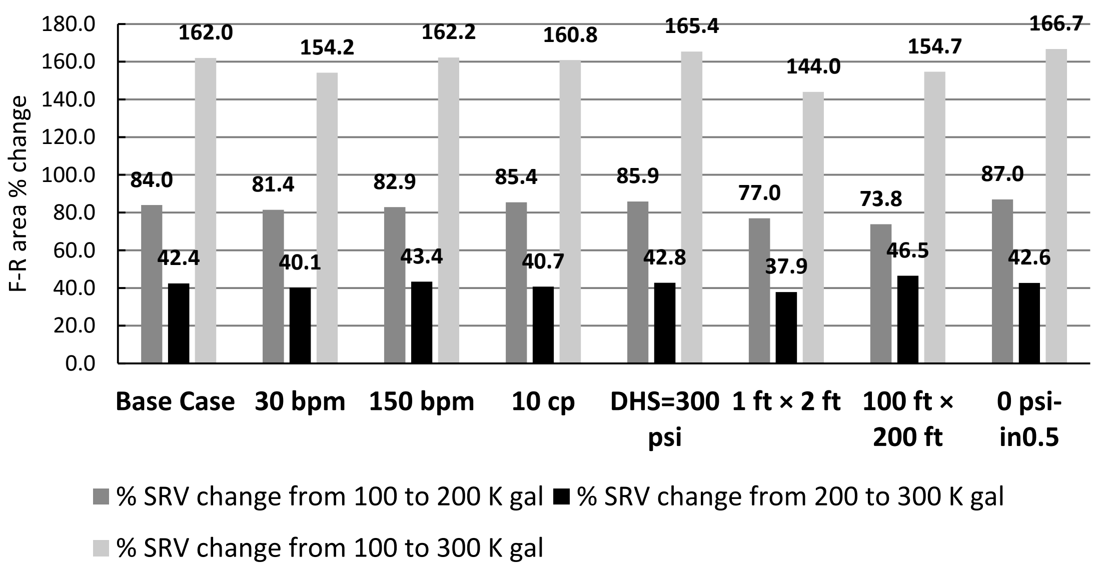

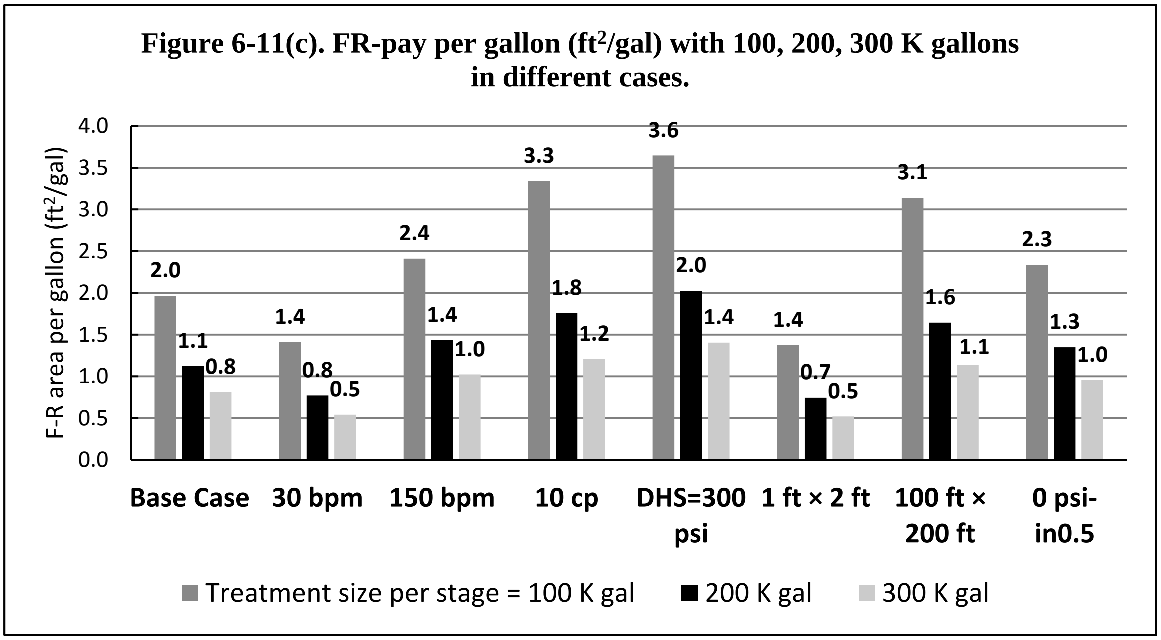

Figure 6-11. (a) FR-pay, (b) the percentage change of FR-pay, and (c) FR-pay per a gallon of fracture fluid for 100, 200, and 300 K gal. . The x-axis indicates different cases, treatment rate (bpm), fluid viscosity (cp), DHS (psi), NF spacing (ft×ft), and fracture toughness (psi-in$^{0.5}$) accordingly.

The effect on the fracture width: The width at the perforation (wf_{perf}) is increased as the treatment size increases for all cases. In the base case, wf_{perf} increases from 0.197 to 0.225 and 0.244 inch as treatment size increases from 100 to 200 and 300 K gal and it increases for all cases (**Figure 6-12(a)**). The width is ranging from 0.138 to 0.421 inch. The percentage increase of wf_{perf} due to increase of treatment size is largest at the case with treatment rate of 150 bpm (**Figure 6-12(b)**). From 100 to 300 K gal, wf_{perf} increases 27.4%. The smallest percentage is reached by the case with 100 ft × 200 ft having 8.3% increase. However, increasing treatment from 100 to 300 K gal is not as effective as increasing the treatment rate from 30 to 150 bpm. Comparing the base case, treatment size generated 24.1% increase while treatment rate has 85.9% and this trend holds for all cases.

This explains the opposite behavior of SRV-pay and FR-pay between treatment rate and size. Increasing the size of treatment has more benefit over SRV-pay and FR-pay while higher rate cause wider width. Increasing the size of treatment has more benefit over SRV and F-R area while higher rate cause wider width.

Figure 6-12(a). wf_{perf} (in) with 100, 200, 300 K gallons in different cases (Base Case = 90 bpm, 2cp, 100psi, 10ft × 20ft, 1500 psi-in$^{0.5}$) .

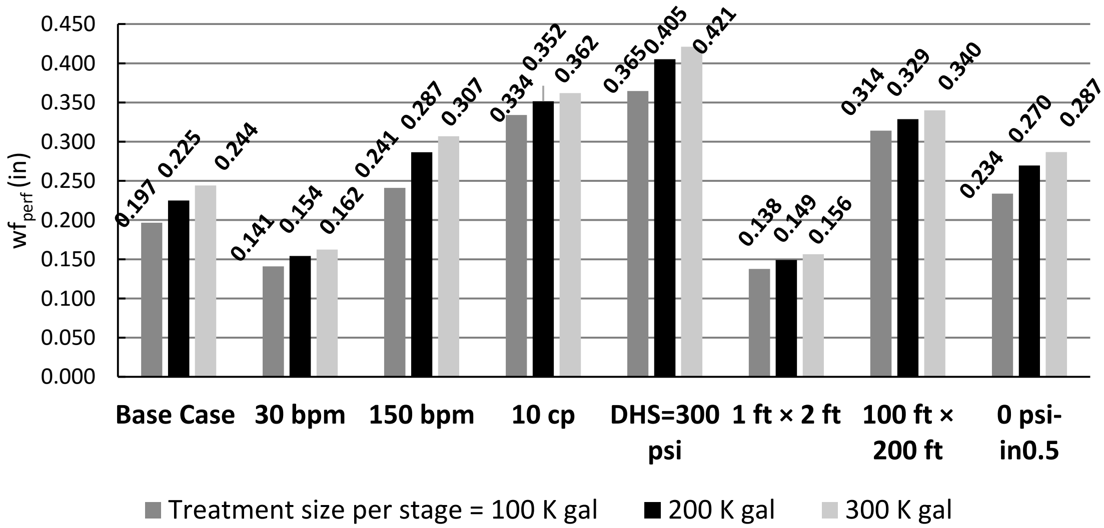

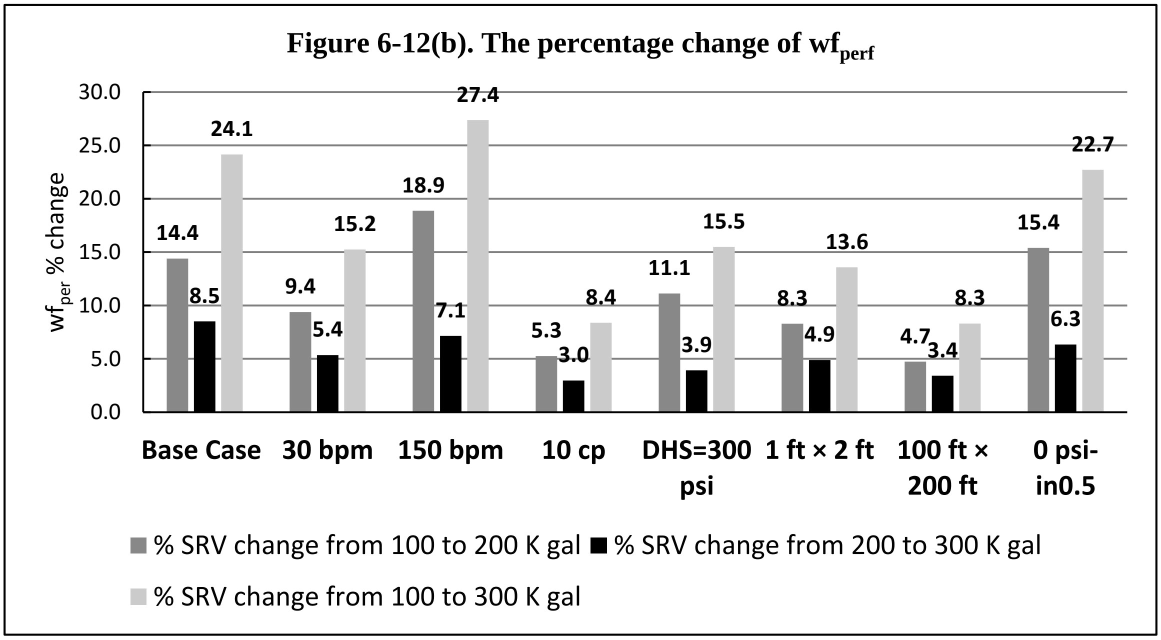

Figure 6-12. (a) wf_{perf} and (b) the percentage change of wf_{perf} with 100, 200, 300 K gal for different cases. The x-axis indicates treatment size (K gal), fluid viscosity (cp), DHS (psi), NF spacing (ft×ft), and fracture toughness (psi-in$^{0.5}$) accordingly.

The effect on intensity factor: **Figure 6-13(a)** shows the intensity factor results for this study. The increase of the treatment size also contributes to a negligible increase of intensity factor. For the base case, the intensity factor increases from 0.234 to 0.239 and 0.242 ft^2/ ft^3. The largest intensity is driven by the case having 1 ft × 2 ft NF spacing (2.760, 2.758, 2.793 ft^2/ ft^3) and the least is acquired from 100 ft × 200 ft case (0.0544, 0.0537, 0.0531 ft^2/ ft^3). The percentage increase of intensity factor from 100 to 300 K gal is resulted between -2.4% and 20% (**Figure 6-13(b)**). As mentions above, at 100 ft × 200 ft case, SRV-pay increase rate is larger than FR-pay such that the intensity factor decreases about 2.4% but the incremental is very small 0.001 ft^2/ ft^3 and except this case, the intensity change is positive ranging 6.8% to 29%) is relatively smaller than the change driven by treatment rate (21.7% to 35.8%). Thus, increasing the treatment rate from 30 to 150 bpm more effective than increasing the size from 100 to 300 K gal.

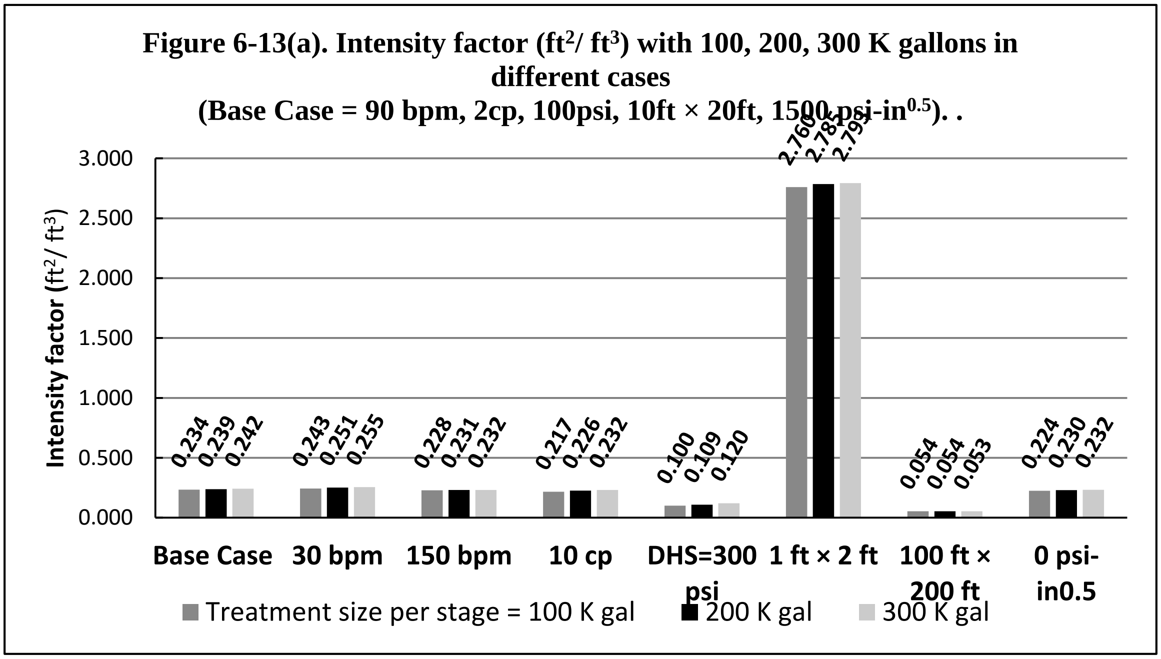

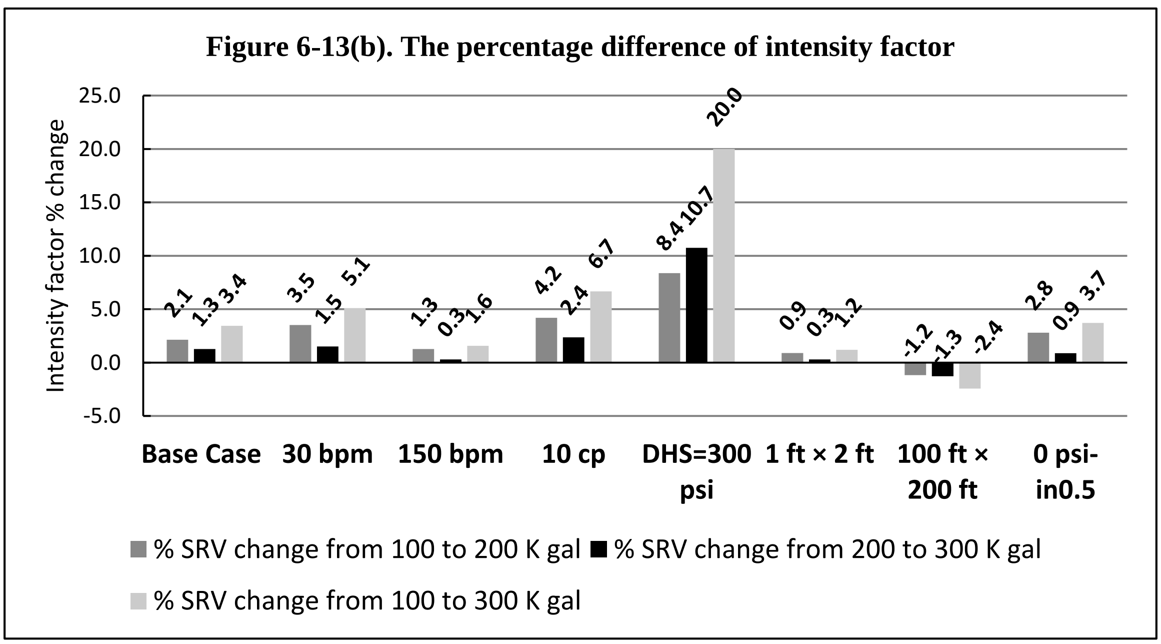

Figure 6-13. (a) Intensity factor and (b) the percentage change of intensity factor with 30, 90, 150 bpm for different cases. The x-axis indicates treatment size (K gal), fluid viscosity (cp), DHS (psi), NF spacing (ft×ft), and fracture toughness (psi-in$^{0.5}$) accordingly.

6.3.4 Effect of fracture fluid viscosity

Fracture fluid viscosity is another important parameter that one could change to achieve optimized stimulation. Viscous fluid increases the net pressure in a fracture such that it tends to create wider fracture width. This subsection presents numerical simulation results and analyses for the effect of viscosity on SRV-pay, FR-pay, wf_{perf}, and intensity factor. Total 9 sets of different cases are evaluated. One set includes two results from the fracture fluid viscosity 2 cp and 10 cp. The base case represents the results from injection rate of 90 bpm, treatment size of 200 K gal, DHS of 100 psi, NF spacing of 10 ft × 20 ft, and fracture toughness of 1500 psi-in$^{0.5}$ and one of these parameter varies by each set similar to previous sections.

The effect on SRV-pay: **Figure 6-14(a)** shows 9 sets of two SRV-pay results using 2 cp and 10 cp fracture fluid viscosities. SRV decreases as fracture fluid viscosity increases and this trend is held for all cases studied. Similar to increasing treatment rate, the volume of fluid creates wider width rather than increasing the length of fractures. From the figure, we can see that the case with 10 cp and 30 bpm has almost same SRV-pay (≈9.3 MMcf) as the base case with 2 cp. Thus, in this case, increasing the viscosity from 2 cp to 10 cp and decreasing the rate from 90 to 30 bpm have same degree of impact on SRV-pay. The percentage SRV-pay changes are illustrated in **Figure 6-14(b)**. At the case with 300 psi DHS, SRV-pay shows -38.2% change from 2 cp to 10 cp. Compared to the SRV-pay percentage changes caused by treatment rate change from 90 to 150 bpm are lower than that of 2 cp to 10 cp changes.

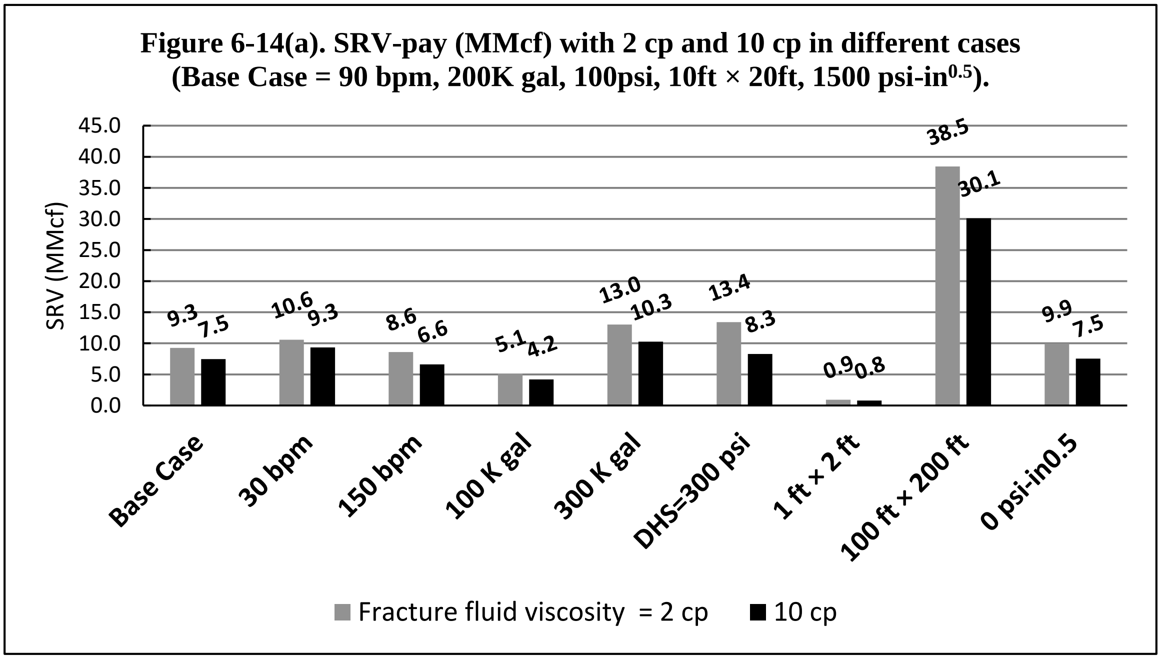

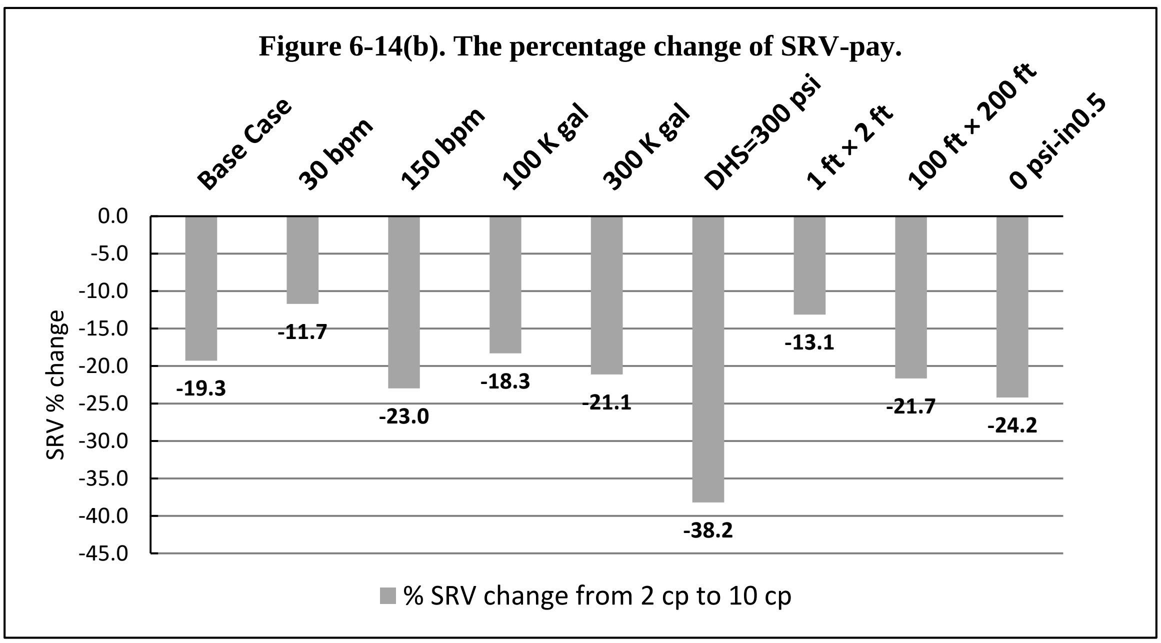

Figure 6-14. (a)SRV-pay (in log scale results) and (b) the percentage change of SRV-pay for fluid viscosity 2 and 10 cp. The x-axis indicates different cases, treatment rate (bpm) and size (K gal), DHS (psi), NF spacing (ft×ft), and fracture toughness (psi-in$^{0.5}$) accordingly.

The effect on FR-pay: FR-pay decreases with increased viscosity in all cases studied. It decreases from 2.21 to 1.69 MMsf when the viscosity is increased from 2 to 10 cp in base case (**Figure 6-15(a)**). Similar to SRV-pay, FR-pay from 10 cp with 30 bpm and 2 cp with 150 bpm has approximately same value of 1.99 MMsf, whereas the case with 10 cp and 300 K gal results in different value, slightly larger FR-pay of 2.38 MMsf. As we discussed in previous section, FR-pay is more sensitive to treatment size than SRV-pay such that it made the difference with larger treatment size. The percentage change ranges from -18.7% to -24.9% as shown in **Figure 6-15(b)**. As injection rate increases, FR-pay becomes less sensitive to the viscosity change. At 30 bpm FR-pay changes -24.9%, -23.5% at 90 bpm, and -21.1% at 150 bpm. The changes in treatment size, DHS, and fracture toughness show less than 1% differences in FR-pay sensitivity over fluid viscosity. In contrast to SRV-pay, changing viscosity has more negative impact over varying treatment rate in the case with 1 ft × 2 ft. The viscosity change generates -20.9% while treatment rate shows -4.2%.

Figure 6-15(a). FR-pay (MMcf) with 2 cp and 10 cp in different cases (Base Case = 90 bpm, 200K gal, 100psi, 10ft × 20ft, 1500 psi-in$^{0.5}$).

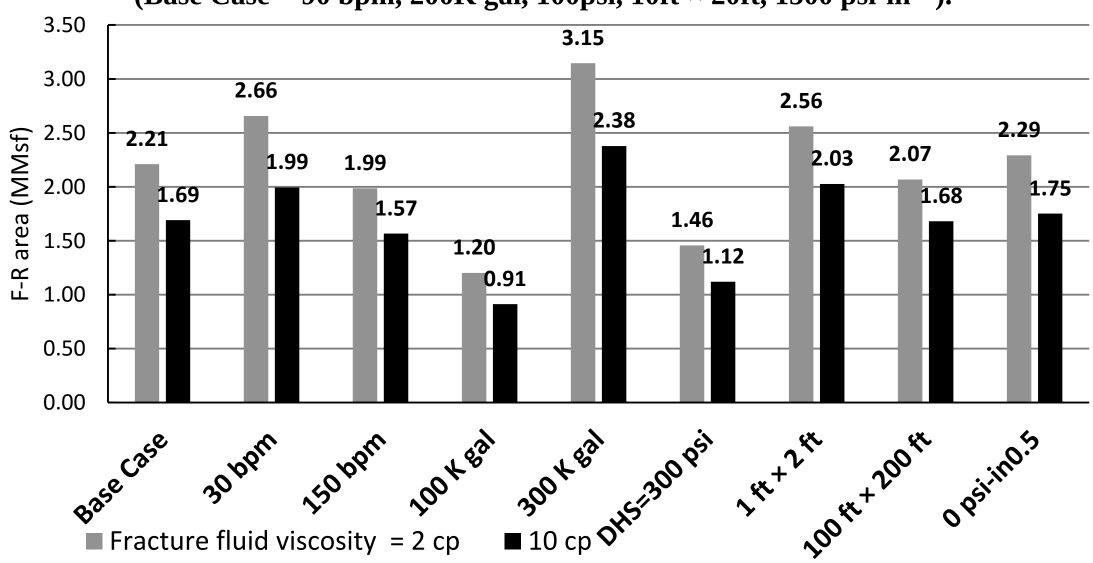

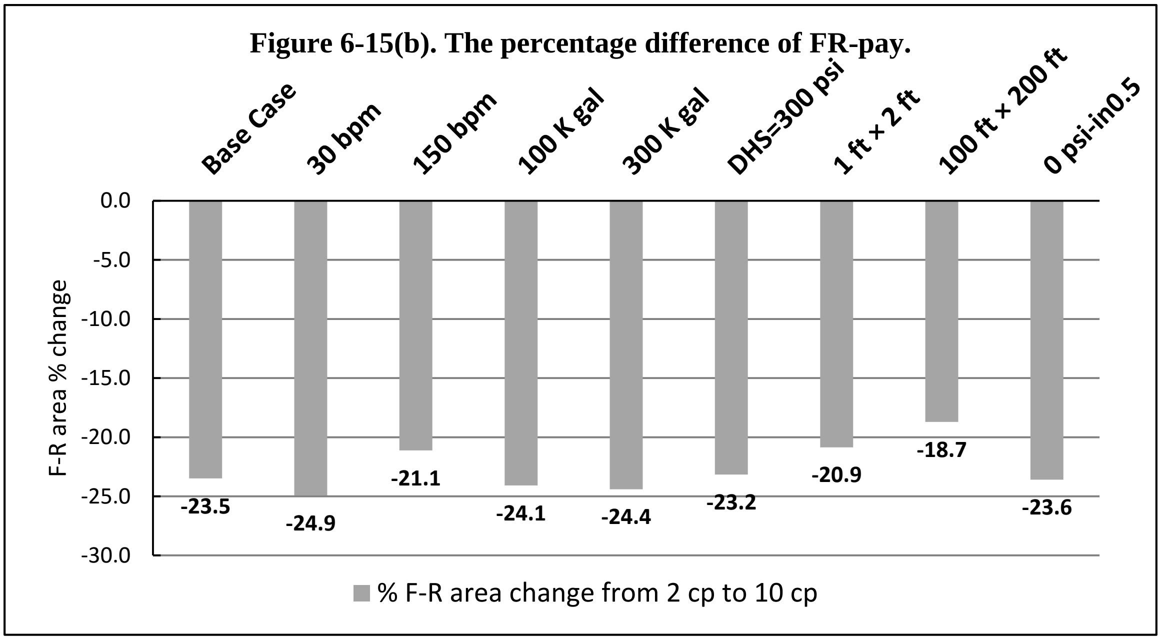

Figure 6-15. (a) FR-pay (MMsf) and (b) the percentage change of FR-pay for fluid viscosity 2 and 10 cp. The x-axis indicates different cases, treatment rate (bpm) and size (K gal), DHS (psi), NF spacing (ft×ft), and fracture toughness (psi-in$^{0.5}$) accordingly.

The effect on the fracture width: In the base case, wf_{perf} increases from 0.225 to 0.352 inch and it increases for all cases as viscosity increases (**Figure 6-16(a)**). Similar to SRV-pay and FR-pay, the width at the case with 10 cp and 30 bpm (0.286 in) is approximately same as the one from 2 cp with 150 bpm (0.287 in). However, the case with 10 cp and 300 K gal has a lot larger width of 0.362 inch. Unlike FR-pay, this change is generated because fracture width is more sensitive to the viscosity change than SRV-pay and FR-pay. From the figure, we can see that increasing the treatment size from 200 K gal to 300 K gal at 10 cp shows the width change from 0.352 to 0.362 inch about 0.01 inch increase. The viscosity change at 300 K gal generates wf_{perf} increase from 0.244 to 0.362 inch which increments 0.118 inch. The percentage change due to viscosity is ranging from 30.2% to 85.7% while varying treatment size causes the change between 3.43% to 24.1%. **Figure 6-16(b)** presents the percentage change from the fluid viscosity, treatment rate and size increases. Except the case with 30 bpm, increasing the viscosity is more effective than changing the injection rate to 150 bpm and treatment size has the least effect. In the case with 30 bpm, increasing viscosity from 2 cp to 10 cp (85.7%) makes 0.2% smaller changes than varying the injection rate from 30 to 150 bpm (85.9%).

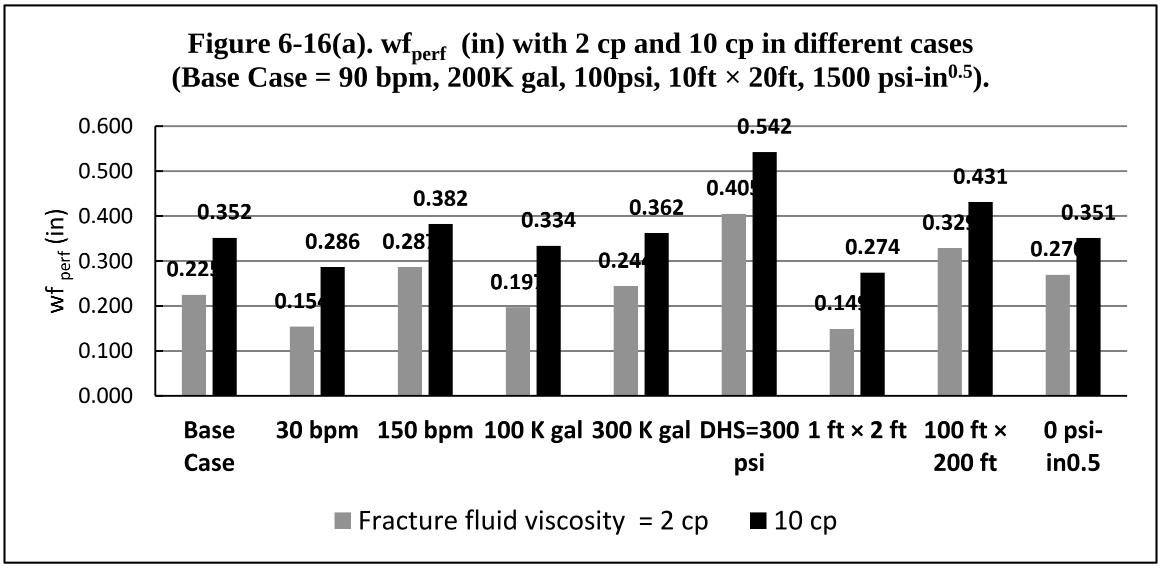

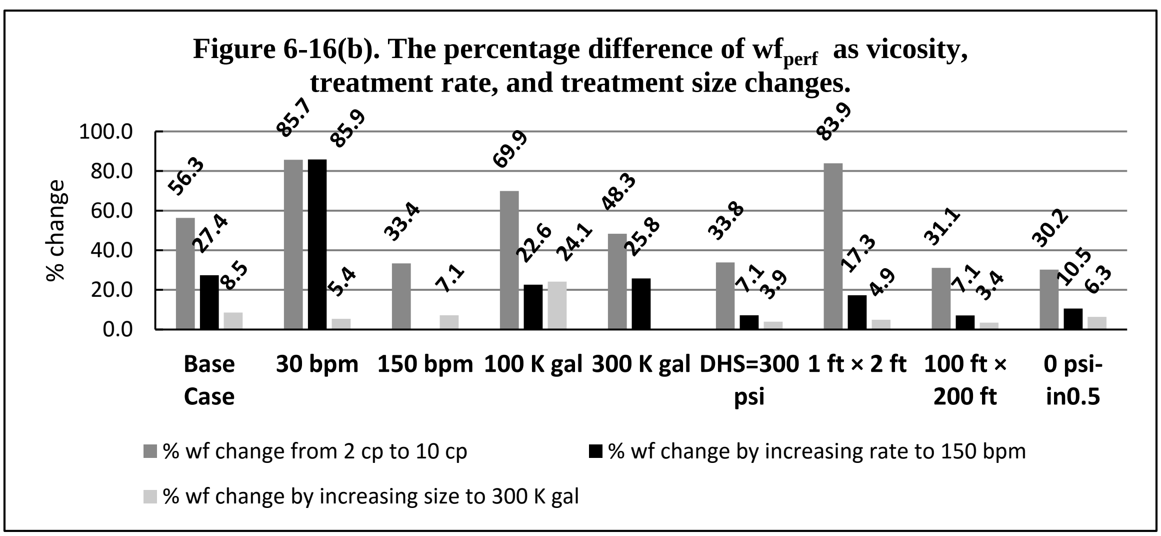

Figure 6-16. (a) wf$_{perf}$ results and (b) the percentage change of wf$_{perf}$ by varying viscosity, treatment rate and size for different cases. The x-axis indicates different cases, treatment rate (bpm) and size (K gal), DHS (psi), NF spacing (ft×ft), and fracture toughness (psi-in$^{0.5}$) accordingly.

The effect on intensity factor: **Figure 6-17(a)** shows the intensity factor results for this study. It is decreased slightly with increased viscosity at all cases excluding 150 bpm, DHS of 300 psi, and 100 ft × 200 ft. For the base case, the intensity factor decreases from 0.24 and 0.23 ft^2/ft^3. The largest intensity is driven by the case having 1 ft × 2 ft NF spacing (2.79, 2.54 ft^2/ft^3) and the least is acquired from 100 ft × 200 ft case (0.0393 and 0.413 ft^2/ft^3). In general, increasing viscosity to 10 cp has less advantage in intensity factor over increasing treatment rate and size (**Figure 6-17(b)**). The cases of 150 bpm, DHS of 300 psi, and 100 ft × 200 ft show opposite effects. The intensity in these cases increases when viscosity increases because the percentage decrease in SRV-pay is less than that of FR-pay. Thus, it is decreased according to **Equation 6-3**.

Figure 6-17(a). Intensity factor (ft^2/ft^3) with 2 cp and 10 cp in different cases.
(Base Case = 90 bpm, 200K gal, 100psi, 10ft × 20ft, 1500 psi-in$^{0.5}$).

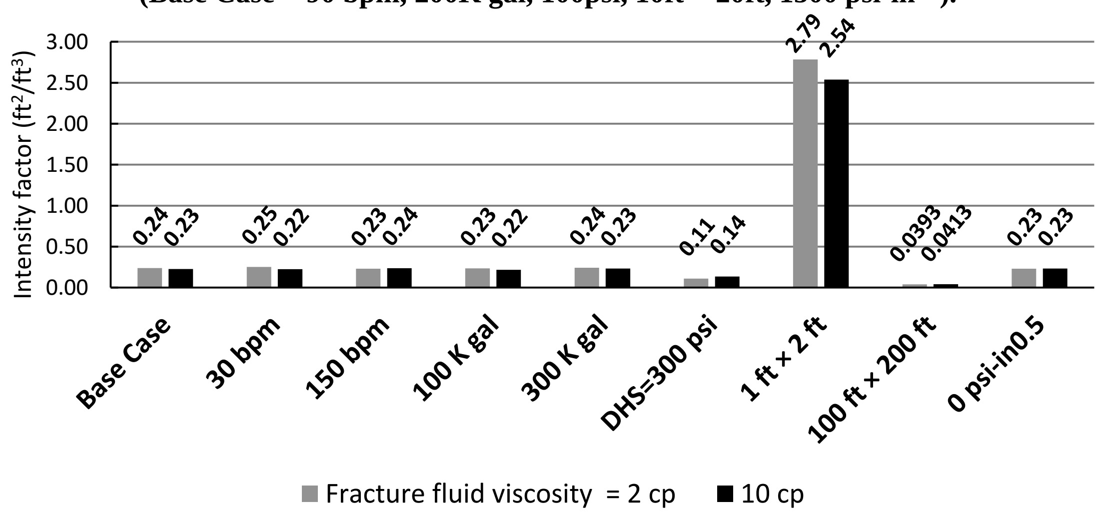

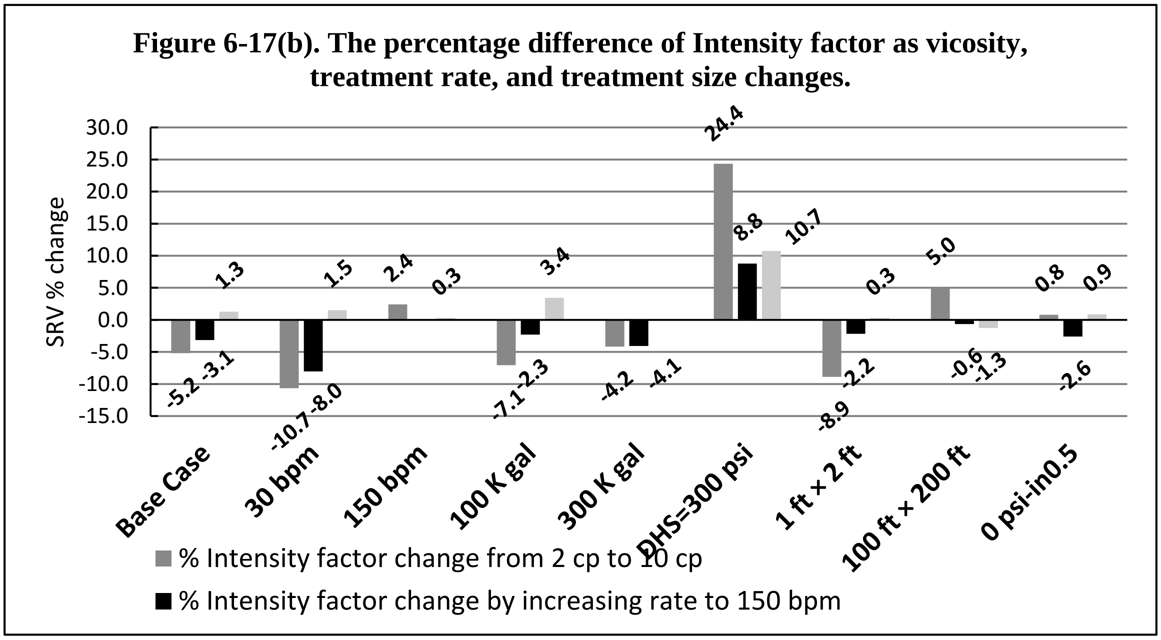

Figure 6-17. (a) Intensity factor and (b) the percentage change of intensity factor by varying viscosity, treatment rate and size for different cases. The x-axis indicates different cases, treatment rate (bpm) and size (K gal), DHS (psi), NF spacing (ft×ft), and fracture toughness (psi-in0.5) accordingly.

6.3.5 Effect of differential horizontal stress (DHS)

The impact of geomechanical properties is evaluated using the knowledge acquired from previous sections. Larger differential horizontal stress (DHS) constrains the fracture growth in secondary direction but enhances SRV, height growth, and width expansion such that created fracture network exhibits losses in intensity and FR-pay for all cases. The comparison of the results between DHS of 100 and 300 psi can be made by evaluating the results from **Figure 6** to **17**. The base case with DHS of 300 psi results SRV-pay of 13.4 MMcf which is about 4.1 MMcf (44.4%) larger than the same case having 100 psi (9.3 MMcf). However, FR-pay decreases from 2.21 MMsf to 1.46 MMsf (-34.1%), wfper increases from 0.225 in to 0.405 inch (80.1%), and intensity changes from 0.24 to 0.11 ft2/ft3 (-54.4%). DHS also alters the shape of created fracture network. The ratio of WHF/LHF for base case changes from 0.218 to 0.005 when DHS is increased from 100 psi to 300 psi.

When DHS is increased, the increase of SRV-pay and wfper, and decrease of FR-pay and intensity factor is expected. Since larger DHS enables accumulation of net pressure in the primary fracture, without increasing treatment rate and size, fluid viscosity, it generates relatively large wf_{perf} (40.6% to 123.5% increase compare to 100 psi case). Thus, the selection of larger proppant is recommended for the reservoir having large DHS. This may increase fracture conductivity and compensate the major loss of FR-pay and intensity factor due to increased DHS. On the other hand, in cases where DHS is lower, focusing on maximizing propped fracture dimension is suggested to increase well productivity.

6.3.6 Effect of natural fracture (NF) spacing

In addition to DHS, NF spacing is another important formation property affecting the hydraulic fracture propagation and reservoir flow capacity. As the NF spacing increases from 1 ft × 2 ft to 10 ft × 20 ft and 100 ft × 200 ft, the increase of SRV-pay and wf_{perf}, and decrease of FR-pay and intensity are observed. SRV-pay are significantly increased about 25 to 45 times ranging from 0.52 MMcf to 57 MMcf and wf_{perf} is also increased 8.1% to 128% (0.11 to 0.43 inches) from 1 ft × 2 ft to 100 ft × 200 ft depending on the cases. In contrast, FR-pay and intensity decreases as NF spacing increases. The intensity from 1 ft × 2 ft to 100 ft × 200 ft changed about -96.2% to -

98.1% with maximum of 2.88 ft^2/ft^3 and minimum of 0.046 ft^2/ft^3. The figures of SRV-pay, FR-pay, wf_{perf}, and intensity are shown below (**Figure 6-18**).

Figure 6-18(a). SRV-pay (MMcf) with 1 ft × 2 ft, 10 ft × 20 ft, 100 ft × 200 ft in different cases (Base Case = 90 bpm, 200 K gal, 2cp, 100psi, 1500 psi-in$^{0.5}$)

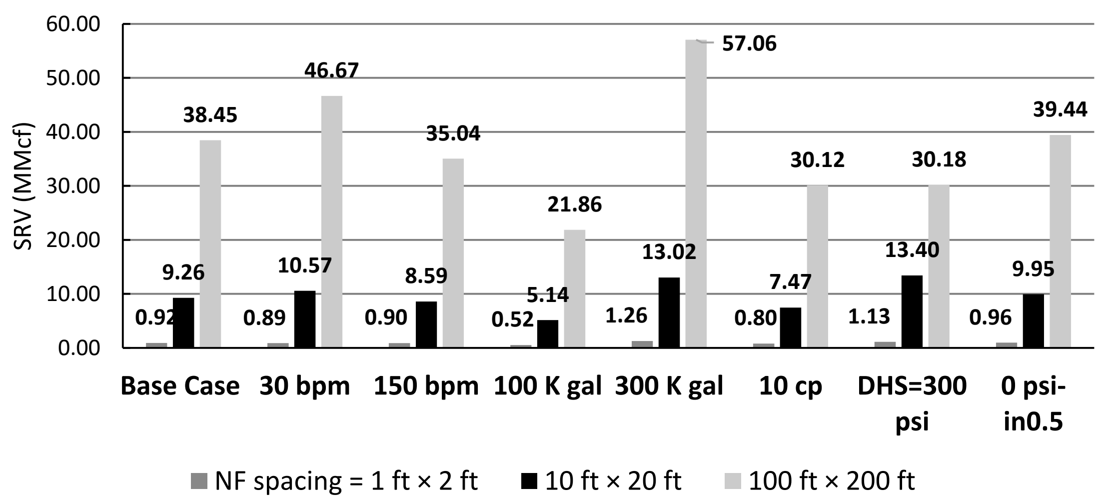

Figure 6-18(b). FR-pay (MMsf) with 1 ft × 2 ft, 10 ft × 20 ft, 100 ft × 200 ft in different cases

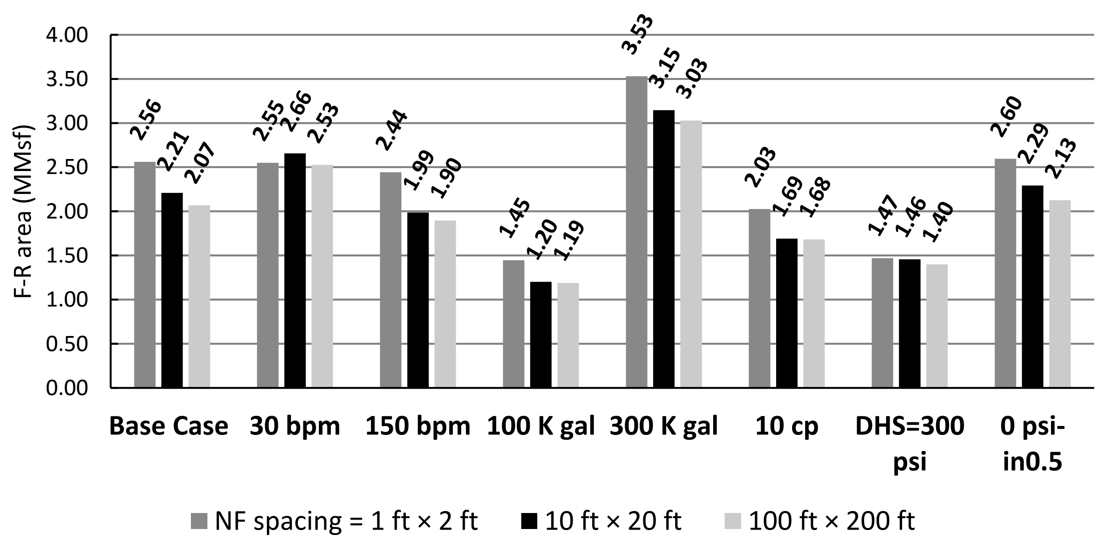

Figure 6-18(d). Intensity factor (ft²/ ft³) with 1 ft × 2 ft, 10 ft × 20 ft, 100 ft × 200 ft in different cases

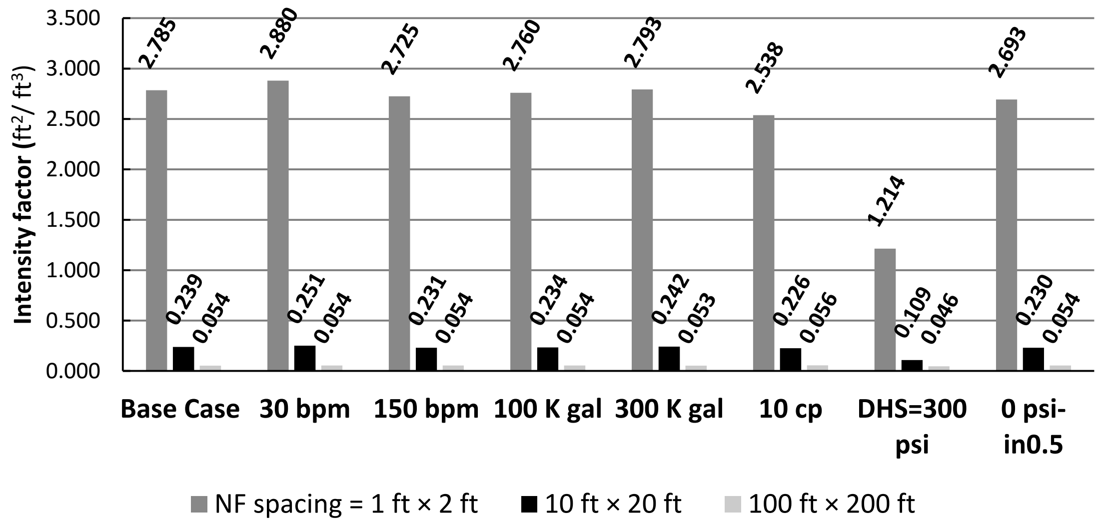

Figure 6-18(c). wf_{perf} (in) with 1 ft × 2 ft, 10 ft × 20 ft, 100 ft × 200 ft in different cases

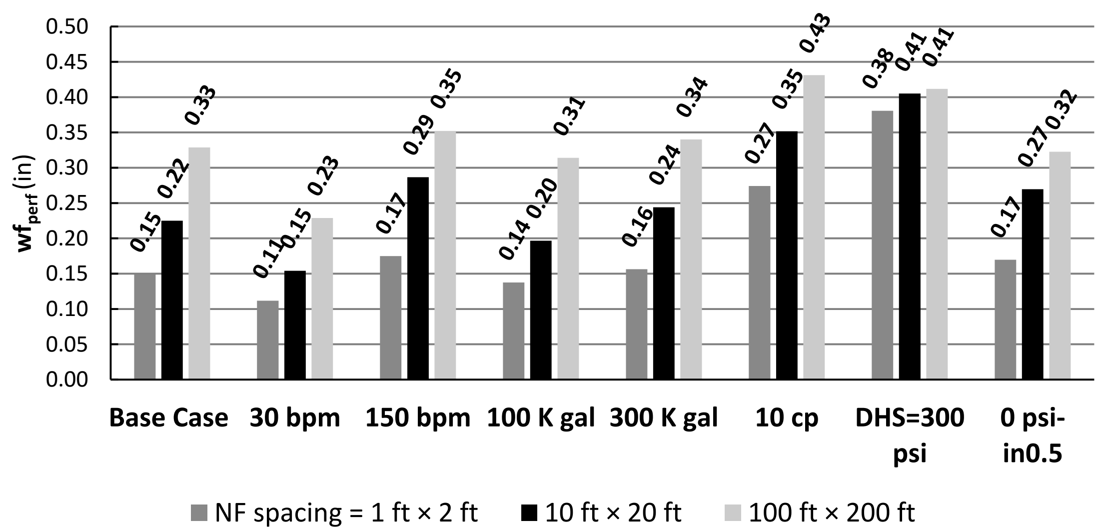

Figure 6-18. (a) SRV-pay (MMcf), (b) FR-pay (MMsf), (c) wf_{perf} (in), and (d) intensity factor by varying viscosity, DHS, K_{IC}, treatment rate and size for different cases. The x-axis indicates different cases, treatment rate (bpm) and size (K gal), viscosity (cp), DHS (psi), and fracture toughness (psi-in0.5) accordingly.

The FR-pay with 30 bpm in **Figure 18(b)** shows different pattern having the largest FR-pay at 10 ft × 20 ft while all other cases shows the largest FR-pay at 1 ft by 2 ft. At 30 bpm case, SRV-pay and FR-pay are limited by the significant amount of fluid leakoff. The fluid efficiency of 1 ft × 2 ft case with 30 bpm drops down to 26.3% from 67.9% with 90 bpm. However, as NF spacing gets larger, lowering treatment rate becomes more and more effective on increasing SRV-pay and FR-pay. Stimulation of formation with small NF spacing such as 1 ft × 2 ft creates FR-pay and intensity but results in a small drainage. It is recommended to us smaller well spacing and closer stage spacing to increase recovery in formation with dense NF. In formation with larger system, less viscous fracture fluid such as gas or energized fluid could enlarge SRV-pay.

The formation having dense NF such as 1 ft × 2 ft case has advantages over FR-pay and intensity but its SRV-pay and wf_{perf} is not comparably larger than in cases where the formation has larger NF spacing. In other words, stimulating a reservoir with large density of NF is similar to creating a reservoir with small drainage radius and larger thickness. Thus, in this case, increasing the density of fracture stages is recommended. It could be better choice than shortening the cluster interval in a single stage because reduction of treatment rate at the perforation may negatively impact SRV-pay or FR-pay. Other options would be re-fracturing or in-fill drilling to recover the loss of SRV-pay. In contrast, if coarse NF is placed in a formation, focusing on increasing FR-pay and intensity factor is recommended.

6.3.7 Effect of fracture toughness

SRV-pay, FR-pay and wf_{perf} are slightly increased when K_{IC} is set to 0. Fracture toughness alters the height, width and length of individual fractures in a network. Consequently, the geometry of the final fracture network is also influenced. However, the changes are relatively small as compared to those resulting from changes in factors considered above. Comparing the base case with 0 psi-in$^{0.5}$ and 1500 psi-in$^{0.5}$, SRV-pay increased from 9.26 MMcf (1500 psi-in$^{0.5}$) to 9.95 MMcf (0 psi-in$^{0.5}$) which is about 7% increase. FR-pay increases from 2.21 to 2.29 MMsf about 3.8%, wf_{perf} increases from 0.225 to 0.27 inch about 19.8%, and the intensity factor decreases from 0.24 to 0.23 about -3.5%.

6.3.7 Guidelines for optimized treatment

The cases having best-performing SRV-pay and FR-pay in different DHS and NF spacing are listed on **Table 6-5**. For NF spacing of 1 ft × 2 ft, best-performing SRV-pay is reached using 30 bpm, 300 K gal and 10 cp and best-performing FR-pay is observed at 90 bpm, 300 K gal and 2 cp with both DHS of 100 psi and 300 psi. For 10 ft × 20 ft and 100 ft × 200 ft cases, 30 bpm, 300 K gal and 2 cp is the case that yields both best-performing SRV-pay and FR-pay. As discussed in Section 6.3.6, lowering both treatment rate and fluid viscosity in 1 ft × 2 ft formation results in excessive fluid loss so that its best-performing SRV-pay is reached with increased fluid viscosity and best-performing FR-pay observed with increased treatment rate compare to larger NF spacing cases. We can also observe that, in 1 ft × 2 ft, increasing fluid viscosity is more effective to increase SRV-pay and increasing treatment rate increases FR-pay better.

Table 6-5. The case having best-performing SRV-pay and FR-pay in different formation settings (NF spacing and DHS). The cases are represented by treatment rate, size, and fluid viscosity.

Formation setting (NF spacing, DHS)	Best-Performing SRV-pay (Treatment rate, size, viscosity)	SRV-pay (MMcf)	Best-Performing FR-pay (Treatment rate, size, viscosity)	FR-pay (MMsf)
1. 1 ft × 2 ft, 100 psi	30 bpm, 300 K gal, 10 cp	2.13	90 bpm, 300 K gal, 2 cp	3.56
2. 1 ft × 2 ft, 300 psi	30 bpm, 300 K gal, 10 cp	2.32	90 bpm, 300 K gal, 2 cp	1.90
3. 10 ft × 20 ft, 100 psi	30 bpm, 300 K gal, 2 cp	14.59	30 bpm, 300 K gal, 2 cp	3.72
4. 10 ft × 20 ft, 300 psi	30 bpm, 300 K gal, 2 cp	22.21	30 bpm, 300 K gal, 2 cp	2.24
5. 100 ft × 200 ft, 100 psi	30 bpm, 300 K gal, 2 cp	65.93	30 bpm, 300 K gal, 2 cp	3.52
6. 100 ft × 200 ft, 300 psi	30 bpm, 300 K gal, 2 cp	51.07	30 bpm, 300 K gal, 2 cp	2.40

6.4 Chapter conclusion

A series of parametric studies were conducted to investigate seven pertinent factors that impact the final fracture network geometry resulting from hydraulic fracture treatment in a naturally fractured shale gas reservoir, as predicted using a coupled 3-diemnesional, 2-phase dual continuum hydraulic fracture simulator. A total of 216 cases were simulated by varying treatment rate, size, natural fracture spacing, fracture fluid viscosity, differential horizontal stress, and fracture toughness. The final fracture geometries are then characterized in terms of the descriptive metrics of: SRV-pay, FR-pay (fracture surface area), fracture width at perforation, and the intensity. Conclusions are summarized below.

1. Increasing the treatment rate from 30 to 90 and 150 bpm reduces SRV-pay (-0.8% to -29.1%) and FR-pay (0.4 to -25.9%) but wf_{perf} is increased 33.5% to 89%. The intensity

factors are decreased -1.3% to -9.1% for all cases except the cases using 10 cp and DHS of 300 psi because the rate decrease of SRV is larger than FR area decrease rate.

2. Larger treatment size increases SRV-pay, FR-pay, wf_{perf}, and intensity factor. However, the efficiency of these parameters (per gallon) are reduced as treatment size increases. The efficiency of SRV-pay drops between -13% to -26.3%, FR-pay -11.1% to -18.7%, wf_{perf} -57.5% to -63.9%, and the intensity factor -60% to 67.5%.

3. Increased fluid viscosity decreases SRV-pay and FR-pay but increases wf_{perf}. Compare to the case increasing the treatment rate for 90 bpm to 150 bpm, increasing fluid viscosity from 2 cp to 10 cp provides bigger impact on the evaluation parameters for all cases. 90 bpm to 150 bpm decreases SRV-pay between -0.8 to -14.4% but changing viscosity from 2 cp to 10 cp results in -13.1% to -38.2% changes.

4. Larger differential horizontal stress (DHS) results in the increase of SRV-pay and wf_{perf}, and results in decreased FR-pay and intensity factor. It also alters the shape of created fracture network. The ratio of WHF/LHF for base case changes from 0.218 to 0.005 when DHS is increased from 100 psi to 300 psi.

5. Larger NF spacing increases SRV-pay and wf_{perf}, and decreases of FR-pay and intensity are observed. It is recommended to us smaller well spacing and closer stage spacing to increase recovery in formation with dense NF. In formation with larger system, less viscous fracture fluid such as gas or energized fluid could enlarge SRV-pay.

6. Lowering fracture toughness from 1500 psi-in$^{0.5}$ to 0 psi-in$^{0.5}$ results in a slight increase of SRV-pay, FR-pay and wf_{perf}, and the decrease of intensity factor. The changes are observed between (-4.3% to 8.4%). Fracture toughness slightly alters the shape of final fracture network.

In conclusion, the findings help to elucidate important trends in hydraulic fracturing of shale reservoirs that are helpful in the improved design of treatments for specific reservoir settings. For further work, the case-specific (geologic case) optimization of treatment design to maximize one or more of the discussed objective functions will be studied.

6.5 Nomenclature

c_t = total compressibility (psi^{-1})

FR-pay = fracture-reservoir contact area in pay (MMsf)

hf = fracture height (ft)

K_{IC} = fracture toughness (psi-in$^{0.5}$)

k = permeability (md)

L_{HF} = length of final fracture network (ft)

S_w = water saturation (fraction)

SRV-pay = stimulated reservoir volume in pay (MMcf)

wf_{perf} = the fracture width at perforation (in)

W_{HF} = width of final fracture network (ft)

μ = viscosity (cp)

ϕ = porosity (fraction)

σ = stress (psi)

6.6 Chapter reference

52. Ahn, C. H., Chang, O. C., Dilmore, R., & Wang, J. Y. (2014a, August 28). A Hydraulic Fracture Network Propagation Model in Shale Gas Reservoirs: Parametric Studies to Enhance the Effectiveness of Stimulation. Society of Petroleum Engineers. doi:10.15530/urtec-2014-1922580
53. Ahn, C. H., Dilmore, Robert and Wang, J.Y. 2014b. Development of innovative and efficient hydraulic fracturing numerical simulation model and parametric studies in unconventional naturally fractured reservoirs. Journal of Unconventional Oil and Gas Resources Vol. 8: pg25-45. doi:10.1016/j.juogr.2014.06.003
54. Cipolla, C. L., Mack, M. G., Maxwell, S. C., & Downie, R. C. (2011b, January 1). A Practical Guide to Interpreting Microseismic Measurements. Society of Petroleum Engineers. doi:10.2118/144067-MS
55. Cipolla, C. L., Maxwell, S. C., & Mack, M. G. (2012, January 1). Engineering Guide to the Application of Microseismic Interpretations. Society of Petroleum Engineers. doi:10.2118/152165-MS
56. Cipolla, C., & Wallace, J. (2014, February 4). Stimulated Reservoir Volume: A Misapplied Concept? Society of Petroleum Engineers. doi:10.2118/168596-MS
57. Chatas, A. 1953. A practical treatment of nonsteady-state flow problems in reservoir systems. The petroleum engineer, B-44
58. Daungkaew, S., F. Hollaender, and A. Gringarten. 2000. Frequently asked questions in well test analysis. SPE 63077, SPE ATCE, Dallas, Texas.
59. Daniels, J. L., Waters, G. A., Le Calvez, J. H., Bentley, D., & Lassek, J. T. (2007, January 1). Contacting More of the Barnett Shale Through an Integration of Real-Time Microseismic Monitoring, Petrophysics, and Hydraulic Fracture Design. Society of Petroleum Engineers. doi:10.2118/110562-MS
60. Fisher, M. K., Wright, C. A., Davidson, B. M., Goodwin, A. K., Fielder, E. O., Buckler, W. S., & Steinsberger, N. P. (2002, January 1). Integrating Fracture Mapping Technologies to Optimize Stimulations in the Barnett Shale. Society of Petroleum Engineers. doi:10.2118/77441-MS
61. Gu, H., Weng, X., Lund, J.B., Mack, M.G., Ganguly, U. and Suarez-Rivera, R. 2011. Hydraulic Fracture Crossing Natural Fracture at Non-Orthogonal Angles, A Criterion, Its Validation and Applications. Paper SPE-139984-MS presented at the SPE HFTC, Woodland, Texas, 24-26 Jan. doi: 10.2118/139984-MS.
62. Keshavarzi, R. and Mohammadi, S. 2012. A new Approach for numerical Modeling of Hydraulic Fracture Propagation in Naturally Fractured Reservoirs. SPE 152509-MS
63. Mayerhofer, M. J., Lolon, E., Warpinski, N. R., Cipolla, C. L., Walser, D. W., & Rightmire, C. M. (2010, February 1). What Is Stimulated Reservoir Volume? Society of Petroleum Engineers. doi:10.2118/119890-PA
64. Meyer, R. B. and Lucas W. Bazan. 2011. A Discrete Fracture Network Model for Hydraulically Induced Fractures - Theory, Parametric and Case Studies. Paper SPE 140514 presented at SPE Hydraulic Fracturing Technology Conference, 24-26 January 2011, The Woodlands, Texas, USA. doi: 10.2118/140514-MS

65. Taleghani, A.D. and Olson, J.E. 2011. Numerical modeling of Multistranded-hydraulic-Fracture Propagation: Accounting for the interaction Between Induced and Natural Fractures. SPEJ 16 (3): 575-581. SPE-124884-PA. doi: 10.2118/124884-PA.
66. Taleghani, A.D. and Olson, J.E. 2013. How Natural Fractures Could Affect Hydraulic-Fracture Geometry. SPEJ SPE-167608-PA. doi: 10.2118/167608-PA.
67. Weng, X., Kresse, O., Cohen C., Wu R., and Gu H. 2011. Modeling of Hydraulic Fracture Network Propagation in a Naturally Fractured Formation. SPE Production & Operations 26 (4): 368-380. SPE-140253-PA. doi: 10.2118/9878-PA. doi: 10.2118/140253-PA.
68. Wu, R., Kresse, O., Weng, X., Cohen, C.-E., & Gu, H. (2012, January 1). Modeling of Interaction of Hydraulic Fractures in Complex Fracture Networks. Society of Petroleum Engineers. doi:10.2118/152052-MS
69. Wu, K., & Olson, J. E. (2015, April 1). Simultaneous Multifracture Treatments: Fully Coupled Fluid Flow and Fracture Mechanics for Horizontal Wells. Society of Petroleum Engineers. doi:10.2118/167626-PA

Chapter 7 CONCLUSION & RECOMMENDATION

A 3-dimensional, 2-phase hydraulic fracturing simulator was developed, and its performance was verified against other accepted hydraulic fracture propagation models. This model is capable of simulating the propagation of hydraulic fractures into a formation with pre-existing natural fractures. The dynamic change of reservoir pressure due to the fracture flow leakoff is also included in the model. In addition, the separation of domains into fracture and matrix domains and the use of the moving coordinate approach will reduce the simulation time compared to the single porosity approach so a complex fracture network can be simulated with time efficiency. The features of the model are:

1. 3-dimensional hydraulic fracture geomechanical changes can be captured using the finite volume method with the equilibrium multi-layer height growth and can account for the effect of the stress shadow in settings with pre-existing natural fractures;

2. Fracture fluid leakoff, or the flow from fracture-to-matrix, can be modeled with the dual-porosity and dual-permeability method with a pressure dependent multi-phase flow applied to simulate the effect of capillary imbibition and relative permeability;

3. Iterative coupling between the fracture and matrix domain enables tracing of dynamic reservoir property changes, including three-dimensional saturation and effective permeability effects.

This verified model can be utilized to develop credible insights into the dynamics of fracturing in shale and can be used to advance the understanding of how a naturally fractured formation can be stimulated to maximize resource recovery.

In this study, three sets of parametric studies were conducted. Two sets were performed using a 2D, single-phase model and the other using a 3D, two-phase model. The parameters studied include treatment rate, treatment size, differential horizontal stress, natural fracture spacing, fracture fluid viscosity, proppant size, and fracture toughness. The effect of these parameters was evaluated using SRV, the fracture-reservoir contact area, w_{perf}, and the fracture intensity factor to provide a better indication of the effectiveness of the created fracture network. The key findings from the parametric studies are:

4. Increasing the treatment rate from 30 to 90 and 150 bpm reduces SRV-pay (-0.8% to -29.1%) and FR-pay (0.4 to -25.9%), but wf_{perf} increased from 33.5% to 89%. The intensity factors decreased from -1.3% to -9.1% for all cases except the cases using 10 cp and DHS of 300 psi because the rate decrease of SRV is larger than FR area decrease rate.

5. Larger treatment size increased SRV-pay, FR-pay, wf_{perf}, and the intensity factor; however, the efficiency of these parameters (per gallon) was reduced as the treatment size increased. The efficiency decreased from -13% to -26.3% for SRV-pay, -11.1% to -18.7% for FR-pay, -57.5% to -63.9% for wf_{perf}, and -60% to 67.5% for the intensity factor.

6. Increased fluid viscosity decreases SRV-pay and FR-pay but increases wf_{perf}. Compared to the case of increasing the treatment rate from 90 bpm to 150 bpm, increasing the fluid viscosity from 2 cp to 10 cp provides a larger impact on the evaluation parameters for all

cases. An increase from 90 bpm to 150 bpm decreases SRV-pay from -0.8% to -14.4%, but changing the viscosity from 2 cp to 10 cp results in a change from -13.1% to -38.2%.

7. A larger differential horizontal stress (DHS) results in the increase of SRV-pay and wf_{perf} and results in the decrease of FR-pay and the intensity factor. It also alters the shape of the created fracture network. The ratio of WHF/LHF for base case changes from 0.218 to 0.005 when DHS is increased from 100 psi to 300 psi.

8. A larger NF spacing increases SRV-pay and wf_{perf}, and decreases in FR-pay and intensity are observed. It is recommended to use a smaller well spacing and closer stage spacing to increase recovery in a formation with a dense NF. In a formation with a larger system, a lower amount of viscous fracture fluid, such as gas or energized fluid, could increase SRV-pay.

9. Lowering the fracture toughness from 1500 psi-in$^{0.5}$ to 0 psi-in$^{0.5}$ results in a slight increase of SRV-pay, FR-pay, and wf_{perf} and results in a decrease of the intensity factor. The changes are observed between -4.3% and 8.4%. Fracture toughness slightly alters the shape of the final fracture network.

10. Decreasing the size of the proppant can increase the propped SRV but would decrease the conductivity of propped fractures. When changing the proppant size from 20/40 to 40/70 to 70/140, the propped SRV (PSRV) increased 567% from 20/40 to 40/70 and 150% from 40/70 to 70/140.

11. The best-performing SRV-pay and FR-pay was found when the treatment rate and fracture fluid viscosity was lower, and the treatment size is larger for a reservoir that has a larger

NF spacing; however, if NF spacing is small (close to 1 ft × 2 ft), lowering both the treatment rate and the fluid results in excessive fluid loss. Therefore, its best-performing SRV-pay was reached with increased fluid viscosity, and its best-performing FR-pay was observed with an increased treatment rate.

In conclusion, the findings are useful in elucidating the important trends in the hydraulic fracturing of shale reservoirs and are helpful in the improved design of treatments for specific reservoir settings. In further studies, the case-specific (geologic case) optimization of the treatment design to maximize one or more of the discussed objective functions will be studied.

APPENDIX

SI METRIC CONVERSION FACTORS

cp×1.0* E – 03 =Pa.s

ft × 3.048 E – 01 = m

ft^3×2.831 685 E – 02 = m^3

in.×2.54* E – 00 = cm

psi.× 6.894 747 E – 00 =kPa

*Conversion factor is exact

VITA

Chong Hyun Ahn was born in Seoul, South Korea, on November 12, 1980. After finishing high school in 1999, he performed his military service in the Korean army. Between 2005 and 2009 he studied mathematics at the University of Texas at Austin and received B.S.. He received an M.S. in petroleum and natural gas engineering from the Pennsylvania State University in August 2012, and a Ph.D. in energy and mineral engineering in August 2016.